ENERGY AND BUILT ENVIRONMENT

Volume 2 April 2021

CONTENTS

INDEXED/ABSTRACTED IN:
Energy and Built Environment, Compendex, Architectural Periodicals Index, Cambridge Scientific Abstracts, Current Contents - Engineering, Technology & Applied Sciences, Current Energy Information, Energy Abstracts, EIC/Intelligence (Energy Index), Environmental Periodicals Bibliography, Focus On: Global Change, Fuel and Energy Abstracts, Scopus, Science Citation Index Expanded, INSPEC, Also covered in the abstract and citation database SCOPUS®. Full text available on ScienceDirect®.

2666-1233(202104)2:2;1-D

ISSN 2666-1233

Printed by CPI Antony Rowe, Pegasus Way, Melksham, UK

KeAi

Production and Hosting by Elsevier on behalf of KeAi

ISSN: 2666-1233

Energy and Built Environment

Volume 2 • Issue 2 • April 2021

ScienceDirect
Available online at **www.sciencedirect.com**

Aims and Scope:

Energy and Built Environment (EBE) is an international journal disseminating original research articles on energy harvest and utilization in built environment. The aim is to present new research results focused on promoting energy efficiency, clean energy utilization, and environment quality in built environment related to buildings and transportation.

We encourage submissions in the following areas

- Energy conservation and balances in built environment
- Energy storage technologies and their applications in built environment
- Application and integration of renewable energy technologies in built environment
- Evaluation and control of indoor environment quality (acoustic, visual, thermal and air quality)
- Impact of climate change on built environment performance
- Modelling and prediction technologies for built environment

Energy and Built Environment

Volume 2 (2021)

ELSEVIER
Amsterdam • Boston • London • New York • Oxford • Paris • Philadelphia • San Diego • St Louis

Energy and Built Environment

Energy and Built Environment 2 (2021) 127–136

Contents lists available at ScienceDirect

Energy and Built Environment

journal homepage: http://www.keaipublishing.com/en/journals/energy-and-built-environment/

Analysis of influence of the length of ground heat exchangers on the operation characteristics and economy of ground source heat pumps

Hongzhi Zhang[a], Zongwei Han[a,*], Lingyan Yang[b], Jiawei Yuan[a], Xinlu Cheng[a], Mingzhen Ji[a], Gui Li[a]

[a] *SEP Key Laboratory of Eco-Industry, School of Metallurgy, Northeastern University, Shenyang 110819, China*
[b] *China Academy of Building Research, Beijing 100013, China*

ARTICLE INFO

Keywords:
Buried depth
Dynamic simulation
Coefficient of performance
Economic analysis

ABSTRACT

A three-dimensional finite element dynamic simulation platform of the ground source heat pump system (GSHPS) is established. According to the outlet temperature of ground heat exchangers (GHEs) required by the code in summer and winter, the calculated minimum buried depth of GHEs meeting the requirements is 60 m, when the number of borehole is 9. By using the established platform, the annual operation performance and cost of the GSHPS under different buried pipe depths are studied. The results show that the deeper the buried depth of GHEs is, the better the heat exchange effect of GHEs is. Compared with the GHEs with 60 m buried depth, when the buried depth of GHEs is 65 m, 70 m, 75 m and 80 m, the average coefficient of performance (COP) of the unit increases by 4.1%, 6.3%, 7.7% and 8.2% in cooling period and 1.0%, 1.6%, 1.8% and 1.9% in heating period, respectively. Considering the performance and initial investment of the GHSPS comprehensively, the optimal buried depth of GHEs is 60 m. However, considering the performance the system and the total cost of the system running for 20 years comprehensively, the optimal buried depth of GHEs is 70 m.

1. Introduction

In recent years, the energy consumption of heating and air conditioning in buildings has increased sharply, accounting for about 40% of the total social energy consumption [1]. The ground source heat pump system (GSHPS) has been widely used in the world because of its high-efficiency and environmental-friendly characteristics [2–4].

As one of the crucial parts of the GSHPS, ground heat exchangers (GHEs) are mostly responsible for the performance and cost of the whole system [5,6]. The primary design parameter for GHEs is their buried depth [7], as it determines the possible heat extraction from the soil. The deeper the buried depth of GHEs is, the higher the possible heat extraction is. But the increase of buried pipe depth will also lead to the increase of drilling cost. Due to these limitations, on the basis of satisfying the total thermal energy demand of the GSHPS, the buried depth of GHEs should be as small as possible [8].

For the experimental research on the buried depth of GHEs, Li et al. [9] set up a set of experiments to assess the influence of buried pipe depth on the performance of the GSHPS. The results showed that the maximum energy efficiency coefficient of GHEs with 60 m buried depth is 0.15 higher than that of GHEs with 40 m buried depth in summer. Esen and Turgut [10] carried out experimental research on the GHEs under three different buried depths. They found that the larger the buried depth of GHEs is, the higher the coefficient of performance (COP) of the ground source heat pump (GSHP) unit is. Compared with the GHEs with 30 m depth, the average COP of the unit increased by 0.44 and 1.10 respectively, when the buried depth of GHEs is 60 m and 90 m. Chang and Kim [11] used the in-situ thermal response test to identify soil thermal conductivity under different buried pipe depths. The results showed that the soil thermal conductivity of the ground heat exchanger with 150 m buried depth was 34.1% higher than that of the ground heat exchanger with 100 m buried depth. Zhai et al. [12] designed and installed a minitype GSHPS in the green energy building of Shanghai Jiao Tong University. In this system, the buried depth of GHEs is 50 m, 60 m and 80 m respectively. They found that in typical heating mode, compared with the GHEs with 80 m buried depth, the average outlet temperature of GHEs decreased by 0.9 °C and 0.6 °C respectively, when the buried depth of GHEs is 50 m and 60 m.

Studies on the influence of buried pipe depth on the performance of the GSHPS are mostly based on the numerical simulation. Wang et al. [13] developed a comprehensive simulation model, and simulated the heat transfer process of GHEs with different buried depths by using Computational Fluid Dynamic technique. They found that the buried depth of GHEs must be larger than 40 m to guarantee the sustainability for heating, and it should be not less 70 m to guarantee a higher

* Corresponding author.
E-mail address: hanzongwei_neu@163.com (Z. Han).

https://doi.org/10.1016/j.enbenv.2020.09.003
Available online 11 September 2020

Nomenclature

Symbols

λ_s	thermal conductivity of soil [W/(m•K)]
λ_b	thermal conductivity of backfill material [W/(m•K)]
ρ_s	density of soil [kg/m^3]
ρ_b	density of backfill material [kg/m^3]
c_s	specific heat capacity of soil [J/(kg•K)]
c_b	specific heat capacity of backfill material [J/(kg•K)]
T	temperature [°C]
t	time [s]
q_h	heating capacity of unit [kW]
q_c	cooling capacity of unit [kW]
q_{hd}	rated heating capacity of unit [kW]
q_{cd}	rated cooling capacity of unit [kW]
p_h	power consumption under heating condition [kW]
p_c	power consumption under cooling condition [kW]
p_{hd}	rated power consumption under heating condition [kW]
p_{cd}	rated power consumption under cooling condition [kW]
$T_{out,\ h}$	outlet temperature under heating condition [°C]
$T_{out,\ c}$	outlet temperature under cooling condition [°C]
$T_{in,\ h}$	inlet temperature under heating condition [°C]
$T_{in,\ c}$	inlet temperature under cooling condition [°C]
a_1	fitting parameter [°C^{-1}]
b_1	fitting parameter
c_1	fitting parameter [°C^{-1}]
d_1	fitting parameter
a_2	fitting parameter [°C^{-1}]
b_2	fitting parameter
c_2	fitting parameter [°C^{-1}]
d_2	fitting parameter
ρ'	fluid density in pipes [kg/m^3]
c'	specific heat capacity of fluid in pipes [J/(kg•K)]
S	total cross-sectional area of buried pipes [m^2]
v	fluid velocity in pipes [m/s]
m_d	cost of drilling [RMB]
m_b	cost of backfilling material [RMB]
m_g	cost of single U-tube GHEs [RMB]
l	total length of GHEs [m]
u_d	cost per unit pipe length of drilling [RMB/m]
u_b	cost per unit pipe length of backfilling material [RMB/m]
u_g	cost per unit pipe length of single U-tube GHEs [RMB/m]
m_i	total cost of buried pipes [RMB]
m_e	electricity charge of system running for 20 years [RMB]
n	power consumption of system running for 1 year [kWh]
u_e	electricity charge per kilowatt hour [RMB/kWh]
m_r	total cost of system running for 20 years [RMB]

Superscripts

i	previous moment
i + 1	next moment

Acronyms

GSHPS	Ground Source Heat Pump System
GSHP	Ground Source Heat Pump
GHEs	Ground Heat Exchangers
COP	Coefficient of Performance

long-term energy efficiency of the system. Han et al. [14] established a dynamic simulation model of the GSHPS, designed GHEs according to the ASHRAE method, and studied the influence of buried pipe depth on the design error of the ASHRAE method. The design error is the ratio of the difference between the actual outlet temperature and the set outlet temperature to the set outlet temperature. It was concluded that when the buried depth of GHEs increased from 60 m to 80 m, the design error of ASHRAE method increased in summer and decreased in winter. Sandler et al. [15] used a steady-state numerical model to assess the overall U-pipe performance. The results indicated that when the buried depth of the ground heat exchanger increased from 30 m to 100 m, the absolute temperature difference between the inlet and outlet of the ground heat exchanger increased by 36%. Casasso and Sethi [16] ran a set of heat transport simulations to evaluate the impact of different parameters on the operation performance of the GSHPS. The results proved that the buried depth of the ground heat exchanger was the most important parameter in the design of the GSHPS. When the buried depth of the ground heat exchanger increased from 50 m to 75 m, the minimum inlet temperature of the ground heat exchanger increased by 4.15 °C during heating period. Chen et al. [17] developed a three-dimensional unsteady numerical model of the ground heat exchanger by using the finite volume method, and simulated the heat transfer flux of the ground heat exchanger under different buried depths. They found that when the inlet flow rate of the ground heat exchanger was equal, the heat transfer flux per unit borehole depth of the ground heat exchanger with 50 m buried depth was 23.15 W/m higher than that of the ground heat exchanger with 100 m buried depth. Li et al. [18] established a three-dimensional equivalent rectangular numerical model to evaluate the fluid temperature variation along the pipe. The results showed that compared with the ground heat exchanger with 80 m buried depth, the temperature difference between the inlet and outlet of the ground heat exchanger increased by 17% and 27% respectively, when the buried depth of the ground heat exchanger is 120 m and 200 m.

The buried depth of GHEs not only affects the performance of the GSHPS, but also affects the cost of the GSHPS. Esen et al. [19] studied the performance and cost of the GSHPS under different buried pipe depths by experimental method. According to the experimental results, the performance of the GSHPS can reach the best when the buried depth of the ground heat exchanger is 90 m. When considering the cost of digging, the optimum buried depth of the ground heat exchanger is 60 m. Chen et al. [20] presented a numerical heat transfer model for vertical U-tube GHEs, and simulated the heat transfer performance of GHEs with different buried depths (from 60 m to 100 m). The results demonstrated that the heat transfer flux per unit pipe length of GHEs is the same when the buried pipe depth is 60 m and 70 m. Compared with GHEs under other buried depths, the heat transfer flux per unit pipe length of GHEs with the buried depth of 60 m and 70 m is the largest. When the buried depth of GHEs is 70 m, the total length of GHEs is the shortest, and the initial investment of the system is the lowest. Zhou et al. [21] established a detailed numerical model to analyze the thermal performance and economic efficiency of the GSHPS under different buried pipe depths. The results showed that the optimal buried depth of the ground heat exchanger was 40 m when considering only the thermal performance of the GSHPS. When the unit price per meter of the borehole drilling was ¥70/m, the optimal buried depth of the ground heat exchanger is 60 m, but when the unit price per meter of the borehole drilling was ¥150/m, the optimal buried depth of the ground heat exchanger was 40 m.

To summarize, the buried depth of the ground heat exchanger has a great impact on the GSHPS. However, the references [9–18] only study the influence of buried depth of the ground heat exchanger on the performance of the GSHPS, but do not study the influence of buried depth of the ground heat exchanger on the cost of the GSHPS. In addition, the studies on buried pipe depth in references [9,10,12,13] are based on the constant load condition, and the studies on buried pipe depth in references [11,15–18] are based on the single borehole model.

Currently, there are few studies that not only consider the influence of buried pipe depth on the performance of the GSHPS, but also consider the influence of buried pipe depth on the cost of the GSHPS. Although references [19–21] study the influence of buried pipe depth on the performance and cost of the system, the studies on buried pipe depth in

Table 1
Parameters of each part of the model.

Outer diameter of buried pipes	Inner diameter of buried pipes	Center distance of pipe legs	Drilling diameter	Borehole spacing
32mm	26mm	70mm	150mm	4.5m

references [19,20] are also based on the constant load condition, and the studies on buried pipe depth in references [19,21] are also based on the single borehole model.

In the actual operation process of the GSHPS, the load in the building can not be the same every day, that is to say, the building load can not be constant. On account of the defects of above research and in order to be more close to the actual working process of the GSHPS, this paper establishes a three-dimensional finite element dynamic simulation platform of the GSHPS. There are 9 boreholes in this simulation platform, and the simulation platform realizes that the inlet and outlet temperature of GHEs changes with the change of the daily building load. By using this platform, the influence of buried depth of GHEs on the performance of the GSHPS is studied, the cost of the GSHPS under different buried pipe depths is compared, and the optimum buried depth of GHEs is obtained, which will provide a reference for the actual engineering design and operation of the GSHPS.

2. Establishment and validation of the simulation platform

2.1. Physical model

To analyze the influence of the buried depth of GHEs on the GSHPS, the three-dimensional pipe group physical model with different buried depths is established. There are 9 boreholes in the model, and the layout of buried pipes is arranged in square. According to the difference of buried depth, the buried depth of GHEs can be divided into the shallow buried (less than 30 m), medium buried (30~100 m) and deep buried (more than 100 m). In the research of this paper, the selected buried depth of GHEs is the medium buried. The parameters of each part of the model are shown in Table 1. In order to improve the calculation speed, the areas far away from the center of boreholes with relatively smaller temperature gradient change are divided into rough meshes. To ensure the accuracy of calculation, the U-tube group with larger temperature gradient change and its surrounding areas are divided into fine grids. The grid distribution of the model is shown in Fig. 1.

2.2. Mathematical model

In order to reduce the difficulty of solution, the following assumptions are made in the process of establishing the mathematical model:

(1) The soil is homogeneous and isotropic;
(2) Neglecting the flow of water in soil;
(3) The thermal contact resistance between buried pipes and backfill material and that between backfill material and soil are ignored;
(4) The thermophysical properties of soil, buried pipes and circulating fluid in pipes are independent of temperature.

The mass conservation equation, momentum conservation equation, energy conservation equation and Navier-Stokes (N-S) equation are used to establish the mathematical model of the heat transfer process of circulating fluid in pipes. The heat conduction process of soil and backfill material can be expressed by the three-dimensional unsteady heat conduction differential equation [22,23]:

$$\rho_s c_s \frac{\partial T}{\partial t} = \frac{\partial}{\partial x} \cdot \left(\lambda_s \frac{\partial T}{\partial x}\right) + \frac{\partial}{\partial y} \cdot \left(\lambda_s \frac{\partial T}{\partial y}\right) + \frac{\partial}{\partial z}\left(\lambda_s \frac{\partial T}{\partial z}\right) \tag{1}$$

$$\rho_b c_b \frac{\partial T}{\partial t} = \frac{\partial}{\partial x} \cdot \left(\lambda_b \frac{\partial T}{\partial x}\right) + \frac{\partial}{\partial y} \cdot \left(\lambda_b \frac{\partial T}{\partial y}\right) + \frac{\partial}{\partial z}\left(\lambda_b \frac{\partial T}{\partial z}\right) \tag{2}$$

where ρ represents the density; c represents the specific heat capacity; λ represents the thermal conductivity; the subscripts s and b represent soil and backfill material respectively; T is temperature; t is time.

In the GSHPS, the outlet temperature of GHEs is equal to the inlet temperature of the unit at the heat source side. When the rated inlet temperature of the unit at the heat source side is 24 °C under cooling condition, and the rated inlet temperature of the unit at the heat source side is 0 °C under heating condition, the performance of the unit under the variable load condition can be obtained from Eq. (3) to Eq. (6).

$$q_h = q_{hd} \cdot (a_1 T_{out,h} + b_1) \tag{3}$$

$$p_h = p_{hd} \cdot (c_1 T_{out,h} + d_1) \tag{4}$$

$$q_c = q_{cd} \cdot (a_2 T_{out,c} + b_2) \tag{5}$$

$$p_c = p_{cd} \cdot \left(c_2 T_{out,c} + d_2\right) \tag{6}$$

where q_h represents heating capacity of the unit; q_c represents cooling capacity of the unit; q_{hd} represents rated heating capacity of the unit; q_{cd} represents rated cooling capacity of the unit; p_h and p_c are power consumption under heating and cooling conditions respectively; p_{hd} and p_{cd} are rated power consumption under heating and cooling conditions respectively; $T_{out,\,h}$ and $T_{out,\,c}$ are outlet temperature of GHEs under heating and cooling conditions respectively; a_1, b_1, c_1, d_1, a_2, b_2, c_2 and d_2 are fitting parameters.

Under cooling and heating conditions, the inlet temperature of GHEs is calculated by Eqs. (7) and (8), respectively:

$$T_{in,c}^{i+1} = T_{out,c}^{i} + \frac{q_c^i + p_c^i}{c' \cdot \rho' \cdot S \cdot v} \tag{7}$$

$$T_{in,h}^{i+1} = T_{out,h}^{i} - \frac{q_h^i - p_h^i}{c' \cdot \rho' \cdot S \cdot v} \tag{8}$$

where i represents the previous moment, $i + 1$ represents the next moment; $T_{in,\,c}$ and $T_{in,\,h}$ are inlet temperature of GHEs under cooling and heating conditions respectively; c' represents specific heat capacity of fluid in pipes; ρ' is fluid density in pipes; S is total cross-sectional area of buried pipes; v is fluid velocity in pipes.

The circulating fluid in pipes is water. Some parameter values used in the simulation process are shown in Table 2.

The top surface of the heat exchange area is set as the convective boundary, which considers the convective heat transfer between soil and air. Bottom surface and other far boundaries of the heat exchange area are set to a constant temperature equal to the initial soil temperature T_i.

The outlet boundary of GHEs is defined as free flow, and the initial outlet temperature of GHEs is set to T_{iout}. The inlet temperature of GHEs is determined by the outlet temperature of GHEs and the heat intake/emission of the unit calculated at the previous moment.

The pipe walls of GHEs are set as the fixed walls without sliding. The heat transfer between GHEs and backfill material, and that between backfill material and soil are both coupled heat transfer.

The above model is solved by the finite element software COMSOL Multiphysics. To improve the efficiency of calculation, the time step of simulation is set to 1 day.

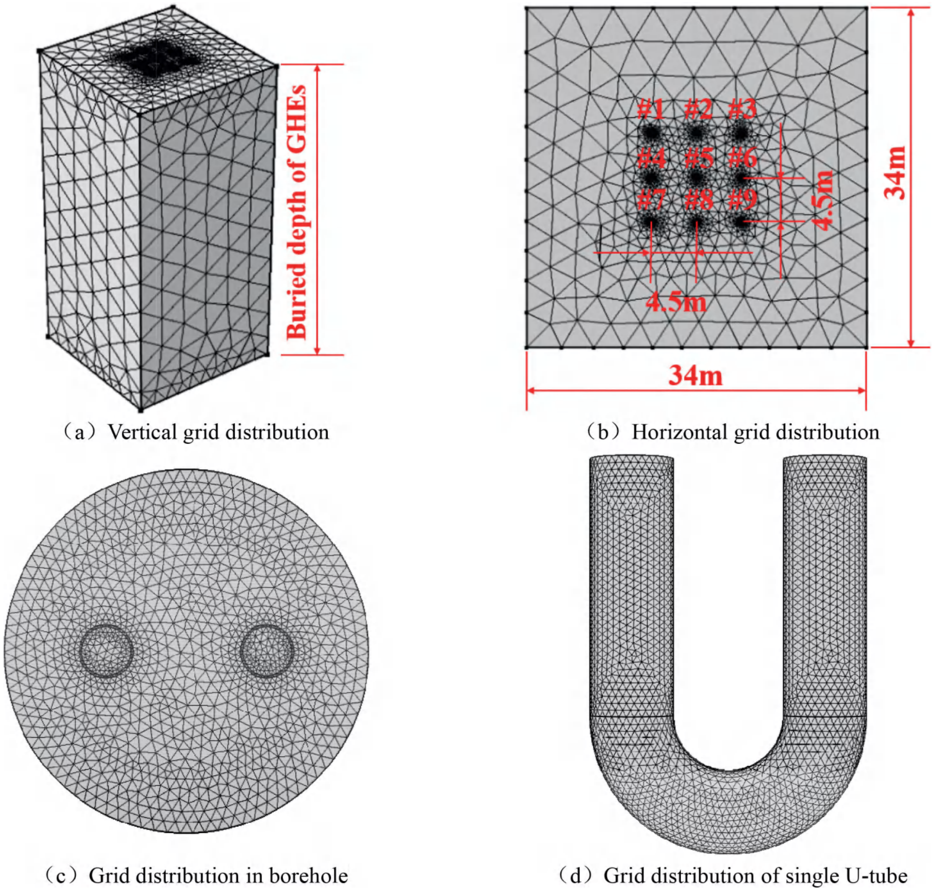

Fig. 1. Grid distribution of the pipe group model.

Table 2
Some parameter values used in the simulation process.

Name of the parameters	Values	Name of the parameters	Values
Thermal conductivity of soilλ_s	1.83 W/(m•K)	Rated power consumption under heating conditionp_{hd}	15.5kW
Thermal conductivity of backfill materialλ_b	2.10 W/(m•K)	Rated power consumption under cooling conditionp_{cd}	11.7kW
Thermal conductivity of waterλ_l	0.60 W/(m•K)	Fitting parametera_1	0.0672 °C^{-1}
Thermal conductivity of buried pipes materialλ_g	0.42 W/(m•K)	Fitting parameterb_1	1
Density of soilρ_s	1875 kg/m^3	Fitting parameterc_1	0.0473 °C^{-1}
Density of backfill materialρ_b	1860 kg/m^3	Fitting parameterd_1	1
Density of waterρ_l	998.2 kg/m^3	Fitting parametera_2	−0.0029 °C^{-1}
Density of buried pipes materialρ_g	940 kg/m^3	Fitting parameterb_2	1.1
Specific heat capacity of soilc_s	2100 J/(kg•K)	Fitting parameterc_2	0.015 °C^{-1}
Specific heat capacity of backfill materialc_b	840 J/(kg•K)	Fitting parameterd_2	0.64
Specific heat capacity of waterc_l	4182 J/(kg•K)	Fluid velocity in pipes$v$	0.37 m/s
Specific heat capacity of buried pipes materialc_g	2300 J/(kg•K)	Initial soil temperatureT_i	12 °C
Rated heating capacity of unitq_{hd}	53kW	Initial outlet temperatureT_{iout}	12 °C
Rated cooling capacity of unitq_{cd}	60kW		

2.3. Model validation

Due to the lack of experimental research under the variable load condition, the experimental data under the constant load condition in reference [12] are used to verify the accuracy of the heat transfer process of the simulation model under the variable load condition in this paper. Because the heat transfer mechanism between GHEs and soil is the same whether under the variable load condition or constant load condition, it is feasible to verify the accuracy of the heat transfer process of the simulation model under the variable load condition by using the experimental data under the constant load condition. At the same time, in order to verify the accuracy of the simulation model under the variable load condition, the simulation data under the variable load condition in literature [24] are selected. The validation results are shown in Fig. 2. In Fig. 2(a), the outlet temperature of GHEs in this paper is compared with that in reference [12]. It can be seen that simulation results in this paper are in good agreement with experimental results in reference [12], and the maximum relative error (the ratio of the difference between the experimental value and the simulated value to the experimental value) is 3.4%. Fig. 2(b) compares the soil temperature in this paper and that in literature [24]. It can be seen that the variation trend of the simulation results in this paper is consistent with that in literature [24], and the maximum relative error is 2.8%. In addition, the grid independence of the simulation model is verified. In this paper, the total number of grid cell in the model is 2.38 million. The total number of grid cell in the model is reduced to 2.00 million or increased to 2.80 million to verify the independence of the grid respectively. In Fig. 2, when the total number of grid cell decreases or increases, the simulation results hardly

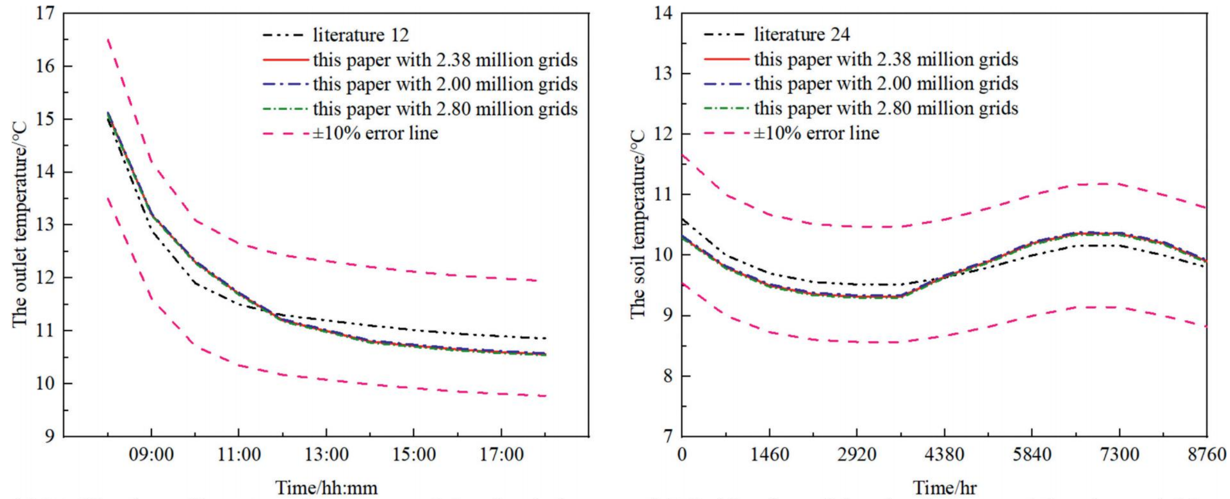

(a) Verification of heat transfer process of the simulation model

(b) Verification of the simulation model under variable load condition

Fig. 2. Verification of simulation model accuracy and grid independence.

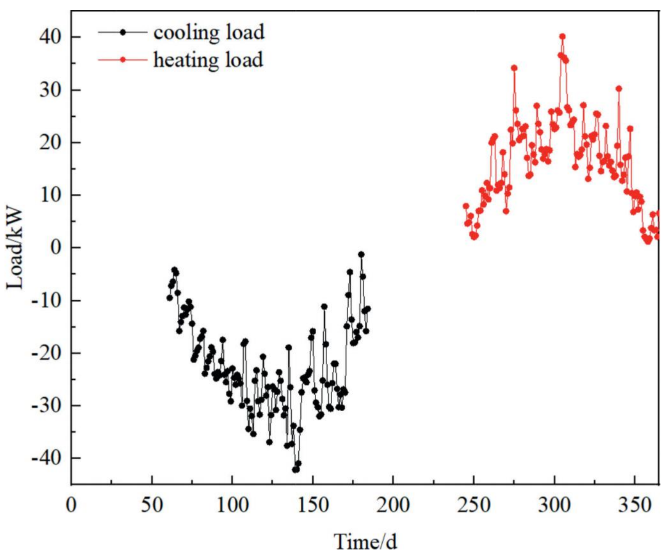

Fig. 3. Change curve of building cooling and heating loads in Beijing area.

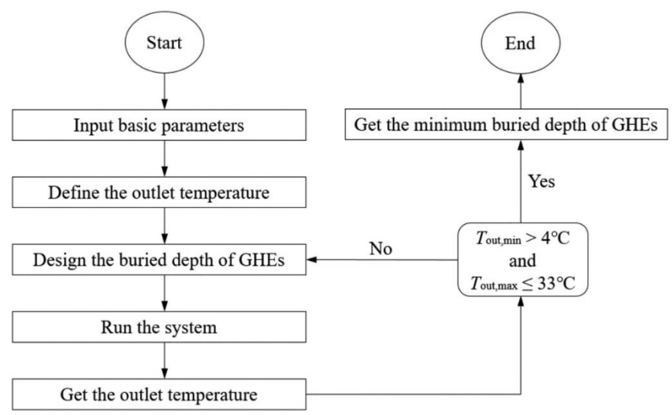

Fig. 4. flowchart for calculating the minimum buried depth of GHEs.

change. In conclusion, the simulation model established in this paper has higher accuracy to simulate the heat transfer process of GHEs.

3. Results and discussion

This paper takes an office building in Beijing as the research object. Beijing (40°N, 116°E) belongs to temperate monsoon climate, with high temperature and rainy in summer and cold and dry in winter. The office building has only one floor, with a floor height of 4.2 m. Its total building area is 207m^2, including 183m^2 of air conditioning area. The main rooms in the building are used for office and meeting. In cooling period, the indoor air conditioning design temperature of the building is 26 °C, and in heating period, the indoor air conditioning design temperature of the building is 20 °C. The cooling and heating loads of the building are calculated by DeST software, as shown in Fig. 3. In Fig. 3, the first day is March 16 of the first year. The cooling period of the first year is from May 15 of the first year (61rd day) to September 15 of the first year (184rd day), and the heating period of the first year is from November 15 of the first year (245rd day) to March 15 of the second year (365rd day). In cooling period, the maximum cooling load is 42.11 kW, and the cumulative cooling load is 67,344.24 kWh. In heating period, the maximum heating load is 40.20 kW, and the cumulative heating load is 46,824.24 kWh.

3.1. Design of the minimum buried depth of GHEs

In cooling period, if the outlet temperature of GHEs is higher than 33 °C, the operation condition of the GSHPS will be equivalent to that of the conventional cooling tower, which can not fully reflect the energy saving property of the GSHPS. In heating period, if the circulating fluid temperature entering the GSHP unit at the heat source side is too low, freezing may occur in the GSHP unit, thus reducing the energy efficiency ratio of the system. Therefore, the Chinese national standard "Engineering technical code for the ground source heat pump system (GB50336–2009)" clearly stipulates the outlet temperature of GHEs should be less than or equal to 33 °C in summer, and that of GHEs without adding antifreeze should be higher than 4 °C in winter. In this paper, the maximum outlet temperature $T_{out,\ max}$ is less than or equal to 33 °C in summer and the minimum outlet temperature $T_{out,\ min}$ is more than 4 °C in winter as the limiting conditions, the minimum buried depth of GHEs that meets the requirements of the code is calculated, as shown in Fig. 4. When the number of borehole is 9, the calculated minimum buried depth of GHEs is 60 m. Taking 5 m as the increase range of minimum buried depth of GHEs, five groups of buried pipe depth are simulated to analyze the influence of the buried depth of GHEs on the GSHPS.

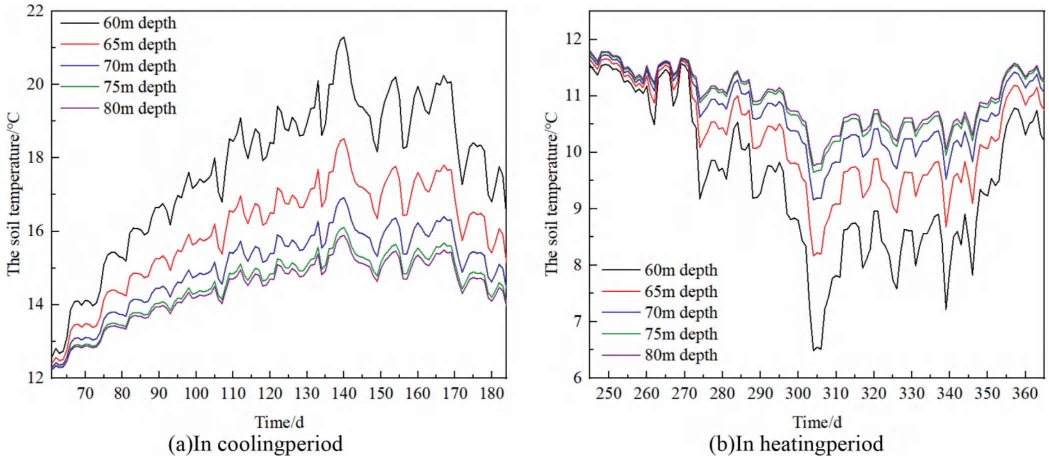

Fig. 5. Change curve of soil temperature under different buried pipe depths.

Table 3
Maximum (minimum) and average values of soil temperature under different buried pipe depths.

Buried depth	Maximum value in cooling period	Average value in cooling period	Minimum value in heating period	Average value in heating period
60m	21.30 °C	17.70 °C	6.49 °C	9.52 °C
65m	18.52 °C	16.01 °C	8.17 °C	10.26 °C
70m	16.92 °C	15.03 °C	9.16 °C	10.69 °C
75m	16.10 °C	14.53 °C	9.65 °C	10.91 °C
80m	15.90 °C	14.40 °C	9.76 °C	10.97 °C

3.2. Soil temperature field

To analyze the influence of buried depth of GHEs on the soil temperature field, the soil temperature under different buried pipe depths is simulated, as shown in Fig. 5. In the figure, the deeper the buried depth of GHEs is, the lower the soil temperature is in cooling period, and the higher the soil temperature is in heating period. This is because with the increase of buried depth of GHEs, the heat exchange area between GHEs and soil will increase correspondingly, which is conducive to enhancing the heat exchange effect of GHEs and reducing the energy loss of soil. Table 3 shows the maximum (minimum) and average values of soil temperature under different buried pipe depths. Compared with the GHEs with 60 m depth, when the buried depth of GHEs is 65 m, 70 m, 75 m and 80 m, the maximum soil temperature is reduced by 2.78 °C, 4.38 °C, 5.20 °C and 5.40 °C in cooling period, the minimum soil temperature is increased by 1.68 °C, 2.67 °C, 3.16 °C and 3.27 °C in heating period, and the average soil temperature is reduced by 1.69 °C, 2.67 °C, 3.17 °C and 3.30 °C in cooling period and increased by 0.74 °C, 1.17 °C, 1.39 °C and 1.45 °C in heating period, respectively. It can be seen that with the increase of the buried pipe depth, the change range of the soil temperature will also increase, but the change rate of the soil temperature (the ratio of the change range of soil temperature to the increase range of the buried pipe depth) will decrease.

To understand the change of soil temperature in the long-term operation process of the GSHPS, the soil temperature is simulated for 20 years by taking the pipe group model with 60 m buried depth as an example, as shown in Fig. 6. Fig. 7 shows the change of average soil temperature in cooling and heating period of each year. It can be seen from Fig. 7 that with the increase of the operation time of the system, the average soil temperature gradually decreases, and finally it almost remains the same. In cooling period, the average soil temperature of 20 years is 17.411 °C, the maximum average soil temperature is 17.700 °C, and the minimum average soil temperature is 17.394 °C. Compared with the average soil temperature of 20 years, the maximum average soil temperature increases by 0.289 °C, and the minimum average soil temperature decreases by 0.017 °C. In heating period, the average soil temperature of 20 years is 9.450 °C, the maximum average soil temperature is 9.520 °C, and the minimum average soil temperature is 9.445 °C. Compared with the average soil temperature of 20 years, the maximum average soil temperature increases by 0.070 °C, and the minimum average soil temperature decreases by 0.005 °C. It can be seen that in the continuous operation process of the system for 20 years, the change of soil temperature is relatively small.

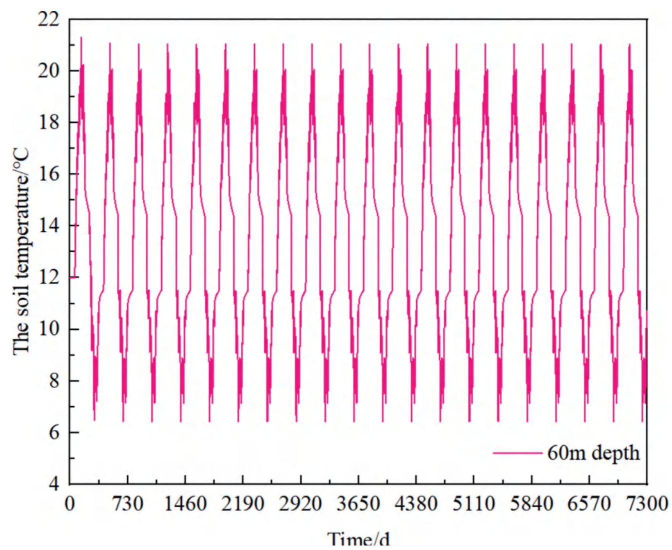

Fig. 6. Change curve of soil temperature in the operation process of the GSHPS for 20 years.

3.3. Operation performance of the GSHP unit

Fig. 8 shows the change of inlet and outlet temperature of GHEs with different buried depths. In the figure, with the increase of buried depth of GHEs, the inlet and outlet temperature will decrease in cooling period

Table 4
Maximum (minimum) and average values of outlet temperature of GHEs with different buried depths.

Buried depth	Maximum value in cooling period	Average value in cooling period	Minimum value in heating period	Average value in heating period
55m	27.18 °C	21.03 °C	1.19 °C	7.39 °C
60m	23.12 °C	18.62 °C	4.17 °C	8.65 °C
65m	19.61 °C	16.54 °C	6.69 °C	9.72 °C
70m	17.79 °C	15.45 °C	7.95 °C	10.26 °C
75m	16.68 °C	14.80 °C	8.77 °C	10.60 °C
80m	16.33 °C	14.59 °C	9.05 °C	10.72 °C

Table 5
Minimum and average COP values of the unit under different buried pipe depths.

Buried depth	Minimum value in cooling period	Average value in cooling period	Minimum value in heating period	Average value in heating period
60m	5.37	5.84	3.66	3.83
65m	5.73	6.08	3.77	3.87
70m	5.93	6.21	3.81	3.89
75m	6.06	6.29	3.84	3.90
80m	6.10	6.32	3.85	3.903

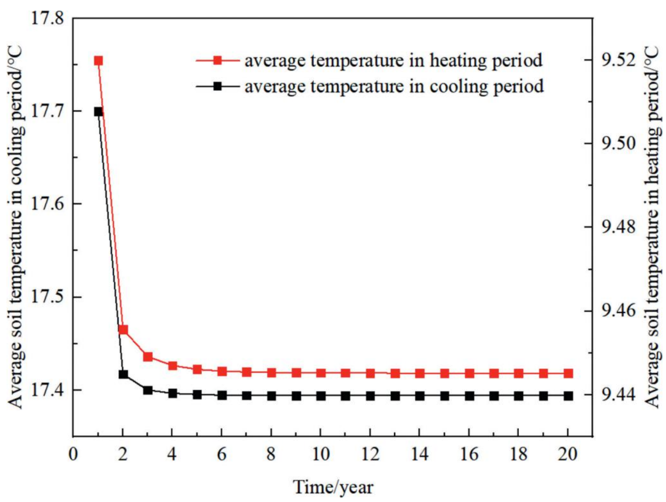

Fig. 7. Change curve of average soil temperature in cooling and heating period of each year.

and increase in heating period. Table 4 shows the maximum (minimum) and average values of outlet temperature of GHEs under different buried pipe depths. In Table 4, the minimum outlet temperature of GHEs with 55 m buried depth in heating period is 1.19 °C, which does not meet the requirements of the code, so the minimum buried depth of GHEs is determined to be 60 m. Compared with the GHEs with 60 m depth, when the buried depth of GHEs is 65 m, 70 m, 75 m and 80 m, the maximum outlet temperature decreases by 3.51 °C, 5.33 °C, 6.44 °C and 6.79 °C in cooling period, the minimum outlet temperature increases by 2.52 °C, 3.78 °C, 4.60 °C and 4.88 °C in heating period, and the average outlet temperature decreases by 2.08 °C, 3.17 °C, 3.82 °C and 4.03 °C in cooling period and increases by 1.07 °C, 1.61 °C, 1.95 °C and 2.07 °C in heating period, respectively. As mentioned above, the deeper the buried depth of GHEs is, the larger the contact area between GHEs and soil is, and the better the heat exchange effect of GHEs is.

Fig. 9 shows the COP variation of the GSHP unit under different buried pipe depths. In the figure, with the increase of buried pipe depth, the COP of the unit will also increase. Table 5 shows the minimum and average COP values of the unit under different buried pipe depths. Compared with the GHEs with 60 m depth, when the buried depth of GHEs is 65 m, 70 m, 75 m and 80 m, the minimum COP increases by 6.7%, 10.4%, 12.8% and 13.6% in cooling period and 3.0%, 4.1%, 4.9% and 5.2% in heating period, and the average COP increases by 4.1%, 6.3%, 7.7% and 8.2% in cooling period and 1.0%, 1.6%, 1.8% and 1.9% in heating period, respectively.

3.4. Cost of the GSHPS

Eqs. (9)–(11) are used to calculate the cost of drilling, backfilling material and single U-tube GHEs respectively. The calculation of the total cost of buried pipes is shown in Eq. (12). According to the relevant literature [20,25], the cost per unit pipe length of drilling, backfilling material and single U-tube GHEs is ¥73/m, ¥10/m and ¥15/m respectively. The total cost of buried pipes (initial investment of the GHSPS) under different buried depths is shown in Table 6. In Table 6, with the increase of the buried depth, the total cost of buried pipes will also increase. Compared with the GHEs with 60 m depth, when the buried depth of GHEs is 65 m, 70 m, 75 m and 80 m, the total cost of buried pipes increases by 8.3%, 16.7%, 25.0% and 33.3%, respectively. The GHEs with 60 m buried depth not only meet the outlet temperature required by the code, but also make the total cost of buried pipes reach the lowest. Therefore, considering the performance and the initial investment of the system comprehensively, the optimal buried depth of GHEs is 60 m.

$$m_d = l \cdot u_d \quad (9)$$

$$m_b = l \cdot u_b \quad (10)$$

$$m_g = l \cdot u_g \quad (11)$$

$$m_i = m_d + m_b + m_g \quad (12)$$

where m_d, m_b and m_g represent the cost of drilling, backfilling material and single U-tube GHEs respectively;l represents the total length of GHEs;u_d, u_b and u_g represent the cost per unit pipe length of drilling, backfilling material and single U-tube GHEs respectively; m_i represents the total cost of buried pipes.

As mentioned above, during the continuous operation of the GSHPS for 20 years, the change of soil temperature is quite small. It can be approximately considered that the heat exchange effect between soil and GHEs is the same every year, and the power consumption of the GSHPS is also the same every year. Table 7 shows the power consumption of the system running for 1 year under different buried pipe depths. The calculation of electricity charge of the system running for 20 years is shown in Eq. (13), and the calculation of total cost of the system running for 20 years is shown in Eq. (14).The electricity charge per kilowatt hour for the office building in Beijing is ¥0.82/kWh [26]. The total cost of the system running for 20 years under different buried pipe depths is shown

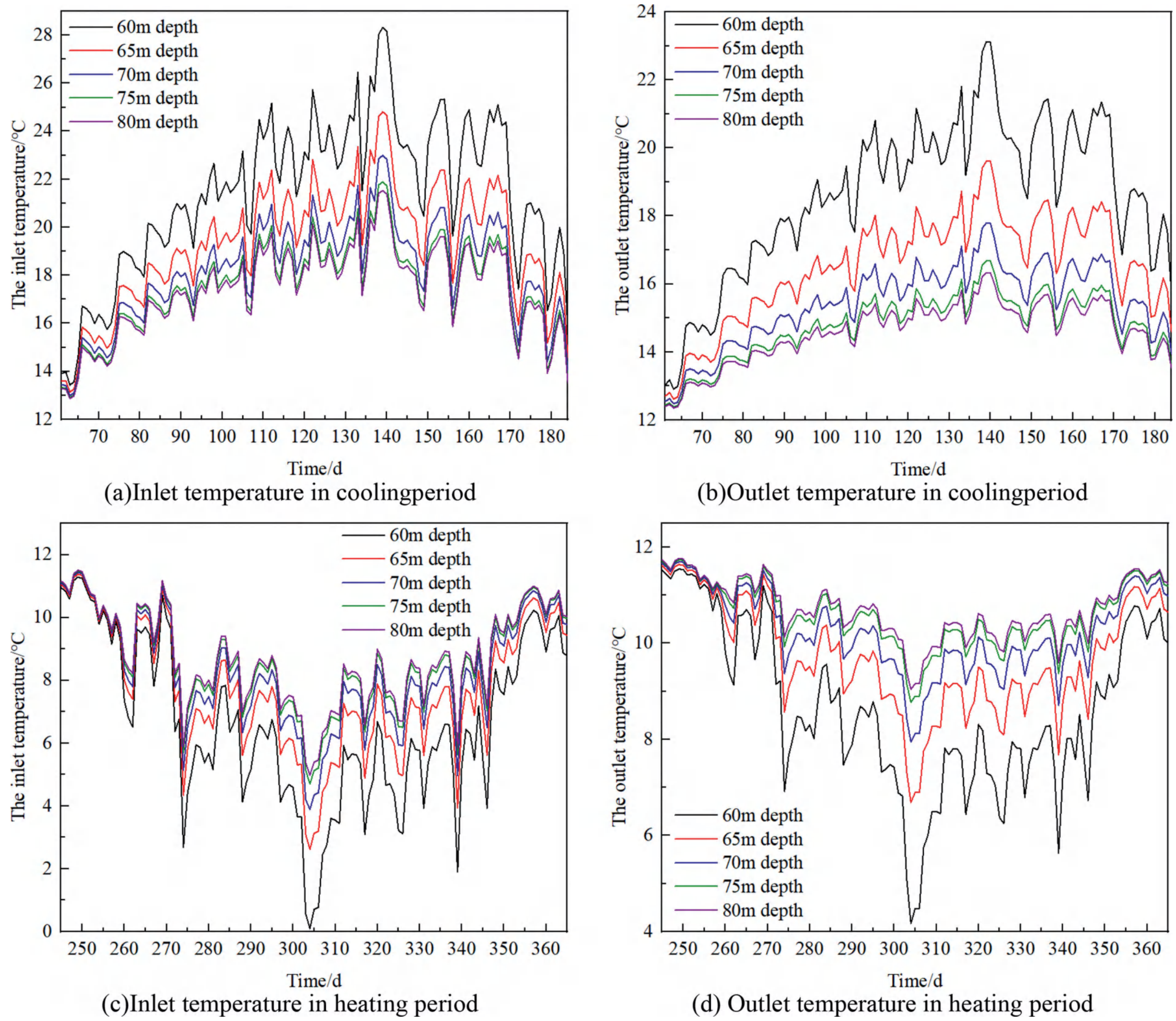

Fig. 8. Change curve of inlet and outlet temperature of GHEs with different buried depths.

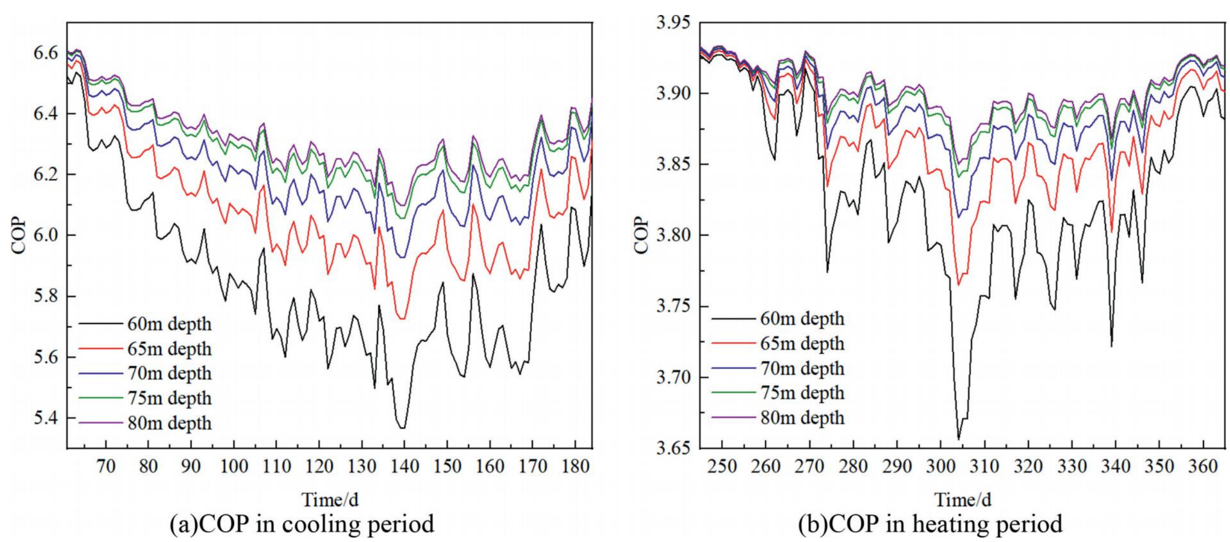

Fig. 9. COP change curve of the unit under different buried pipe depths.

Table 6
Total cost of buried pipes under different buried depths.

Buried depth	Total length of GHEs	Cost of drilling [RMB]	Cost of backfilling material [RMB]	Cost of Single U-tube GHEs [RMB]	Total cost of buried pipes [RMB]
60m	540m	39,420	5400	8100	52,920
65m	585m	42,705	5850	8775	57,330
70m	630m	45,990	6300	9450	61,740
75m	675m	49,275	6750	10,125	66,150
80m	720m	52,560	7200	10,800	70,560

Table 7
Power consumption of the system running for 1 year under different buried pipe depths.

Buried depth	60m	65m	70m	75m	80m
Power consumption [kWh]	23,991.63	23,333.27	23,002.14	22,804.72	22,741.85

Table 8
Total cost of the system running for 20 years under different buried pipe depths.

Buried depth	Total cost of buried pipes [RMB]	Electricity charge of the system running for 20 years [RMB]	Total cost of the system running for 20 years [RMB]
60m	52,920	393,462.73	446,382.73
65m	57,330	382,665.63	439,995.63
70m	61,740	377,235.10	438,975.10
75m	66,150	373,997.41	440,147.41
80m	70,560	372,996.34	443,556.34

in Table 8. In Table 8, the electricity charge decreases with the increase of buried depth of GHEs. When the buried depth of GHEs is 70 m, the total cost of the system running for 20 years is the lowest, and when the buried depth of GHEs is 60 m, the total cost of the system running for 20 years is the highest. Compared with the GHEs with 70 m depth, when the buried depth of GHEs is 60 m, 65 m, 75 m and 80 m, the total cost of the system running for 20 years increases by 1.7%, 0.23%, 0.27% and 1.0%, respectively. The GHEs with 70 m depth not only meet the outlet temperature required by the code, but also make the total cost of the system running for 20 years reach the lowest. Therefore, considering the performance the system and the total cost of the system running for 20 years comprehensively, the optimal buried depth of GHEs is 70 m. It can be seen that the operating cost (electricity charge) of the system has a great influence on changing the optimal buried depth of GHEs.

$$m_e = 20 \cdot n \cdot u_e \tag{13}$$

$$m_r = m_i + m_e \tag{14}$$

where m_e represents the electricity charge of the system running for 20 years; n represents the power consumption of the system running for 1 year; u_e represents the electricity charge per kilowatt hour; m_r represents the total cost of the system running for 20 years.

4. Conclusions

Based on the established three-dimensional finite element dynamic simulation platform, the minimum buried depth of GHEs meeting the requirements of the code is calculated, and the soil temperature, annual performance and total cost of the GSHPS under different buried pipe depths are studied. The following conclusions are drawn:

(1) The deeper the buried depth of GHEs is, the lower the soil temperature is in cooling period, and the higher the soil temperature is in heating period. Compared with the GHEs with 60 m depth, when the buried depth of GHEs is 65 m, 70 m, 75 m and 80 m, the average soil temperature decreases by 1.69 °C, 2.67 °C, 3.17 °C and 3.30 °C in cooling period and increases by 0.74 °C, 1.17 °C, 1.39 °C and 1.45 °C in heating period, respectively. In the continuous operation process of the GSHPS for 20 years, the change of soil temperature is relatively small.

(2) Increasing the buried depth of GHEs can improve the heat transfer effect of GHEs and the operation performance of the system. Compared with the GHEs with 60 m depth, when the buried depth of GHEs is 65 m, 70 m, 75 m and 80 m, the average COP of the unit increases by 4.1%, 6.3%, 7.7% and 8.2% in cooling period and 1.0%, 1.6%, 1.8% and 1.9% in heating period, respectively.

(3) Considering the performance of the GSHPS and the total cost of buried pipes comprehensively, the optimal buried depth of GHEs is 60 m. However, when considering the performance the system and the total cost of the system running for 20 years comprehensively, the optimal buried depth of GHEs is 70 m. The operating cost of the system has a great influence on changing the optimal buried depth of GHEs.

Declaration of Competing Interest

The authors declare that they have no known competing financial interests or personal relationships that could have appeared to influence the work reported in this paper.

Acknowledgments

The authors gratefully acknowledge the support from the Natural Science Foundation of China (grant No. 51778115) and the Fundamental Research Funds for the Central Universities (grant No. N182502043).

References

[1] B. Li, Z. Han, C. Bai, H. Hu, The influence of soil thermal properties on the operation performance on ground source heat pump system, Renew. Energy 141 (2019) 903–913.
[2] Y. Noorollahi, R. Saeidi, M. Mohammadi, A. Amiri, M. Hosseinzadeh, The effects of ground heat exchanger parameters changes on geothermal heat pump performance – A review, Appl. Therm. Eng. 129 (2018) 1645–1658.
[3] S. Karytsas, H. Theodoropoulou, Public awareness and willingness to adopt ground source heat pumps for domestic heating and cooling, Renew. Sustain. Energy Rev. 34 (2014) 49–57.
[4] J. Luo, J. Rohn, W. Xiang, D. Bertermann, P. Blum, A review of ground investigations for ground source heat pump (GSHP) systems, Energy Build. 117 (2016) 160–175.
[5] L. Ni, J. Dong, Y. Yao, C. Shen, D. Qv, X. Zhang, A review of heat pump systems for heating and cooling of buildings in China in the last decade, Renew. Energy 84 (2015) 30–45.

[6] G. Jin, X. Zhang, S. Guo, X. Wu, W. Bi, Evaluation and analysis of thermal short-circuiting in borehole heat exchangers, Energy Proc. 105 (2017) 1677–1682.
[7] C. Han, X. Yu, Sensitivity analysis of a vertical geothermal heat pump system, Appl. Energy 170 (2016) 148–160.
[8] S. Miglani, K. Orehounig, J. Carmeliet, A methodology to calculate long-term shallow geothermal energy potential for an urban neighbourhood, Energy Build. 159 (2018) 462–473.
[9] B. Li, M. Zheng, M. Shahrestani, S. Zhang, Driving factors of the thermal efficiency of ground source heat pump systems with vertical boreholes in Chongqing by experiments, J. Build. Eng. 28 (2020) 101049.
[10] H. Esen, E. Turgut, Optimization of operating parameters of a ground coupled heat pump system by Taguchi method, Energy Build. 107 (2015) 329–334.
[11] K.S. Chang, M.J. Kim, Thermal performance evaluation of vertical U-loop ground heat exchanger using in-situ thermal response test, Renew. Energy 87 (2016) 585–591.
[12] X.Q. Zhai, X.W. Cheng, R.Z. Wang, Heating and cooling performance of a minitype ground source heat pump system, Appl. Therm. Eng. 111 (2017) 1366–1370.
[13] X. Wang, Y. Wang, Z. Wang, Y. Liu, Zhu Y, H. Chen, Simulation-based analysis of a ground source heat pump system using superlong flexible heat pipes coupled borehole heat exchanger during heating season, Energy Convers. Manag. 164 (2018) 132–143.
[14] Z. Han, B. Li, S. Zhang, C. Bai, H. Hu, Study on design error of ground source heat pump system and its influencing factors, Appl. Therm. Eng. 144 (2018) 1030–1036.
[15] S. Sandler, B. Zajaczkowski, B. Bialko, Z.M. Malecha, Evaluation of the impact of the thermal shunt effect on the U-pipe ground borehole heat exchanger performance, Geothermics 65 (2017) 244–254.
[16] A. Casasso, R. Sethi, Efficiency of closed loop geothermal heat pumps: a sensitivity analysis, Renew. Energy 62 (2014) 737–746.
[17] S. Chen, J. Mao, X. Han, Heat transfer analysis of a vertical ground heat exchanger using numerical simulation and multiple regression model, Energy Build. 129 (2016) 81–91.
[18] Y. Li, J. Mao, S. Geng, X. Han, H. Zhang, Evaluation of thermal short-circuiting and influence on thermal response test for borehole heat exchanger, Geothermics 50 (2014) 136–147.
[19] H. Esen, M. Inalli, Y. Esen, Temperature distributions in boreholes of a vertical ground-coupled heat pump system, Renew. Energy 34 (2009) 2672–2679.
[20] J. Chen, L. Xia, B. Li, D. Mmereki, Simulation and experimental analysis of optimal buried depth of the vertical U-tube ground heat exchanger for a ground-coupled heat pump system, Renew. Energy 73 (2015) 46–54.
[21] K. Zhou, J. Mao, Y. Li, H. Zhang, Performance assessment and techno-economic optimization of ground source heat pump for residential heating and cooling: A case study of Nanjing, China, Sustain. Energy Technol. Assess. 40 (2020) 100782.
[22] E. Wang, T. Huang, F. Zhang, M. Jia, Q. Zhao, Analysis of the influence of backfill material on the heat exchange efficiency of ground source heat pump system, Refrig. Air Cond. 33 (3) (2019) 240–244 (in Chinese).
[23] X. Liu, Optimization and Simulation of Heat Transfer Model of Buried Pipe in Ground Source Heat Pump, Southwest Jiaotong University, 2016.
[24] Z. Liu, W. Xu, X. Zhai, C. Qian, X. Chen, Feasibility and performance study of the hybrid ground-source heat pump system for one office building in Chinese heating dominated areas, Renew. Energy 101 (2017) 1131–1140.
[25] S. Hong, W. Du, Y. Liu, J. He, Y. Zhou, Y. Jin, Analysis of factors affecting the heat transfer characteristics of the ground heat exchanger in the ground source heat pump, Refrig. Air Cond 30 (4) (2016) 441–445 (in Chinese).
[26] Y. Lei, H. Tan, Y. Li, Technical-economic evaluation of ground source heat pump for office buildings in China, Energy Proc. 152 (2018) 1069–1078.

Energy and Built Environment 2 (2021) 137–148

Contents lists available at ScienceDirect

Energy and Built Environment

journal homepage: http://www.keaipublishing.com/en/journals/energy-and-built-environment/

The reinforcement learning method for occupant behavior in building control: A review

Mengjie Han[a,*], Jing Zhao[b,*], Xingxing Zhang[a], Jingchun Shen[a], Yu Li[c]

[a] School of Technology and Business Studies, Dalarna University, Falun 79188, Sweden
[b] Leisure Management College, Xi'an Eurasia University, Yanta District, Xi'an, China
[c] Luxembourg Institute of Science and Technology LIST, 5, Avenue des Hauts-Fourneaux, L-4362 Esch-sur-Alzette, Luxembourg

ARTICLE INFO

Keywords:
Reinforcement learning
Occupant behavior
Energy efficiency
Building control
Smart building

ABSTRACT

Occupant behavior in buildings has been considered the major source of uncertainty for assessing energy consumption and building performance. Modeling frameworks are usually built to accomplish a certain task, but the stochasticity of the occupant makes it difficult to apply that experience to a similar but distinct environment. For complex and dynamic environments, the development of smart devices and computing power makes intelligent control methods for occupant behaviors more viable. It is expected that they will make a substantial contribution to reducing global energy consumption. Among these control techniques, the reinforcement learning (RL) method seems distinctive and applicable. The success of the reinforcement learning method in many artificial intelligence applications has given an explicit indication of how this method might be used to model and adjust occupant behavior in building control. Fruitful algorithms complement each other and guarantee the quality of the optimization. However, the examination of occupant behavior based on reinforcement learning methodologies is not well established. The way that occupant interacts with the RL agent is still unclear. This study briefly reviews the empirical applications using reinforcement learning, how they have contributed to shaping the modeling paradigms and how they might suggest a future research direction.

1. Introduction

Building energy consumption amounts to approximately 30%–40% of all energy consumed in developed countries [1,2]. The trend of power demand is still increasing. Not only does this increase the operating cost of energy consumption, it also contributes to the increasing emission of greenhouse gasses. Since buildings are also responsible for one-third of global energy-related greenhouse gas emissions [3], developing efficient strategies for reducing the consumption of building energy are urgently required in the future.

Maintaining occupant comfort and use of appliances by occupant generates 80% of building energy consumptions [4]. As is well known, occupant behavior is stochastic and complex. Even when an advanced modeling method is built to include occupant behavior, it is challenging to quickly apply that experience to a similar but distinct environment. There is no general scientific standard outlining appropriate model validation techniques especially when multiple behaviors are modeled [5]. As an extreme case, in a simulation study of different models, occupant behavior with the feature of 'random walk' results in a very large performance gap [6]. It has also been recognized that a building could fail to achieve the desired standards and building designers could miss out on the opportunity of optimizing building design and control for occupancy [7]. Modeling occupant behavior may help to understand and reduce the gap between design and actual building energy performance [8,9]. However, occupant models are usually context dependent [10]. Simply predicting or simulating occupant behavior in one setting has its intrinsic challenge in transferring the knowledge to a more complex scenario.

Studies of occupant behavior have been grouped into three streams: rule-based models, stochastic models, and data-driven methods [11]. It has been discussed that occupant behavior models do not represent deterministic events, but move into a field where behaviors are described by stochastic laws [12]. Stochastic models consider the occupant behavior to be stochastic because behavior varies between occupants and may evolve over time [13]. Data-driven methods, however, are conducted without an explicit aim to understand occupant behavior [11]. A building's physical environment is dynamic and complex. Occupants can respond quickly to a change of the environment in a process that is often non-stationary. Attempts to model all possible features for building operation systems can be intractable and systems accommodating more features often have significant lag times. Data-driven methods do

* Corresponding authors.
E-mail addresses: mea@du.se (M. Han), 1123389851@qq.com (J. Zhao).

https://doi.org/10.1016/j.enbenv.2020.08.005
Available online 2 September 2020

not always set up physical models and often use historical data to characterize features, including occupant behavior.

Rather than on the understanding of occupant behavior, intelligent control methods used to optimize future reward in building systems seem to be an alternative approach. These create an agent that learns from historical behaviors and is trained to adjust the control actions by utilizing occupant behavior. The occupant interacts with the building control system via presence, actual activity and providing comfort feedback through linked building systems, e.g. HVAC, lighting and windows. Thus, an optimal control method integrating building performance and occupant impact offers a novel way of modeling. In a control problem, generally, an agent is built to complete decision-making tasks in a system to achieve preset goal. Building control system, which is a compound of multiple engineering fields, refers to centralized and integrated hardware and software networks [14] and considers the improvement of energy utilization efficiency, energy cost reduction, and renewable energy technology utilization in order to serve local energy loads while keeping indoor comfort [15]. Control targets usually include shading system, window, lighting system, ventilation, and heating/cooling system.

A recently realized Markov decision process based machine learning method, known as reinforcement learning (RL), can work in both model-based and model-free environments [16]. Nevertheless, it is the classic model-free learning algorithms, such as Q-learning and $TD(\lambda)$, that makes RL much more attractive and efficient in artificial intelligence applications [17–20]. The effort to solve deep RL problems, for example [21,22], opens up the possibility of working on large continuous datasets. The distinctive feature of RL is that the agent, via trial-and-error search, can make optimal actions without having a supervisor, which fits the goal of a control problem.

These building control systems are able to make decisions based on data-driven modeling outcomes. The RL method is able to work in a stochastic environment and to adapt existing data to extract underlying logic for decision-making, that is, a data-driven method. The agent of RL treats occupant behavior as an unknown factor and learns to adapt itself form what has been observed of human interactions. The RL method has been in existence for over seventy years, but it was not until the past decade that researchers started to commit themselves to expanding its applications. Neither systematic approaches to applying RL on occupant behavior nor relevant literature reviews have been analyzed from the methodological point of view. The indication for future RL application is still unclear. Therefore, the aim of this study is to review the empirical articles on how RL methods have been implemented for adjusting occupant behavior in buildings, and provide instructive directions for future research.

Thus, contributions of this study are threefold. Firstly, we present the results of our literature search and identify the key points emerging from this research topic in recent years. Secondly, we provide a comprehensive understanding of how RL works for building control and an overview of its implementation requirements. Finally, we identify the current research gap surrounding building control and propose future research ideas for modeling occupant behavior.

In the second section of this study, we present the literature searching scope and the outcomes. In Section 3 we briefly introduce the philosophy of RL and its corresponding algorithms. Section 4 then analyzes the empirical articles. A discussion is presented in Section 5 and Section 6 concludes with some findings and possible new research directions.

2. Methods and search outcomes

2.1. Methods

We conducted our literature search using the search engine *Scopus*. The first reason is that it provides us with multiple document features that we can adjust such as funding details and conference information. The second reason is that an interface to the R package *bibliometrix,* an open-source tool for executing science mapping analysis, can be created for conducting analytical bibliometrics where three steps are considered for the workflow [23]. In step 1, data is loaded and converted to the R data frame. In step 2, the descriptive analysis and citation networks are produced; the visualization is made available in step 3.

Our searching keywords and operations are

(("reinforcement learning" OR "Q-learning" OR "policy gradient" OR "A3C" OR "actor-critic" OR "SARSA*") AND "occupant*"), where some prevalent algorithms for RL, for example, Q-learning and policy gradient, are also included to guarantee adequate coverage. Adding the wildcard to *occupant** ensures hits using both singular and plural forms are returned. The same was done for *SARSA** because there are a number of variants of the SARSA algorithm that can be used for some algorithm-specific articles. We exclude the words behavior* or behavior* because the RL agent does not only take action based on particular behaviors, but also adjusts its policy by collecting occupant feedback for the control system. We do not limit the search by article type or publication year.

2.2. Search outcomes

The original search returns a total number of forty articles. One of the selection criteria was that articles where either the occupant behavior or occupancy was explicitly considered as an element in a Markov decision process (see Section 3.1) or had an impact on the transition of environmental states were included. In other words, an agent that tried to learn the optimal control strategy only to satisfy occupant comfort and did not include dynamic interactions with the environment was excluded from this analysis. See a relevant review work [24] that examined the RL control for occupant comfort for more articles that we exclude here. Careful reading of each of the forty articles resulted in thirty-two articles that are considered for this analysis. Even though it is not exhaustive, the outcome of this search, we believe, can form a representative sample of current understandings within the field.

2.2.1. Publication sources

The thirty-two documents were published in twenty-three difference sources including international journals, conference proceedings and book chapter. A summary of the top five publication sources from the search is shown in Fig. 1. Most of the articles were published in the Elsevier journal *Building and Environment*, followed by a second Elsevier journal *Energy and Buildings* and the Buildingsys 2019[1] conference. Each of remaining eighteen sources has published one article. Even though full-text articles of some publications are not included in the Scopus search engine, the long-tailed Poisson-like distribution for publication sources covers a range of topics including energy, building, computer science, optimal control, sustainability and engineering. The variety of publication sources establishes a multidisciplinary collaborative framework for future studies. We also anticipate that the emergence of new publication sources may attract studies of RL for occupant behavior and increase public awareness of the topic.

2.2.2. Publication types, years and citations

Of the total articles in this search, the earliest was published in 2007. After that, no article was published until 2013 (Fig. 2). This strongly suggests that difficulties in the implementation of complex problems has hindered the development of RL applications. The success of many deep learning paradigms in the early 2010s, however, seems to have promoted a revival of the use of RL applications, including those in building control. It has generated the publication of a number of articles by

[1] Full name of the conference: BUILDSYS 2019 - PROCEEDINGS OF THE 6TH ACM INTERNATIONAL CONFERENCE ON SYSTEMS FOR ENERGY-EFFICIENT BUILDINGS, CITIES, AND TRANSPORTATION

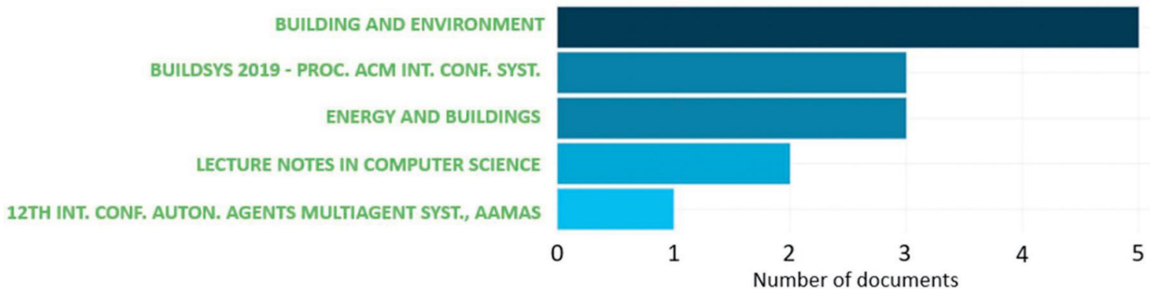

Fig. 1. Top five publication sources.

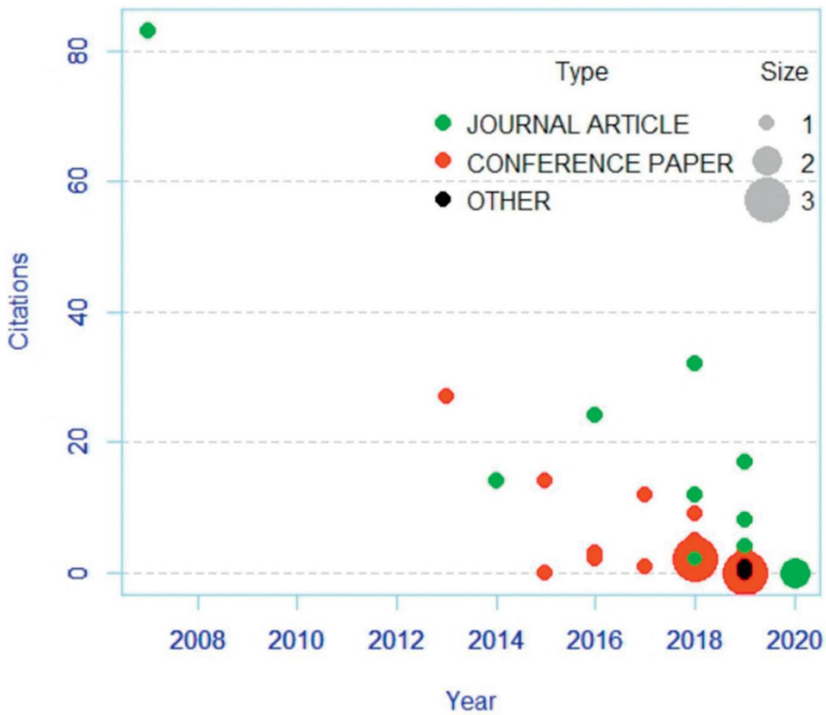

Fig. 2. Type and year of publication and number of citations.

fusing deep RL for solving complex problems. Nevertheless, overall citations are still low. More attention could be paid to this RL literature when intelligent control systems for occupants are developed.

2.2.3. Country collaboration

Collaboration between countries allows researchers to share knowledge, data and research infrastructures. The development of RL control for occupant behavior has just started to be noticed and needs worldwide collaboration for fast growth. Most historical collaborations have been carried out between researchers in the United States and some countries in Europe, as well as in China (Fig. 3). These three regions/countries will likely take the lead in future contributions to the topic. In the meantime their pioneer activity is setting the stage for comprehensive impacts from other regions and countries.

3. The reinforcement learning method

Various studies have reviewed the classification of different control methods in buildings. For example, Shaikh et al. [14] reviewed the intelligent control system for building energy and occupant's comfort, whereas Dounis and Caraiscos [25] focused on the agent-based control system. Aste et al. [26] summarized the model-based strategies for building simulation, control and data analytics. The previous surveys provide a framework of how the different methods relate to each other and the pros and cons of each. A generic challenge of conventional methods (e.g. PID, on-off, model predictive control, etc.) lies in the difficulty of including all unknown environmental factors in the models. Even there is much room to increase model performance, complex model specifications usually bring heavy computations [27].

Compared to the conventional methods the RL technique is still not well developed for buildings. It has not drawn much attention and the performance of RL algorithms has thus not been evaluated yet. Even though Royapoor et al. [28] realized that RL methods are notable, a framework of implementations and explorations on efficient RL methods needs to be systematically investigated and discussed.

The shortage of scientific research publications prevents building users, building managers, device controllers, energy agencies and other related parties from being aware of the neglected technique. An integration with explicit occupant behavior has not been comprehensively examined. The curse of dimensionality, the fact that the number of representative environment states grows exponentially with complex problems, is an inherent problem. Approximate solution methods provide the possibility to overcome this. Deficient consideration of it hinders the development of solutions. Thus, the necessity for investigating current studies and indicating future studies first requires an overview.

The idea of RL derives from the concept of "optimal control", which emerged in the 1950s as a way of formulating problems by designing a controller to minimize a measure of the behavior of a system over

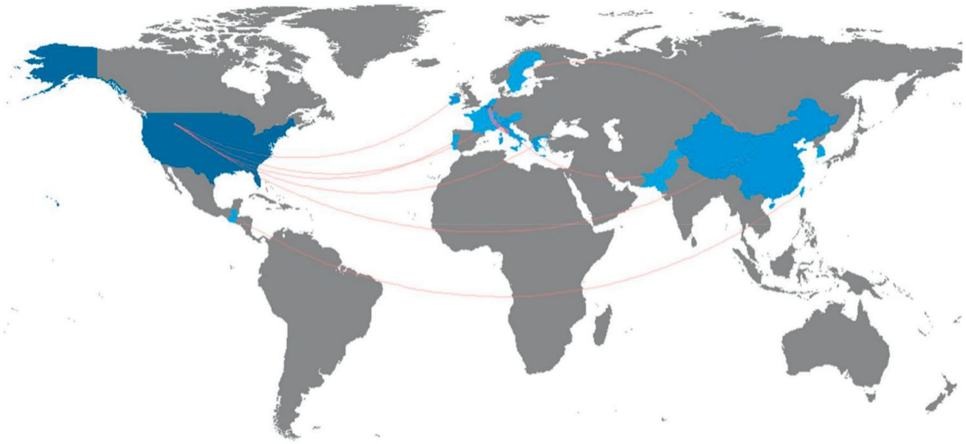

Fig. 3. Country collaboration map.

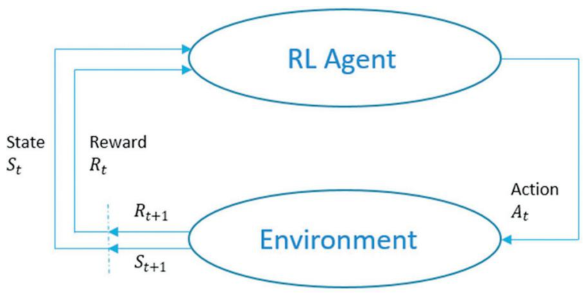

Fig. 4. The interaction between agent and environment in an MDP.

time [29]. Bellman [30] came up with the concept of Markov decision processes (MDPs) or finite MDPs, a fundamental theory of RL, to formulate optimal control problems. Unlike conventional control methods, RL does not require a model. A benefit of a model-free approach is that it simplifies the problem when the system is complex. Different from independent and identically distributed (i.i.d.) data that some conventional models require, the RL agent receives subsequent reward signals from its actions. Another benefit is that the trade-off between exploration and exploitation can be balanced via experiment design. Furthermore, a rich class of learning algorithms fused with deep neural networks [20] provide a potential for accurate estimation of value functions.

3.1. Markov decision processes

In a dynamic sequential decision-making process, the state $S_t \in \mathcal{S}$ of a RL agent refers to a specific condition of the environment at discrete time steps $t = 0, 1, \ldots$. By realizing and responding to the environment, the agent chooses a deterministic or stochastic action $A_t \in \mathcal{A}$ that tries to maximize future returns and receives an instant reward $R_{t+1} \in \mathcal{R}$ as the agent transfers to the new state S_{t+1}. A sequence of state, action and reward is generated to form an MDP (Fig. 4 [24,29]).

The Markov property highlights that the future is independent of the past and depends only on the present. In Fig. 4, S_t and R_t are the outcomes after taking an action and are considered as random variables. Thus, the joint probability density function for S_t and R_t is defined by:

$$p(s', r|s, a) = \mathbb{P}\left[S_t = s', R_t = r|\ S_{t-1} = s, A_{t-1} = a\right], \tag{1}$$

where $s,\ s' \in \mathcal{S},\ r \in \mathcal{R}$ and $a \in \mathcal{A}$. It can be seen from Eq. (1) that the distribution of state and reward at time t depends only on the state and action one step before. From Eq. (1), it is straightforward to obtain the transition probabilities $p(s'|s, a)$ and the expected reward $r(s, a) = \mathbb{E}[R_t|S_{t-1} = s, A_{t-1} = a]$ that are used for formulating the Bellman optimality equation in Section 3.3.

3.2. Policies and value functions

A *policy* π is a distribution over actions given states and can be considered as a function of actions. It fully defines the behavior of an agent by telling the agent how to act when it is in different states. An arbitrary policy targets on evaluating the expected future return when making an action a from time t: $G_t = R_{t+1} + \gamma R_{t+2} + \gamma^2 R_{t+3} + \ldots$ under a given state s, where $0 \le \gamma \le 1$ is the discount parameter, namely:

$$\begin{aligned} q_\pi(s,\ a) &= \mathbb{E}_\pi\left[G_t|S_t = s, A_t = a\right] \\ &= \mathbb{E}_\pi\left[\sum_{k=0}^{\infty} \gamma^k R_{t+k+1}|S_t = s, A_t = a\right],\ for\ all\ s \in \mathcal{S}\ and\ a \in \mathcal{A}. \end{aligned} \tag{2}$$

The task of finding the optimal policy in Eq. (2), π_*, is thus achieved by evaluating the optimal action-value function $q_\pi(s, a)$:

$$q_*(s, a) = \max_\pi q_\pi(s, a). \tag{3}$$

3.3. Value-based algorithms

Strategies to solve Eq. (3) are usually achieved by updating the Bellman optimality equation [31]:

$$q_*(s, a) = r(s, a) + \gamma \sum_{s' \in S} p\left(s'|s, a\right) \max_{a'} q_*\left(s', a'\right). \tag{4}$$

The recursive relationship assists in splitting the current action-value function into the immediate reward and the value of the next action. Eq. (4) directly provides us with the formulation of value-based algorithms within temporal-difference method,[2] where either tabular methods or approximation methods can be adopted for obtaining $q(s, a)$. There is always an explicit state exploration of state-action space for value-based algorithms.

For problems with small and discrete state or state-action sets, it is preferable to formulate the estimations using look-up tables with one entry for each state or state-action value. The tabular method is easy to implement and guarantees convergence [29]. The tabular Q-learning algorithm [32] is the most common RL algorithm used in building control [24]. Easy implementation and accurate solutions make it robust in different building control problems. Other tabular algorithms include tabular SARSA, i.e. the so-called state–action–reward–state–action, value-iteration, and policy-iteration.

For large MDP problems, we do not always want to see separate the trajectory of each entry in the look-up table. The parameterized value function approximation $\hat{q}(s, a; \mathbf{w}) \approx q_\pi(s, a)$ gives a mapping from the state-action to a function value, for which there are many mapping functions available, for example, linear combinations, neural networks,

[2] The Monte Carlo method and dynamic programing method are also value-based. See [29] for more details.

and so on. It generates the state-actions that we may not directly observe. A common way of updating the weight vector, **w**, is the gradient descent, which yields deep Q-learning. Algorithms like *SARSA*(λ) and fitted Q-iteration can also be found in the earlier studies. More recently developed value-based algorithms [33] have also provided a great number of opportunities for training the agent in a more flexible way.

3.4. Policy-based and actor-critic algorithms

Another way to solve large MDP or continuous state RL problems is to apply the policy-based method [34], where the policy is explicitly represented by its own function approximator, independent of the value function, and is updated according to the gradient of expected reward,

$$J(\theta) = \mathbb{E}_{\pi\sim p_\theta(\tau)}[r(\tau)], \quad (5)$$

with respect to the policy parameters θ. $r(\tau)$ is the total reward for a given trajectory τ, representing the interactions between the agent and the environment in an episode. $p_\theta(\tau)$ depicts the probability of getting a specific τ from a stochastic environment under fixed θ. The approach to finding optimal J can be converted to solve the maximization problem using gradient ascent with regard to a set of parameters θ, for example, the weights and biases in a neural network. The policy-based method has an innate exploration strategy and the variance of the gradient is large for episodes with long time steps. Some recent algorithms such as Proximal Policy Optimization [35] and Trust Region Policy Optimization [36] have been developed for complex problems. Subtracting a baseline b from $r(\tau)$ may reduce the variance while keeping the gradient still unbiased. One option is to apply the state-value $v_\pi(s) = \mathbb{E}_\pi[G_t S_t = s]$ to the policy gradient methods, known as an actor-critic algorithm. These algorithms work with parameterized policies by relying exclusively on value function approximation [37]. In practice, the actor-critic algorithms use deep neural networks to estimate the value function [38,39].

3.5. RL for building control

It has been challenging to apply the trained RL agent to buildings irrespective of the type occupant behavior due to rigorous training requirement, control security and robustness, and the ability of method generalization [40]. However, real implementations may validate and improve the method by observing reliable state transitions and reward signals. Appropriate specifications of state, action and reward in MDP have significant impacts on learning outcomes and practical settings.

The states partly determine the complexity of RL control problems. In building applications, states are mostly defined by the variables that are associated to physical environment and weather condition for a building, for example, outdoor temperature, airflow rate, indoor CO_2 level and so on. Sufficient changes in state variables will alter indoor comfort level and energy use, which also update building environment for RL agent to take action. Accurate representation of states will lead to efficient training process and avoid curse of dimensionality. For continuous state or state with large number of levels, building environment becomes too complex to get fully explored. Dimension reduction is an alternative way for resolving the problem [41]. However, it is a collaborative work between building management expert and data scientist to figure out applicable state representation.

The action of an agent is taken based on observed state and the action levels can also affect the problem complexity. For a building system, controlling HVAC (heating, ventilation, and air conditioning) is the most complicated due to various components and control levels [40]. Actions like setting constant temperature set point or airflow rate will cause high energy use, because room occupancy change, outdoor environment and pre-heating/cooling strategy may also generate effects to HVAC performance and energy use. Typical actions of an RL agent do not only try to immediately improve current reward, but also aim to maximize future return. For simpler control problems, for example, window opening/closing [42], action can also be generalized to a continuous domain, which requires more efforts on making acceptable simplifications.

Two types of rewards have been examined in most of the studies: comfort level and energy saving. It seems that occupant comfort gets more priorities when optimization is considered for these two contradictory factors in developed areas. Nevertheless, reward is more related to contextual, psychological, physiological, and social background of an occupant. Using same comfort criteria to different individuals will bring bias to learning process. It is also reasonable to take $\gamma = 1$ indicating that time factor will not give any discount to future comfort.

4. Empirical articles of RL control for occupant behavior

In this section, we will scrutinize the RL applications in two categories: those where occupant behavior or occupancy is explicitly characterized as a state, action or reward in the MPD; and those which not use occupant behavior to directly train an agent, but interact with the environment by adjusting the state transition, estimating the disturbance of reward, providing feedback and changing occupancy schedules.

4.1. Occupant behavior in MDP

Nine representative articles were selected to illustrate the first category of applications. Their workflows are summarized in Table 1 where occupant behavior or occupancy interacting with RL agent will be examined in detail. We also present a breakdown of the specific state, action, reward and algorithms each application uses.

There is always some doubt when selecting state variables. Selecting too many will increase the learning inefficiency exponentially while selecting too few will not fully depict the Markov property. Thus, evaluating the computation power and model accuracy should be considered for making a selection balance. Looking at the actions made on the building systems, the main interventions have been taken with the HVAC system, which directly contributes to affecting occupant thermal comfort and indoor air quality. It is not surprising that comfort and energy consumption are the most studies objectives, represented by reward, for different learning tasks. Incorporating learning efficiency to the reward also provides us with innovative method in designing the experiment [43].

4.1.1. Occupant behavior as a state for HVAC control

Most of the applications focused on controlling HVAC by setting occupancy as the state [44,46,47,50]. This was because the occupant's schedule usually followed a fixed routine or could be predicted with stochastic models. For example, Barrett and Linder [50] developed a HVAC control system by including the prediction of occupancy, where a modified Bayes rule was applied. Initial prior probability and environmental experience were used to obtain the posterior probability. The predicted occupancy followed a multinomial distribution of occupancy for specific times and returned a binary outcome of true and false.

One of the recent studies [44] added expert experience when they considered occupancy as one of the states to control HVAC, where the availability of state-action pairs helped to initialize the neural network and expert policy was used as a baseline for better policies. Valladares et al. [46] believed that occupant has strong influence on CO_2 level and included the number of occupants as one of their states, arguing that CO_2 control requires additional fresh air from the outside environment and increases HVAC loading. Simulations were carried out in their initial study using between 2 and 10 occupants, a number that was extended to 60 occupants in a subsequent study. A pre-training loop was used for the exploration of state-action pairs to guarantee that the agent was able to observe sufficient information for deep Q-learning. Combined with supervised learning for estimating energy consumption given occupant activity, Marantos et al. [47] developed a Neural Fitted Q-iteration, where the Q function was represented in parametric form by a multi-layer perceptron.

Table 1
Occupant behavior in MDP.

References	State	Action	Reward	Algorithms
Jia (2019) [44]	*occupancy*, room temperature, weather, time of day, energy consumption	supply air temperature	energy and comfort	policy gradient
Park (2019) [45]	*occupancy*, light switch position, indoor light level, time of a day	switching lights on/off, doing nothing	energy and comfort	value iteration
Valladares (2019) [46]	*number of people*, indoor/ ambient temperature, levels of CO_2, PMV index, etc.	setting temperature and ventilation system	CO_2 levels, PMV index, and power consumption	deep Q-learning and double Q-learning
Marantos (2019) [47]	*occupant's existence, number and activity*, indoor/outdoor temperature, humidity, solar radiation, etc.	temperature set-point	thermal comfort and energy	neural Fitted Q-iteration
Kazmi (2018) [43]	*environment including occupant behavior*, embodied energy content of vessel, heating mechanism	reheating the storage vessel or not	comfort, energy, exploration bonus	model-based RL
Lee (2018) [48]	*occupant's feeling of cold, comfort, and hot*	*occupancy, occupant's overriding the set point*	point tracking error and energy	policy gradient
Zhang (2018) [49]	*occupancy*, day of the week, hour of the day, outdoor air temperature, outdoor air relative humidity, etc.	supply water temperature set point	energy demand and indoor thermal comfort	Asynchronous Advantage Actor-Critic (A3C)
Barrett (2015) [50]	*occupancy*, room temperature; outside temperature	turning on/off heating turning on/off cooling	indoor temperature, energy	Q-learning
Fazenda (2014) [51]	time that the system has been in operation, lifetime desired for the system, heating on/off	on/off heating/cooling:, temperature set points, opening windows	*user interaction of thermal comfort*, energy	Q-learning with function approximator

4.1.2. Occupant behavior other than as a state for HVAC control

In addition to setting occupancy as the state, Zhang and Poh [49] also used a smart phone app to collect thermal preferences from the occupants. The RL agent figured out the control policy by using the collected feedback. A Bayesian model calibration was implemented for heating energy demand and average indoor air temperature before training RL agent. The training was carried out in OpenAI Gym with customized design, which provides them with flexible options to build an RL agent.

Besides occupancy, other studies used occupant's feeling of cold, comfort, and hot as a state. One simulation-based work [48] also included occupancy, as represented by uniform distribution, and the occupant's override at a set point, as actions. A sample average method was developed for approximating the gradient, a method that was shown to be applicable for complicated stochastic problems. The occupant's interaction with the thermostat was also set as the reward in one study, where the behavior of the occupant was simulated with "out", "working", and "uncomfortable" [51]. All of these studies, however, are based on the assumption that occupant behavior stays constant. If occupants change their behavior from time to time, the learning outcomes demonstrated here may fail to work.

4.1.3. Control for lighting and vessel

Two of the studies used lighting and vessel control respectively as a way to explore occupant behavior. In a study of lighting control [45], occupant was detected by smart device. Their feedback on the control was collected through a survey. RL agent was able to gather the information and the learning were continuously updated to adapt the control parameters via occupant interactions. It has been discussed that the developed method can also control a dimmable light. For vessel control [43], future occupant behavior was modeled as an uncontrollable environmental factor for hot water consumption. This was because of the limitations of the prediction model. Nevertheless, the study did show that specific behavior can be learnt from data and that the RL agent was able to adapt the policy.

4.2. Indirect influence of occupant behavior on MDP

In contrast to the studies that directly characterize occupant behavior in MDP, there are various ways for the occupant to influence the building control method. The RL agent in these studies optimizes its policy not by taking occupant behavior as an immediate input to MPD, but by measuring its indirect effect on the system. A summary of the literatures generates three categories for understanding occupant behavior: occupancy, actual behavior and providing feedback to the control system. For MDP, occupant behavior can have an effect on changing the state or state transition. In most of the studies, occupant behavior can be modeled as a stochastic factor to adjust the reward. Only a few studies associated occupant behavior with action. Detailed references for each application are shown in Table 2. For the building systems, HVAC is the mostly examined one, because it makes a substantial contribution to occupant thermal comfort and indoor air quality. RL controls for lighting, window and vessel, for example, are relatively uncommon in the existing literature; this gap should be addressed in future studies.

4.2.1. Actual behavior and state

Actual behavior includes any activities that occupants carry out to interact with the building system, for example, using hot water, turning on the light, and opening the window. The stochastic behavior will lead to frequent updates of the state in the Q-table. As some studies show, the inclusion of actual behavior in controlling vessels seems to be a viable approach [59–61]. Occupant behavior together with current state and

Table 2
Indirect influence on MDP.

Interactions	MDP State/state transition	Reward	Action
Occupancy	–	HVAC ([52–56]); HVAC and window ([57]); HVAC, lighting, blind and window ([58])	–
Actual behavior	vessel ([59–61]); PV system ([62]); lighting ([63])	HVAC ([53,64]); vessel ([65]); space heating ([66]); lighting ([63])	HVAC ([67])
Feedback	–	HVAC([68,69])	–

action, contributing to the state transition, can be modeled as a stochastic time series sequence using real world occupant behavior when the RL agent develops its policy [61]. Occupant behavior was considered as a perturbations of the vessel states: energy content inside the storage vessel and temperature [59]. The state transitions were modeled based on this assumption. Higher hot water consumption might require shorter episodes to preserve occupant comfort. A SARIMA model learned occupant behavior, with adjustments for the seasonality of individual occupant demand. Similarly, individual occupant behavior, or consumption profiles, was modelled, which defines vessel state transitions [60]. Occupant models were built to offer additional insight into individual occupant behavior types and were used for clustering households. The SARIMA models also provided reliable predictions for houses with regular consumption patterns. Non-stationary, nonlinear and highly irregular consumption profiles were dealt with using the additional bias term. In these case, different occupant behavior might be the reason for the variance of energy savings.

The RL method has also been applied to photovoltaic systems. In [62], stochastic occupant behavior capturing tap water use was included in a heat pump buffer model. It was counted as energy loss to the environment. The tap water model used historical data to relate occupant behavior to hot water demand. This historical data was used to construct a conditional probability, but it could also be used to generate samples of occupant behavior. Besides the stochastic occupant behavior associated with hot water consumption, other behaviors, such as those associated with the use of cooking appliances, lighting, washing machines entertainment devices and other electrical loads, could also be studied. Occupant behavior is the result of complex decisions that are dependent on unpredictable personal factors. One study used a hidden Markov model (HMM) to demonstrate occupant behavior around light usage, where a RL was applied without the need to consider hidden states [63]. The authors considered the whole building as a set of spaces and for each space the occupant occupied a HMM.

4.2.2. Actual behavior and reward

The studies reviewed here also show that occupant behavior can affect the reward. For example, using hot water and having the lights on at the same time can increase energy consumption. When the RL agent specifies the reward, insufficient consideration of human activities can lead to errors. Because it is very challenging to develop explicit physical models that are both accurate and fast, deep RL (DRL) algorithms are necessary to adapt for occupant activities [64]. A deep deterministic policy gradient was developed for a HVAC system in [53]. Occupant behavior was concluded to affect the reward in two ways. First, the system was set to occupied and unoccupied periods. The unoccupied spaces did not have to maintain thermal comfort. Second, variable-air-volume boxes controlling the volume of conditioned air were installed based on the set points set by the occupants. These provide more accurate air temperature controls. The percentage of discomfort occupants in the experiment experienced was represented by averaging the sensor readings from the boxes. In this study, the authors used a long-short-term-memory (LSTM) method to model historical HVAC operational data in order to build a training environment for the DRL agent to interact with. In the LSTM, the environment took the state and the action chosen by the DRL agent as inputs and returned the new state and reward for action as outputs. The DRL agent was able to learn the optimal control policy for a HVAC system by interacting with the training.

For studies that considered heating systems, the profiles of individual occupant behavior were averaged and then applied to simulate the results [65]. When this was done the SARSA(λ) algorithm was then able to learn the desired behavior – the occupant's domestic hot water use - to enhance the heating cycles. The results, however, showed a large difference in the number of heating cycles between the individual and averaged profiles. This was due to individual occupant behavior. Occupants' clothing insulation and activity level, such as sitting, cooking or sleeping, were used to calculate Predicted Mean Vote (PMV) [66]. The simulations considered the number of occupants and their metabolic rate. Typical behaviors during the week (working or studying during the day, eating dinner at home) and activities during the weekend were also simulated to evaluate energy consumption. Because occupants may feel and act differently and wear different clothes, room temperature has to be adjustable to obtain good thermal comfort.

4.2.3. Occupancy and reward

Occupancy is a more general concept where actual occupant behavior is not formulated. A number of occupancy detection methods have been be developed [70–72]. From these techniques, it is now possible to identify if a room is occupied or not and how many occupants it has. Like actual behavior, the level of occupancy is also a stochastic factor to be rewarded. In one study of HVAC systems, the transition function of the MDP was assumed unknown to the agent [52]. The occupants were assumed to affect the CO_2 concentration and to generate heat emission. When the occupancy level changed, the RL agent had sense this change and adjust the CO_2 levels and temperature accordingly. The reward, including CO_2, thermal and energy, was calculated based on a negative sigmoid function. More simply, the indoor air quality was modeled in proportion to the number of occupants [54], where a 24 h period was used to form an episode in which the number of occupants in a building could change. In the simulation, two peak periods for the number of occupants and CO_2 concentrations were found, one at approximately 9:00 am and one at 7:00 pm.

Besides air quality, one of the studies examined thermal comfort in a single-family residential home [55]. The authors assumed that the occupants were at home between 6pm and 7am the next day and that the house was unoccupied between 7am and 6pm. Thus, the RL agent tried to keep a desired temperature range whenever the occupants were at home, and remained indifferent to home temperature when the occupants were out. The setting led to a straightforward setback strategy that turned the system off when the occupants were out and turned it back on once the occupants were at home. Occupancy schedules and counts were used as a future disturbance in another recent study [56]. By the end of the experiment, the agent was able to perform well, irrespective of the number of occupants. In this study, occupancy count was not an initial part of the model the authors used for the real test. When examining the results, however, they found that the amount of cooling required varied drastically with the number of occupants and so

Table 3
Comparison of simplification methods.

	Benefit	Weak point
Variable discretization	easy to implement; problem can quickly become simple	may lose important information
Dimension reduction	able to capture all features	inaccurate description to original data
Function approximation	efficient for really complex problem	not easy to find perfect function

occupancy count was added to their subsequent calculations. Another approach is to replace default occupancy schedules with actual occupancy schedules collected from real target buildings [58]. This system was installed in a test building and the collection of accurate occupancy pattern data at the zone level was then obtained. The RL control system developed in this case could also accept occupants' feedback allowing it to train the agent where only minor modifications were needed.

4.2.4. Feedback and reward

Providing comfort feedback to the control system makes RL agents react more efficiently. Even though comfort standards, for example thermal comfort [73], can help RL agents to figure out the appropriate comfort level, this can be challenging because of data availability and individual variation.

In one study an adaptive occupant satisfaction simulator was used as a measure of user dissatisfaction that originated from the direct feedback of the building occupants [69]. Every time a signal from the simulator became available, the simulator was updated to incorporate the new information. It should be noted that this study was the earliest publication in our document set. The learning speed was slow and the agent was still making errors after four years of training. For example, it was still turning on the heating in summer and cooling during winter. This may have been because the exploration was not enough. It may also have been because the use of the recursive least-squares algorithm $TD(\lambda)$ requires high computational demands and large amounts of memory. Further training should eliminate these wrong decisions. On the positive side, this study clustered thermal conditions to produce homogeneous environments, where the classification was implemented to predict the level of thermal comfort by using the state space, including clothing insulation, indoor air temperature and relative humidity [68]. A confusion matrix was then created to evaluate its performance. It formed a function mapping the state to the reward, which enabled the occupant's feedback to be collected by the RL agent for HVAC control. This approach was able to reach the optimal policy from any start state after a certain number of episodes. The authors pointed out that when new occupant provides feedback to the agent, the model needs to be calibrated for new training.

4.2.5. Actual behavior and action

There are a limited number studies considering occupant behavior as an indication to action, because optimal action is usually learnt by the agent. One exception is to make recommendations [67]. Occupants' historical location and the shift schedule of their arrival and departure times was used for operational recommendations. The occupants' location preferences, consisting of the distribution of time over the spaces, were extracted.by using historical data. Location data was also extracted for the arrival and departure times of each occupant. The occupants could change location after receiving a move recommendation. The Q-table was maintained for learning both move and shift schedule recommendations.

4.3. Training RL agent with deep neural networks

Curse of dimensionality refers to high number of levels for state variable or continuous state, which hinders efficient exploration of the state space and leads to insufficient learning. In Table 3, three types of simplification methods are compared for their pros and cons. For value-based methods with continuous state, variable discretization takes a set of single values to represent the whole state space [50,54,63]. However, including too many such type of variables may easily lose important information in the data and increasing the size of the data will not help to compensate the loss. On the other hand, dimension reduction aims to utilize all dimensions in the variable space to extract principal features that are in relatively low dimensions [41]. Although larger amount of data can utilize more information and extract more representative features, bridging the extracted features to the original values is not straightforward and thus the policies may be misleading.

Artificial neural networks are widely used for nonlinear function approximation. It is a network of interconnected units that have some of the properties of neurons, the main components of nervous systems. Function approximation avoids to create a look-up table to store action values. Instead, approximate value is represented as a parameterized function. Actions are quickly generated by using a neural network to map the state into a set of action-value pairs [51]. The number of hidden layers in a neural network is associated to the degree of nonlinear transformations. Neural network with high number of hidden layers indicates more sophisticated mathematical modeling and better mapping ability, which is also known as deep neural network (DNN). A direct application is to extend Q-learning to deep Q-learning where the demand of data is high [46,64]. Insufficient data input to DNN is not able to optimize thousands of parameters in DNN. Thus, high quantity and quality of data guarantees the convergence of the loss function for a DNN. An alternative way to overcome the data insufficiency is to apply transfer learning technique by freezing most layers of a deep neural network that are pre-trained on data from other source. The model can be then re-trained with much less trainable parameters from the target data. The performance of this transfer learning deep neural network model will keep improving over time while more operational data are streaming into the model [74]. For policy-based implementations [53,56,75], the parameters in the policy network, θ, connect the DNN layers in Eq. (5). Unlike deep Q-network, policy network maps a state to an action that maximizes the expected reward from sampled trajectories. Training policy DNN requires intensive experiments to generate actual behaviors, which is time-consuming and costly in terms of data collection. In Section 5, we will discuss the details of implementing an alternative off-policy strategy.

4.4. The algorithms

Algorithm selection is problem dependent. For problems with small state-action space, value based algorithms are preferred because the optimization can converge quickly. For problems with large state-action space, creating a table to update learnt action values is not feasible. For building control applications, it is common to adopt continuous variables such as temperature, solar radiation, and occupancy duration for the analysis. Discretization to such variables may mitigate the problem, but can also generate bias. Thus, variants of Q-learning algorithms and policy-based algorithms have emerged as ways to achieve more exploration to the state space. As seen in Fig. 5, tabular Q-learning is still the most commonly used algorithm any more, but the relative frequency of this has reduced in recent years compared to earlier work [24]. The variants of Q-learning, for example Q-learning with approximation, and policy-based algorithms now also supply various strategies for dealing with continuous state. The class of actor-critic algorithms seem to be an alternative approach; more applications need to be developed.

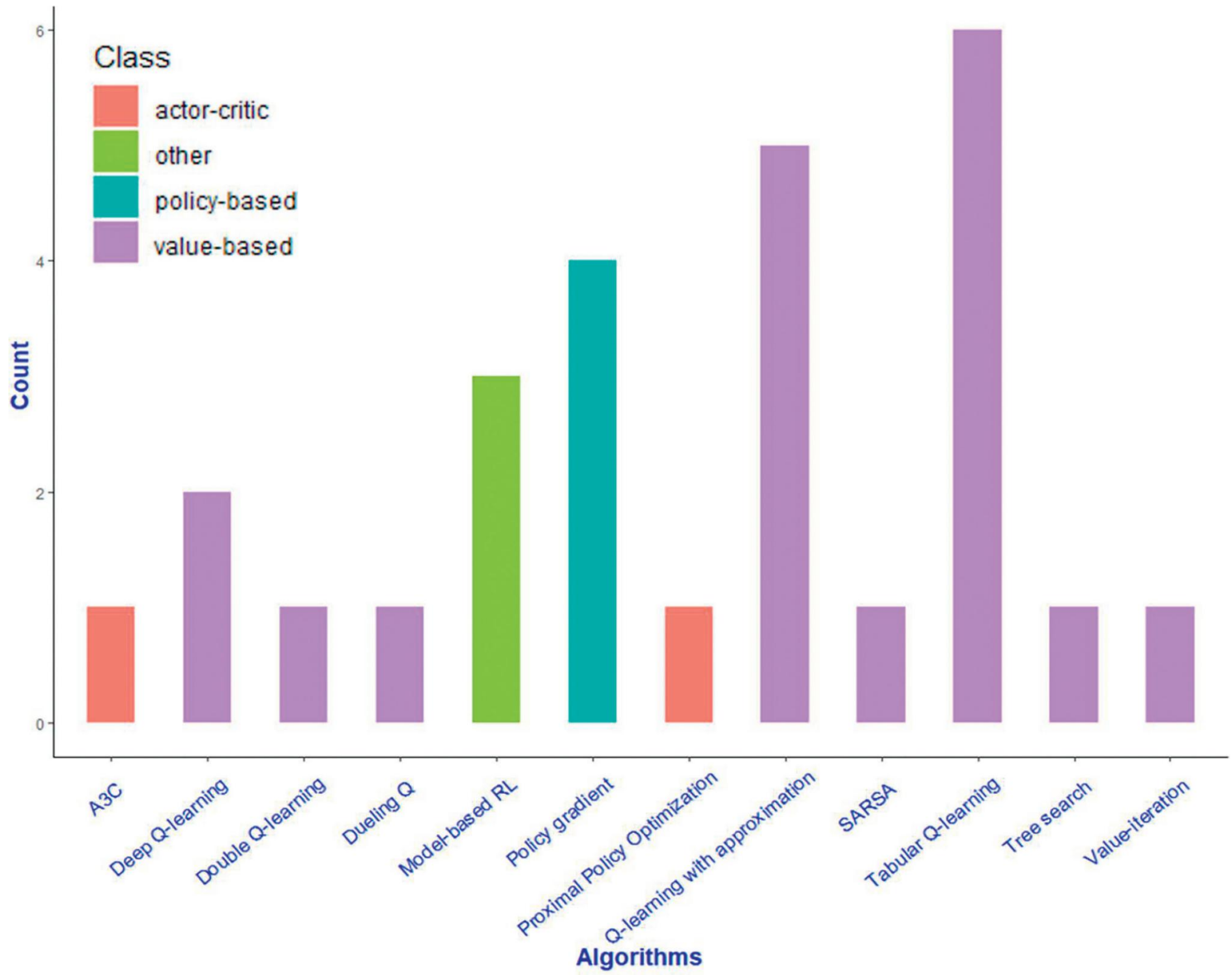

Fig. 5. Algorithms used in the literatures.

4.5. Keywords

The growth of authors' keywords in recent years depicts how the topic in this study has evolved. In Fig. 6, we present keyword growth by using the loess smoothed occurrence. Loess is a nonparametric regression strategy for fitting smooth curves to empirical data [76]. The phase "deep reinforcement learning" is a subclass of RL algorithms. "Deep" in this case refers to the number of layers in a neural network. A shallow network has one so-called hidden layer and a deep network has more than one. Training deep neural networks usually requires a large amount of data and extensive computing resources. Thus, a deep RL agent will outperform over the long run [77]. For the control target, "energy" and "thermal comfort" are the most relevant words and are also likely to be important topics for future study.

5. Discussions

Before training an RL agent, one of two strategies must be selected: on-policy or off-policy. For on-policy training, the agent learning and interacting with the environment is the same. For value-based methods, it estimates the value of the policy being followed. SARSA is on-policy when the agent starts from a state, makes an action, receives a reward, and is transited to next state. Based on the new state, the agent takes an action. The process will be conservative and sensitive to errors, but will be efficient when the exploration penalty is small. On the other hand, agents trained by off-policy are different from those interacting with the environment. Off-policy methods can find the optimal policy even if the agent behaves randomly. Thus, ignoring the interacting agent's policy may lead to a suboptimal policy when most of the rewards are negative. For policy-based methods, there is also a need to consider the gains of applying off-policy learning, because the problems can emerge with large or continuous state-action space and exploration is not feasible. The agent interacting with the environment is usually making policies under the parameter setting θ' that differs from θ for the agent to be trained. Approximations can be made by importance sampling [78] in order to get the gradient. Thus, when an agent is exploring in error-insensitive systems, SARSA may be the preferred option. Agents that do not explore should use Q-learning.

Another issue that needs to be considered is the actual implementation of collecting occupant behavior. On-policy for policy-based methods can only update its gradient when actual actions are made and $J(\theta)$ are observed. Actual deployment of devices in buildings should be able to provide frequent reward and state signals to the agent. Moreover, the repetition of the signals' provision allows the agent to update policy parameter θ. This is still a challenge, not only for devices but also for the occupant to remember to repeatedly react in the same environment so that more sampled trajectories can be collected. Thus, shifting

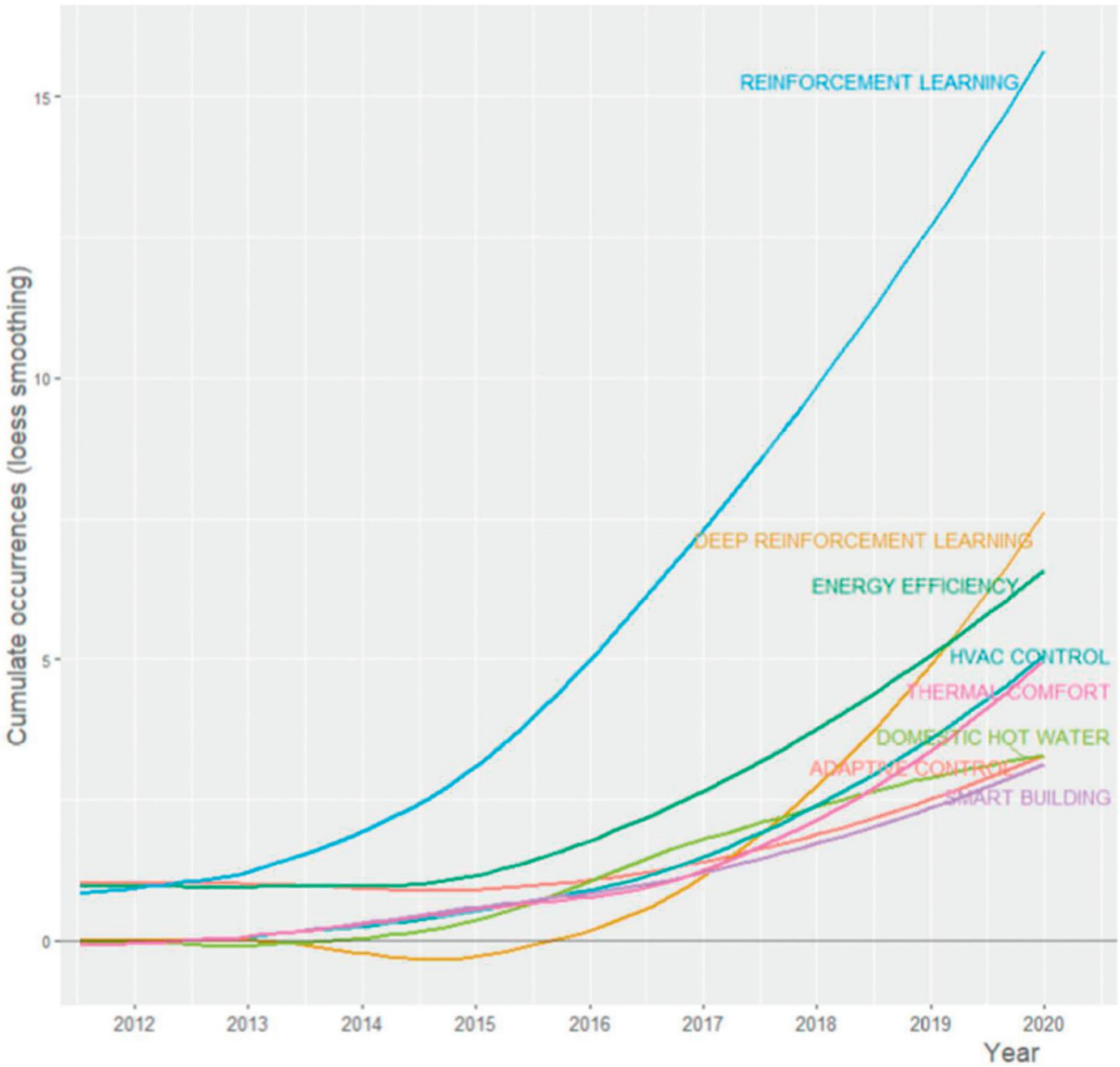

Fig. 6. Keywords growth.

to off-policy methods makes learning more efficient for complex control tasks.

6. Conclusions

This study has briefly reviewed the reinforcement learning methods for building control that incorporate occupant behavior. Since RL methods assume that the agent interacts with a stochastic environment and works in a data-driven fashion, they are of great importance when forming intelligent building systems where occupant behavior has a significant influence on building performance.

Historical publications on this topic were searched for in Scopus to understand the publication sources, types, years, citations and country collaborations of the existing published literature. It can be seen that, because of the success of deep reinforcement learning in game playing, the number of publications in this field has been growing. The topic covers multiple disciplines including energy, building, computer science, optimal control, sustainability and engineering. Integration of diverse domain knowledge may accelerate the construction of more intelligent systems. However, the current number of citations is not high and international collaborations are still only between a small number of countries. Thus, joint efforts should be made in order to strengthen the research around the topic.

In this study, we first analyzed those studies that examined occupant behavior within the MDP framework. Most of the studies we examined considered occupant behavior as a state for controlling HVAC systems. It is likely that this will remain the focus of new and upcoming work. The rest of the literature can be grouped into three categories regarding the ways of interaction: occupancy, actual behavior and providing feedback where occupant behavior poses an indirect effect on MDP. The reward is the MDP element that is most sensitive to occupant behavior, which makes it essential to design the reward in an efficient way [79], because for occupants with different profiles, their preferences for comfort factors will vary [80,81].

Over the course of this review we have noticed that the classical tabular Q-learning algorithm has become insufficient for building control with stochastic and complex occupant behavior. Adopting a Q-table to store action values may yield an unreliable policy. As more approximation algorithms have been applied to actual studies, future research should be able to implement, test and verify these in different scenarios. We also compared simplification method and highlighted the function approximation with deep neural network due to the curse of dimensionality. Finally, we discussed some of the issues to be taken into consideration when using off-policy strategy. The implementation of off-policy control requires frequent signal collection from the occupant.

Individual contributions

Mengjie Han: Methodology, Funding acquisition, Software, Visualization, Roles/Writing – original draft

Jing Zhao: Roles/Writing – original draft, Investigation

Xingxing Zhang: Conceptualization, Writing – review & editing, Funding acquisition

Jingchun Shen: Conceptualization, Writing – review & editing

Yu Li: Writing – review & editing

Declaration of Competing Interest

This manuscript has not been published and is not under consideration for publication elsewhere. All authors are employees of non-profit institutes and have no conflicts of interest to disclose. All authors have also read and understood author's guidelines and ethical policies.

Acknowledgements

The authors are thankful for the financial support from IMMA project of research network (391836), Dalarna University, Sweden and International science and technology cooperation center in Hebei Province (20594501D), China.

References

[1] M.P. Fanti, A.M. Mangini, M. Roccotelli, A simulation and control model for building energy management, Control Eng. Pract. 72 (2018) 192–205 Mar, doi:10.1016/j.conengprac.2017.11.010.
[2] P. Xu, E.H.-W. Chan, Q.K. Qian, Success factors of energy performance contracting (EPC) for sustainable building energy efficiency retrofit (BEER) of hotel buildings in China, Energy Policy 39 (11) (2011) 7389–7398, doi:10.1016/j.enpol.2011.09.001.
[3] P. Nejat, F. Jomehzadeh, M.M. Taheri, M. Gohari, M.Z. Abd. Majid, A global review of energy consumption, CO_2 emissions and policy in the residential sector (with an overview of the top ten CO_2 emitting countries), Renew. Sustain. Energy Rev. 43 (2015) 843–862 Mar, doi:10.1016/j.rser.2014.11.066.
[4] L. Pérez-Lombard, J. Ortiz, C. Pout, A review on buildings energy consumption information, Energy Build. 40 (3) (2008) 394–398 Jan., doi:10.1016/j.enbuild.2007.03.007.
[5] T. Hong, S.C. Taylor-Lange, S. D'Oca, D. Yan, S.P. Corgnati, Advances in research and applications of energy-related occupant behavior in buildings, Energy Build. 116 (2016) 694–702 Mar., doi:10.1016/j.enbuild.2015.11.052.
[6] K.-.U. Ahn, D.-.W. Kim, C.-.S. Park, P. de Wilde, Predictability of occupant presence and performance gap in building energy simulation, Appl. Energy 208 (2017) 1639–1652 Dec., doi:10.1016/j.apenergy.2017.04.083.
[7] W. O'Brien, I. Gaetani, S. Gilani, S. Carlucci, P.-.J. Hoes, J. Hensen, International survey on current occupant modelling approaches in building performance simulation, J. Build. Perform. Simul. 10 (5–6) (2017) 653–671 Nov., doi:10.1080/19401493.2016.1243731.
[8] J. Li, Z.(Jerry) Yu, F. Haghighat, G. Zhang, Development and improvement of occupant behavior models towards realistic building performance simulation: a review, Sustain. Cities Soc. 50 (2019) 101685 Oct., doi:10.1016/j.scs.2019.101685.
[9] T. Hong, Y. Chen, Z. Belafi, S. D'Oca, Occupant behavior models: a critical review of implementation and representation approaches in building performance simulation programs, Build. Simul. 11 (1) (2018) 1–14 Feb., doi:10.1007/s12273-017-0396-6.
[10] A. Mahdavi, F. Tahmasebi, The deployment-dependence of occupancy-related models in building performance simulation, Energy Build. 117 (2016) 313–320 Apr., doi:10.1016/j.enbuild.2015.09.065.
[11] S. Carlucci, et al., Modeling occupant behavior in buildings, Build. Environ. 174 (2020) 106768 May, doi:10.1016/j.buildenv.2020.106768.
[12] T. Hong, D. Yan, S. D'Oca, C. Chen, Ten questions concerning occupant behavior in buildings: the big picture, Build. Environ. 114 (2017) 518–530 Mar., doi:10.1016/j.buildenv.2016.12.006.
[13] D. Yan, et al., Occupant behavior modeling for building performance simulation: current state and future challenges, Energy Build. 107 (2015) 264–278 Nov., doi:10.1016/j.enbuild.2015.08.032.
[14] P.H. Shaikh, N.B.M. Nor, P. Nallagownden, I. Elamvazuthi, T. Ibrahim, A review on optimized control systems for building energy and comfort management of smart sustainable buildings, Renew. Sustain. Energy Rev. 34 (2014) 409–429 Jun., doi:10.1016/j.rser.2014.03.027.
[15] P. Zhao, S. Suryanarayanan, and M.G. Simoes, "An Energy Management System for Building Structures Using a Multi-Agent Decision-Making Control Methodology," 2013, vol. 49(1), pp. 322–330.
[16] L.P. Kaelbling, M.L. Littman, A.W. Moore, Reinforcement Learning: a Survey, J. Artif. Intell. Res. 4 (1996) 237–285.
[17] V. Mnih, et al., Human-level control through deep reinforcement learning, Nature 518 (7540) (2015) 529–533 Feb., doi:10.1038/nature14236.
[18] D. Silver, et al., Mastering the game of Go with deep neural networks and tree search, Nature 529 (7587) (2016) 484–489 Jan., doi:10.1038/nature16961.
[19] D. Silver, et al., Mastering the game of Go without human knowledge, Nature 550 (7676) (2017) 354–359 Oct., doi:10.1038/nature24270.
[20] V. Mnih et al., "Playing Atari with Deep Reinforcement Learning," 2013, Accessed: Jan. 26, 2019. [Online]. Available: http://arxiv.org/abs/1312.5602.
[21] S. Gu, T. Lillicrap, I. Sutskever, S. Levine, Continuous Deep Q-Learning with Model-Based Acceleration, in: Proceedings of the 33rd International Conference on Machine Learning, 48, New York, NY, USA, 2016.
[22] T.P. Lillicrap et al., "Continuous control with deep reinforcement learning," 2016, Accessed: Feb. 02, 2019. [Online]. Available: http://arxiv.org/abs/1509.02971.
[23] M. Aria, C. Cuccurullo, bibliometrix : an R-tool for comprehensive science mapping analysis, J. Informetr. 11 (4) (2017) 959–975 Nov., doi:10.1016/j.joi.2017.08.007.
[24] M. Han, et al., A review of reinforcement learning methodologies for controlling occupant comfort in buildings, Sustain. Cities Soc. 51 (2019) 101748 Nov., doi:10.1016/j.scs.2019.101748.
[25] A.I. Dounis, C. Caraiscos, Advanced control systems engineering for energy and comfort management in a building environment—A review, Renew. Sustain. Energy Rev. 13 (6–7) (2009) 1246–1261 Aug., doi:10.1016/j.rser.2008.09.015.
[26] N. Aste, M. Manfren, G. Marenzi, Building Automation and Control Systems and performance optimization: a framework for analysis, Renew. Sustain. Energy Rev. 75 (2017) 313–330 Aug., doi:10.1016/j.rser.2016.10.072.
[27] F. Ascione, N. Bianco, C. De Stasio, G.M. Mauro, G.P. Vanoli, A new comprehensive approach for cost-optimal building design integrated with the multi-objective model predictive control of HVAC systems, Sustain. Cities Soc. 31 (2017) 136–150 May, doi:10.1016/j.scs.2017.02.010.
[28] M. Royapoor, A. Antony, T. Roskilly, A review of building climate and plant controls, and a survey of industry perspectives, Energy Build 158 (2018) 453–465 Jan., doi:10.1016/j.enbuild.2017.10.022.
[29] R.S. Sutton, A.G. Barto, Reinforcement Learning: An Introduction, 2nd ed., The MIT Press, Cambridge, Massachusetts, 2018.
[30] R. Bellman, A Markovian decision process, J. Math. Mech. 6 (5) (1957) 679–684.
[31] R. Bellman, Dynamic Programming, Princeton University Press, Princeton, 1957.
[32] C.J.C.H. Watkins, Learning from Delayed Rewards Ph.D. thesis, University of Cambridge, 1989.
[33] M. Hessel and J. Modayil, "Rainbow: combining improvements in deep reinforcement learning," pp. 3215–3222.
[34] R.S. Sutton, D.A. McAllester, S.P. Singh, and Y. Mansour, "Policy gradient methods for reinforcement learning with function approximation," pp. 1057–1063.
[35] J. Schulman, F. Wolski, P. Dhariwal, A. Radford, and O. Klimov, "Proximal policy optimization algorithms," 2017, Accessed: Apr. 12, 2020. [Online]. Available: http://arxiv.org/abs/1707.06347.
[36] J. Schulman, S. Levine, P. Moritz, M. Jordan, P. Abbeel, Trust region policy optimization, in: Proceedings of the 31st International Conference on Machine Learning, 37, France, 2015, pp. 1–9.
[37] V.R. Konda, J.N. Tsitsiklis, Actor-Critic Algorithms, Advances in Neural Information Processing Systems (NIPS), 12, Denver, Colorado, 2000, pp. 1008–1014.
[38] M. Babaeizadeh, I. Frosio, S. Tyree, J. Clemons, and J. Kautz, "Reinforcement learning through asynchronous advantage actor-critic on a GPU," 2017, Accessed: Apr. 12, 2020. [Online]. Available: http://arxiv.org/abs/1611.06256.
[39] V. Mnih et al., "Asynchronous Methods for Deep Reinforcement Learning," 2016, Accessed: Feb. 03, 2019. [Online]. Available: http://arxiv.org/abs/1602.01783.
[40] Z. Wang, T. Hong, Reinforcement learning for building controls: the opportunities and challenges, Appl. Energy 269 (2020) 115036 Jul., doi:10.1016/j.apenergy.2020.115036.
[41] F. Ruelens, S. Iacovella, B.J. Claessens, R. Belmans, Learning agent for a heat-pump thermostat with a set-back strategy using model-free reinforcement learning, energies 8 (2015) 8300–8318, doi:10.3390/en8088300.
[42] M. Han, et al., A novel reinforcement learning method for improving occupant comfort via window opening and closing, Sustain. Cities Soc. 61 (2020) 102247 Oct., doi:10.1016/j.scs.2020.102247.
[43] H. Kazmi, F. Mehmood, S. Lodeweyckx, J. Driesen, Gigawatt-hour scale savings on a budget of zero: deep reinforcement learning based optimal control of hot water systems, Energy 144 (2018) 159–168 Feb., doi:10.1016/j.energy.2017.12.019.
[44] R. Jia, M. Jin, K. Sun, T. Hong, C. Spanos, Advanced building control via deep reinforcement learning, Energy Procedia 158 (2019) 6158–6163 Feb., doi:10.1016/j.egypro.2019.01.494.
[45] J.Y. Park, T. Dougherty, H. Fritz, Z. Nagy, LightLearn: an adaptive and occupant centered controller for lighting based on reinforcement learning, Build. Environ. 147 (2019) 397–414 Jan., doi:10.1016/j.buildenv.2018.10.028.
[46] W. Valladares, et al., Energy optimization associated with thermal comfort and indoor air control via a deep reinforcement learning algorithm, Build. Environ. 155 (2019) 105–117 May, doi:10.1016/j.buildenv.2019.03.038.
[47] C. Marantos, C. Lamprakos, K. Siozios, D. Soudris, Towards Plug&Play smart thermostats for building's heating/cooling control, in: K. Siozios, D. Anagnostos, D. Soudris, E. Kosmatopoulos (Eds.), IoT for Smart Grids, Eds., Cham: Springer International Publishing, 2019, pp. 183–207.
[48] D. Lee, S. Lee, P. Karava, J. Hu, Simulation-based policy gradient and its building control application, in: Proceedings of the *Annual American Control Conference (ACC)*, Milwaukee, WI, 2018, pp. 5424–5429, doi:10.23919/ACC.2018.8431592. Jun. 2018.

[49] Z. Zhang, K.P. Lam, Practical implementation and evaluation of deep reinforcement learning control for a radiant heating system, in: Proceedings of the 5th ACM International Conference on Systems for Built Environments, Shenzen, China, 2018, doi:10.1145/3276774.3276775.

[50] E. Barrett, S. Linder, Autonomous HVAC control, A reinforcement learning approach, in: A. Bifet, M. May, B. Zadrozny, R. Gavalda, D. Pedreschi, F. Bonchi, J. Cardoso, M. Spiliopoulou (Eds.), Machine Learning and Knowledge Discovery in Databases, 9286, Eds., Cham: Springer International Publishing, 2015, pp. 3–19.

[51] P. Fazenda, K. Veeramachaneni, P. Lima, U.-.M. O'Reilly, Using reinforcement learning to optimize occupant comfort and energy usage in HVAC systems, J Ambient Intell. Smart Environ. 6 (6) (2014) 675–690, doi:10.3233/AIS-140288.

[52] L. Eller, L.C. Siafara, T. Sauter, Adaptive control for building energy management using reinforcement learning, in: Proceedings of the *IEEE International Conference on Industrial Technology (ICIT)*, Lyon, 2018, pp. 1562–1567, doi:10.1109/ICIT.2018.8352414. Feb..

[53] Z. Zou, X. Yu, S. Ergan, Towards optimal control of air handling units using deep reinforcement learning and recurrent neural network, Build. Environ. 168 (Jan. 2020) 106535, doi:10.1016/j.buildenv.2019.106535.

[54] S. Baghaee, I. Ulusoy, User comfort and energy efficiency in HVAC systems by Q-learning, in: Proceedings of the *26th Signal Processing and Communications Applications Conference (SIU)*, Izmir, Turkey, 2018, pp. 1–4, doi:10.1109/SIU.2018.8404287. May.

[55] D. Urieli, P. Stone, A Learning Agent for Heat-Pump Thermostat Control, Proceedings of the 12th International Conference on Autonomous Agents and Multiagent Systems (AAMAS), Saint Paul, Minnesota, USA, 2013.

[56] B. Chen, Z. Cai, M. Berges, Gnu-RL: A Precocial Reinforcement Learning Solution for Building HVAC Control Using a Differentiable MPC Policy, in: BuildSys '19: Proceedings of the 6th ACM International Conference on Systems for Energy-Efficient Buildings, Cities, and Transportation, New York, NY, USA, 2019, pp. 316–325, doi:10.1145/3360322.3360849.

[57] Y. Chen, L.K. Norford, H.W. Samuelson, A. Malkawi, Optimal control of HVAC and window systems for natural ventilation through reinforcement learning, Energy Build. 169 (2018) 195–205 Jun., doi:10.1016/j.enbuild.2018.03.051.

[58] X. Ding, W. Du, A. Cerpa, OCTOPUS: Deep Reinforcement Learning for Holistic Smart Building Control, in: BuildSys '19: Proceedings of the 6th ACM International Conference on Systems for Energy-Efficient Buildings, Cities, and Transportation, New York, NY, USA, 2019, pp. 326–335, doi:10.1145/3360322.3360857.

[59] H. Kazmi, S. D'Oca, Demonstrating model-based reinforcement learning for energy efficiency and demand response using hot water vessels in net-zero energy buildings, in: Proceedings of the IEEE PES Innovative Smart Grid Technologies Conference Europe (ISGT-Europe), Ljubljana, Slovenia, 2016, pp. 1–6, doi:10.1109/ISGTEurope.2016.7856208. Oct..

[60] H. Kazmi, S. D'Oca, C. Delmastro, S. Lodeweyckx, S.P. Corgnati, Generalizable occupant-driven optimization model for domestic hot water production in NZEB, Appl. Energy 175 (2016) 1–15, doi:10.1016/j.apenergy.2016.04.108.

[61] H. Kazmi, J. Suykens, J. Driesen, Valuing Knowledge, Information and Agency in Multi-agent Reinforcement Learning: a Case Study in Smart Buildings, in: Proceedings of the 17th International Conference on Autonomous Agents and Multiagent Systems (AAMAS 2018), Stockholm, Sweden, 2018, pp. 585–587.

[62] A. Soares, D. Geysen, F. Spiessens, D. Ectors, O. De Somer, K. Vanthournout, Using reinforcement learning for maximizing residential self-consumption – Results from a field test, Energy Build. 207 (2020) 109608 Jan., doi:10.1016/j.enbuild.2019.109608.

[63] X. Pan, B. Lee, An Approach of Reinforcement Learning Based Lighting Control for Demand Response, International Exhibition and Conference for Power Electronics, Intelligent Motion, Renewable Energy and Energy Management, Nuremberg, Germany, Germany, 2016, pp. 558–565.

[64] T. Wei, X. Chen, Model-based and data-driven approaches for building automation and control, in: Proceedings of the International Conference on Computer-Aided Design, San Diego, CA, USA, 2018, pp. 1–8, doi:10.1145/3240765.3243485.

[65] A. Ali, H. Kazmi, Minimizing grid interaction of solar generation and DHW loads in nZEBs using model-free reinforcement learning, in: Data Analytics for Renewable Energy Integration: Informing the Generation and Distribution of Renewable Energy, 10691, Cham, 2017, pp. 47–58, doi:10.1007/978-3-319-71643-5_5.

[66] J. Zhu, F. Lauri, A. Koukam, V. Hilaire, A hybrid intelligent control system based on PMV optimization for thermal comfort in smart buildings, in: Advances in Intelligent Systems and Computing, 358, 2015, pp. 27–36, doi:10.1007/978-3-319-17996-4_3.

[67] P. Wei, S. Xia, X. Jiang, Energy Saving Recommendations and User Location Modeling in Commercial Buildings, in: Proceedings of the 26th Conference on User Modeling, Adaptation and Personalization, Singapore, 2018, pp. 3–11.

[68] S. Lu, W. Wang, C. Lin, E.C. Hameen, Data-driven simulation of a thermal comfort-based temperature set-point control with ASHRAE RP884, Build. Environ. 156 (2019) 137–146 Jun., doi:10.1016/j.buildenv.2019.03.010.

[69] K. Dalamagkidis, D. Kolokotsa, K. Kalaitzakis, G.S. Stavrakakis, Reinforcement learning for energy conservation and comfort in buildings, Build. Environ. 42 (7) (2007) 2686–2698 Jul., doi:10.1016/j.buildenv.2006.07.010.

[70] K. Sun, Q. Zhao, J. Zou, A review of building occupancy measurement systems, Energy Build. 216 (2020) 109965 Jun., doi:10.1016/j.enbuild.2020.109965.

[71] W. Kleiminger, C. Beckel, T. Staake, S. Santini, Occupancy detection from electricity consumption data, in: Proceedings of the 5th ACM Workshop on Embedded Systems For Energy-Efficient Buildings - BuildSys'13, Roma, Italy, 2013, pp. 1–8, doi:10.1145/2528282.2528295.

[72] H. Saha, A.R. Florita, G.P. Henze, S. Sarkar, Occupancy sensing in buildings: a review of data analytics approaches, Energy Build. 188–189 (2019) 278–285 Apr., doi:10.1016/j.enbuild.2019.02.030.

[73] ASHRAEStandard 55–Thermal Environmental Conditions For Human Occupancy, ASHRAE Inc, 2017.

[74] Y. Chen, Z. Tong, Y. Zheng, H. Samuelson, L. Norford, Transfer learning with deep neural networks for model predictive control of HVAC and natural ventilation in smart buildings, J. Clean. Prod. 254 (2020) 119866 May, doi:10.1016/j.jclepro.2019.119866.

[75] J.R. Vazquez-Canteli, J. Kämpf, G. Henze, Z. Nagy, Demo Abstract: CityLearn v1.0 - An OpenAI Gym Environment for Demand Response with Deep Reinforcement Learning, Buildsys, New York, USA, 2019, doi:10.1145/3360322.3360998.

[76] W.G. Jacoby, Loess: a nonparametric, graphical tool for depicting relationships between variables, Elect Stud. 19 (2000) 577–613, doi:10.1016/S0261-3794(99)00028-1.

[77] Y. Duan, X. Chen, R. Houthooft, J. Schulman, P. Abbeel, Benchmarking Deep Reinforcement Learning for Continuous Control, in: Proceedings of the 33rd International Conference on Machine Learning, 48, New York, NY, USA, 2016, pp. 1–10.

[78] H. Hachiya, T. Akiyama, M. Sugiayma, J. Peters, Adaptive importance sampling for value function approximation in off-policy reinforcement learning, Neural Netw. 22 (10) (2009) 1399–1410 Dec., doi:10.1016/j.neunet.2009.01.002.

[79] Z. Zheng, J. Oh, S. Singh, Advances in Neural Information Processing Systems 31 (NIPS), Montréal, Canada, 2018, pp. 1–11.

[80] M. Frontczak, P. Wargocki, Literature survey on how different factors influence human comfort in indoor environments, Build. Environ. 46 (4) (2011) 922–937 Apr., doi:10.1016/j.buildenv.2010.10.021.

[81] A. Zalejska-Jonsson, M. Wilhelmsson, Impact of perceived indoor environment quality on overall satisfaction in Swedish dwellings, Build. Environ. 63 (2013) 134–144 May, doi:10.1016/j.buildenv.2013.02.005.

Energy and Built Environment 2 (2021) 149–156

Contents lists available at ScienceDirect

Energy and Built Environment

journal homepage: http://www.keaipublishing.com/en/journals/energy-and-built-environment/

Experimental measurements of surgical microenvironments in two operating rooms with laminar airflow and mixing ventilation systems

Guangyu Cao[a,*], Ingeborg Kvammen[a], Thea Amalie Solberg Hatten[a], Yixian Zhang[b], Liv-Inger Stenstad[c], Gabriel Kiss[c], Jan Gunnar Skogås[c]

[a] Department of Energy and Process Engineering, Norwegian University of Science and Technology, Kolbjørn Hejes Vei 1B, 7491 Trondheim, Norway
[b] Faculty of Urban Construction and Environmental Engineering, Chongqing University, Chongqing 40045, China
[c] Operating Room of the Future at St. Olavs Hospital, St. Olavs Hospital, Olav Kyrres Gate 10, 7030 Trondheim, Norway

A R T I C L E I N F O

Keywords:
Operating room
Laminar airflow
Mixing ventilation
Surgical microenvironment
Thermal environment

A B S T R A C T

At present, laminar airflow (LAF) systems and mixing ventilation (MV) systems are two commonly used ventilation solutions for operating rooms (ORs) to ensure the required indoor air quality. However, recent studies have shown that there is little difference in the prevalence of surgical site infection (SSI) for the LAF systems and MV systems. The objective of this study was to compare the performance of an LAF system with an MV system in ORs at St. Olavs hospital, Norway. In this study, all the experimental measurements were conducted in real ORs with LAF and MV systems. This study found that the air velocity above the surgical incision is approximately two times higher in the OR with LAF than that in the OR with MV. The use of surgical lamps and different airflow patterns may contribute to the different surgical microenvironment of ORs with LAF and MV.

1. Introduction

A surgical site infection (SSI) is an infection within 30 days post surgery. SSIs account for 36% of nosocomial infections and are the most common hospital-acquired infections for surgical patients in modern hospitals [1]. SSIs can be classified by their location, which indicates their severity. Superficial infections involve only the skin or subcutaneous tissue, while those involving deep soft tissues are referred to as deep incisional infections. The most severe infections involve organs or body spaces [2]. In Norway, the average SSI rate of hip surgery ranged from 3.3% to 3.6% between 2015 and 2018. However, more severe variations can be observed for St. Olav's Hospital over the same time period [3]. The general health and disease states of the patient, as well as proper technique and sound judgment being exercised by the surgical team, are the most critical factors in avoiding postoperative infections and are difficult to quantify. However, especially for procedures with low infection rates (<3%), the development of SSIs is related to airborne exogenous microorganisms [4].

A Spanish study including 18,910 patients investigated both environmental and patient variations in relation to SSIs [5]. A percentage of 6.7% experienced SSIs, but the definitions and procedures related to tracking SSIs vary, causing uncertainty when performing comparisons. Superficial SSIs were associated with environmental factors, such as temperature, humidity and surface contamination. Higher relative humidity was linked to a higher risk of SSIs. However, these were room characteristics and not directly linked to the surgical wound environment. Another study regarding humidity in operating rooms also found an increase in SSI rates with increased humidity, although the differences in the study were not statistically significant [6].

Thermal comfort is defined as that condition of mind that expresses satisfaction with the thermal environment and is assessed by subjective evaluation [7]. An operating room is one of the most controlled work environments, and it is important that the environment is perceived as comfortable and healthy for both the surgical staff and the patient [8]. For the surgical staff, it is important to maintain thermal comfort so that they can perform their work. If the surgical staff experience thermal discomfort, they are either too cold or too warm in their working environment. The sensation of thermal discomfort can affect their well-being and lead to poor work efficiency, headache and dizziness. Thermal discomfort for the patient could mean that the thermoregulatory responses of the human body are suppressed, which can cause illness and, in some cases, death [9].

Thermal comfort depends on six parameters. They are divided into two groups: environmental parameters, which consist of the air temperature, mean radiant temperature, relative air velocity and relative humidity of the air, and personal parameters, which consist of the metabolic rate and clothing insulation [7]. According to ASHRAE [7], an acceptable thermal environment is an environment that 80% of occupants find thermally acceptable. The focus should be to achieve the environmen-

* Corresponding author.
E-mail address: guangyu.cao@ntnu.no (G. Cao).

https://doi.org/10.1016/j.enbenv.2020.08.003
Available online 25 August 2020

Nomenclature

A	wound area (m^2)
B	temperature factor (K)
c_p	specific heat at constant pressure (J/kg•K)
h_c	convection heat transfer coefficient (W/m^2 •K)
h_r	radiation heat transfer coefficient (W/m^2 •K)
h_m	convection mass transfer coefficient (m/s)
h_{fg}	the latent heat of vaporization (J/kg)
k_{air}	conductivity of air (W/m•K)
L	characteristic length (m)
Le	Lewis number
M_w	molecular weight of water (kg/kmol)
n''_w	vapor transfer (kg/m^2•s)
$P_{w,i}$	water pressure at the temperature of the point above the incision (N/m^2)
$P_{w,sat}$	saturated water pressure at the temperature of the point above the incision (N/m^2)
q''_{conv}	convective heat transfer (W)
q''_{rad}	radiant heat transfer (W)
q	heat transfer (W)
R	gas constant (J/kg •K)
Ra_L	Rayleigh number by length scale.
Nu	Nusselt number
T	temperature (K)
T_i	air temperature above wound (K)
T_s	surface temperature (K)
T_{sur}	surrounding temperature (K)
ε	emissivity (0< ε <1)
σ	*Stefan–Boltzman constant* (5.67×10^{-8} W/m^2 •K^4)
ρ	density of fluid (kg/m^3)
$\rho_{w,s}$	density at the temperature of the surface (kg/m^3)
$\rho_{w,i}$	density at the temperature of the point above the incision (kg/m^3)

tal conditions where the highest possible percentage of the occupants feel thermally comfortable [10]. Standards and guidelines regarding the ventilation of operating rooms often provide ranges for environmental parameters rather than one specific value. This has to do with the different surgical procedures being performed at a hospital and each procedure's requirements for the indoor environment. When determining the requirements for one specific OR, the needs of the patient and the surgical team and the security aspects of infection control need to be considered [11]. Two ventilation strategies usually used in operating rooms are mixing ventilation (MV) and laminar airflow (LAF).

The working principle of MV is to supply air to a room with an air velocity high enough to create full mixing throughout the room [12]. The air velocity must be high enough so that the total air volume in the room is moved [13]. It is important to supply air at a velocity that can create full mixing in the room while considering that noise might be generated. The purpose of creating full mixing throughout the room is to mix the supply air with the existing air to dilute whatever the contaminants are present. To avoid draught in the zone of occupancy, the supply diffusers are usually located in the ceiling or on the wall.

LAF is normally used in cleanrooms such as operating rooms to prevent back swirling of polluted air. Cleanroom ventilation requires high airflow rates, which is why the ventilation is typically arranged by recirculating the air through a bank of high efficient particulate air filters (HEPA) [13]. In a hospital environment, the ventilation is a unidirectional airflow through the clean zone or room. This unidirectional airflow typically has a velocity between 0.3 and 0.5 m/s [13]· The airflow is highest at the center of the HEPA filter and decreases towards the periphery. The movement of the surgical staff is an important factor with LAF ventilation and can transport bacteria to a sterile zone [1]. Fig. 1 shows the working principle of both MV and LAF. As a matter as fact, using LAF has been recommended in several national guidelines and standards [14–17]. The great effort of previous studies have been made on the performance of various ventilation solutions regarding airborne contamination levels and the whole airflow pattern in the room [18–22]. However, very little studies have been done regarding the surgical microenvironment under various ventilation strategies [23]. The objective of this study was to investigate the effects of LAF systems and MV systems on the surgical microenvironments in ORs at St. Olavs Hospital. A surgical microenvironment is defined as the area close to the surgical incision, illustrated in Fig. 1.

2. Theoretical modeling

Room airflow distribution may affect the heat transfer from the surgical incision by convective heat transfer mechanisms. In addition, radiation from surfaces, including equipment and personnel, induce heat transfer. Wet surfaces can cause additional heat loss due to the evaporation of fluids [24].

The total heat transfer from the surgical wound can be denoted as shown in Eq. (1)

$$q = q''_{conv} + q''_{rad} \tag{1}$$

where A_s is the wound area, q''_{conv} is the convective heat transfer, q''_{rad} is the radiant heat transfer. The convective and radiant heat transfer rates are shown in Eqs. (2) and (3) [24]:

$$q''_{conv} = h_c\left(T_s - T_i\right) * A_s \tag{2}$$

$$q''_{rad} = h_r\left(T_s - T_{sur}\right) * A_s \tag{3}$$

$$h_r = \varepsilon\sigma\left(T_s + T_{sur}\right)\left(T_s^2 + T_{sur}^2\right) \tag{4}$$

The radiation heat transfer coefficient, h_r, is determined from the surface temperature and surrounding temperature. The convective heat transfer is determined from the surface temperature and temperature directly above the wound, T_i.

Assuming the wound geometry is nearly a flat plate with very low velocities (<0.08 m/s), with the characteristic length $L = A_s/P$, the convective heat transfer coefficient, h_c, can be found from the following Nusselt number correlation in Eq. (5):

$$Nu_L = \frac{h_c L}{k_{air}} = 0.52 Ra_L^{\frac{1}{5}} \tag{5}$$

where k_{air} is the conductivity of air, and Ra_L is the Rayleigh number by length scale.

In this study, mass transfer is limited to moisture transportation. Water vapor transfer can be expressed in a manner similar to that of heat transfer by Eq. (6) [24]:

$$n''_w = h_m\left(\rho_{w,s} - \rho_{w,i}\right) \tag{6}$$

where ρ is the density at the temperature of the surface or the point above the incision. The heat and mass transfer relations for a particular geometry are interchangeable, resulting in the following relationship between the heat and mass transfer coefficients as shown in Eq. (7):

$$\frac{h}{h_m} = \rho * c_p * Le^{1-n} \tag{7}$$

Neglecting the net radiative heat transfer under steady-state conditions and treating the air as an ideal gas, the cooling effect of evaporation can be determined from Eq. (8)

$$\left(T_i - T_s\right) = \frac{M_w * h_{fg}}{R * \rho_{air} * c_p * Le^{\frac{2}{3}}} * \left[\frac{p_{w,sat(T_s)}}{T_s} - \frac{p_{water,i}}{T_i}\right] \tag{8}$$

Retrieved by the heat and mass transfer relation $\frac{h}{h_m} = \rho c_p Le^{1-n}$, n is assumed to be 1/3, where ρ, c_p and Le are all air properties. ρ is the

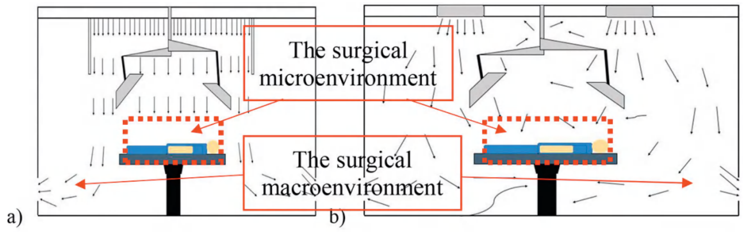

Fig. 1. Principle of ventilation systems in ORs: (a) a vertical LAF system and (b) a MV system [13].

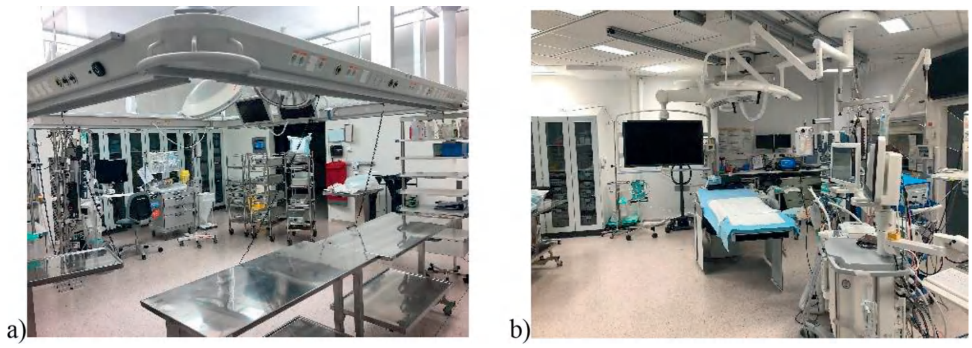

Fig. 2. Experimental setup with measurement points: (a) photo of the LAF OR; (b) photo of the MV OR.

density, c_p is the specific heat at constant pressure and Le denotes the Lewis number. M_w is the molecular weight of water, and h_{fg} is the latent heat of vaporization. All the properties are evaluated at T_i. In situations of very low humidity, $P_{w,\,i}$ can be neglected, and the surface temperature is calculated from Eq. (9):

$$T_s = \frac{T_i + \sqrt{T_i - 4B}}{2} \tag{9}$$

where

$$B = \frac{M_w h_{fg} P_{w,sat}}{R\rho c_p Le^{\frac{2}{3}}} \tag{10}$$

The evaporative heat loss can be shown in Eq. (11):

$$Q_{evap} = h_{fg} n'' A_s \tag{11}$$

3. Experimental setup

In this study, all the measurements were taken from two ORs at St. Olavs hospital in Trondheim, Norway. The OR with an LAF system had an area of 56 m^2 with a laminar airflow zone of 11 m^2 and was surrounded by 1.1 m long partial walls, as shown in Fig. 2. During the experimental measurements, the ventilation system was operated at the full load, and the room temperature was commonly set to 22.4 °C. During the experiments, the supply air temperature was measured as 20±1 °C. The designed supply air in the orthopedic LAF OR was 10,580 m^3/h, comprising 4280 m^3/h of outdoor air and 6300 m^3/h of recirculated air.

The OR with an MV system was equipped with four ceiling-mounted diffusers. For the exhaust, there were two wall-mounted exhaust outlets and one near the ceiling. The MV OR had an area of 59.7 m^2. The supply air temperature was set to 23.0 °C in all the scenarios. The supply airflow rate was 3700 m^3/h, and the exhaust airflow was 3600 m^3/h. During measurement, an adjustable stand was used to carry the anemometers.

In this study, three scenarios (see Table 1) that included six different cases were investigated. Scenario 1 (cases 1 and 2) investigated the thermal environment in the ORs. Scenario 2 (cases 3 and 4) measured the temperature and relative humidity in the ORs to calculate the heat and mass transfer. Scenario 3 (cases 5 and 6) measured the air velocity of surgical microenvironment in the ORs.

4. Measurement instruments

A variety of measuring devices were used to obtain valid results for temperature, relative humidity and velocity both in the macro- and microenvironments. To measure temperature and relative humidity close to the surgical incision, the humidity and temperature probe HMP9 (Vaisala, Finland) for rapidly changing environments was used, with a diameter of 5 mm, a measurement range of −40 to 120 °C and 0–100%RH, and measurement accuracies of ±0.8%RH and ± 0.1 °C at 23 °C. The manufacture calibration of HMP9 instrument was still valid.

A Bosch PTD 1 is a thermal detector based on infrared technology that detects the surface temperature of the surgical incision. The measuring range for surface temperatures is −20 to 200 °C for ambient temperatures between −10 and 40 °C. The accuracy at a measuring distance of 0.75–1.25 m, in an ambient environment of 22 °C, is ± 1 °C for surface temperatures between 10 and 30 °C and ± 3 °C for a temperature range of 30–90 °C. A Flir E60, displaying IR images in addition to the surface temperatures of the assigned spots, recorded thermal images and surface temperatures. Temperature measurements by the device have an accuracy of ± 2 °C for ambient temperatures between 10 and 35 °C Surface temperatures range from −20 to 120 °C, with a thermal sensitivity of 0.05 °C at 30 °C. The minimum focus distance is 0.4 m.

The TSI velocity meter was used to measure the velocity in a given direction, which was determined by the rotation of the telescoping probe. For air temperatures within −10 to 60 °C, the readings have an accuracy of 3% read value or 0.02 m/s, whichever is greater. TinyTag loggers were used to record the temperature and relative humidity room conditions in the real operating rooms at intervals of 5 min. A Pegasor Indoor Quality, with an operating temperature range of 0–40 °C, was used to measure the room conditions in cases 3 and 4. The device has an accuracy of ± 2 °C and ±1.5%RH.

The air velocity was measured at two points near the wound by using a Swema 03+ anemometer: The range of air velocity measured was 0.05–3 m/s at 15–30 °C. At 20–25 °C, the measurement uncertainty was ±0.03 m/s in the velocity range of 0.05–1 m/s or and ±3% read value in the velocity range of 1.0–3.0 m/s. At 15–30 °C, the measurement uncertainty was ±0.04 m/s at 0.05–1 m/s or ±4% read value at 1.0–3.0 m/s. The logging time for each point was 10 min, with a time interval of 1 s. The manufacture calibration was still valid.

Table 1
Scenarios of the experimental measurements.

Scenario	Case	Number of people	Ventilation mode	Remarks
S1 – real surgeries	Case 1	6	LAF	Thermal images were taken during:
	Case 2	10–12	MV	1 h 24 min (LAF), 3 h (MV)
S2 – simulated surgeries	Case 3	6	LAF	Parameters in surgical environment:
	Case 4	6	MV	relative humidity, air temperature
S3 – simulated surgeries	Case 5	6	LAF	Air velocity
	Case 6	6	MV	

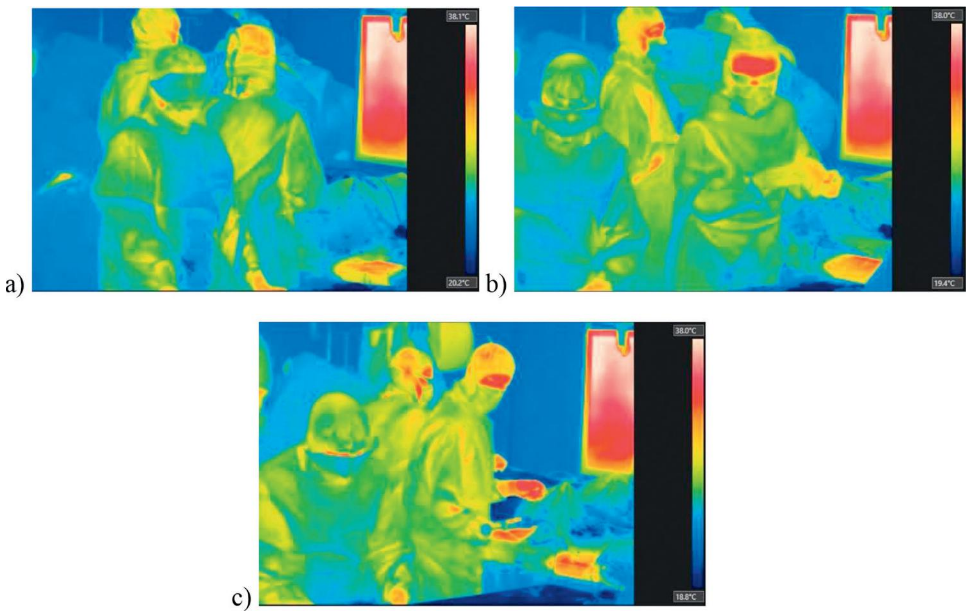

Fig. 3. Thermal images of the surgeon, assistant surgeon and sterile nurse in MV OR: (a) After 40 min; (b) After 1 h and 40 min; (c) After 2 h and 40 min.

5. Results and discussion

5.1. Thermal images of the surgical microenvironments in two operating rooms

The footage from the thermal camera is used to evaluate the surface temperature distributions in both operating rooms. Figs. 3–5 show the temperature distribution of the surgeon, assistant surgeon and sterile nurse in both operating rooms. The surgery in the MV OR was the insertion of a stent graft to prevent an aneurysm from growing. This surgery lasted for approximately 3 h. The surface temperatures of the surgeon and assistant surgeon are generally higher than the surface temperature of the sterile nurse (Fig. 3). This can be explained in two ways. The first is that the surgeons have a higher activity level than the sterile nurse, which leads to more sweating and heat released from the body. The second aspect is the fact that the surgeons are located closer to the surgical lamps and medical equipment. The equipment releases heat, which can be absorbed by the clothing of the surgeons, thus increasing the surface temperature. It can also be observed that the surface temperatures of all three members of the surgical staff is increase during the surgery, which is the expected result. The workload during the surgery, in addition to being in the same room with high air temperature and low relative humidity, leads to an increasing surface temperature throughout the surgery.

For the LAF OR, a knee replacement was conducted, which lasted for approximately 1.5 h. The tendencies observed (Figs. 4 and 5) are the same as those in the MV OR. Generally, the surface temperature of the surgeons is higher than that of the sterile nurse but not as clearly as Fig. 3 shows. Mainly the head and facial region has a higher surface temperature. This could be because of sweat from the forehead due to hard and tiresome work. One explanation for why the temperature difference between the surgeons and the sterile nurse is smaller under LAF could be the impact of the lamps. The field measurements show that the lamps in the MV OR emit more heat than the lamps in the LAF OR. Because of this, the surgeons in the LAF OR absorb less heat from the lamps. This could affect the surface temperature of the clothing and be a causative factor as to why the difference between the surgeons and sterile nurses is smaller. For the MV OR, the surface temperatures for all three individuals increase during the surgery, as expected.

5.2. Measured temperature and relative humidity

The surgical macroenvironment parameters, including air temperature and relative humidity (see in Fig. 2), were measured by a Pegasor Indoor Quality and were very stable throughout the experiments. The measured average room temperature in LAF OR is 21.2 $\pm$0.47 °C, and the measured average relative humidity is 14.6 $\pm$ 0.73%. The measured average room temperature in MV OR is 24.6$\pm$0.17 °C, and the measured average relative humidity is 21.7$\pm$0.55%.

In the surgical microenvironment, the temperature and relative humidity were measured approximately 1–2 cm above the simulated surgical incision by a Vaisala HMP 9. Fig. 6(a) shows that the measured air temperature above the simulated incision in case 3 is stable, with an exception immediately after approximately 3000 s. A drop in the measured surface temperature and temperature directly above the incision can be observed simultaneously as the relative humidity increases. The surface temperature was recorded every minute by the Bosch PTD 1, while the Vaisala HMP 9 placed approximately 2 cm above the incision measured the relative humidity and temperature close to the incision.

Fig. 6(b) shows that the surface temperature is already below a realistic value and environmental temperature; nevertheless, it is decreasing steadily. Towards the end of the simulated surgery, the air temperature

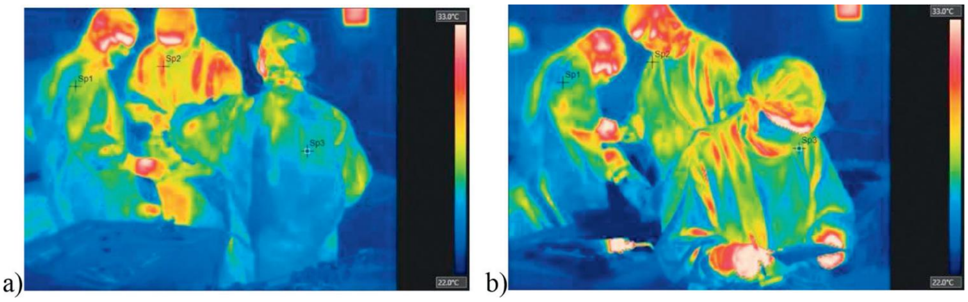

Fig. 4. Thermal images of surgeon and assistant surgeon in LAF OR: (a) After 20 min; (b) After 1 h and 20 min.

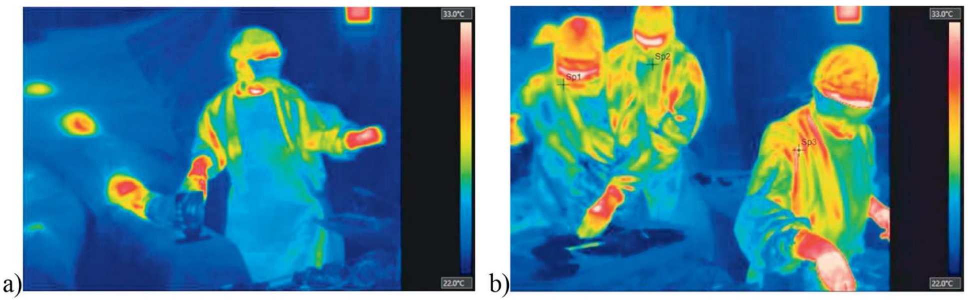

Fig. 5. Thermal images of sterile nurses in LAF OR: (a) After 1 min; (b) After 1 h.

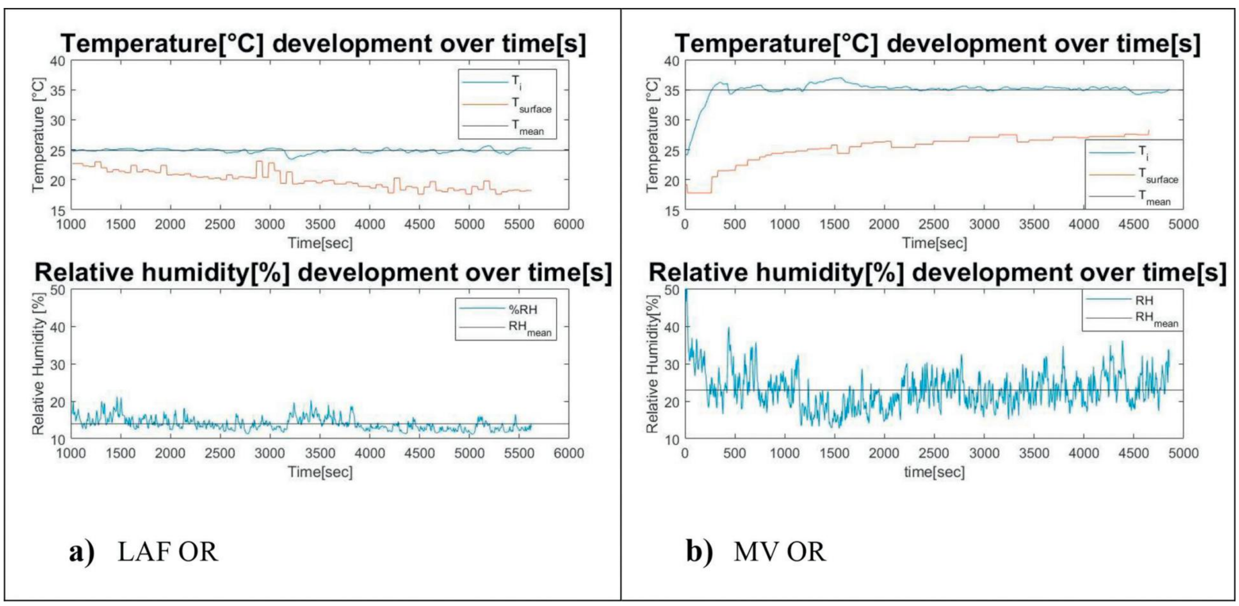

Fig. 6. Surface temperature of the incision, in addition to temperature and relative humidity measured close to the surgical wound during (a) case 3 in the OR with LAF (b) case 4 in the OR with MV.

is approximately 8 °C higher than the surface temperature. The higher air temperature in the surgical microenvironment may be caused by low air velocity comparing with the situation with LAF. Nevertheless, the surface temperature is still decreasing. The liquid always remaining at the surface suggests that the cooling effect of evaporation is larger than the heating from the higher room temperature under the given conditions.

Prior to the "start", surgical lamps are turned off in case 4. A slight decrease in the temperature above the incision can be observed at this stage. However, when the surgical lamps are turned on, a rapid change in the air temperature occurs. The surface temperature also increases, but naturally with a slower pace. The relative humidity levels follow an inverse pattern, resulting in a humidity peak at the lowest air and surface temperature measured. An explanation for the inverse pattern is the capability of warmer air to hold more moisture. This implies that for the same absolute humidity level, lower relative humidity is reached in warmer air. This justification suggests that the absolute humidity level does not increase enough to obtain the same relative humidity, even when evaporation from the incision occurs. After some time, the surface temperature converges towards a value of approximately 28–29 °C. Being able to have a significantly higher and more realistic surface temperature in the beginning would probably cause a more stable value throughout the surgery.

The correlation between the relative humidity and temperature suggests that low humidity levels appear for higher temperatures. Further investigation shows that almost one-third of all the measuring points are below the recommended RH value, as shown in Fig. 7. For higher temperatures, even lower RH values are measured. Near 37 °C, the lowest RH value is observed, slightly below 13%. The goal of the mixing airflow ventilation principle is a uniform air distribution. However, the mi-

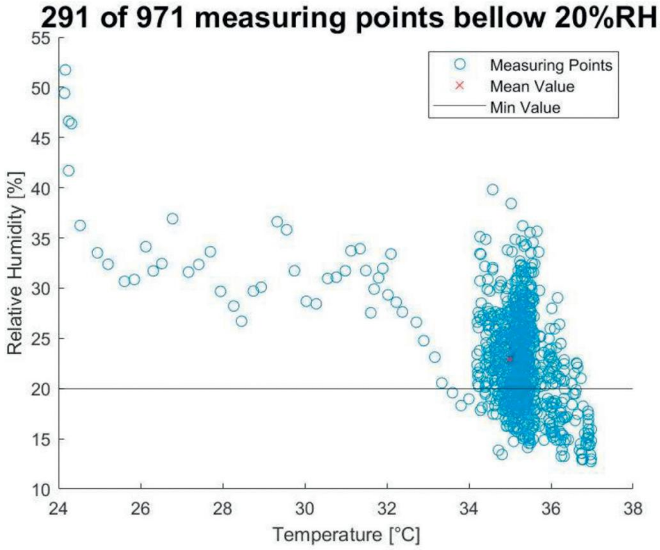

Fig. 7. Relative humidity plotted with the corresponding temperature.

croenvironment differs significantly from the overall room conditions. The results suggest that to obtain a certain relative humidity in the operating microenvironment, temperature is critical, which here is affected by the surgical lamps.

5.3. Calculated incision surface temperature

The theoretical modeling applied to case 3 suggests the introduction of a time-dependent variable for better approximation of the surface temperature. As almost a linear trend is observed for the surface temperature, a linear time parameter should be further investigated.

Applied to case 4, another trend can be observed. Going towards the steady surface temperature, the approximation is close. However, the inertia in surface heating, due to the thermal properties of the incision, is not sufficiently considered and should be studied in further work. Moreover, the dynamic process of evaporation of the surgical incision may not be accurately expressed and should be studied in further work.

Fig. 8 presents the results calculated by Eqs. (9) and (10), while all air and water properties are found in tables [24].

5.4. Measured airflow velocities

Fig. 9 shows that the air velocity fluctuates over time. Point 1 was above the wound, and Point 2 was above the knee at a height of 3.3 cm from the wound and knee. The point close to the wound experiences a higher air velocity than the point close to the knee. In the LAF OR, the vertical laminar airflow directly flows to the surgical microenvironment. In the MV OR, the supply air swirls into the room from four ceiling-mounted diffusers, and the airflow velocity is decreasing in the surgical microenvironment. Hence, the air velocity above the wound and knee is higher in the LAF OR than that in the MV OR. This may support one of the latest studies which found that in ORs with high-volume, unidirectional vertical airflow systems had lower risk of revision due to infection than in ORs with MV systems [25].

6. Conclusion

This study focused on the surgical microenvironment in two ORs with LAF and MV systems. By using a thermal camera, the thermal environment and comfort of the surgeon, assistant surgeon and sterile nurse were investigated. Based on the measurement results, conclusions regarding the surgical microenvironment can be drawn as follows:

(1) The surface temperatures of the surgeon and assistant surgeon are higher than that of the sterile nurse in both ORs.
(2) A higher surface temperature over time leads to the sensation of being warmer in the OR with MV than in the OR with LAF and thus causes thermal discomfort.
(3) The temperature of surgical incision microenvironment in the OR with MV becomes warmer than in the OR with LAF due to lower airflow velocity.
(4) The air velocity at a point of 3.3 cm from the surgical incision is approximately two times higher in the OR with LAF than that in the OR with MV.
(5) The use of surgical lamps and different airflow patterns may contribute to the different surgical microenvironment of ORs with LAF and MV.

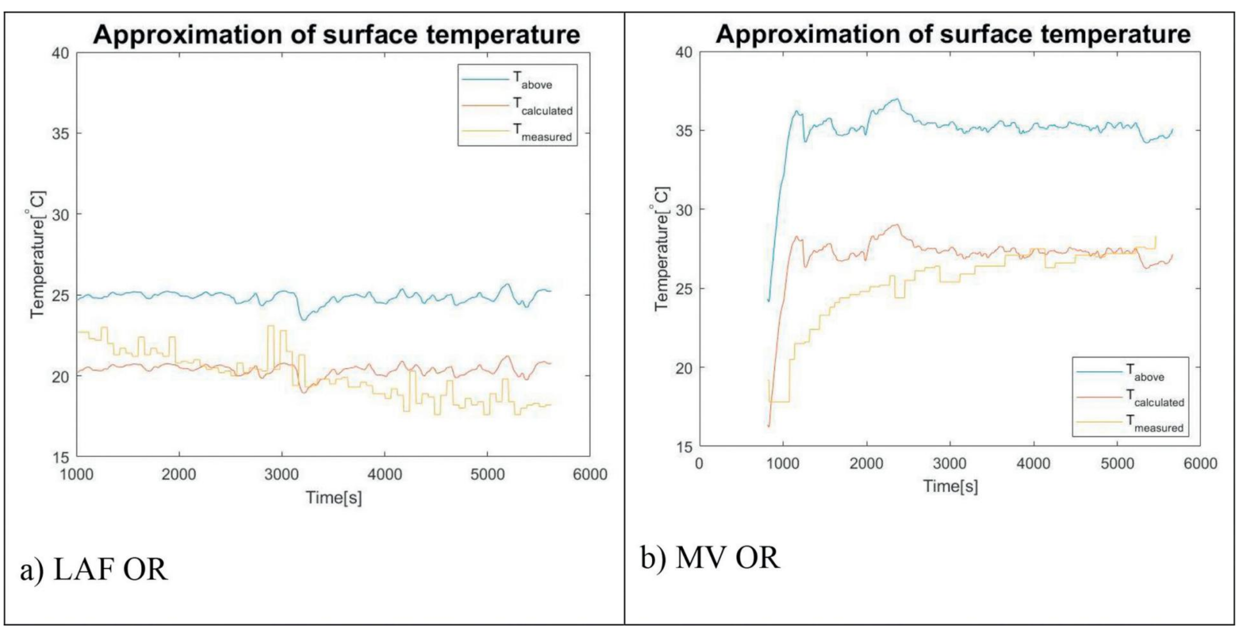

Fig. 8. Measured temperature approximately 2 cm above the incision, compared with calculated and measured surface temperatures for (a) case 3 (b) case 4.

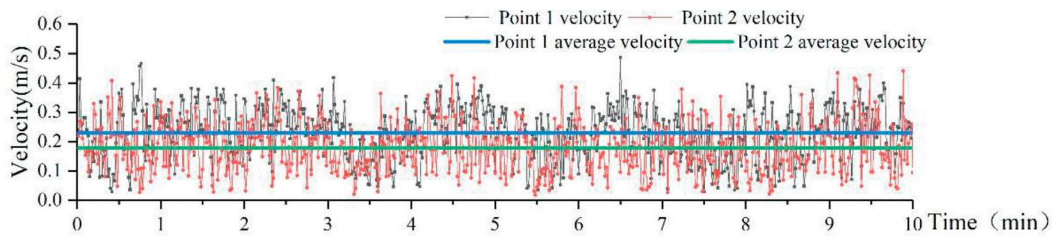

a) LAF OR

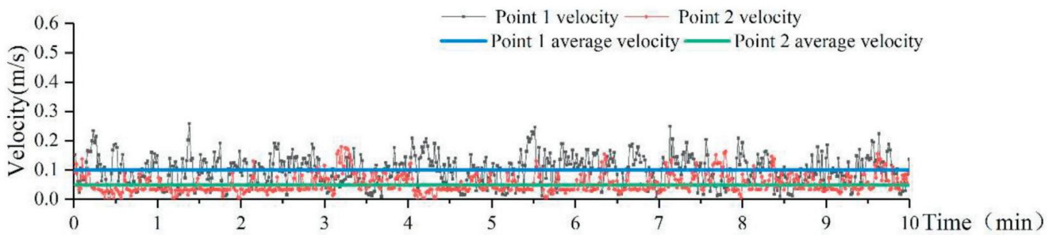

b) MV OR

Fig. 9. The velocity measurements at two points close to the wound in two ORs for (a) case 5 (b) case 6.

The surface temperatures of the surgical staff differ because of differences in movement and location in relation to medical equipment. The fact that one OR experienced more heat emitted from the surgical lamps could have an impact on the results of thermal comfort and the surface temperature distribution obtained from observations with the thermal camera.

The results obtained from measurements in the surgical microenvironment are consistent with those of the thermal macroenvironment. In case 4, the emitted heat caused temperatures far above the recommended values, while the corresponding relative humidity values were below the recommendations. The goal of the mixing airflow ventilation principle is a uniform air distribution. However, the microenvironment differs significantly from the overall room conditions. The results suggest that to obtain a certain relative humidity in the operating microenvironment, one critical factor is local temperature, which will be affected by the surgical lamps.

In case 3, less heating from surgical lamps causes a slower evaporation of wound moisture. However, the evaporative cooling effect is suggested to be greater than the net heat gain due to radiation and convection from warmer, ambient environments. As the set values in the investigated operating room are below recommended values, further investigation is needed to evaluate the impact of these parameters. The presented equations provide a reasonable estimate of surface temperature in the surgical microenvironment. Nevertheless, further investigations and confirmation of these results are necessary. In particular, theoretical models related to moisture transfer need more validation.

Declaration of Competing Interest

None.

Acknowledgments

The authors greatly appreciate the collaboration with the Operating Room of The Future (FOR) – St. Olavs hospital, which provided real operating rooms for field measurements. Norwegian University of Science and Technology provided in-kind funding to support the field measurements at St. Olavs hospital.

Reference

[1] G. Cao, M. Storås, A. Aganovic L. Stenstad, J.G. Skogås, Do surgeons and surgical facilities disturb the clean air distribution close to a surgical patient in an orthopedic operating room with laminar airflow, Am. J. Infect. Control 46 (2018) 1115–1122.
[2] T. Chopra, J. Jing, G. Alangaden, M. Wood, K. Kaye, Preventing surgical site infections after bariatric surgery: value of perioperative antibiotic regimens, Exp. Rev. Pharmacoecon. Outcomes Res. 10 (2010) 317–328.
[3] Helsedirektoratet, Postoperative Infeksjoner Etter Innsetting av Hemiprotese (hofte), 2019 https://www.helsedirektoratet.no/statistikk/statistikk/kvalitetsindikatorer/infeksjoner/postoperative-infeksjoner-etter-innsetting-av-hemiprotese-(hofte)
[4] R.L. Nichols, Preventing surgical site infections, Clin. Med. Res. 2 (2004) 115–118.
[5] J. Alfonso-Sanchez, I.M. Martinez, R.S. Gonzalez, F. Botia, Analyzing the risk factors influencing surgical site infections: the site of environmental factors, Can. J. Surg. 60 (2017) 155–161.
[6] N. Bruce, C. Ouellet, K. Suh, V. Roth, Does high humidity in the operating room (OR) impact surgical site infection (SSI) rates, Am. J. Infect. Control 35 (2007).
[7] American Society for Heating, Refrigerating and Air-Conditioning Engineers Inc, in: Thermal Environmental Conditions for Human Occupancy, ANSI/ASHRAE, Atlanta, USA, 2013, pp. 55–2013.
[8] R. Van Gaever, V.A. Jacobs, M. Diltoer, L. Peeters, S. Vanlanduit, Thermal comfort of the surgical staff in the operating room, Build. Environ. 81 (2014) 37–41.
[9] D.I. Sessler, Perioperative thermoregulation and heat balance, The Lancet 387 (2016) 2655–2664.
[10] P.O. Fanger, Thermal Comfort: Analysis and Application in Environmental Engineering, McGraw-Hill, New York, 1970.
[11] M. Melhado, J. Hensen, M. Loomans, Review of Operating Room Ventilation, Society of Environmental Engineering, Eindhoven, Netherlands, 2006.
[12] S. Ingebrigsten, Ventilasjonsteknikk – Del 1, VVS-foreningen/Nemitek, 2019.
[13] P.E. Nilsson, in: Achieving the Desired Indoor Climate: Energy Efficiency Aspects of System Design, 82–83, Studentlitteratur AB, 2003, pp. 248–249. 2003.
[14] Department of HealthHeating and Ventilation Systems-Specialised Ventilation for Healthcare Premises, Part A: Design and Validation HTM 03-01:2007, Department of Health, London, 2007.
[15] DIN Deutsches Institut für Normung. Normenausschuss Heiz- und Raumlufttechnik. (Ventilation and air conditioning. Part 4, VAC systems in buildings and rooms used in the health care sector) DIN 1946-4:2008 Raumlufttechnik. Teil 4, Raumlufttechnische Anlagen in Gebäuden und Räumen des Gesundheitswesens. Berlin : DIN Deutsches Institut für Normung : Beuth Verlag. Berlin, Germany. 2008.
[16] National Standard. Architectural technical code for hospital chean operating department, GB50333-2002, Beijing, China.
[17] A. Aganovic. Airflow distribution for minimizing human exposure to airborne contaminants in healthcare facilities. PhD thesis, Norwegian University of Science and Technology, 2019.
[18] T. Hirsch, H. Hubert, S. Fischer, A. Lahmer, M. Lehnhardt, H.U. Steinau, L. Steinstraesser, H.M. Seipp, Bacterial burden in the operating room: impact of airflow systems, Am. J. Infect. Control 40 (2012) 228–232.
[19] M. Diab-Elschahawi, J. Berger, A. Blacky, O. Kimberger, R. Oguz, R. Kuelpmann, A. Kramer, O. Assadian, Impact of different-sized laminar air flow versus no laminar

air flow on bacterial counts in the operating room during orthopedic surgery, Am. J. Infect. Control 39 (2001) 25–29.
[20] S. Sadrizadeh, A. Afshari, T. Karimipanah, U. Håkansson, P.V. Nielsen, Numerical simulation of the impact of surgeon posture on airborne particle distribution in a turbulent mixing operating theatre, Build. Environ. 110 (2016) 140–147.
[21] A.A.L.R. Traversari, Aerogenic Contamination Control in Operating Theatres: Studies Towards Effective Use of UDF Systems Doctoral Thesis, Maastricht University, 2019.
[22] A. Tammelin, A. Blomfeldt, Comparison of two single-use scrub suits in terms of effect on air-borne bacteria in the operating room, J. Hosp. Infect. 95 (2017) 324–326.
[23] G. Cao, A.M. Nilssen, Z. Cheng, L. Stenstad, A. Radtke, J.G. Skogås, Laminar airflow ventilation and mixing ventilation: which is better for operating rooms regarding airflow distribution near an orthopedic surgical patient? Am. J. Infect. Control 47 (2018) 737–743.
[24] F.P. Incropera, D.P. Dewitt, T.L. Bergman, A.S. Lavine, Principles of Heat and Mass Transfer, John Wiley and Sons Singapore Pte. Ltd., 2017.
[25] H. Langvatn, J.C. Schrama, G.Y. Cao, G. Hallan, O. Furnes, E. Lingaas, G. Walenkamp, L.B. Engesæter, H. Dale, Operating room ventilation and the risk of revision due to infection after total hip arthroplasty – assessment of validated data in the Norwegian Arthroplasty Register, J. Hosp. Infect. (2020) Accepted April 9pii: S0195-6701(20)30185-7, doi:10.1016/j.jhin.2020.04.010.

Energy and Built Environment 2 (2021) 157–166

Contents lists available at ScienceDirect

Energy and Built Environment

journal homepage: http://www.keaipublishing.com/en/journals/energy-and-built-environment/

Application analysis of efficient heat dissipation of electronic equipment based on flexible nanocomposites

Dongsheng Yang[a,*], Qi Yao[a], Mintao Jia[a], Jun Wang[b], Lixin Zhang[a], Yingli Xu[a], Xi Qu[c]

[a] *Beijing Spacecrafts, Beijing 100094, China*
[b] *School of Aeronautic Science and Engineering, Beihang University, Beijing 100191, China*
[c] *Institute of Manned Space System Engineering, China Academy of Space Technology, Beijing 10094, China*

ARTICLE INFO

Keywords:
Nanocomposites
Electronic equipment
Network thermal resistance
Efficient heat dissipation
Thermal analysis

ABSTRACT

The efficient heat dissipation of electronic equipment is very important, its heat dissipation performance directly determines the life of the equipment itself. A hand-held electronic communications equipment, when used in surface temperature is exorbitant, need to heat dissipation equipment efficiently, to ensure that the use of comfort in the handheld. In accordance with this requirement, this article presents a flexible composite material based on nano-efficient cooling methods that can keep the layout, through the improvement of internal thermal path, it can achieve the effective heat dissipation. The network thermal resistance method is used to analyze the heat transfer in the equipment, and the thermal analysis of the local thermal resistance is carried out. At the same time, through the modeling of electronic equipment and the analysis of finite elements, the temperature drop of the equipment after improvement is accurately judged. Finally, the device experimental performance comparison before and after the optimization of the standby mode and working mode is verified. The results show that the optimized equipment heat source temperature can be reduced by up to 8.5°C, the surface temperature of the equipment can be reduced by about 5°C~7°C, and the final control equipment in the steady standby state of the temperature of about 39±0.5°C, to ensure the comfort of use, and also improved the service life of the equipment. The efficient thermal design of electronic equipment based on flexible nanocomposites can provide a convenient and reliable cooling solution for high-heat flow density devices.

1. Introduction

In recent years, with the rapid development of electronic technology, electronic equipment is not only used in aircraft, satellites, space shuttles and ships and submarines and other military fields, but also widely used in industrial production, communications systems and personal computers and other civilian fields [1–3]. Along with social development, electronic device development in the increasingly sharp contradictions, on the one hand, electronic equipment is small, it has lots of features, portability, wide adaptability to environment and development needs, and the device itself as a result of thermally constrained, thermal control becomes increasingly difficult problem [4]. Especially in the field of aerospace and military electronic equipment, it is need to have good environmental adaptability, high reliability and so on. Therefore, effective thermal control of electronic equipment is the key point to improving product reliability [5,6].

By current research at home and abroad, electronic devices efficient heat dissipation generally forms thermal analysis, thermal design and test the design architecture [7–9]. Thermal analysis includes software such as ANSYS, Flotherm, ICEPAK, ALGOR, BETAsoft, Padsthermal, COOLIT [10–14], and coupling optimization analysis that combines thermal properties with multiple objectives such as fluids and structures [15,16]. Thermal design mainly includes the spatial structure layout of electronic components, internal cooling equipment components (fan, heat pipe, heat sink, etc.) design, local high heat flow density microchannel cooling and interface-enhanced cooling, new high-efficiency heat dissipation materials, etc. [17–20]. Thermal testing can be used by thermocouple method, integrated circuit measurement method, thermistor measurement and optical fiber measurement, but thermal testing is greatly affected by the ambient temperature, the thermal effect evaluation of electronic equipment should establish a more accurate thermal testing way [21–23].

In these studies, most of the optimization design methods research are carried out before the development of equipment, once the equipment development, it is difficult to take a more effective way for efficient thermal design. Based on the problem of high surface temperature of a handheld high-power communication equipment developed, this paper relies on a highly efficient thermal material used in spacecraft and satellite platforms - flexible nanocomposite material [24], without changing

* Corresponding author.
E-mail address: 273060531@qq.com (D. Yang).

https://doi.org/10.1016/j.enbenv.2020.07.008
Available online 12 August 2020

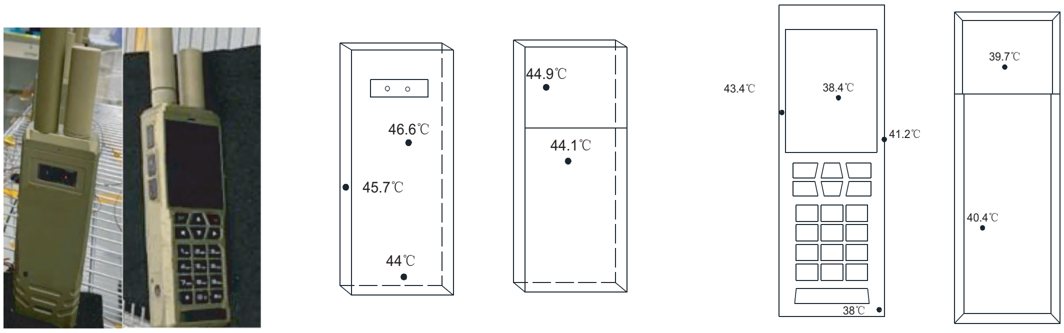

Fig. 1. Terminal equipment and temperature testing.

the original structure layout, the cooling of two types of equipment are improved efficiently. The local thermal efficiency is evaluated by network thermal resistance method, and the optimal simulation analysis and test verification are used to provide an effective solution for the efficient cooling of high-heat flow density equipment.

2. Thermal analysis of electronic terminal equipment

The communication devices used to analyze thermal effects in this article, with long-range emergency wireless communication, positioning navigation and other functions, internal heat sources are mainly power amplifiers, batteries, CPUs, transformers, rectifiers and inductors. The electronic terminal equipment is divided into basic and enhancement types, and enhancement type increased the ergonomic design based on the basic model, including the display and the function buttons, its function is consistent with the basic type, the internal structure is also consistent, but the overall external size is slightly larger. The structural size of enhancement and basic type are: 190mm × 68mm × 38mm, 160mm × 60mm × 32mm, respectively. The metal structure is aluminum alloy 5A06, non-metallic structure is mainly PCB board and electronic components, battery capacity is about 25000mA. When the device used, it is divided into two modes: standby mode and operation mode, the total power consumption in standby is about 7.5W, while it is 9.6W when operating, and the device will produce power peak under this condition. In addition, in order to adapt to the complex work environment, such as salt fog, moisture and mold, the communications terminal equipment designed the closed shell with aluminum alloy material, the emissivity of surface coating is 0.78.

The equipment has the characteristics of small size, high power consumption and scattered heat source that caused the temperature-to-external cooling path of the internal heat source is very limited. When the device used in hand, it often causes uncomforting because the surface temperature is too high. Two models of the device were preliminary tested under standby mode, with an ambient temperature of 25°C. The test thermocouple has an accuracy of 0.001°C, and the power consumption of each of the 2 units is basically the same, the testing results was shown in Fig. 1.

After the equipment running 2 hours under standby mode, the equipment reached the steady state, the basic equipment surface temperature tested 46.6 °C, enhancement type reached about 43.4 °C. As the equipment belongs to the handset, the surface temperature of the environment at room temperature is too high, when people used under harsh environments, it would be seriously affecting human comfort, therefore, the equipment need to be efficient thermal design to satisfies the normal operation requirements.

3. Efficient cooling scheme design

The commonly efficient cooling technology used includes natural cooling, forced air cooling technology, liquid cooling technology, evaporative cooling technology and heat pipe technology et al. [25,26]. As the electronic device belongs to closed communication, its internal heat flow density is relatively large, and it cannot be used to drill a cooling hole in the metal housing of the device or add a fan outside the device to force heat dissipation. When the equipment effectively the radiation effect enhanced, three aspect factors consideration should be following:

(1) Control the product design process, reduce the generation of heat resistance between the components as far as possible;
(2) In terms of structural design, to the maximum extent possible to make electronic components can effectively transfer the flux to the metal shell;
(3) Try to make the heat transfer effectively raised from equipment chassis metal shell to the environment.

Through the structural analysis of the device, most of the device heat source is concentrated on the internal PCB board, and the thermal path of the heat source is very limited, so that the heat source inside the device does not have an effective transmission way. In this paper, flexible nanocomposite materials would be used, focusing on the establishment of the equipment's internal heat source and external structure of the rapid cooling channel, so that creating a good heat flux path.

Flexible nanocomposite material is a kind of carbon fiber reinforced carbon composites (C/C composites) [27,28]. The material is mainly based on the requirements of high heat flux under the current high thermal flow density equipment, based on the lack of heat flux transmission of single-layer graphene carbon-based materials, combined with the aromatic structure advantages of high flatness and high orientation of polyimide (PI) fibers, through the design and craft processing of PI-based carbon fiber, the microscopic structure of fiber is developed from two-dimensional graphite structure to an orderly three-dimensional layer structure.

Polyimide (PI) fiber is a kind of polymer fiber with aromatic ring and imide ring in the main chain, it can be carbonized and graphitized to prepare high crystallinity graphite fiber. The manufacturing method is as follows: The mass ratio of PMDA and the sum of two amines is 1.02: 1, the two amines are 3,5-diaminobenzoic acid (DABA) and p-phenylenediamine (p-PDA), the mass ratio of DABA to p-PDA is 5:95, the carboxyl groups in the molecular chain of PI fiber can form hydrogen bond and physical crosslink. The copolymerized PI (co-PI) fibers were first carbonized in nitrogen at 1400 °C for 1 h, then graphitized in argon at 2800 °C for 1 h. The physical crosslinking co-PI fiber forms a compact and uniform skin core structure, which improves the thermal stability and carbon residue rate, the highest thermal conductivity is 245.6 w/(m k). With the increase of DABA content, the graphitization degree of graphite fiber first increased and then decreased.

Through very multi-layered graphite alkene membrane graphitization, it formed the graphite alkene film, and realized to have the good ductility and the thermal conductivity. At the same time, considered the request of the device electronic installation, the graphite alkene membrane surface was insulated, this method not only satisfied the highly effective heat transfer, it also guarantees the security of electronic components inside the device. In the production of materials, first, the material

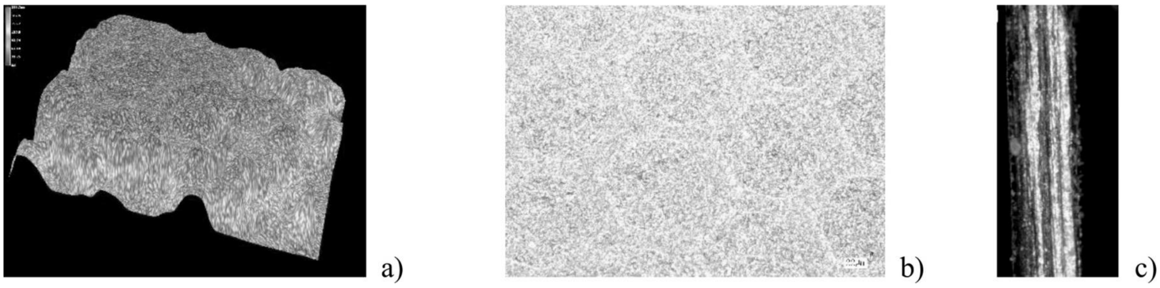

Fig. 2. Microstructure of nanocomposites (a) material 3D surface features construction, (b) material surface carbon structure connection form, (c) material multi-layer composite structure.)

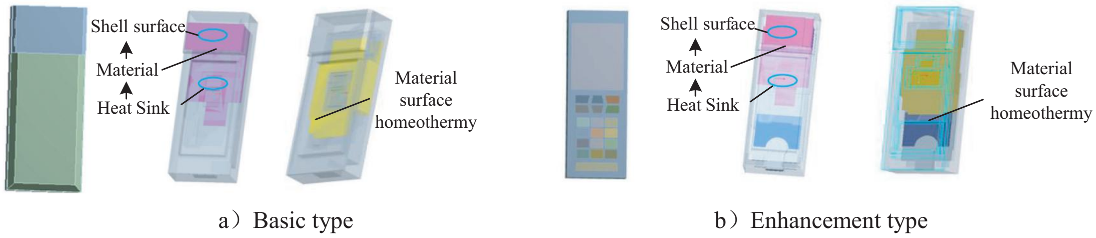

Fig. 3. Two kind of equipment outward appearances and nanometer compound materials design.

Table 1
Nanocomposite performance parameters.

Num.	Content	Parameters
1	Thickness	0.3mm/0.5mm
2	Superficial cellophane thickness	0.05mm
3	Graphite alkene film number	200/400 layer
4	Crosswise thermal conductivity	1600–1800 W/(mK)
5	Longitudinal thermal conductivity	220–280 W/(mK)
6	Flexibility	180° bend stowable
7	Strength	800–1000 MPa
8	Density	600 kg/m^3

layer graphene, and then, using a layer of 0.5-micron film first attached to the insulation layer, and then the insulation layer and graphene film bonded together. With a very thin film connection method, can not only ensure good heat transfer performance, but also have good insulation. Microstructure of nanocomposites and performance parameters have shown in Fig. 2 and Table 1, respectively.

Nanocomposites have the characteristics of good environmental adaptability and high thermal conductivity, and have been widely applied to high-power equipment in spacecraft. Based on the thermal effect of the equipment and the efficient cooling method in the spacecraft and satellite platform, the following cooling scheme is adopted for the equipment:

(1) Adding an embedded substrate to the circuit board of an electronic component, it can increase the contact area between the heat source and the embedded substrate, and increase the contact stress so that reducing the contact thermal resistance.
(2) Increase the contact surface, according to the terminal device internal space and heat source distribution, the nano-composite materials are trimmed into different shapes, and bonding with metal shell by adhesive film, and this may realize the metal shell highly effective fast soaking. The remaining part of the small power heating element, use the thermal grease directly to the metal shell.
(3) Increase the heat sink between the heat source and the rear shell at the rear of the PCB board to improve the heat channel.

Finally, a thermal optimization design model for the device is formed, as shown in Fig. 3 below. The gray part is a simplified structural model of the equipment, adding nanocomposites to the front and rear shells of the device, represented by different colors, all structures are flexible nanocomposites, with different colors, such as pink, yellow, light blue and dark blue, representing different shapes of the conforming material to facilitate the placement of the conforming material in different spatial positions inside the device, and the front part of the device is the increased heat sink.

4. Efficient thermal analysis

4.1. Network thermal resistance model

When the temperature change struck in the device, the thermal flow rate in the device will change accordingly. When the device is operating, the internal temperature, heat flow rate, boundary conditions, and system change significantly over time, the temperature of the transient balance equations are expressed in the following formula [29]:

$$[C]\left\{\dot{T}\right\} + \left[\Delta T_i\right][R]^{-1} = \{Q\} \quad (1)$$

In the formula (1), [R] is the thermal resistance matrix, including heat conduction thermal resistance and counter-flow thermal resistance, $[C]$ is a heat matrix that contains an increase in energy within the system, $[\Delta T_i]$ is the temperature vector matrix of the node, $\{\dot{T}\}$ is the temperature-to-time derivative, $\{Q\}$ is the amount of node heat flow, including the heat generation rate. When steady state is reached, the device is thermally stable, namely $Q_{in} + Q_{gen} + Q_{out} = 0$, Based on energy balance, a steady-state equation is established as follows.

$$\left[\Delta T_i\right][\mathrm{R}]^{-1} = \{Q\} \quad (2)$$

As the heat source in the terminal equipment have about 16, and the structure is irregular, Thermal resistance can be used to trace the thermal conductivity inside the device and establish a thermal resistance network of multiple heat sources through the thermal flow path, as shown in the Fig. 4. Among them, the red thermal resistance is the increased thermal resistance after optimizing the design, and the rest of the thermal resistance is the thermal resistance network formed in the original state of the equipment.

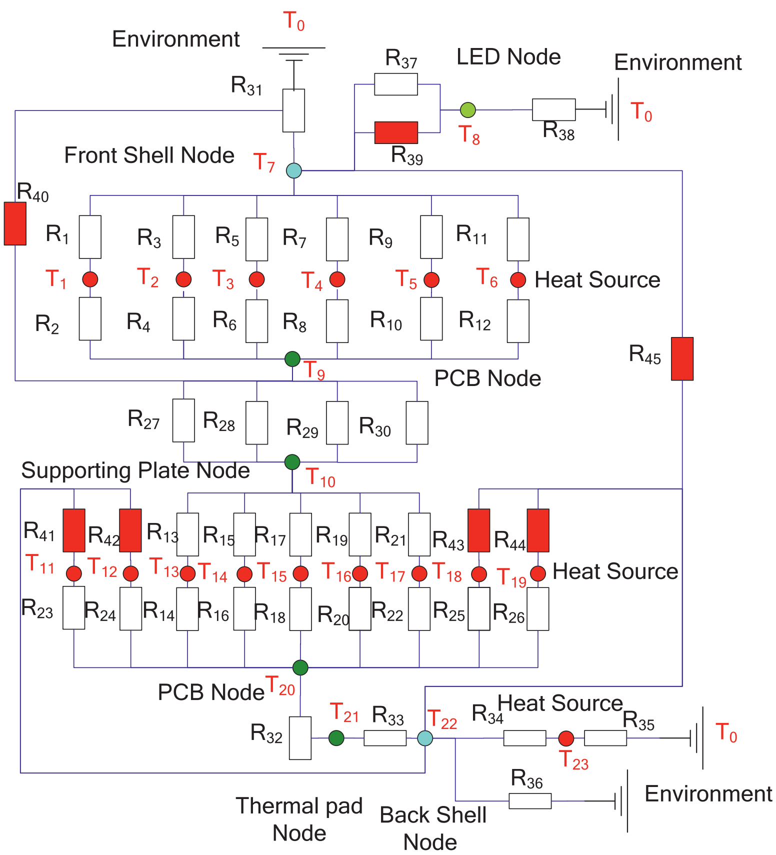

Fig. 4. Thermal resistance network of electronic terminal equipment.

Combined with a thermal resistance network model, define the temperature thermal resistance matrix and shown in the following type.

$$[\Delta T] = [T_1,\ T_2,\ \dots,\ T_{23}] - \begin{bmatrix} T_7, T_1, T_1, T_1, T_1, T_1, \dots, T_1 \\ T_9, T_2, T_2, T_2, T_2, T_2, \dots, T_2 \\ T_7, T_3, T_3, T_3, T_3, T_3, \dots, T_3 \\ T_9, T_4, T_4, T_4, T_4, T_4, \dots, T_4 \\ \dots \end{bmatrix},$$

$$[R] = \begin{bmatrix} R_1, 0, 0, 0, 0, 0, \dots, 0 \\ R_2, 0, 0, 0, 0, 0, \dots, 0 \\ R_3, 0, 0, 0, 0, 0, \dots, 0 \\ R_4, 0, 0, 0, 0, 0, \dots, 0 \\ \dots \end{bmatrix} \tag{3}$$

According to the classical definition of the thermal resistance of heat conduction and convection, the thermal resistance can be expressed as formula (4) shows.

$$R_i = \frac{L}{\lambda_i A} = \frac{\Delta T_i}{Q};\ R_j = \frac{1}{h_j A} = \frac{\Delta T_j}{Q}; \tag{4}$$

In the formula, R_i is the thermal resistance of thermal conductivity of inside the device, R_j is convective heat resistance on the surface of the device, ΔT_j is the temperature difference at the internal node *j*, ΔT_w is the temperature difference at the surface node *w*, when a multi-heat source is heat-transferred in a multidimensional direction, the thermal resistance matrix [R] can be expressed as:

$$[R] = [R_i; R_j],\quad [\Delta T] = [\Delta T_i; \Delta T_j] \tag{5}$$

Considering the external radiant heat dissipation of the surface of its equipment, radiation energy can be calculated as follows:

$$Q_j = \varepsilon A C_0 \left(\left(\frac{T_j}{100} \right)^4 - \left(\frac{T_0}{100} \right)^4 \right) \tag{6}$$

$$[Q] = \begin{bmatrix} Q_1 \\ Q_2 \\ \dots \end{bmatrix},\ \sum_{1}^{16} Q_i + Q_j = W \tag{7}$$

Formula (3)–(7) has composed the stable state the equipment internal heat transfer model, $T_1 \sim T_6$, $T_{11} \sim T_{19}$, T_{23} indicates the heat source. $R_1 \sim R_{38}$ is the thermal resistance of the device, Under the network thermal resistance, series thermal resistance is mainly R_{31} to R_{38}, and R_{31}, R_{35}, R_{36}, R_{38} is the convective thermal resistance between the shell and the environment. For series connected thermal resistance, when any of the simple point increased, it possibly affects the whole effect of the cooling. The optimization measure is, as far as possible, establishing the heat transfer path between the internal heat source and the external housing. After the equipment optimized in Chapter 3, the thermal resistance R_{39} to R_{45} is added. In order to better analyze and optimize the characteristics of the design in the thermal resistance network, the thermal resistance network in Fig. 4 is simplified and formed as shown in Fig. 5.

As can be seen in Fig. 5, after the optimized design, the heat source of $T_{1\sim6}$ was added in parallel with R_{39} and R_{40}. The R_{40} is the heat resistance of the thermal pad increased at design time, R_{45} is the increased heat resistance of the heat sink, and R_{39}, $R_{41\sim44}$ is the thermal resistance produced by the high-performance nanocomposite. Due to its $R_{41\sim44}$ thermal conductivity is about 10 times higher than that of aluminum alloy, and 10^3 times higher than the thermal conductivity on the PCB board. Considering the thermal conductivity area and interface thermal resistance influence, $R_{41\sim44}$ is about 1/100 of $R_{23\sim26}$, and 1/10 of $R_{32\sim33}$. This is equivalent to the establishment of an efficient heat transfer path directly between the heat source and the device shell, and can greatly reducing the heat barrier effect during multi-layer heat resistance transfer. Particularly, the small contact area of local heat sources led to $R_{1\sim12}$, $R_{13\sim16}$ thermal resistance increased, and the low

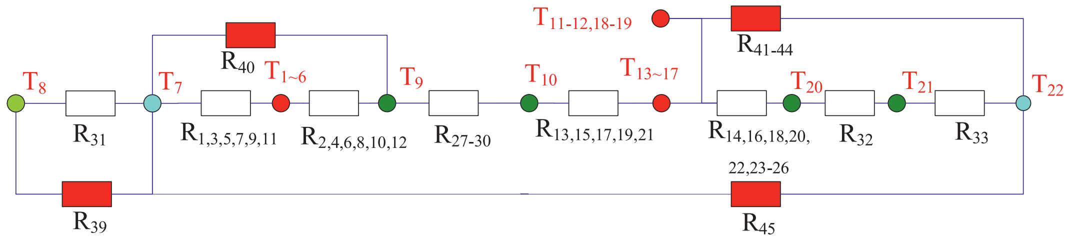

Fig. 5. Thermal Resistance Network Simplification Model.

thermal conductivity of PCB panels and other non-metallic materials in the equipment keeps the R_{27} to R_{30} thermal resistance large. Although there are multiple thermal resistances in parallel, the thermal resistance values are close, and the total thermal resistance remains in the same order of magnitude. Take the thermal resistance between $T_{11\sim12,18\sim19}$ and T_{22} as an example, the total thermal resistance after parallel ingesting is:

$$R_{Total} = \frac{1}{\frac{1}{R_{23}} + \ldots + \frac{1}{R_{26}}} + R_{32} + R_{33} \tag{8}$$

In the thermal resistance network, the various thermal resistances in R_{23} to R_{26}, R_{41} to R_{44} are basically the same. According to the R_{41}=1/100 R_{23}=1/10 R_{32}, Thermal resistance in the formula (8) is $R_{Total} = 45R_{41}$, After $R_{41\text{-}44}$ paralleled, $R_{41\sim44}$=1/4 R_{41}, the total thermal resistance after optimization is:

$$\frac{1}{R'_{Total}} = \frac{1}{45R_{41}} + \frac{1}{0.25R_{41}} \tag{9}$$

As can be seen from the formula (9), with the addition of high thermal conductivity materials, the local thermal resistance to the interior of the equipment is reduced by about 180 times. The thermal transfer path optimization design by ultra-high thermal coefficient material can be a good solution for the problem of high local temperature.

By matrix analysis, it can be seen that, the establishment of thermal resistance network analysis has a clear heat transfer path, which can be simply analyzed. However, the temperature vector produced by the device space in the three dimensions is not the same, and the calculation method of network thermal resistance is not accurate enough. Also, the heat of the internal heat source affects each other, and it is difficult to judge the temperature transfer vector. Efficient cooling methods need to be calculated with the help of thermal analysis software to evaluate the effectiveness and accuracy of this cooling scheme. In this paper, using the finite element method of ANSYS software, the analysis and comparison is carried out before and after the optimization of the terminal equipment to determine the temperature drop effect of this cooling scheme for the equipment.

4.2. Finite element optimization analysis

Inside the equipment, the internal heat source of the electronic device is distributed in different locations, and the internal heat conduction path is transmitted in multiple dimensions. The inside of the device is confined, so the heat conducting is the main way, the surface of the device and the environment belong to the natural convective heat exchange, and the surface has a high radiation rate coating to dissipate heat outwards, the relevant dimensions of the equipment are shown in the Table 2 below.

Thermal simulation analysis used the Steady Thermal module in ANSYS to analyze the temperature field of the device in a steady state [30]. In steady-state simulation, the differential equation is:

$$\frac{\partial}{\partial x}\left(k_{xx}\frac{\partial T}{\partial x}\right)+\frac{\partial}{\partial y}\left(k_{yy}\frac{\partial T}{\partial y}\right)+\frac{\partial}{\partial z}\left(k_{zz}\frac{\partial T}{\partial z}\right)+\dot{q}=0 \tag{10}$$

Expand the full derivative of the time to get:

$$\frac{dT}{dt}=\frac{\partial T}{\partial t}+V_x\frac{\partial T}{\partial x}+V_y\frac{\partial T}{\partial y}+V_z\frac{\partial T}{\partial z} \tag{11}$$

Among them, V_x, V_y, V_z is the speed of the conduction medium. When steady state is reached, the steady-state matrix formed by the nodes in the 3-D model is [31]:

$$[K(T)]\{T\} = \{Q(T)\} \tag{12}$$

[K] is the temperature function, $\{Q\}$ represents a stable heat source, and treated as a constant. The meaning of Eq. (12) and Eq. (2) is similar, except that the temperature function in the software embedded model is used instead of the thermal resistance in Eq. (2).

The cell node temperature matrix is [32–33]:

$$T = \{N\}^T\{T_e\} \tag{13}$$

Among them, $\{N\}^T$ is a cell shape function, $\{T_e\}$ is a cell node temperature vector. The contact between the components is considered Bonded, and the surface smoothness, surface roughness, pressure and thermal grease of the material itself are identified by the steady-state thermal analysis model itself.

The outer surface was calculated by natural convection, with a convective heat exchange coefficient set to 10 W/(m^2 K), the external radiation rate of the outer surface set to 0.78, the thermal source of the electronic component was set to the body heat source according to the actual space layout, with a total power consumption of 7.5 to 9.6W. Due to the device is in standby model most frequently, the simulation adopted the device's standby state power consumption, about 7.5W.

The thermal simulation of the two devices was carried out in a steady state to obtain the temperature field of the surface and internal heat source of the equipment, the temperature distribution is shown in Fig. 6:

Before the equipment optimized, the internal maximum and minimum temperature sits in line with the temperature initially tested in Chapter 2. For the basic type, in the simulation, the maximum temperature inside the device is 59.5 °C and the maximum temperature on the outer surface is 46.5 °C. The measured equipment external surface temperature was 46.6 °C, the simulation results agree well with test results. Through optimization, the maximum temperature inside the equipment can be reduced to 47.9 °C, the maximum temperature of the equipment surface is reduced to 43.7 °C, both the internal and shell temperature drop is about 6.5 °C.

For the enhancement type, the heat source of the simulated equipment is 57.5 °C and the outer surface temperature is 44.5 °C, while in the actual test, the maximum temperature of the equipment surface is 43.4 °C. After optimized, the equipment within the highest temperature is 44.2 °C, the highest surface temperature of 39.1 °C. Compared with data before optimization, internal and surface temperature drop is 9.8 °C and 5.1 °C respectively.

Through the equipment simulation and experiment comparison before and after the optimization of the two models, we can see that: (1) the simulation results have some errors with the actual test, mainly due to the structural simplification of the internal structure of the unit, enabling the interface thermal resistance internal between the heat source and the PCB, the heat source and metal structure. That makes the inter-

Table 2
Terminal equipment heat source and main component size parameters.

Name	Dimensions (L × W × H)/mm	Materials	Power Consumption/W	Description
CPU	22 × 22 × 2	Aluminium package	0.25 × 4	4 in total
ICH	25 × 10 × 1.5	Aluminium package	0.1 × 3	3 in total
Memory	13 × 10 × 1	Aluminium package	0.1~0.4	
Battery	60 × 425 × 8	Aluminium package	1.6	
PCB Board 1	130 × 55 × 1.5	FR4 with copper	/	λ=0.4W/(mK)
PCB Board 2	130 × 55 × 1.5	FR4 with copper	/	λ=0.4W/(mK)
Thermal pad	30 × 35 × 2	Thermal media	/	λ=3W/(mK)
Adapter	48 × 40 × 2	Aluminium package	0.7	
Amplifier chip	25 × 25 × 2	Plastic package	3	
Front Shell	190 × 68 × 26	Aluminium	/	λ=180W/(mK);ε=0.78
Back Shell	190 × 68 × 10	Aluminium	/	λ=180W/(mK);ε=0.78
LED Screen	75 × 60 × 1.5	PTFE	/	λ=0.05W/(mK)
Capacitive chip	50 × 35 × 2	Aluminium package	0.2–0.8	
DSP	32 × 27 × 2	Aluminium package	0.1 × 3	
I/0 chip	10 × 10 × 1.5	Aluminium package	0.3–1.2	
Antenna	420 × Φ30	Aluminium package	/	
Total Power Consumption			7.5–9.6	

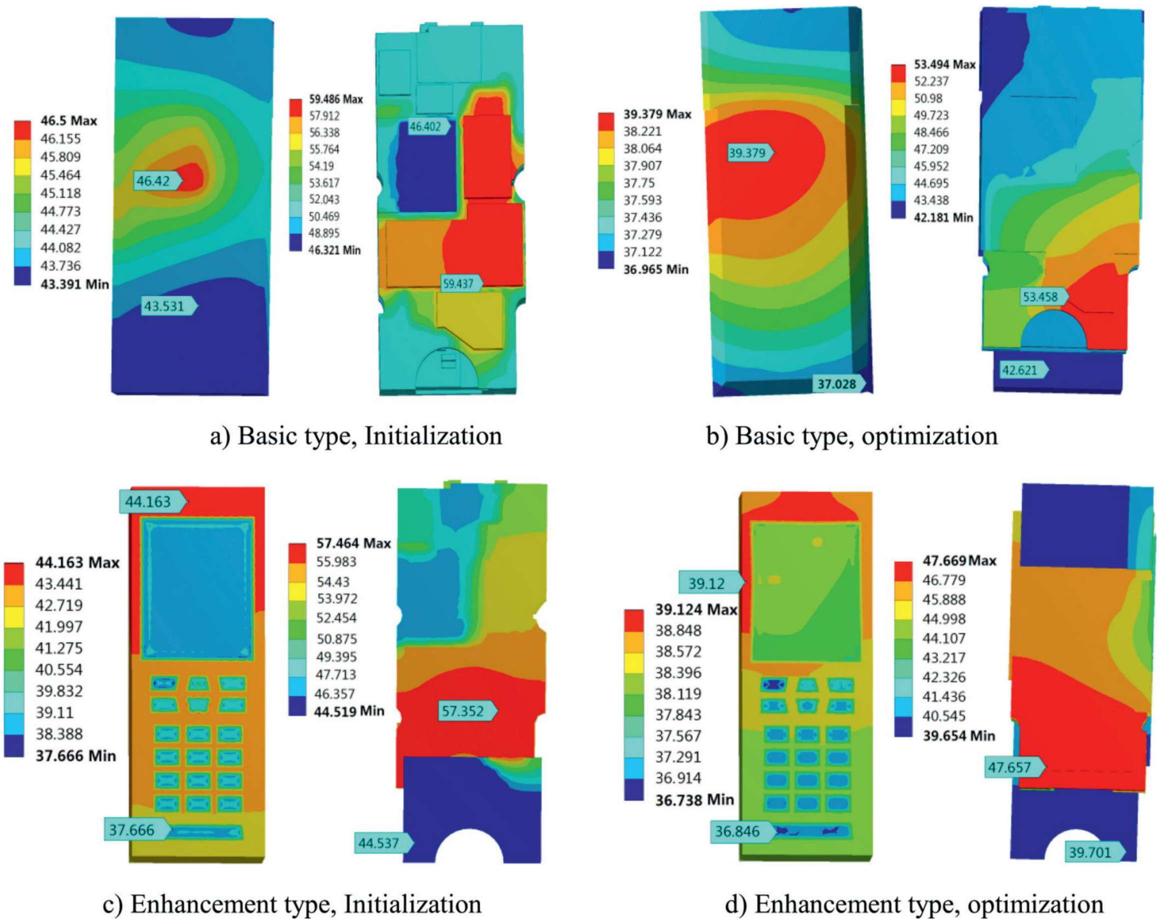

Fig. 6. Comparison of steady-state temperature field distribution in standby mode of two devices.

face thermal resistance is difficult to calculate accurately, so, there are some error for simulation temperature field and the actual test temperature point. (2) Through the optimization design of the inside equipment, nanocomposite increased the function of thermal resistance in parallel, which can realize homeothermy quickly, eventually making equipment inside and outside temperature cooled down considerably. (3) The enhancement equipment volume is relatively big, surface area of convection heat exchange to the environment correspond larger, so the temperature drop effect is also better.

4.3. *Test verification*

Based on the optimized analysis of high-efficiency heat dissipation in Chapter 3, it is shown that the optimized cooling scheme has good temperature-lowering performance, in order to verified the actual performance, the corresponding optimization on the equipment was developed.

The nanocomposites were attached the structure of the device for rapid average temperature, using the good flexibility of nanocomposites,

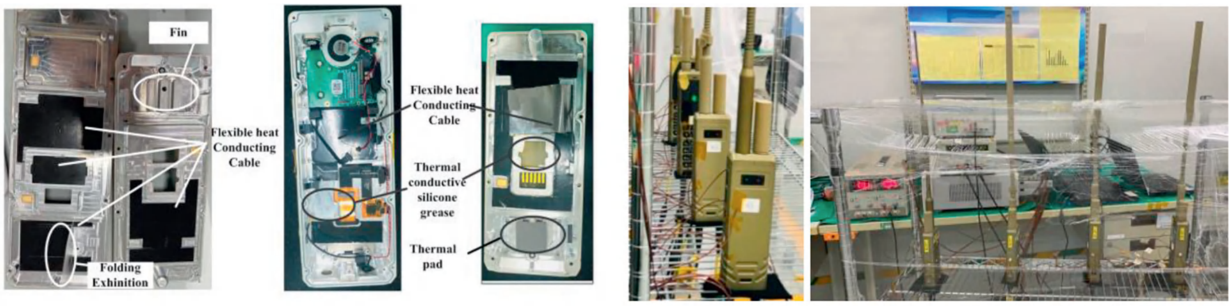

a) Back shell b) Front shell c) Performance test

Fig. 7. Equipment optimization and testing.

the front shell and heat source of the device are bonded together with polyimide film, meanwhile, the space available on the front and rear shells was paste the nanocomposites. Before pasting, heat the material to 60–70°C to avoids trace gases between the films and maximizes the area of contact between interfaces. In addition, thermal pads and heat sinks have also be added to the interior of the device. The thermal pad is mainly to establish a heat channel between the CPU and the rear shell, the heat sink is built between memory and the front shell, this allows multiple thermal resistances to be paralleled to reduce the overall thermal resistance in the thermal resistance network, as shown in Fig. 7.

When optimized device was tested for performance, the Agilent temperature detector was available with 40 channels and the scan rate of 100 channels/s, the thermal offset $<3\mu V$, which can be applied to a variety of temperature sensor signal conversion. For testing, two devices were used for each type, one device was optimized and the other kept the initialization serve as a contrast. The devices tested at the same environment can avoid the interference caused by external factors. In addition, in order to guarantee the external environment disturbance, used transparent thin film to establish the good natural convection environment around the experimental platform, also, the indoor environment temperature control at 23±0.5°C.

The experiment tested the temperature change of the device in standby and operating state. In standby, when the temperature fluctuation range kept within 0.5 °C, is considered to be stable state. When working, the device works for 5min every 15min standby, the temperature peak error of the final measuring point is considered to be stable when the error is within 0.5°C. Finally, it forms the temperature variation curves under two conditions, as shown in Fig. 8.

According to the usage status of the two devices, the temperature change of the device was tested before and after optimization in the standby mode and operating mode. Fig. 8 selected two typical locations, Fig. 8(a) and (b) as the most power-consuming internal heat source measuring point, which is also the highest internal temperature, Fig. 8(c) and (d) are the hottest measuring points on the outer surface of the device.

The curves of internal heat source in standby mode shown as in Fig. 8(a). The temperature rose faster before the basic type optimized, and reached thermal equilibrium at about 60min, eventually, the balance temperature approximately 58.4±0.2 °C. After the optimization, the internal heat source tends to be stable basically around 52min, the final temperature maintains at 52.0±0.1 °C. For enhancement devices, the power consumption is basically the same as the basic type, but the shape envelope is larger, so the internal heat source temperature is slightly lower than the basic type. It achieved the stable state after 80min, and the final temperature approximately in 56.5±0.2 °C. After the process optimization, the internal heat source temperature approximately achieved the balance after 70 min, the final stable state temperature is 49.1±0.1 °C.

In Fig. 8(b), when the internal heat source is operating, the power consumption is about 2W higher than that of standby, operating mode is carried out according to working 5min, standby 15min. Before the basic equipment is optimized, the temperature peak is stable at 64.0±0.1 °C after about 4 cycles in this operating mode. After optimization, the device starts to rise from the standby stable temperature (approximately 52.0 °C). The stable peak also reached at the fourth cycle, stable around 55.5±0.1°C. For the enhanced type, the pre-optimized temperature begins to stabilize the cycle at 60min, the peak value finally stabilizes in 61.9±0.2 °C. After optimization, the temperature is basically stable in the second cycle, with a peak temperature of 53.6±0.2 °C.

Fig. 8(c) represents the highest point on the surfaces of the two devices in standby. For basic device, the steady state temperature before optimization is 46.2±0.1°C, and the optimized temperature is about 39.6 °C. Meanwhile, the enhancement type has a steady temperature of 43.6±0.2 °C when initialization, and after optimization, the steady state temperature reduced to 38.7±0.2 °C.

In Fig. 8(d), the temperature change on the surface of the device in operating mode was described. In alternating operating mode, the peak temperature of the basic equipment before optimization reached 50.3±0.1 °C. After optimization, the maximum temperature of the peak stabilized at 43.3±0.1 °C. For enhancement device, the peak temperature before the equipment optimization reaches 47.1±0.1 °C, after which the stable peak temperature kept 42.7±0.2 °C (Table 3).

The test results in Fig. 8 showed that, there has a significant temperature reduction before and after the optimization of the device, the steady-state measuring point data as shown in Table 4.

Table 4 shows that, whether basic or enhancement, the higher the temperature is, the better the temperature drop effect of heat source through optimization method is, two type devices were cooled by 8.5 °C and 8.3 °C, respectively, in operation. In addition, by optimizing the design, in standby state, the temperature of the surface of the equipment is reduced by 5–7 °C (kept at about 39 °C), basically close to the surface temperature of the human body, it can be satisfied with the comfort of use. In short-term operating mode, the surface temperature of the device increases rapidly. Although the temperature is 4–7 °C lower than initialization, further structural optimization improvements stilled required to achieve good comfort.

In addition, the test results are compared with the simulation results to verify the accuracy of the simulation analysis, as shown in Fig. 9.

In Fig. 9, only the standby mode data compared, there was no comparison of the operating mode data. Because the device was in a "work-standby" loop operating state in operating mode, the temperature peak tested was only in the operating mode, it did not reach the steady peak in the working mode. From the simulation and test results in Fig. 9, we can see that: (1) compared with the actual test results, the simulation analysis before and after optimization and the error of the measured results showed within 2°C, the results have good consistency. This also showed that simulation analysis is still one of the main ways to achieve efficient cooling of electronic components, through the conformity modeling of the physical object, it is possible to accurately predict the temperature

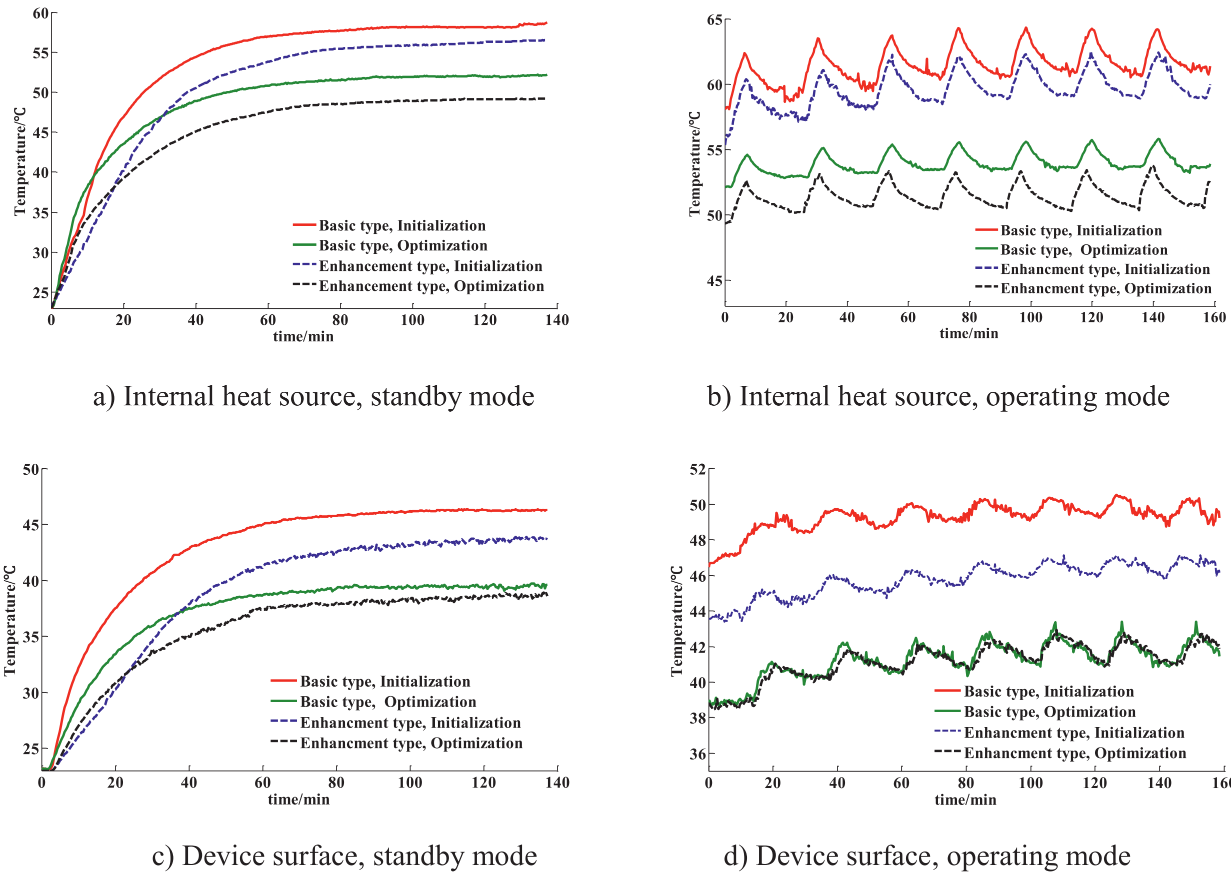

Fig. 8. Performance test curves before and after optimization of two model devices.

Table 3
Comparison of simulation results before and after terminal standby optimization.

NO.	Type	Content	Position	Initialization/°C	Optimization/°C
1	Basic	Internal maximum temperature	Amplifier chip	59.5	53.4
2		Internal minimum temperature	PCB board	46.3	42.2
3		Surface maximum temperature	Upper front shell	46.5	39.7
4		Surface minimum temperature	Bottom of front shell	43.4	37.0
5	Enhancement	Internal maximum temperature	Amplifier chip	57.5	47.7
6		Internal minimum temperature	PCB board	44.5	39.7
7		Surface maximum temperature	Upper front shell	44.2	39.1
8		Surface minimum temperature	Bottom of front shell	37.8	36.7

Table 4
Comparison of test and simulation results before and after equipment optimization.

No.	Type	Position	State	initialization/°C	Optimization/°C	Temperature drop value /°C
1	Basic	Heat Source	Standby	58.4	52.0	6.4
3		Heat Source	Work	64.0	55.5	8.5
4		Shell	Standby	46.2	39.6	6.6
6		Shell	Work	50.3	43.3	7
7	Enhancement	Heat Source	Standby	56.5	49.1	7.4
9		Heat Source	Work	61.9	53.6	8.3
10		Shell	Standby	43.6	38.7	4.9
12		Shell	Work	47.1	42.7	4.4

field for equipment. (2) The temperature at the thermal source location of the equipment was higher, and the temperature dropped more obvious after optimization. The temperature of the enhancement device in each operating condition reflected lower than that of the basic type, no matter before or after the optimization, this showed that, under certain conditions of the internal heat source, it is one of the effective ways to improve the thermal heat by increasing the thermal area of the device surface.

5. Conclusion

This paper focused on the problem of the high surface temperature when used by a handheld high-power communication equipment, A flexible nanocomposite material with high thermal flow density heat dissipation was used, the material have been applied to the spacecraft and satellite platforms before. An efficient thermal guide path was established without changing the structure of the inside equipment. Through

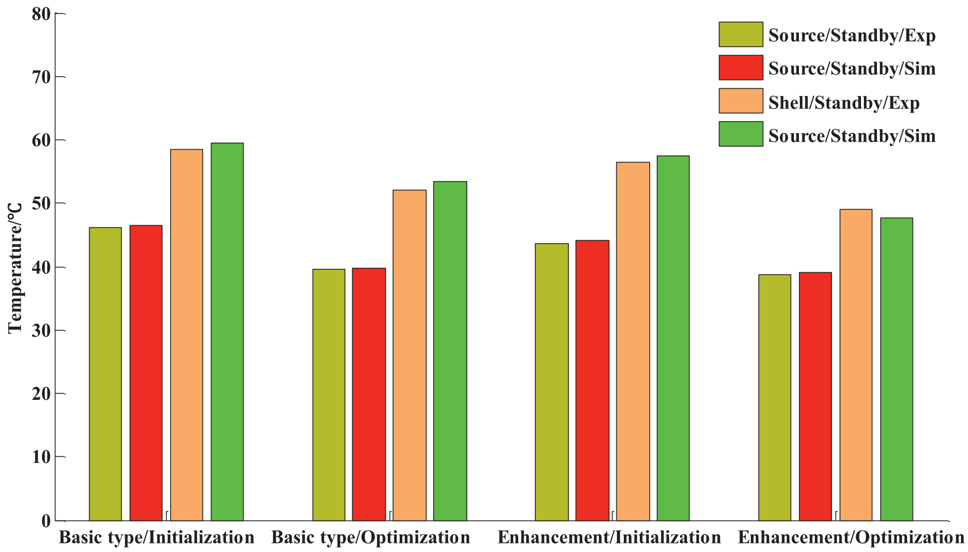

Fig. 9. Test and simulation analysis before and after two device optimizations under different operating conditions.

thermal resistance network analysis and simulation analysis, the rapid heat transfer can be achieved. Through thermal resistance network analysis and simulation analysis, local thermal resistance can be greatly reduced, and rapid heat transfer can be achieved. In addition, the experimental verification of two working modes of the optimized equipment was carried out, obtained the conclusion to be as follows.

(1) Using network thermal resistance model analysis, it is very convenient and clear to analyze the improvement of local thermal resistance. Based on the design of flexible nanocomposite materials, local thermal resistance of the original equipment can be reduced by about 180 times, it can be satisfied with the demand of the efficient heat dissipation of local heat source. However, for complex thermal resistance networks with multi-dimensional, multi-heat source and multi-working conditions, simulation software was used for simulating analysis.
(2) Simulation analysis accurately determines the temperature improvement of the equipment after optimization. Compared with the test results, the temperature of the heat source obtained by the simulation and the temperature error of the shell surface were controlled to within 2 °C. This analysis method can be used to quickly prejudge and evaluate the thermal capacity of equipment optimization, and can provide the technical guidance for the thermal design of high-power electronic equipment.
(3) The experimental test fully verified the accuracy of simulation analysis and the high-performance heat transfer capability of flexible nanocomposites. Both devices have been verified and analyzed by standby and working modes, the core temperature is cooled by about 8.5 °C, and the surface temperature is reduced by 5–7 °C, respectively. The surface temperature is maintained at about 39 °C in standby, which can content the comfort and reliability requirements of hand-holding.
(4) Under the condition of limited space and no-changing the equipment structure, flexible nanocomposites with ultra-high thermal conductivity can improve the problem of insufficient thermal capacity of equipment. In the optimized design of this equipment, due to the limited space inside the equipment, the equipment in the short-term operation, although the pre-optimization temperature is reduced by 8.5 °C, the temperature still reached about 43 °C. If the comfort of the equipment continues to be improved in operating mode, the subsequent combined structure design is required to be further improved to realize the efficient cooling of the equipment surface to the environment.

Declaration of Competing Interest

None.

Acknowledgment

This work was funded by the Manned spaceflight project in advance (020301).

References

[1] K. Chen, M. Song, W. Wei, et al., Design of the structure of battery pack in parallel air-cooled battery thermal management system for cooling efficiency improvement, Int. J. Heat Mass Transf. 132 (2019) 309–321, doi:10.1016/j.ijheatmasstransfer.2016.09.062.
[2] S.K. Oh, J.S. Lundh, S. Shervin, et al., Thermal management and characterization of high-power wide-bandgap semiconductor electronic and photonic devices in automotive applications, J. Electr. Pack 141 (2) (2019) 020801 1-17.
[3] D Zhao, in: Thermal design of electronic devices, Electronic Industry Press, Beijing, 2009, pp. 132–141. (In Chinese).
[4] S. Xu, X. Li, Analysis on thermal reliability of key electronic components on PCB board, 15(12) (2011) 58–60. 10.1109/ICQR2MSE.2011.5976567.
[5] F. Yang, C. He, Q. Xu, et al., The study on thermal analysis method of PCB, IOP Conf. Mater. Eng. 782 (2020) 022042, doi:10.1088/1757-899X/782/2/022042.
[6] R. Caillaud, C. Buttay, R. Mrad, et al., Thermal considerations of a power converter with components embedded in printed circuit boards, IEEE 99 (2019) 1-1, doi:10.1109/TCPMT.2019.2939969.
[7] P. Gao, X. Zhao, Y. Gu, et al., Coupled electromagnetic and thermal analysis of an axial flux permanent magnet synchronous machines with printed circuit board winding, Int. J. Appl. Electr. Mech. 1 (2020) 1–17, doi:10.3233/JAE-190107.
[8] T.T. Lee, B. Chambers, M. Mahalingam, Application of CDF technology to electronic thermal management, IEEE 18 (3) (1995) 511–519, doi:10.1109/ECTC.1994.367557.
[9] M. Mazlan, A. Rahim, M. Mohd, et al., Thermal Management of electronic components by using computational fluid dynamic (CFD) software, FLUENTTM in several material applications (epoxy, composite material & nanosilver), Adv. Mater. Res. 795 (2013) 141–147, doi:10.4028/www.scientific.net/AMR.795.141.
[10] J. Akbar, M.S. Iqbal, S. Massey, et al., Kinetics and mechanism of thermal degradation of pentose- and hexose-based carbohydrate polymers, Carbon Polym. 90 (3) (2012) 1386–1393, doi:10.1016/j.carbpol.2012.07.008.
[11] T. Fukue, M. Ishizuka, S. Nakagawa, et al., Model for predicting performance of cooling fans for thermal design of electronic equipment, Heat Transf. Res. 40 (4) (2011) 369–386, doi:10.1002/htj.20347.
[12] L.T. Yeh, R.C. Chu, W.S. Janna, Thermal management of microelectronic equipment: heat transfer theory, analysis methods, and design practices, ASME 56 (2003) B46–B48, doi:10.1115/1.1566408.
[13] C. Kral, A. Haumer, M. Haigis, et al., Comparison of a CFD analysis and a thermal equivalent circuit model of a TEFC induction machine with measurements, IEEE 24 (4) (2009) 809–818, doi:10.1109/TEC.2009.2025428.
[14] M. Tencer, J.S. Moss, T. Zapach, Arrhenius average temperature: the effective temperature for non-fatigue wearout and long term reliability in variable thermal conditions and climates, IEEE 27 (3) (2004) 602–607, doi:10.1109/TCAPT.2004.831834.
[15] P.C. Johnson, G.M. Saidel, Thermal model for fast simulation during magnetic resonance imaging guidance of radio frequency tumor ablation, Ann. Biol. Engl 30 (9) (2002) 1152–1161, doi:10.1114/1.1519263.

[16] Z. Shang, H. Qi, X. Liu, et al., Structural optimization of lithium-ion battery for improving thermal performance based on a liquid cooling system, Int. J Heat. Mass Transf. 130 (2019) 33–41, doi:10.1016/j.ijheatmasstransfer.2018.10.074.
[17] T. Suwa, H. Hadim, Multidisciplinary placement optimization of heat generating electronic components on a printed circuit board in an enclosure, IEEE 30 (3) (2007) 0–410, doi:10.1109/tcapt.2007.901674.
[18] T. Suwa, H.A. Hadim, Multidisciplinary placement optimization of heat generating electronic components on printed circuit boards, IEEE Trans. Comp. Packag. Technol. 129 (2007) 402–410, doi:10.1115/1.2429715.
[19] M. Cheralathan, R. Velraj, S. Renganarayanan, Effect of porosity and the inlet heat transfer fluid temperature variation on the performance of cool thermal energy storage system, Heat Mass Transf. 43 (2007) 833–842, doi:10.1007/s00231-006-0163-1.
[20] W Zhao, C Zhu, S Chen, et al., Thermal design of high-mobility radar closed chassis, Mach. Electr. 9 (2019) 12–15, doi:10.3969/j.issn.1001-2257.2019.09.003.
[21] E.P. Zafiropoulos, E.N. Dialynas, Methodology for the optimal component selection of electronic devices under reliability and cost constraints, Qual. Reliab. Eng. 23 (8) (2007) 885–897, doi:10.1002/qre.850.
[22] N. Song, D. Cao, X. Luo, et al., Highly thermally conductive polypropylene/graphene composites for thermal management, Compos. A Appl. Manuf. 135 (2020) 105912, doi:10.1016/j.compositesa.2020.105912.
[23] M.Iyengar Bar-Cohen, Design and optimization of air-cooled heat sinks for sustainable development, IEEE Trans. Comp. Packag. Technol. 25 (4) (2002) 584–591, doi:10.1109/TCAPT.2003.809112.
[24] Y. Kitamura, M. Ishizuka, S. Nakagawa, Study on the chimney effect in natural air-cooled electronic equipment casings under inclination: proposal of a thermal design correlation that includes the porosity coefficient of an outlet opening, Heat Transf. 35 (2006) 122–136, doi:10.1109/TCAPT.2003.809112.
[25] A. Bar-Cohen, M. Iyengar, Compact modeling of electrical devices for electrothermal analysis, IEEE 25 (4) (2002) 465–476, doi:10.1109/TCAPT.2003.809112.
[26] A.S. Bahman, F. Iannuzzo, T. Holmgaard, et al., Reliability-oriented environmental thermal stress analysis of fuses in power electronics, Micro Reliab. 76–77 (sep) (2017) 25–30, doi:10.1016/j.microrel.2017.06.089.
[27] M Xiao, H Xu, Z Ma, et al., Effect of crosslinking method on the microstructures and properties of polyimide-based graphite fibers, New Carbon Mater. 34 (1) (2019) 19–28.
[28] C.Y. Yu, X.Z. Yu, W.M. Yang, A preliminary study on the techniques for thermal analysis/design/test of electronic equipments, Electro-Mech. Eng. 23 (2007) 5–10 https://doi.org/CNKI:SUN:MINI.0.2000-05-012.
[29] J Yu, H Gao, Y Xie, in: Thermal Design and Analysis Technology of Electronic Equipment, Behang University Press, Beijing, 2008, pp. 5–7.
[30] N Li, Z Ma, M Chen, et al., Structures and performance of graphene/polyimide composite graphite fibers, J. Mater. Eng. 45 (9) (2017) 31–37, doi:10.11868/j.issn.1001-4381.2016.000251.
[31] Y Zhao, Z Ma, H Song, et al., Synthesis and characterization of carbon fibers multi-scale reinforcement with grafted graphene oxide, CA J. Mater. Res. 30 (2016) 229–234, doi:10.11901/1005.3093.2015.020.
[32] J. Zhang, L. Cheng, H. Yuan, et al., Identification of viscosity and solid fraction in slurry pipeline transportation based on the inverse heat transfer theory, Appl. Therm. Eng. 163 (2019) 114328, doi:10.1016/j.applthermaleng.2019.114328.
[33] Z Fang, G Fu, Z Gao, Application research on thermal analysis software of electronic systems, J. Beijing Univ. Aerosp. Astrol. 8 (29) (2003) 737–740, doi:10.13700/j.bh.10015965.2003.08.019.

Energy and Built Environment 2 (2021) 167–174

Contents lists available at ScienceDirect

Energy and Built Environment

journal homepage: http://www.keaipublishing.com/en/journals/energy-and-built-environment/

Building occupancy and energy consumption: Case studies across building types

Sicheng Zhan[a], Adrian Chong[a,*]

Department of Building, School of Design and Environment, National University of Singapore, 4 Architecture Drive, Singapore 117566, Singapore

A R T I C L E I N F O

Keywords:
Occupancy
WiFi
Building energy
Clustering
Energy conservation

A B S T R A C T

Past research has shown that occupancy information can be used to reduce building energy consumption through occupant-based controls and by mitigating wasteful occupant behavior. In this study, we investigate the dynamic relationship between WiFi connection counts (as a proxy to occupancy) and building electricity consumption across four building typologies (office, lab, health center, and library). Our findings based on one year of data show a strong positive linear correlation between electricity consumption and WiFi count across all four building when the building is in operation. The data exploration also indicates higher interactions between occupants with the plug and lighting loads in office and lab space types as compared to in a health center and a library. Next, using principal component analysis (PCA) for feature extraction followed by Density-based spatial clustering of applications with noise (DBSCAN), we show that distinct clusters could be generated, characterized by an increase in the between-cluster variance and smaller within-cluster variation. Lastly, we apply linear regression to manifest how the clustering results can be used to better model the variables.

1. Introduction

The building and construction sector is responsible for the largest proportion of both final energy use (36%) and energy-related CO_2 emissions (39%) [1]. A major source of rising energy use and emissions by the global building stock is electricity, the use of which has increased more than 19% between 2010 and 2018. One of the barriers to improving building energy efficiencies is understanding the factors causing the significant discrepancies that often exists between what the building was designed for, and its real energy use [2]. Occupant activities and behavior has been recognized to be a major contributor to the variability around building energy use [3,4]. As green building energy codes and standards become more stringent with an increasing emphasis on passive design and more efficient active systems, occupant behavior is expected to have a rising influence on building energy performance.

Occupancy information can be used to detect and mitigate wasteful behavior. For instance, 35.5% energy saving potential was identified by occupant activity recognition using power meters, motion sensors, and light sensors [5]. Masoso and Grobler [6] found that more energy was consumed during non-working hours as a result of wasteful occupant behavior of leaving lights and equipment on, and partly due to poor zoning and controls. This illustrates how simple behavior change identified with occupancy monitoring can be used to reduce energy wastage significantly. In addition, it also exemplifies the importance of introducing occupant-centric design to existing energy codes and standards [7]. Occupancy information has also been used to proportionally control building systems (lighting, HVAC, etc.). The use of occupancy information for building operation and controls has been studied extensively and ranges from simple presence-based switching of lighting systems and demand control ventilation to more complex frameworks involving model predictive control or reinforcement learning [8–10].

Currently, occupancy detection in buildings is usually achieved by monitoring indoor CO_2 levels or through passive infrared (PIR) sensors. CO_2 sensors are often used for demand control ventilation, where ventilation or fresh air is supplied to the space based on CO_2 ppm levels. However, detection time using CO_2 sensors was found to be too slow for use in commercial buildings [11], resulting in occupants being in a state of discomfort. PIR sensors are typically used for occupancy-based lighting controls. Past researches have shown that occupant-based controls are able to provide lighting energy savings of up to 30% [12]. However, PIR sensors require a direct line of sight to achieve proper motion detection [13]. Therefore, it is prone to "false-off" (i.e., lights being turned off despite the room being occupied) [14]. Electricity and water consumption data has also been used to enable more efficient occupancy inference [15].

Melfi et al. [16] defined 16 combinations of spatial, temporal and occupant resolution (Fig. 1), where the resolution required depends on its application. An extensive sensor network can help improve the accuracy

* Corresponding author.
E-mail address: adrian.chong@nus.edu.sg (A. Chong).

https://doi.org/10.1016/j.enbenv.2020.08.001
Available online 28 August 2020

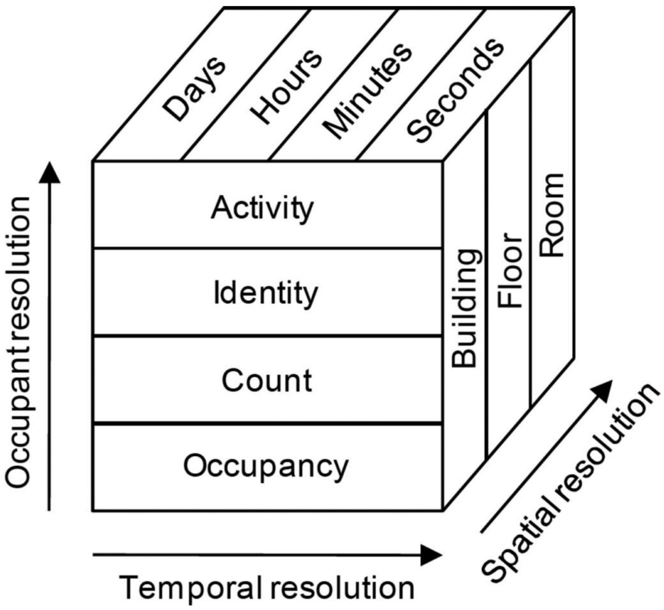

Fig. 1. Different resolution of spatial, temporal, and occupancy resolution [16].

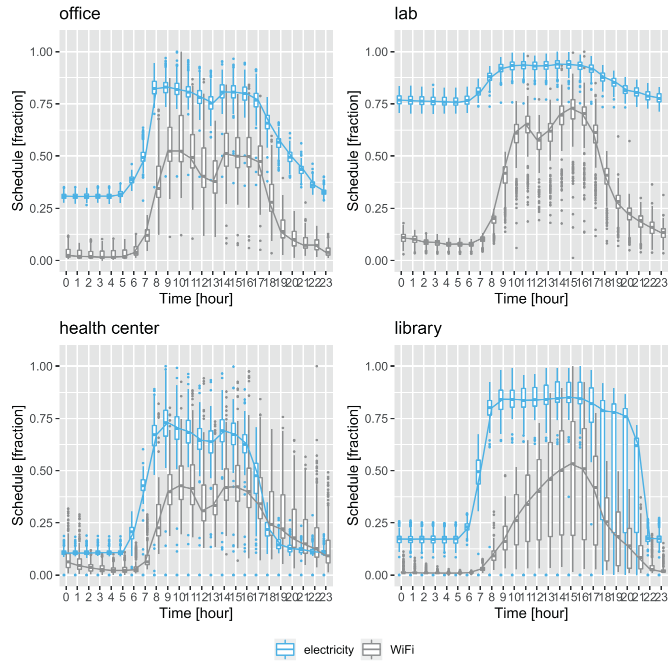

Fig. 2. Normalized twenty-four hour profile of electricity energy consumption and WiFi count for weekdays (excluding public holidays) across four building with different typologies and functions.

in occupancy number detection [17]. 80–95% accuracy was achieved using CO_2, lighting, temperature, humidity, and presence sensors[18]. However, the deployment of sensors to directly measure occupancy is synonymous with high installation cost and the need to maintain the associated data acquisition system continuously. Put differently, there is a trade-off between cost, accuracy, and resolution.

In commercial non-residential buildings, WiFi activity provides an opportunity for detecting/monitoring occupancy count without any modification to the building's existing infrastructure other than the collection and processing of data. The effectiveness of using WiFi data to detect and predict building occupancy has been demonstrated through case study buildings [19–21]. Although accuracy in measuring occupancy within the building was high, floor and room level accuracy were significantly lower due to devices being connected to different WiFi access points that are not in the same area as the occupant [16]. WiFi connection counts have also been shown to be positively correlated and able to partially explain the trends observed in building electricity consumption [22].

WiFi signal has been used as implicit occupancy sensors for the purpose of HVAC and lighting control. Zou et al. [23] showed that WiFi-based occupancy control was able to provide more than 90% and 80% lighting energy savings as compared to static schedules and passive infrared (PIR) based control respectively [23]. For HVAC, Balaji et al. [24] demonstrated savings of 17% by leveraging the existing WiFi network infrastructure to actuate the HVAC system. Wang et al. [25] proposed an occupancy-link energy-cyber-physical system that incorporates occupancy information by actively scanning WiFi connection requests and responses. The proposed framework was able to achieve about 26% savings in cooling and ventilation energy consumption.

Although there are existing literature investigating the relationship between occupancy and a building's energy usage, the conclusion from most studies were based on a single typically office or residential case study building. However, occupancy profiles may have distinct features depending on the building typology. For instance, one would expect a library or a concert hall to have higher variability as compared to an office building that typically plateaus during office hours. Therefore, the purpose of this study is to explore and understand the dynamic relationship between building electricity consumption and WiFi count across four different building typologies and functions. The four building case studies include an office, a lab, a health center and a library. We propose a new integrated clustering approach to better understand and define the usage patterns across the four building typologies. Based on the clustering results, we apply liner regression models to further interpret the relationship and demonstrate the benefit of a better understanding.

2. Case study

A case study approach is used to examine the relationship between WiFi count (occupant presence) and building electricity consumption across four buildings located on the campus of National University of Singapore. Table 1 summarizes the dataset used in this study. The four buildings were primarily selected to have different typologies and functions, including an office, a lab or laboratory, a health center, and a library. The heating, ventilation, and air-conditioning (HVAC) system for all four buildings is a variable air volume system served by a central district cooling system. Given Singapore's tropical climate, there is no heating required. To allow for inter-comparison across buildings, the data collected from each of the four buildings are from the same time period (1 January 2018 to 31 December 2018) and consists of the following:

- Hourly total building electricity consumption that is made up of equipment or plug and process energy, lighting energy, and air handling unit (AHU) fan energy consumption. Note that the electricity consumption data investigated in this study does not include the energy consumption from other HVAC systems aside from the AHU fan energy.
- Hourly number of WiFi connections in the building. The number of connections serves as an implicit measurement of the hour to hour variations in occupant count, and have been shown to exhibit a similar trend to the number of building occupants [16]. Therefore, it serves as a suitable estimate for the hour to hour variation of occupant presence.

3. Exploratory data analysis

Figs. 2 and 3 show the variation in the number of WiFi count and building electricity consumption aggregated over a 24-h profile respec-

Table 1
Summary statistics of dataset used in this study.

Building type	Floor area	Data	Unit	n	Missing / Erroneous[a]	Mean[b]	(5th, 50th, 95th) percentile[b]
Office	5335 m^2	Electricity Energy	kWh	8748	0	34.8	(20.4, 27.1, 59.6)
		WiFi Count	No.	8228	532	94	(5, 40, 307)
Lab	25,523 m^2	Electricity Energy	kWh	8725	35	1124	(998, 1093, 1299)
		WiFi Count	No.	8063	697	161	(36, 97, 447)
Health center	3708 m^2	Electricity Energy	kWh	8740	8	36.0	(12.25, 16.75, 95.75)
		WiFi Count	No.	8395	365	7	(5, 46, 200)
Library	26,036 m^2	Electricity Energy	kWh	8476	272	191.5	(58.0, 99.5, 401.7)
		WiFi Count	No.	8063	697	394	(23, 91, 1805)

[a] Erroneous values include negative values and values that were too large to be correct (e.g. values that are more than 1000 times larger than the mean value).
[b] Values are computed after removing missing and erroneous values.

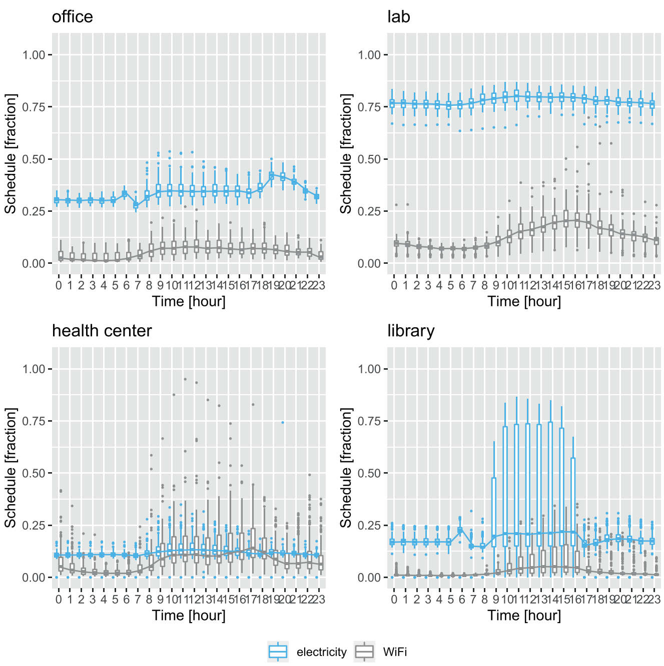

Fig. 3. Normalized twenty-four hour profile of electricity energy consumption and WiFi count for weekends (including public holidays) across four building with different typologies and functions.

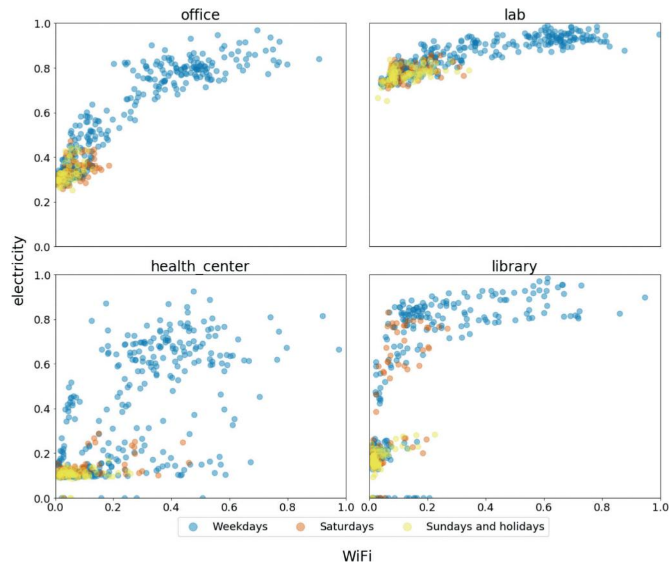

Fig. 4. Scatter plot of hourly electricity against WiFi count for weekdays in blue, Saturdays in orange, and Sundays (including public holidays) in yellow. For better visualization, we illustrate with a random selection of 500 data points.

Table 2
Correlations between building electricity consumption and WiFi connection count.

Building Type	Whole Year	Weekdays	Weekends
Office	0.93	0.92	0.45
Lab	0.88	0.88	0.48
Health Center	0.67	0.65	0.29
Library	0.74	0.72	0.66

tively for weekdays and weekends. The profiles were normalized by diving by maximum so that all data can be compared over the same range [0, 1] without losing the relative comparisons of their baseload ratios [26]. An initial comparison revealed that building electricity consumption and WiFi count tends to follow similar trends, with higher similarity observed in the office building as compared to the other three buildings (lab, health center, and library). As shown in Table 2, electricity consumption is positively correlated with WiFi count across all four building case studies, with the correlation being more significant during the weekdays (0.65–0.92) as compared to the weekends (0.29–0.66). In addition, WiFi data from the office and the lab building have a higher linear correlation (0.88–0.93) with electricity consumption as compared to the health center and the library building (0.67–0.74). This is further illustrated in Fig. 4, which shows a strong positive linear relationship between electricity consumption and WiFi connection counts for the office and the lab building. In contrast, two data clusters with a weak positive relationship between the two variables are observed for the health center. The library shows more diversity with several data clusters and a large proportion remaining constant over time. As depicted in Fig. 5, this is due to a relatively constant electricity consumption during operating hours.

The variations in WiFi count for the office, lab, and health center are mostly similar to those that one would expect from occupancy in these buildings: increasing in the morning, stabilizing during working hours with a slight dip around lunch, a decrease towards the evening, and a flat profile during the weekends (see Figs. 2 and 3). The office and lab show the smallest electricity and WiFi count variance within each hour, indicating that the daily occupancy profiles tend to remain the same throughout the year. Notably, the lab building shows considerably higher baseload ratio (0.75) as compared to the other three buildings (approximately 0.25), which can be attributed to the high equipment load that is typical of laboratories.

It comes as no surprise that the library building has the largest variance in hourly WiFi count, indicating significant diversity in occupancy profiles over the year. An investigation revealed that this is brought about by differing operating hours (See Fig. 5): 8 a.m. to 10 p.m. during the semester, 8:30 a.m. to 6 p.m. during the vacation, 10 a.m. to 5 p.m.

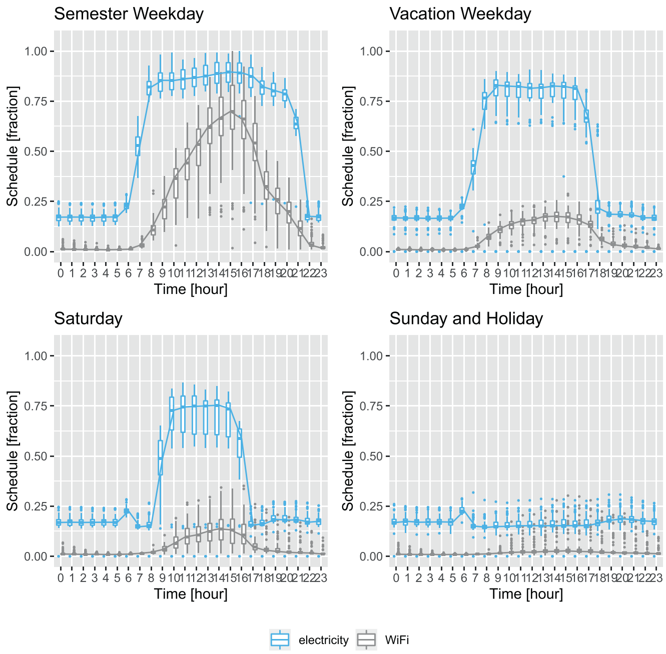

Fig. 5. Breakdown of profiles based on library building operating hours.

on Saturdays and closed on Sundays and Public Holidays. The hourly variability previously observed in Figs. 2 and 3 is also significantly reduced when segregating the profiles by the building's operating hours. From Fig. 5, it can be observed that the electricity consumption of the library plateaus during its operating hours. Conversely, the WiFi data shows a different trend that is consistent across the days that the library is operating: increases at a decreasing rate in the morning until it peaks in the afternoon (with no dip during lunch), and decreases towards the evening. Such a profile is also expected for occupancy in a typical library. Correspondingly, this provides an indication that lighting and equipment loads are not as dependant on occupancy as the other building types. This observation is not unusual given that occupants have less control over the lights and contribute less to the equipment loads in a library as compared to an office building. Despite the large proportion of the electricity consumption remaining constant over time for the library building, a significant positive linear correlation is still found with WiFi count (Table 2).

4. Clustering analysis

As mentioned in the preceding section, the linear correlation between electricity consumption and WiFi count is significantly lower for the weekends as compared to the weekdays (Table 2). However, separating the weekends from the weekdays did not result in a stronger linear relationship between electricity consumption and WiFi count. This observation is consistent across all four buildings, suggesting that separating the dataset into weekday and weekend data does not result in better explainability of the variance in electricity consumption using WiFi data. From Figs. 2 and 3, it can be seen that the variance remains for both WiFi count and electricity consumption even after separating the weekdays and weekends. This indicates the possibility that the buildings have different usage patterns during certain periods of the year.

Subsequently, we apply clustering methods [27] to identify and group periods with similar patterns. Clustering methods have been widely used to extract profiles of electricity consumption [26] and occupant number [28]. The present work differentiates from existing studies by using both electricity consumption and WiFi count data, which improves the clustering performance. Z-score standardization is applied so that the data has a mean of zero and unit variance. As part of the study, we also evaluate different feature engineering and clustering methods as summarized in Table 3 with details as follows:

Case 1 k-means [29] algorithm was applied to a concatenated 48 feature dataset. The 48 features is a concatenation of a 24-h electricity consumption profile (24 features) and a 24-h WiFi data profile (24 features). We concatenate electricity consumption and WiFi profiles because it provided more distinct clusters, suggesting that the two profiles together can better define the buildings' daily usage pattern.

Case 2 Similar to case 1 but using the Density-based spatial clustering of applications with noise (DBSCAN) [30] algorithm for the clustering. Unlike distance-based k-means, DBSCAN is a density-based clustering algorithm that was designed to be able to identify clusters of arbitrary shapes in datasets containing noise and outliers.

Case 3 Similar to case 1 but using the k-shape algorithm [31] for the clustering. The k-shape algorithm considers the shapes of time series in the clustering by using a normalized version of the cross-correlation measure as its distance measure. This is a newly proposed clustering method that emphasizes on the shape-based similarity of time series data.

Case 4 Similar to case 1 but using Hierarchical Density Based Clustering (HDBSCAN) [32] for the clustering. It extends DBSCAN by converting it into a hierarchical clustering algorithm, and then using a technique to extract a flat clustering based in the stability of clusters.

Case 5 Similar to case 1 but principal component analysis (PCA) is applied to remove noise and redundancy in the dataset. Only the first two principal components were used for the clustering since they explained more than 95% of the variance.

Case 6 Similar to case 5 but using the Density-based spatial clustering of applications with noise (DBSCAN) [30] algorithm for the clustering.

The Calinkski Harabasz (CH) Score [33] was used to evaluate clustering performance on both the electricity and WiFi datasets. CH Score is also known as variance ratio criterion (i.e., the ratio of between-cluster variance to within-cluster variance). Therefore, a higher CH score relates to more distinct clusters. However, it is worth noting that the absolute value of CH score is affected by the scale of the profiles, and therefore, is only comparable for the same measurements of the same building. From Table 3, case 6 (PCA followed by DBSCAN) gave the highest CH Scores in four out of the eight cases, and comparatively high CH Scores in the remaining three cases. Fig. 6 shows the clustering results of case 6. Based on the clustering results, the following observations can be made. First, WiFi count profiles contain significantly higher within-cluster variability as compared to the electricity consumption profiles, which is in agreement with the stochasticity in occupant behavior demonstrated in previous studies [4]. Second, using PCA for feature extraction led to more distinct clusters (see first column of Fig. 6), and higher CH scores (Table 3). Third, DBSCAN outperforms k-means by excluding insignificant outliers and identifying the minor profile clusters (such as cluster 3 in lab and health center). More detailed comparison and discussion about different profile clustering methods can be found in Zhan et al. [34].

Fig. 7 shows the clustering results in a calendar map format. The colors represent the corresponding clusters illustrated in Fig. 6. From Fig. 7, it can be seen that each cluster comprises of profiles over a specific period in the year. The clusters and corresponding periods for each building, as well as the correlations during the periods, are summarized in Table 4. A comparison of the cluster centroids (Fig. 6) and when they occur temporally (Fig. 7) provides deeper insights into the relationship between total WiFi connection counts and total building electricity consumption, as follows:

- For the office, the lab and the health center, there is a period when the number of WiFi connection is significantly higher or lower than

Table 3
Summary of Calinski Harabasz (CH) Scores with/without principal component analysis (PCA) and different clustering methods.

Case	Clustering Algorithm	PCA	Measure	Calinski Harabasz Score[a]			
				Office	Lab	Health Center	Library
1	k-means	No	WiFi	1267	1396	**354**[b]	599
			electricity	1657	347	1149	1259
2	DBSCAN	No	WiFi	1060	1571	111	217
			electricity	2025	404	843	**1388**
3	k-shape	No	WiFi	767	1439	90	496
			electricity	968	394	184	206
4	HDBSCAN	No	WiFi	503	1063	229	116
			electricity	2767	**421**	707	1005
5	k-means	Yes	WiFi	1124	1299	282	**655**
			electricity	1626	244	1496	368
6	DBSCAN	Yes	WiFi	**1705**	**1730**	184	587
			electricity	**3040**	418	**1684**	756

[a] Calinski Harabasz (CH) Score is an effective measurement when evaluating clustering performance of the same type of measurement in the same building [33].
[b] Highest scores are highlighted in bold.

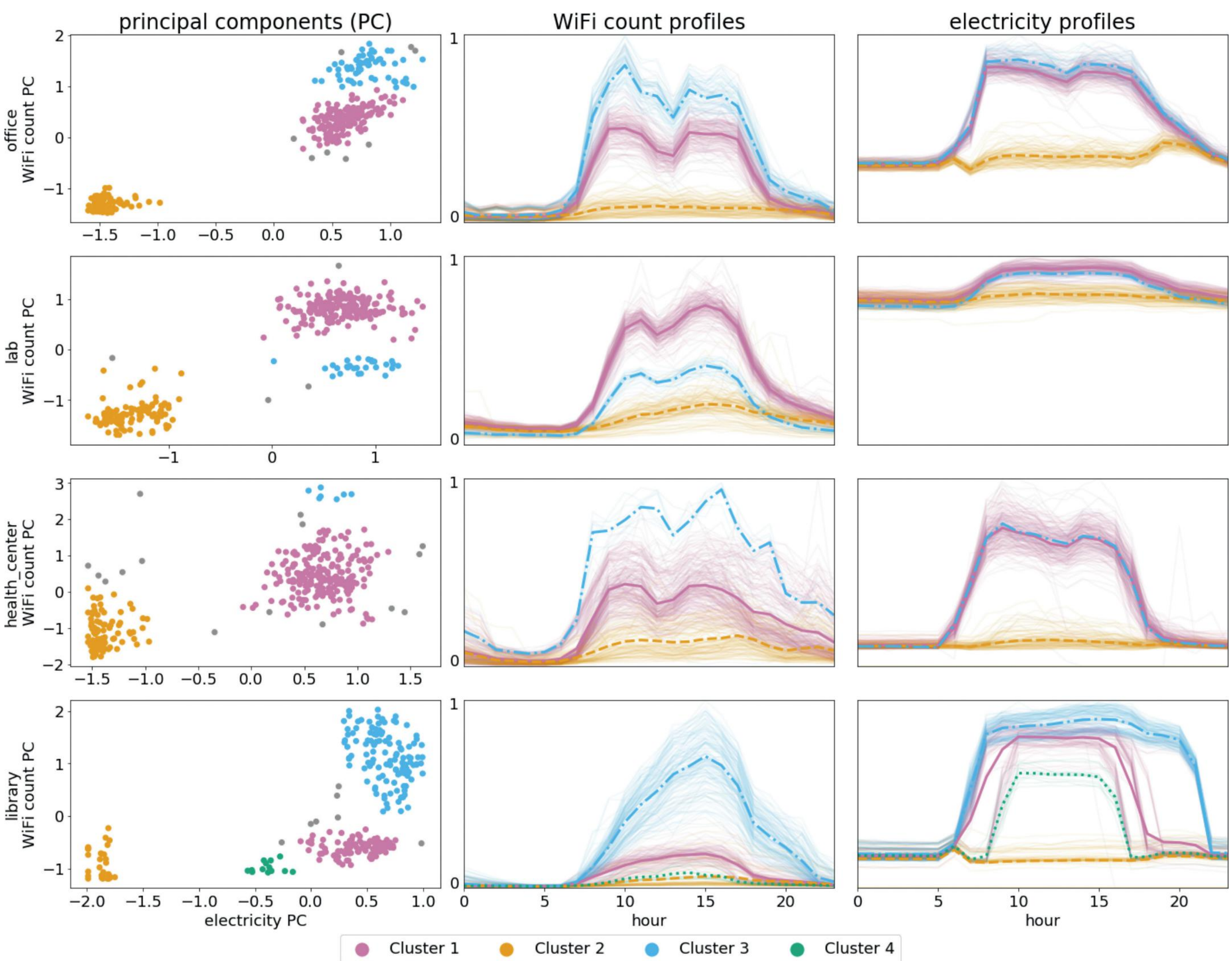

Fig. 6. Clustering results. Left column: scatter plots of the first principal component for electricity consumption against the first principal component for WiFi connection counts; Middle column: Profile plots for WiFi connection counts; Right column: Profile plots for electricity consumption.The color across all plots indicate the corresponding cluster that they belong to.

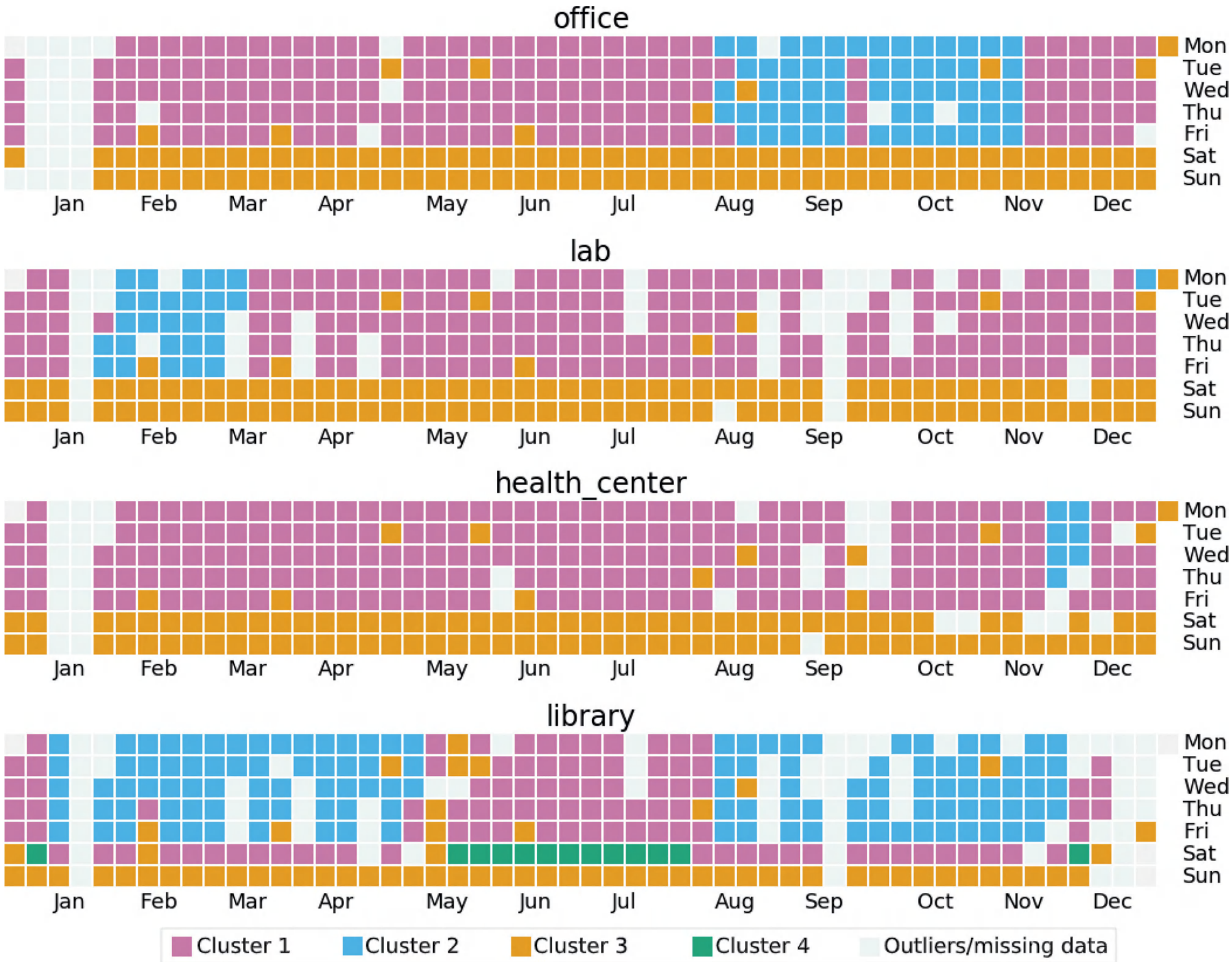

Fig. 7. Clustering results visualized in calendar maps. The blanks are missing data/cluster outliers.

Table 4
Summary of the clusters, and their corresponding periods and correlation between building electricity consumption and WiFi connection counts. Cluster numbers are color coded following the clustering results presented in Figs. 6 and 7.

Building type	Cluster no.	Corresponding period	Correlation
Office	1	Weekdays beyond semester 2	0.94
	2	All weekends and holidays	0.45
	3	Weekdays in semester 2	0.95
lab	1	Most weekdays	0.89
	2	All weekends and holidays	0.49
	3	Weekdays from late January to early March	0.92
Health Center	1	Most weekdays	0.68
	2	All weekends and holidays	0.15
	3	Weekdays in last two weeks of semester 2	0.83
Library	1	Saturdays during semester and weekdays during vacation	0.86
	2	All Sundays and holidays	0.11
	3	Weekdays during semester	0.78
	4	Saturdays during vacation	0.79

Table 5
Root mean squared error (RMSE) and coefficients of linear regression with (w/) and without (w/o) clustering. Cluster numbers are color coded following the clustering results presented in Figs. 6 and 7.

Building Type	RMSE (kWh)		Coefficient					Intercept				
	w/o	w/	w/o	1	2	3	4	w/o	1	2	3	4
Office	5.69	4.49	0.13	0.15	0.08	0.11	N/A	22.45	23.19	21.66	23.12	N/A
Lab	46.64	43.49	0.62	0.58	0.54	1.08	N/A	1021	1035	1016	989	N/A
Health Center	23.37	20.53	0.33	0.35	0.02	0.26	N/A	12.93	17.36	14.31	1.86	N/A
Library	92.65	70.49	0.18	0.54	0.03	0.14	0.79	118.1	76.04	65.83	150.3	62.06

the rest of the year (blue cluster in Figs. 6 and 7), while the electricity consumption remains at a similarly high level.

- An increase in linear correlation in clusters representative of operating days (e.g. weekdays) can be observed. A corresponding decrease in linear correlation in clusters representative of non-operating days (e.g. weekends and holidays) was also observed. This comes as no surprise because the portion of the WiFi data that has a stronger relationship with electricity consumption (operating days) is now separated from the portion with a weaker correlation. Consequently, clustering the profiles as a pre-processing step for applications like energy prediction or occupancy schedule extraction may help improve prediction or modeling performance.

To demonstrate the improved explainability brought by clustering, linear regression is applied to model the relationships between electricity consumption and occupants. While linear regression is a simple model, its parameters can be physically interpreted. The coefficient represents by how much occupants affect electricity consumption, and the intercept implies the unaffected baseload. Table 5 summarizes the results with and without the clustering, including Root mean squared errors (RMSE) and the model coefficients. Based on RMSE, the model performance of all buildings is improved by fitting within each clustered period. The change of coefficients and intercepts illustrates the reason. For example, the lab has a significantly higher coefficient for cluster 3 than the other 2, indicating higher per capita consumption. Also, the library has an around twice larger intercept, or baseload, on weekdays during the semester than other days. In summary, the clustering effectively separates different interrelationships and improves model performance.

5. Discussion

This paper focuses on the relationship between building electricity consumption and WiFi connections counts (as a proxy of occupancy). Variations in total WiFi connection counts and total building electricity consumption tend to follow similar trends (Figs. 2 and 3), with some differences between the four case study buildings (office, lab, health center, and library).

Opportunities for energy savings can be identified by comparing the corresponding cluster centroids for electricity consumption and WiFi connections (Fig. 6) and when they occur temporally (Fig. 7). For example, for the office, the lab, and the health center, there is a period when the number of WiFi connections is significantly higher or lower (blue clusters in Fig. 6) than the profile you would expect on a typical operating day (pink clusters in Fig. 6). However, the corresponding electricity consumption is similar between the two clusters. A similar situation is also observed for the library when the electricity consumption remains high as the WiFi connection gradually increase and decrease. Possible reasons include (1) the building is being operated on a static schedule and/or (2) poor zoning and controls leading to energy wastage. The mismatch between occupancy and electricity consumption indicates an opportunity to conserve energy by proportionally operate building systems based on occupancy. Past studies have shown that occupant-based controls can bring about reductions in lighting energy consumption by about 30% [12] and HVAC energy consumption by about 20% [24,25].

Fig. 6 also clearly shows that the lab building has a very high baseload compared to the other buildings despite being unoccupied (WiFi connections are close to zero). This might be due to equipment that are required to run continuously, indicating opportunities for saving energy by switching these equipment to more energy-efficient ones. The high base load might be due to wasteful occupant behavior [6] and/or poor equipment efficiencies causing a performance gap [35]. However, it should be noted that both studies were on office buildings and thus might not be directly applicable.

Results from this study indicate that WiFi connection counts have a stronger positive correlation with building electricity consumption during operating hours as compared to when the building is not in operation (Table 4). This observation is consistent across all building types and consistent with the study by Melfi et al. [16], where a higher correlation was found for weekdays as compared to weekends. The strong positive correlation is also in agreement with the study by Martani et al. [22]. The office and the lab showed a higher correlation between WiFi count and electricity consumption as compared to the health center and the library (Table 4). The electricity consumption in this study only includes equipment, lighting, and AHU fan consumption. Therefore, a possible reason for the higher correlation is the interactions between the plug and lighting loads and the occupants. Put differently, occupants in offices and labs have more influence over the plug and lighting loads than in the health center and library.

It is acknowledged that WiFi count is not an exact measurement of occupant number [16]. Potential problems include: (1) inconsistent WiFi connectivity resulting in devices losing connections to APs leading to false negatives (devices not being counted even though it is within the building), and (2) overlapping access point (AP) coverage resulting in devices being connected to APs that are not in the same area as the occupant. However, overlapping AP coverage is not an issue in this study because the focus is on aggregated WiFi connection counts, which has been shown to be a good enough estimate for whole building analysis [19].

6. Conclusion

In this paper, we explored and analyzed the dynamic relationship between total WiFi connection count (as a proxy for occupancy) and total building electricity consumption across four different building types (office, lab, health center, and library). We showed that

- Using PCA for feature extraction followed by DBSCAN for clustering generated distinct clusters with the highest CH-scores (ratio of between cluster variance to within-cluster variance). This led to stronger positive linear correlation across all four building types on days the building is in operation.
- The proposed clustering approach could be used as a preprocessing step to better model the variables using methods like linear regression.

- Clustering using both WiFi connection counts and electricity energy consumption data provided more distinct profiles that better define a building's energy usage patterns.
- A higher correlation was observed across all four building when the building is in operation. Additionally, a stronger relationship was found in buildings where occupancy does not deviate much (office and lab) as compared to buildings where higher variability in occupancy is expected (health center and library).
- WiFi data provide levels of detail about occupant presence. By analyzing WiFi connection counts (as a proxy of occupant presence) with electricity consumption, indications of energy saving opportunities can be identified. Examples include energy saving potential from introducing occupant-centric controls as well as opportunities to mitigate energy wastage when the building is not in operation.

The similarity in trends and the high positive correlation with electricity consumption suggest that WiFi connection count is suitable for modeling the hour to hour variations in electrical loads. Since relative changes in electricity consumption are at least partially a function of occupant presence, the rationalization of the WiFi profiles also suggests that the number of WiFi connections might be a suitable indicator of building occupancy. The advantage of using WiFi data lies in not needing any modifications to the existing building infrastructure other than the collection and processing of data.

Declaration of Competing Interest

We wish to confirm that there are no known conflicts of interest associated with this publication and there has been no significant financial support for this work that could have influenced its outcome.

References

[1] IEA, Global Status Report for Buildings and Construction, International Energy Agency, Paris, 2019.
[2] C. Turner, M. Frankel, et al., Energy performance of leed for new construction buildings, New Build. Inst. 4 (2008) 1–42.
[3] IEA EBC annex 53: Total energy use in buildings analysis and evaluation methods, Energy Build. 152 (2017) 124–136, doi:10.1016/j.enbuild.2017.07.038.
[4] D. Yan, W. O'Brien, T. Hong, X. Feng, H.B. Gunay, F. Tahmasebi, A. Mahdavi, Occupant behavior modeling for building performance simulation: current state and future challenges, Energy Build. 107 (2015) 264–278, doi:10.1016/j.enbuild.2015.08.032.
[5] S. Ahmadi-Karvigh, A. Ghahramani, B. Becerik-Gerber, L. Soibelman, Real-time activity recognition for energy efficiency in buildings, Appl. Energy 211 (2018) 146–160, doi:10.1016/j.apenergy.2017.11.055.
[6] O. Masoso, L.J. Grobler, The dark side of occupants' behaviour on building energy use, Energy Build. 42 (2) (2010) 173–177, doi:10.1016/j.enbuild.2009.08.009.
[7] An international review of occupant-related aspects of building energy codes and standards, Build. Environ. (2020).
[8] S. Naylor, M. Gillott, T. Lau, A review of occupant-centric building control strategies to reduce building energy use, Renew. Sustain. Energy Rev. 96 (2018) 1–10, doi:10.1016/j.rser.2018.07.019.
[9] T. Hong, S.C. Taylor-Lange, S. D'Oca, D. Yan, S.P. Corgnati, Advances in research and applications of energy-related occupant behavior in buildings, Energy Build. 116 (2016) 694–702, doi:10.1016/j.enbuild.2015.11.052.
[10] J.Y. Park, M.M. Ouf, B. Gunay, Y. Peng, W. O'Brien, M.B. Kjærgaard, Z. Nagy, A critical review of field implementations of occupant-centric building controls, Build. Environ. 165 (2019) 106351, doi:10.1016/j.buildenv.2019.106351.
[11] W.J. Fisk, A pilot study of the accuracy of co2 sensors in commercial buildings (2008).
[12] V. Garg, N.K. Bansal, Smart occupancy sensors to reduce energy consumption, Energy Build. 32 (1) (2000) 81–87, doi:10.1016/S0378-7788(99)00040-7.
[13] X. Guo, D. Tiller, G. Henze, C. Waters, The performance of occupancy-based lighting control systems: a review, Light. Res. Technol. 42 (4) (2010) 415–431, doi:10.1177/1477153510376225.
[14] Y. Jin, D. Yan, H. Sun, Lighting system control in office building using occupancy prediction based on historical occupied ratio, in: IOP Conference Series: Earth and Environmental Science, 238, IOP Publishing, 2019, p. 012009, doi:10.1088/1755-1315/238/1/012009.
[15] T. Vafeiadis, S. Zikos, G. Stavropoulos, D. Ioannidis, S. Krinidis, D. Tzovaras, K. Moustakas, Machine learning based occupancy detection via the use of smart meters, in: 2017 International Symposium on Computer Science and Intelligent Controls (ISCSIC), IEEE, 2017, pp. 6–12, doi:10.1109/ISCSIC.2017.15.
[16] R. Melfi, B. Rosenblum, B. Nordman, K. Christensen, Measuring building occupancy using existing network infrastructure, in: 2011 International Green Computing Conference and Workshops, IEEE, 2011, pp. 1–8.
[17] B. Dong, B. Andrews, K.P. Lam, M. Höynck, R. Zhang, Y.-S. Chiou, D. Benitez, An information technology enabled sustainability test-bed (itest) for occupancy detection through an environmental sensing network, Energy Build. 42 (7) (2010) 1038–1046, doi:10.1016/j.enbuild.2010.01.016.
[18] H. Elkhoukhi, Y. NaitMalek, A. Berouine, M. Bakhouya, D. Elouadghiri, M. Essaaidi, Towards a real-time occupancy detection approach for smart buildings, Procedia Comput. Sci. 134 (2018) 114–120, doi:10.1016/j.procs.2018.07.151.
[19] M.M. Ouf, M.H. Issa, A. Azzouz, A.-M. Sadick, Effectiveness of using WiFi technologies to detect and predict building occupancy, Sustain. Build. 2 (2017) 1–10, doi:10.1051/sbuild/2017005.
[20] Z. Wang, T. Hong, M.A. Piette, M. Pritoni, Inferring occupant counts from Wi-Fi data in buildings through machine learning, Build. Environ. 158 (2019) 281–294, doi:10.1016/j.buildenv.2019.05.015.
[21] K. Akkaya, I. Guvenc, R. Aygun, N. Pala, A. Kadri, IoT-based occupancy monitoring techniques for energy-efficient smart buildings, in: 2015 IEEE Wireless Communications and Networking Conference Workshops (WCNCW), IEEE, 2015, pp. 58–63.
[22] C. Martani, D. Lee, P. Robinson, R. Britter, C. Ratti, Enernet: studying the dynamic relationship between building occupancy and energy consumption, Energy Build. 47 (2012) 584–591, doi:10.1016/j.enbuild.2011.12.037.
[23] H. Zou, Y. Zhou, H. Jiang, S.-C. Chien, L. Xie, C.J. Spanos, Winlight: a WiFi-based occupancy-driven lighting control system for smart building, Energy Build. 158 (2018) 924–938, doi:10.1016/j.enbuild.2017.09.001.
[24] B. Balaji, J. Xu, A. Nwokafor, R. Gupta, Y. Agarwal, Sentinel: occupancy based HVAC actuation using existing WiFi infrastructure within commercial buildings, in: Proceedings of the 11th ACM Conference on Embedded Networked Sensor Systems, 2013, pp. 1–14, doi:10.1145/2517351.2517370.
[25] W. Wang, T. Hong, N. Li, R.Q. Wang, J. Chen, Linking energy-cyber-physical systems with occupancy prediction and interpretation through WiFi probe-based ensemble classification, Appl. Energy 236 (2019) 55–69, doi:10.1016/j.apenergy.2018.11.079.
[26] S. Zhan, Z. Liu, A. Chong, D. Yan, Building categorization revisited: a clustering-based approach to using smart meter data for building energy benchmarking, Appl. Energy 269 (2020) 518–530, doi:10.1016/j.apenergy.2020.114920.
[27] F. Pedregosa, G. Varoquaux, A. Gramfort, V. Michel, B. Thirion, O. Grisel, M. Blondel, P. Prettenhofer, R. Weiss, V. Dubourg, J. Vanderplas, A. Passos, D. Cournapeau, M. Brucher, M. Perrot, E. Duchesnay, Scikit-learn: machine learning in Python, J. Mach. Learn. Res. 12 (2011) 2825–2830.
[28] G. Jiefan, X. Peng, P. Zhihong, C. Yongbao, J. Ying, C. Zhe, Extracting typical occupancy data of different buildings from mobile positioning data, Energy Build. 180 (2018) 135–145, doi:10.1016/j.enbuild.2018.09.002.
[29] A. Lavin, D. Klabjan, Clustering time-series energy data from smart meters, Energy Effic. 8 (4) (2015) 681–689, doi:10.1007/s12053-014-9316-0.
[30] M. Ester, H.-P. Kriegel, J. Sander, X. Xu, et al., A density-based algorithm for discovering clusters in large spatial databases with noise., in: Kdd, 96, 1996, pp. 226–231.
[31] J. Paparrizos, L. Gravano, k-shape: efficient and accurate clustering of time series, in: Proceedings of the 2015 ACM SIGMOD International Conference on Management of Data, 2015, pp. 1855–1870, doi:10.1145/2723372.2737793.
[32] R.J. Campello, D. Moulavi, J. Sander, Density-based clustering based on hierarchical density estimates, in: Pacific-Asia Conference on Knowledge Discovery and Data Mining, Springer, 2013, pp. 160–172, doi:10.1007/978-3-642-37456-2_14.
[33] T. Caliński, J. Harabasz, A dendrite method for cluster analysis, Commun. Stat.-theory Methods 3 (1) (1974) 1–27, doi:10.1080/03610927408827101.
[34] S. Zhan, A. Chong, A robust unsupervised framework for high-resolution building energy consumption profiling, in: Proceedings of the International Building Performance Simulation Association, International Building Performance Association (IBPSA), 2019.
[35] A.C. Menezes, A. Cripps, D. Bouchlaghem, R. Buswell, Predicted vs. actual energy performance of non-domestic buildings: using post-occupancy evaluation data to reduce the performance gap, Appl. Energy 97 (2012) 355–364, doi:10.1016/j.apenergy.2011.11.075.

Energy and Built Environment 2 (2021) 175–187

Contents lists available at ScienceDirect

Energy and Built Environment

journal homepage: http://www.keaipublishing.com/en/journals/energy-and-built-environment/

Comparative analysis of window operating behavior in three different open-plan offices in Nanjing

Jiawen Ren[a], Xin Zhou[a,*], Jingjing An[b], Da Yan[b], Xing Shi[a], Xing Jin[a], Shaoyan Zheng[c]

[a] School of Architecture, Southeast University, Nanjing 210096, China
[b] School of Architecture, Tsinghua University, Beijing 100084, China
[c] Bureau of Housing and Urban-Rural Development of XUYI County, China

ARTICLE INFO

Keywords:
Open-plan office
Window operating behavior
Field measurement
Influencing factor
Pattern comparison

ABSTRACT

Research on the window operating behavior of offices is of great significance for reducing building energy consumption and improving indoor comfort. The open-plan office is a common office form that involves a large number of people and a complex staff composition. The window operating behaviors in open-plan offices are also random and various. This study took three open-plan offices with different situations (area, office type, staff composition, etc.) as an example, which provides a new perspective on how people behave differently when opening or closing windows. The window operating behaviors in two typical seasons (summer and transition seasons) were recorded and analyzed. The occupants' schedules and influencing factors of window operating behavior were investigated by questionnaire surveys. In addition, the indoor environmental parameters, occupancy situation, and on-off statuses of windows and air conditioning were acquired through field measurements. Furthermore, the differences in window operating behaviors in the three open-plan offices were compared from the perspectives of influencing factors, duration of the window on-off statuses, and cause of window control actions, among others. In addition, Spearman Correlation Coefficient was used to analyze the ranks of the candidate motivations for window operating behaviors. The preliminary results show that influenced by the personnel composition, type of air conditioner and adjustable degree of windows, the window operating behaviors of different office buildings have larger discrepancies than that in the same building. However, there were some common characteristics in the window regulation behaviors of the three open-plan offices: they were generally influenced by the coupling of environmental factors, schedule factors, and equipment factors. This study reveals that when expand the research object from a single building to multiple buildings, more difficulties and challenges would be involved into behavior research.

1. Introduction

The energy consumption of office buildings accounts for approximately 20% of the total energy consumption of global buildings [1]. Therefore, it is important to reduce the energy consumption of office buildings while ensuring indoor comfort. According to the study of IEA Annex 53, the energy consumption of office buildings is mainly affected by four factors, namely meteorological parameters, envelope performance, equipment performance, and occupant behavior [2]. Among the various factors influencing building energy consumption, occupant behavior has been of great concern [3–5]. As one of the most common occupant behaviors in buildings, window operating behavior directly affects the indoor thermal environment and indoor air quality [6]. Therefore, window operating behavior has an important impact on indoor comfort and building energy consumption [7–9], and it is of great significance to conduct in-depth analysis and research on this behavior.

In order to effectively reduce the energy consumption of buildings, natural ventilation and mixed ventilation have been widely used in buildings in summer, even though air conditioning (AC) has been popularized [10]. Karin Schakib Ekbatan et al. [11] found that outdoor temperatures as well as indoor air temperatures influence window opening by monitoring 35 offices. D'Oca and Hong [12] analyzed a data set with measured indoor and outdoor physical parameters and human interaction with operable windows in 16 offices. They found that indoor air temperature, outdoor air temperature, time of day, and occupancy presence are the drivers for window operating behaviors. Rijal et al. [13] found that the proportion of windows open is related to the season and is a function of the indoor and outdoor temperature. After conducting a field study of the manual control of windows in 21 offices in Germany, Herkel et al. [14] found that user behavior has a strong correla-

* Corresponding author.
E-mail address: 101012014@seu.edu.cn (X. Zhou).

https://doi.org/10.1016/j.enbenv.2020.07.007
Available online 13 August 2020

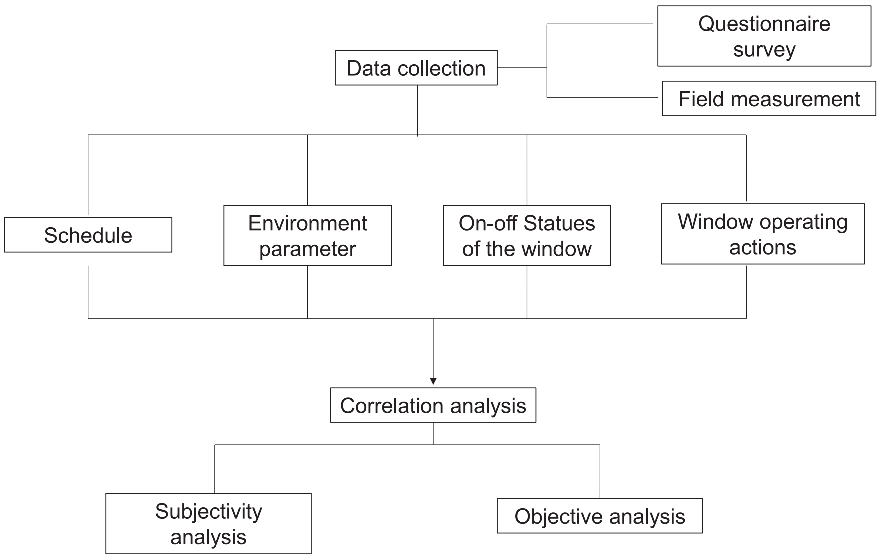

Fig. 1. Technical route.

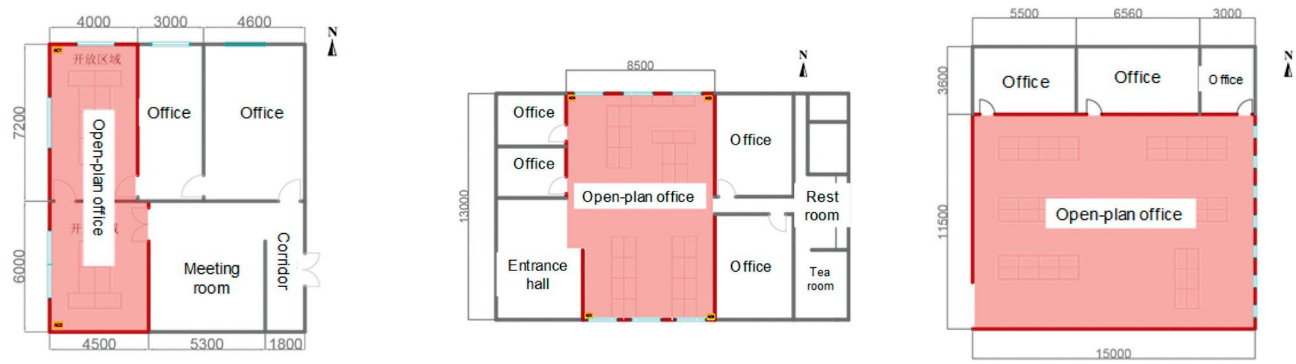

(a): Office A plan (b): Office B plan (c): Office C plan

Fig. 2. Office plans.

Table 1
Basic information of the three offices.

	Office A	Office B	Office C
Location	University campus	Residential building	Commercial office area
Area (m^2)	56	110	172
Orientation	West	South	East
Window type	Sliding window	Sliding window	Top-hung window
Window location	West/North	South/North	East/West/South
AC system	Split AC	Split AC	FAN COIL + OA
Occupants	Graduates(10 persons)	Graduates and construction practitioners (20 persons)	Construction practitioners (35 persons)

Notes: AC (Air Conditioning); OA (Outdoor Air).

(a) magnetic switch recorder (b) temperature and humidity recorder (c) HOBO Occupancy/light Logger ux90-006

Fig. 3. Measurement instruments.

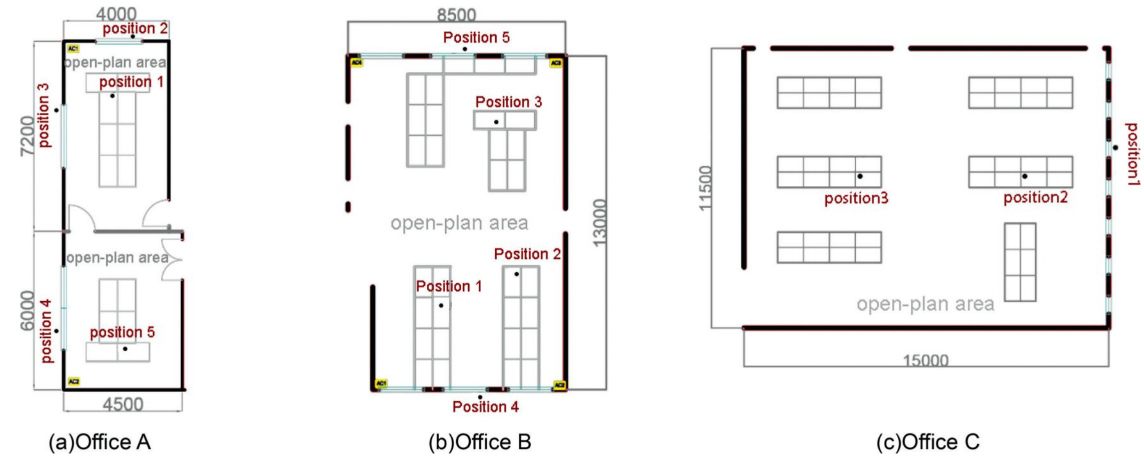

Fig. 4. Measurement point locations.

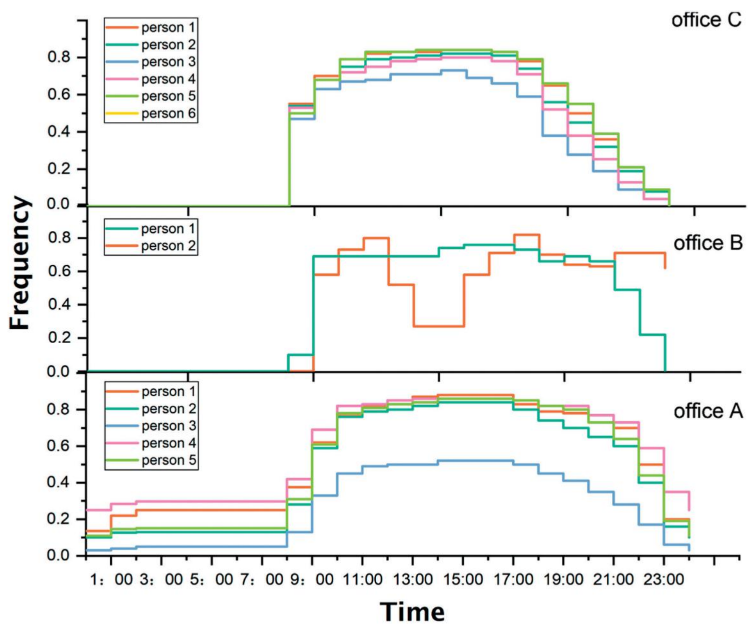

Fig. 5. Frequency of the presence of office workers in the three offices.

tion with the percentage of open windows and the time of year, outdoor temperature, and building occupancy patterns. However, even if the external factors affecting the window opening behavior are the same, the occupants of the building will still have different operating behaviors [15]. Wei et al. [16] explored the effects of non-environmental factors and found that season, floor level, gender, and personal preference had a statistically significant effect on the window operation in an examined building. Zhang and Barrett [17] found that the window orientation produces distinctly different control responses owing to solar radiation and the prevailing wind direction.

Many data driven methodologies and models have been developed to obtain new insights on the window operating behaviors [18-20]. Logit regression and normal distribution functions were combined to replicate the diversity of window operating behavior in Canadian residential buildings [21]. D'Oca and Hong [12] used two kinds of data mining approaches to discover window operating patterns, and four aspects of window operations were clustered in the study. Li et al. [22] pointed out that the correlation between occupant behavior and window operating has not been well explored. Logistic regression and tree-based data-driven models were used to analyze the importance of influencing factors on window operating behavior. Chen et al. [23] applied Cox model to consider the influence of environmental factors and window-opening durations on window operating behaviors. In [24], Reliable prediction on occupants' actions was obtained by using logistic regression by taking into account summer and winter conditions. Sun et al. [25] analyzed the influencing factors motivating behavior, defined the window-opening behavior patterns by using cluster and logistic analysis and formed the behavioral profiles that were used in building performance simulation software. Wei et al. [26] compared three data mining method, logistic regression model, Markov model, and ANN model as the methodologies to model window opening behaviors in office building.

Current research on window operating behavior mainly focuses on single offices. However, few studies have compared the window operating behaviors of offices in different buildings. The window operating behavior in a single office is mainly affected by individuals, while the window regulation behavior in a multi-person office is more random and complex owing to the large number of people and the different composition of occupants. In view of the above shortcoming, a comparison of the window operating behaviors in open-plan offices in different build-

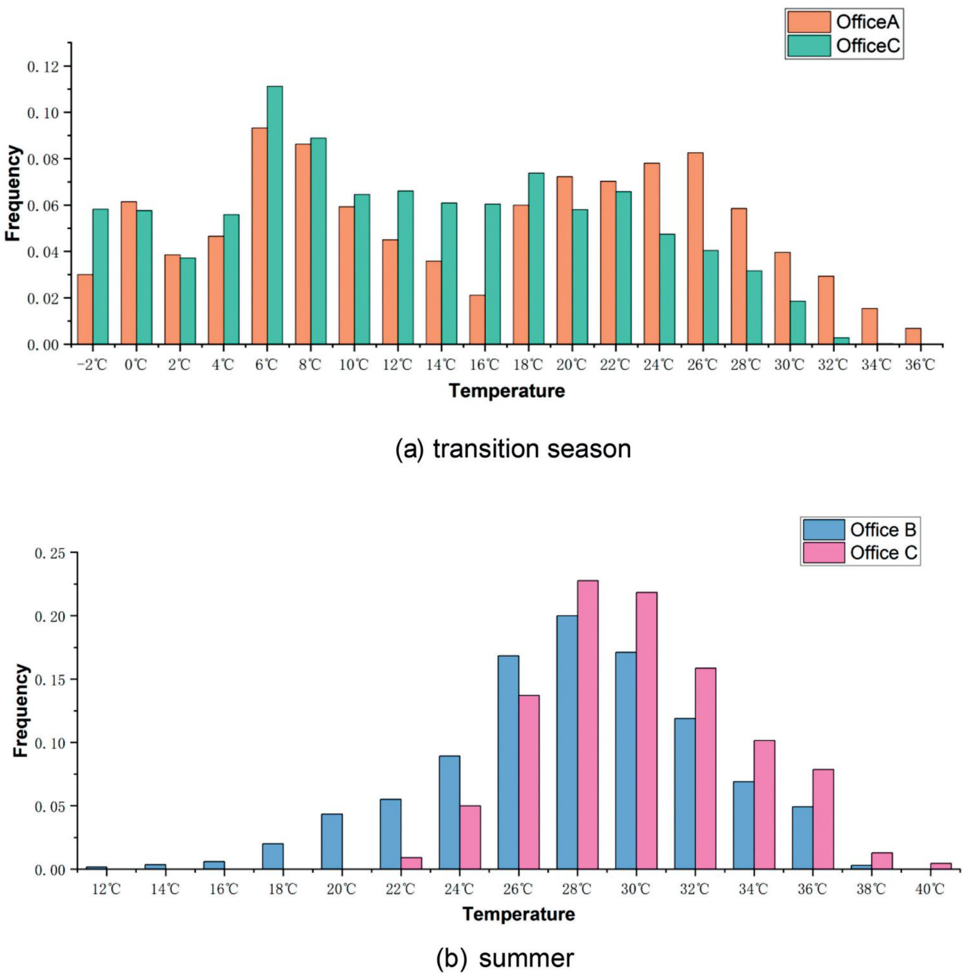

Fig. 6. Outdoor temperature distribution.

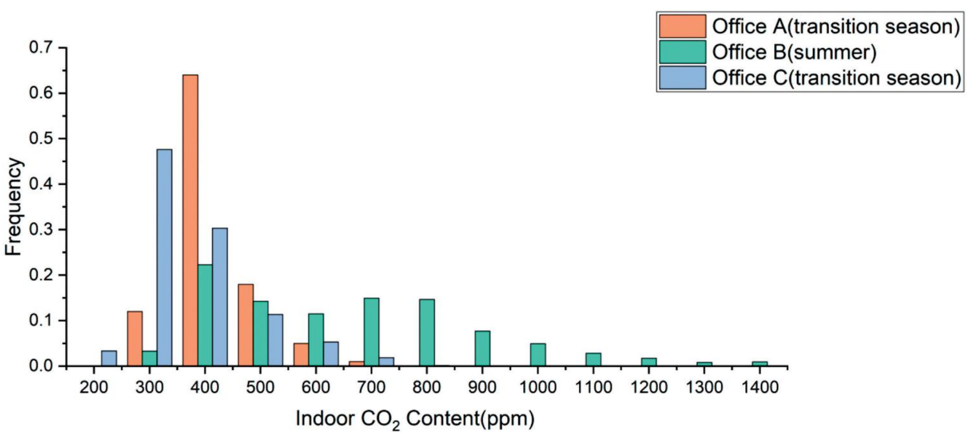

Fig. 7. Indoor CO_2 distribution.

ings was presented in this study, which provides a new perspective on how people behave differently when opening or closing windows.

Thus, the aim of this study is to analyze the window operating behavior in three open-plan offices with different conditions in Nanjing, China. The three offices were located in different buildings with different occupant compositions. Subjective analysis and objective analysis were applied to understand the correlations of window operating behavior and other influencing factors. The contribution of this study is to expand the research object from a single building to multiple buildings, which reveals more difficulties and challenges to behavior research.

2. Methodology

The general approach of this study is shown in Fig. 1. The data collection was composed of questionnaire survey and field measurement. The questionnaire survey on the staff's daily schedule and the factors affecting the window operating behavior was conducted. Field measurements recorded the indoor environmental parameters, occupancy, and on-off statuses of the windows and air conditioners. All these data were divided into four section, namely schedule, environmental parameters, on-off statuses of windows and window operating actions. Correlation analysis from subjective and objective perspectives were conducted to

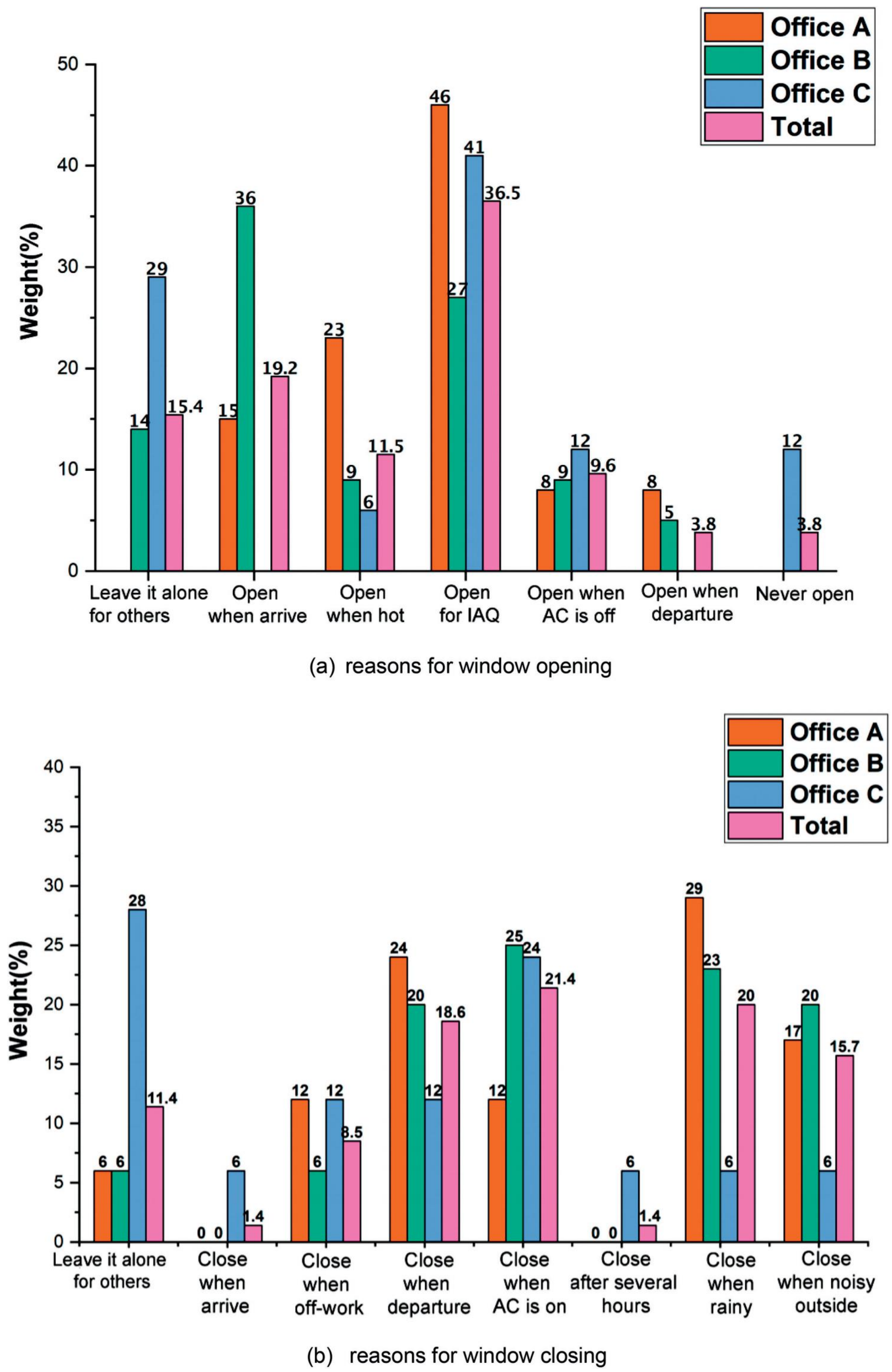

Fig. 8. Reasons for window opening and closing based on the questionnaire results.

reveal how window operating behavior differs among different buildings.

3. Data collection

Three different open-plan offices in Nanjing were examined, the basic situations of which were as follows:

Office A (Fig. 2(a)) is a student studio located at a university campus, and the office covers an area of 56 m^2. Office B [27] (Fig. 2(b)) is located in a residential area, and the area of the office is approximately 110 m^2 (not including the hall). Office C (Fig. 2(c)) belongs to a commercial office block, and the office area of 172 m^2 is divided into the open office area and three single office spaces. The three test subjects adopted a mixture of natural ventilation and mechanical ventilation. The windows in office A and office B are sliding windows, which are located on the west side and north side of office A and on the south side and north side of office B. Office C uses a top-hung window on the east side of the office area. For the AC system, offices A and B adopt a split AC system, while office C applies fan coil with centralized fresh air system. In terms of the composition of the office staff, the staff of office A is comprised of

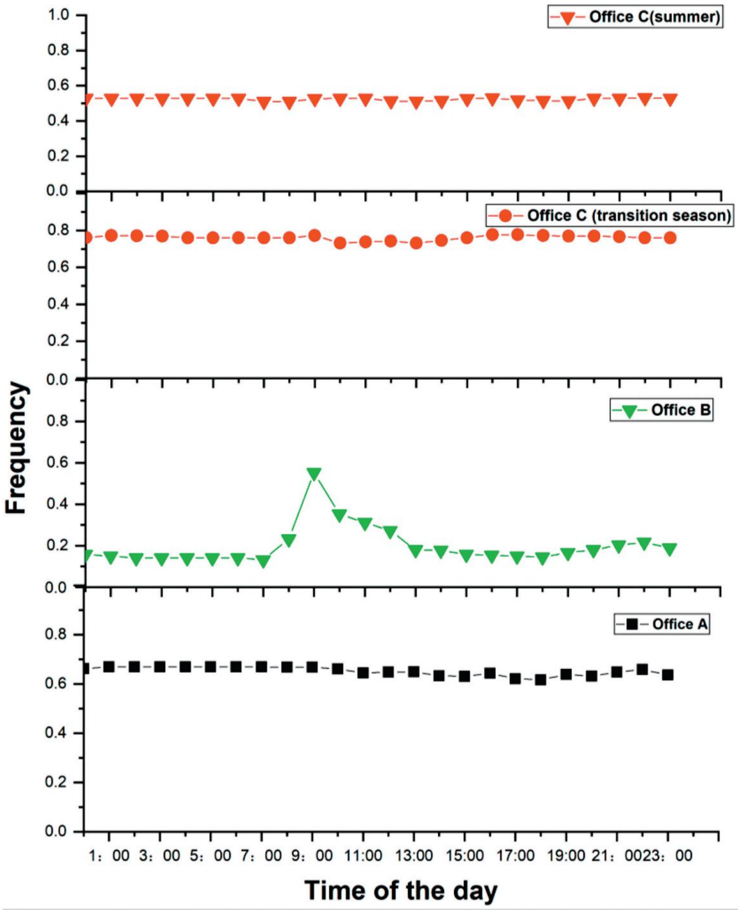

Fig. 9. Time distribution of the opening rate.

Table 2
Time of data collection.

	Test time
Office A	2018.01–2018.06
Office B	2016.08–2016.102018.07–2018.09
Office C	2018.01–2019.01

Table 3
Opening rate comparison.

Test object	Opening rate
Office A (transition season)	0.658
Office B (summer)	0.220
Office C (transition season)	0.760
Office C (summer)	0.520

graduates from universities with a total of 10 people. Office B is mainly staffed by 20 occupants, including graduates and construction practitioners. Office C is staffed by 35 construction practitioners. The basic information of the three offices is shown in Table 1.

3.1. Questionnaire survey

The questionnaire was divided into two parts, including basic information about the office and the method of office energy use.

Basic information about the office included the age and gender of the occupants. The time spent in the office for different occupants was also investigated. The calibration method was used to make records of the room conditions of staff occupancy within one week in order to reflect the schedule of the occupants, which was convenient for comparative analysis with the measured data at a later stage.

Table 4
Window operation counts.

Test object	Opening	Closing
Office A (transition season)	0.56	0.56
Office B (summer)	0.51	0.49
Office C (transition season)	0.17	0.16
Office C (summer)	0.21	0.21

The method of energy use covered the window operating behavior and the behavior frequency of different occupants operating the windows in order to extract the active personnel of the open-plan office. An investigation of the reasons why the staff might conduct the window operating behavior under certain office situations was also conducted.

3.2. Measured data

In order to record the basic environmental data and occupant operating behavior, this study conducted field surveys on the three open-plan offices. In order to obtain continuous recording data, test instruments with self-recording functions were used during the measurement (Fig. 3). Among them, a magnetic switch recorder mainly recorded the on-off statuses of the windows. The temperature and humidity of the room were recorded by a temperature and humidity recorder, which also helped to determine the on-off statuses of the air conditioners by arranging them in the outlet of the air conditioners in office B. A HOBO Occupancy/Light Logger ux90-006 was used to record the occupancy in the room. All the measuring equipment used 5 min time steps for data

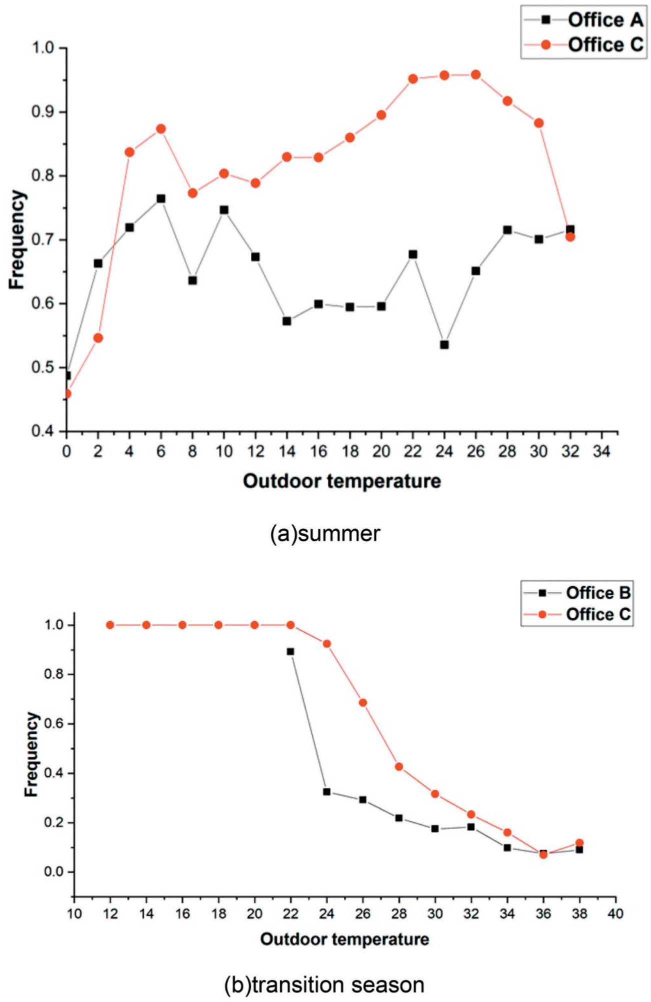

Fig. 10. Temperature distribution of the opening rate.

recording. The relevant test instruments were arranged approximately 0.75 m above the ground. The specific arrangement of measuring points is shown in Fig. 4.

The data collection time of test object A was from January 2018 to June 2018. Due to the indoor decoration in summer of 2018, no data was collected in summer. The data for test object B was collected during the summers of 2016 and 2018.The data collection time of test object C is the whole year of 2018.The data collection is shown in Table 2.

4. Results and analysis

4.1. Data analysis

The dataset was analyzed from four perspective: schedule, environment parameter, On-off statuses of windows and windows operating actions.

A. Working schedule

According to the questionnaire results, we selected five graduate students in office A, two members in office B, and six practitioners of the construction industry in office C as the research objects. They expressed positive control of windows in the questionnaire. Based on the measured data, a frequency chart according to their presence in the room at each moment was created, as shown in Fig. 5. The occupants in office A had a relatively random working schedule with no clear regularity. This is because office A is located in a studio in a university, and the working schedule of the staff is relatively random. Owing to the different properties of work, the two members in office B had different work and rest times in the room. The graduate students (person 2 in office B) had a clear lunch and dinner break, but left at relatively random times at night. Practitioners in the construction industry (person 1 in office B) had fixed arrival times at the office but random departure times. The work and rest schedules of employees in office C showed clear regularity. This is because office C is located in a commercial company and has a clear work and rest schedule; work starts at 8:30 and ends at 17:30. Except for some accidental factors, the working schedule is relatively fixed.

B. Environmental parameter

The outdoor temperature distribution of the three offices in different seasons is shown in Fig. 6. It can be detected that the outdoor temperature in transition season has a wider range, which changes from −2 °C to over 30 °C. Two relative peaks can be distinguished from the data (one at around 6 °C and the other at around 26 °C). The outdoor temperature in summer followed a totally different trend. The temperature range is more concentrated, and only one peak can be detected.

The Indoor CO_2 distribution is shown in Fig. 7. It can be detected that the range of CO_2 concentration in Office B is larger than the other two, and the high concentration (larger than 800 ppm) accounts for a relatively large amount. The CO_2 concentration of Office A and Office C is mainly concentrated between 300 and 500 ppm.

C. On-off statuses of windows

In this study, the opening rate was used to evaluate the on-off statuses of windows. The window opening rate is calculated using Eq. (1):

$$\text{Window opening rate} = \frac{\text{Time of windows remaining open}}{\text{Total time for data collection}} \tag{1}$$

The window opening time of the three offices during the period of measurement was statistically analyzed, and the results were distinguished among different seasons, as shown in Table 3. From the comparison of the window opening rate between the transition season and the summer, it can be found that the window opening rate in the transition season was generally higher than that in the summer. The opening rate of office A in the transition season was approximately 3 times greater than that of office B in the summer. Meanwhile, for office C, the window opening rate in the transition season was nearly 1.5 times greater than that in the summer.

D. Window opening or closing actions

The average daily number of windows opening and closing actions of three offices in different seasons are counted in Table 4. It can be found that the window adjustment frequency of office C was lower than that of office A and Office B, which also proved that the window adjustment frequency of office C was lower than that of office A and B.

4.2. Correlation analysis

Correlation analysis between window state/ window switch action, working schedule and environmental parameters were conducted from subjective (questionnaire) and objective (measured data) perspectives.

4.2.1. Subjective analysis

In the questionnaire survey, the office staff provided reasons for the window opening and closing actions, and the main trigger reasons were identified, as shown in Fig. 8.

As shown in Fig. 8, the trigger reasons for the window operating behavior of office workers in the different open-plan offices were significantly different. The main causes of window operating behavior in office A was the indoor air quality (accounting for 46% of the trigger causes of window opening behavior) and outdoor environment (accounting for 29% of the trigger causes of window closing behavior), and those in office B were schedules (accounting for 36% of the trigger causes of window opening behavior and 20% for window closing behavior), indoor air quality (accounting for 27% of the trigger causes of window opening behavior), and equipment factors (accounting for 25% of the trigger

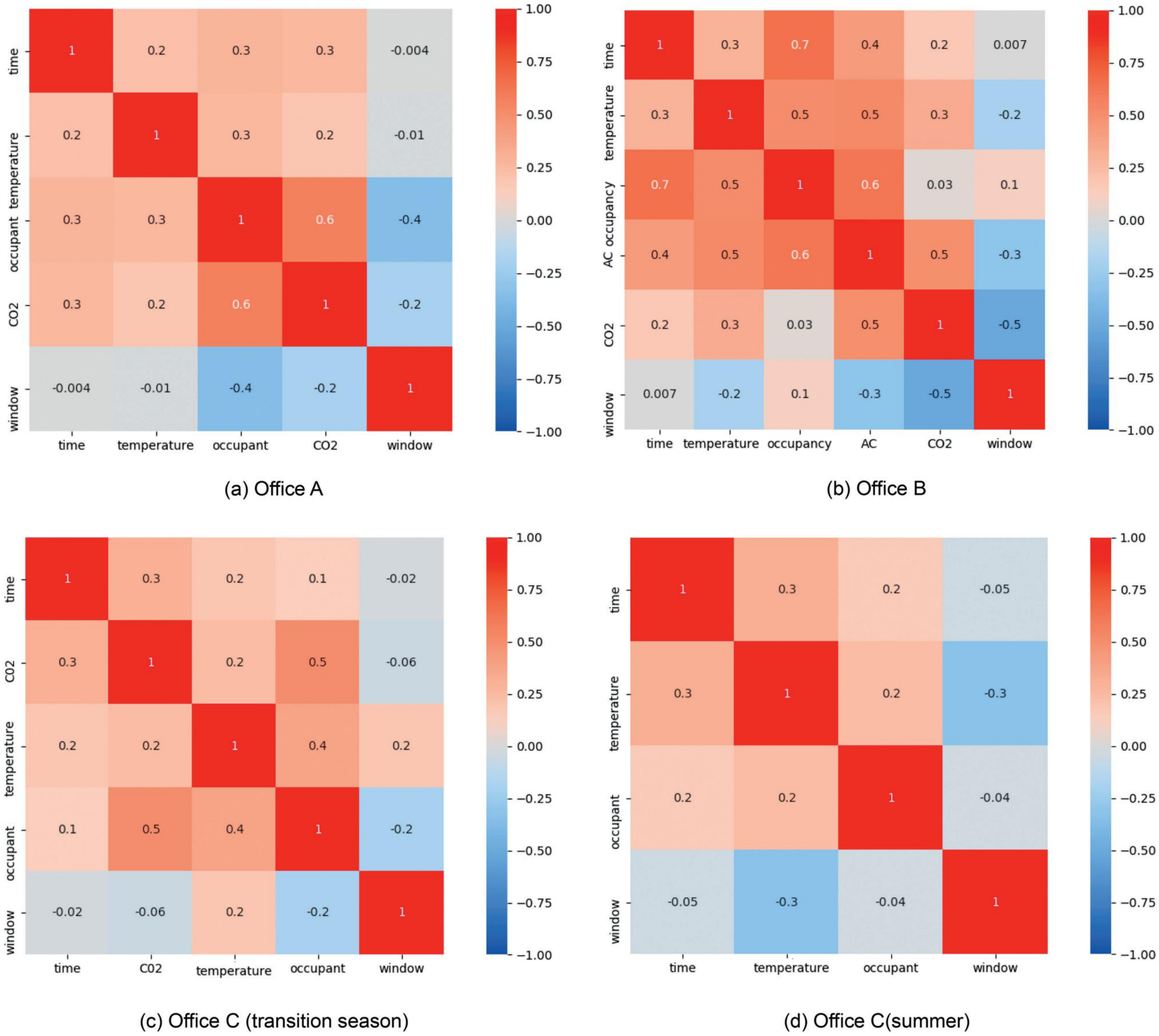

Fig. 11. Window state correlation.

causes of window opening behavior). Therefore, in offices A and B, window operating behavior was more sensitive to environmental elements. This is mainly because office A and office B are located on a campus and in a residential area, respectively, the adjustable area of windows is larger, and split air conditioners are adopted. Therefore, the occupants' window operating behavior was more flexible. Compared with those of offices A and B, the occupants' window operating behavior in office C demonstrated clearer conformity. The questionnaire results showed that many people in office C chose to ignore the windows and let others take care of them (accounting for 29% of the trigger causes of window opening behavior and 28% of the trigger causes of window closing behavior). This is because office C is located in a commercial area with a large number of occupants, the windows can only be opened to a small degree, and the central AC system is used for AC (only the office entrance is provided with a partition switch), so the flexibility of window control behavior is poor.

According to Fig. 8, although there were some differences in the trigger causes of window operating behavior in different offices, the window operating behavior in the three open-plan offices also had common characteristics. Specifically, the window opening action was mainly triggered by (1) environmental factors, namely opening the window when the indoor air smells bad or feels stuffy (36.5%) or when feeling hot (11.5%); (2) schedule factors, namely opening the window upon entering the office (19.2%); and (3) equipment factors, namely opening the window when turning off the AC (9.6%). The trigger causes of window closing action mainly included (1) environmental factors, namely shutting off the AC when it is noisy outside (15.7%) or when the outdoor environment is rainy (20.0%); (2) schedule factors, namely shutting off the AC when people leave the office (18.6%); and (3) equipment factors, namely closing the window when turning on the AC (21.4%). Therefore, the main trigger factors affecting the window operating behavior of the three offices can be summarized as environmental factors, schedule factors, and equipment factors.

4.2.2. Objective analysis

A. On-off statuses of windows

The distribution of the window on-off statuses in the three offices under different times of day and under different outdoor temperatures were further analyzed, as shown in Figs. 9 and 10. As shown in Fig. 9, in terms of the time distribution, the window opening rate of office B was always relatively low, but the window opening rate increased significantly around 9:00. This was mainly because when the staff arrived at

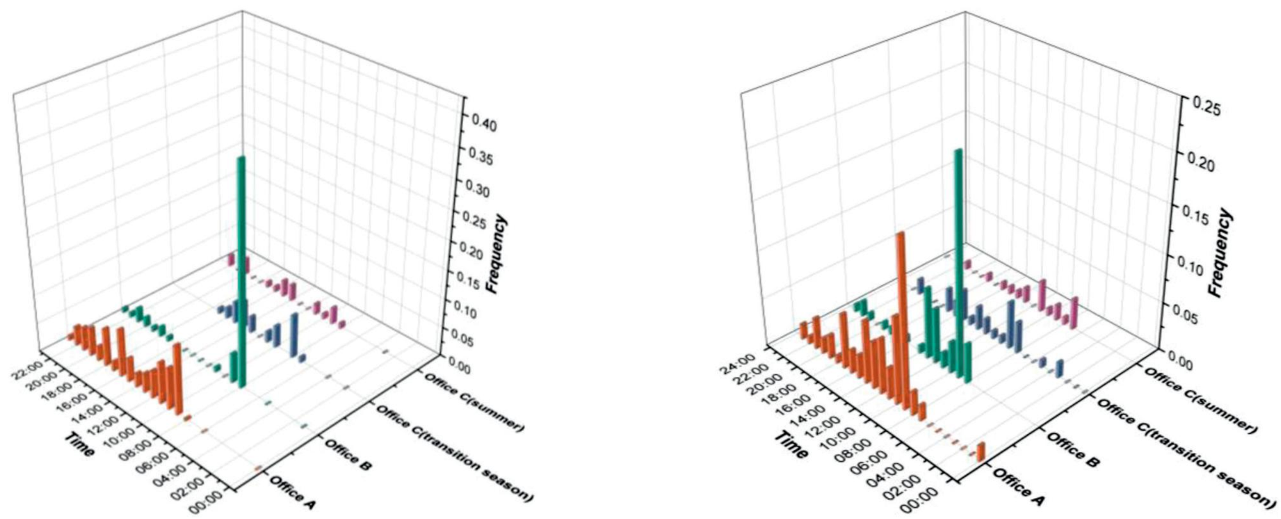

(a) Time distribution of window opening action

(b) Time distribution of window closing action

Fig. 12. Time distribution of window opening and closing actions.

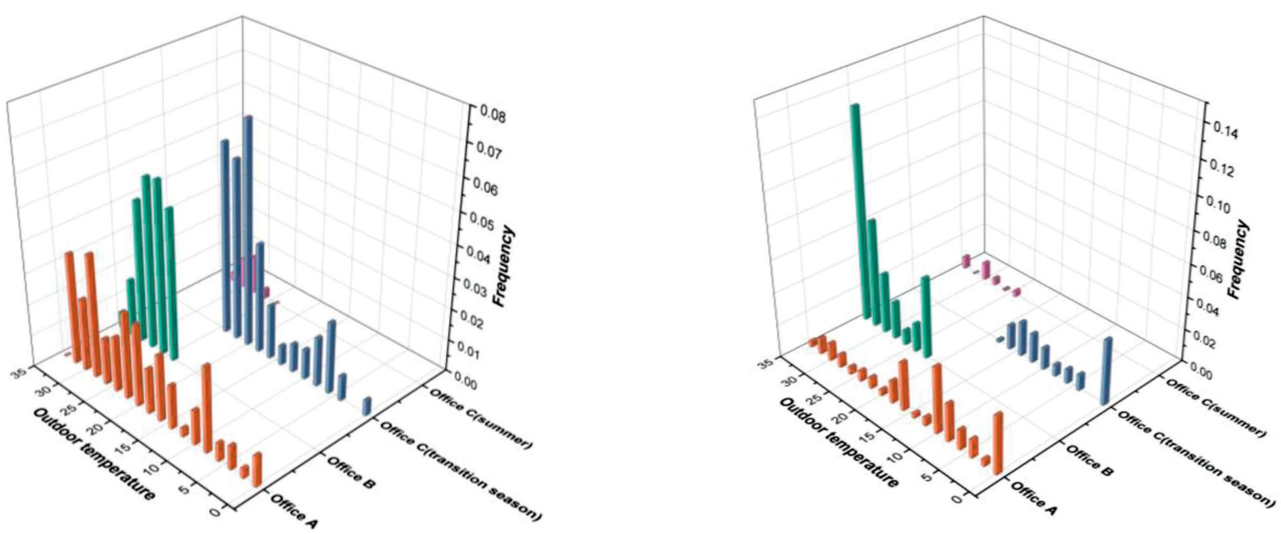

(a) Temperature distribution of the window opening action

(b) temperature distribution of the window closing action

Fig. 13. Temperature distribution of window opening and closing actions.

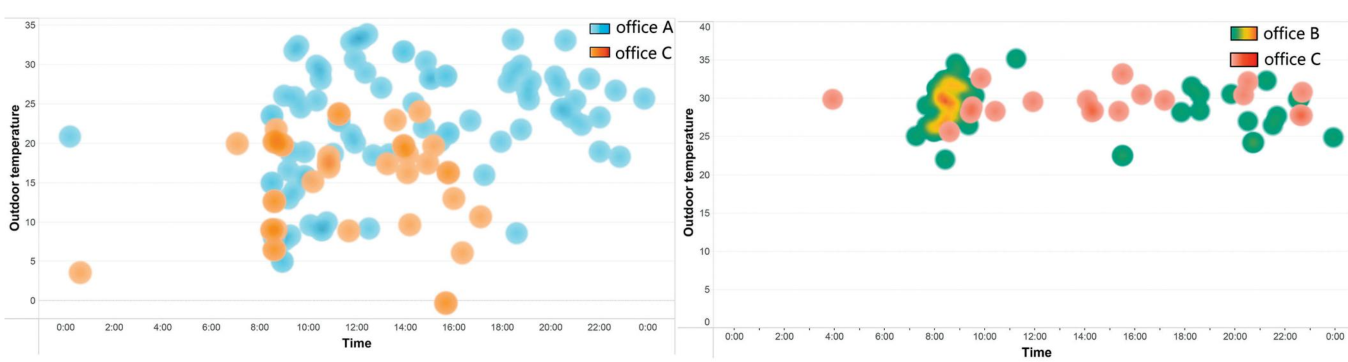

(a)transition season

(b)summer

Fig. 14. Coupling analysis of window opening time and outdoor temperature.

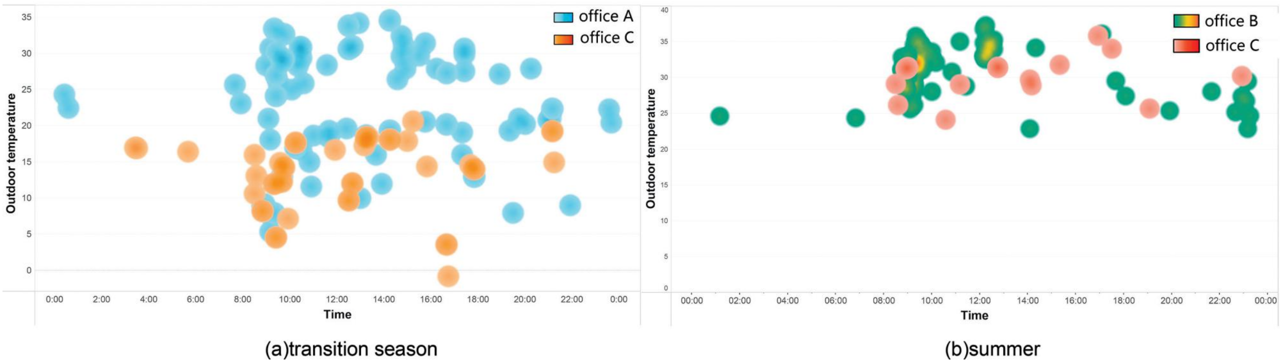

Fig. 15. Coupling analysis of window closing time and outdoor temperature.

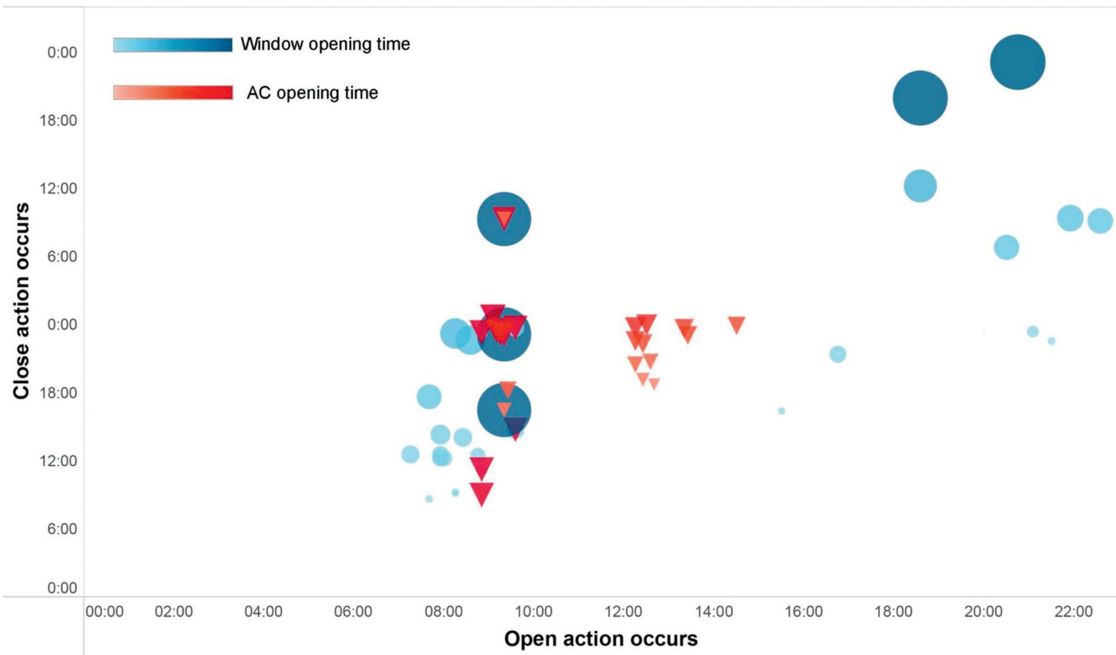

Fig. 16. Interaction of the operating actions of windows and air conditioners (Office B).

the office around 9:00, they opened the window for ventilation. However, there was no significant change in the opening rate at offices A and C during the day either during the summer or during the transition season. According to Fig. 10(a), the window open state of office A and office C did not reflect the temperature sensitivity within the temperature range of the transition season. According to Fig. 10(b), within the outdoor temperature distribution range in summer, the temperature had little influence on the window opening rate at temperatures lower than 22 °C. With the further increase in outdoor temperature, the window opening rates of office B and office C decreased with the increase in temperature. This is because in the summer, when the temperature surpasses 30 °C, people preferred to use AC to cool the indoor temperature. People tended to close the window when the AC was turned on.

Spearman Correlation Coefficient [28] was applied to analyze the correlation between window status and other parameters. Spearman Correlation Coefficient is a kind of rank correlation coefficient. It can be understood that the achievement is a sort or order, then it is solved according to the sort position of the original data. No matter how the data of the two variables change and what kind of distribution they conform to, we only care about the order in which each value is arranged in the variable. If the corresponding values of the two variables are in the same or similar order in each group, they have a significant correlation. The correlation between window status and other parameters is shown in Fig. 11. As Fig. 11(a) shows, there is a strong correlation between the window on-off statuses of Office A and the presence of people in the room, and the correlation with time and temperature is not obvious. In office B, there is a strong negative correlation between the window status and indoor CO_2, and the effect of AC on the window status is second. This shows that Office B is more sensitive to the indoor environment. Office C has no obvious sensitive factors in the transition season, but in summer it is more sensitive to outdoor temperature.

B. Switch actions

The time and outdoor temperature when the window state change occurred were analyzed. This analysis based on the action only focused on the temperature and time parameters at the time of the window state change. The data analysis and test time had the same time step of 5 min. The analysis results are shown in Figs. 12 and 13.

According to Fig. 12, occupants in office A frequently opened and closed the windows in the transition season. From the perspective of time distribution, office A was more likely to open the windows around 9:00. Over time, the trend decreased. According to the statistical results of window operating action in office B in summer, there was clear clustering at the time of window opening and closing in the summer. The summer window operating behavior was more likely to occur between 8:00 and 10:00, which was the time when the staff arrived at the of-

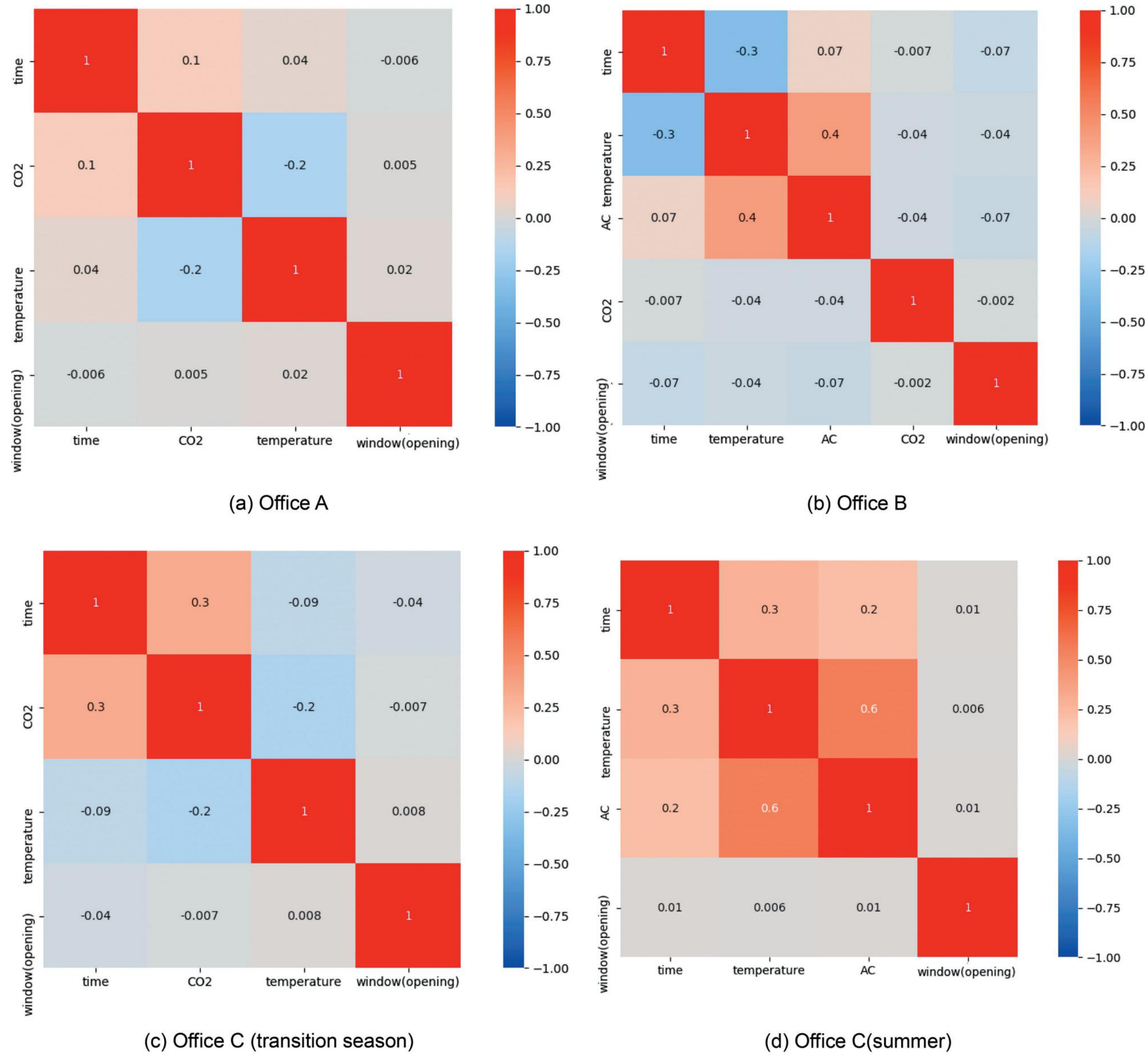

Fig. 17. Window opening action correlation.

fice. However, regardless of the season, the number of window opening actions in office C was significantly lower than that in offices A and B. Office C in the transition seasons and summer had a higher opening rate, as shown in Table 2, which reveals that occupants in office C rarely adjusted the windows after opening them, except in extreme weather situations (such as rain), which led to a low frequency of window operating behavior.

As shown in Fig. 13, during the transition season, the distribution of window operating actions in office A under different outdoor temperatures was relatively average, with little regularity with the variation in outdoor temperature. This was consistent with the previous analysis of the window opening rate. According to the statistical results of office B and office C's window operating actions in summer, the window operating actions in summer also had clear convergence with the temperature distribution. In summer, the window opening action was more likely to occur at temperatures below 30 °C, and mostly within 24–28 °C; in addition, the window closing actions were concentrated at 30 °C and above. Meanwhile, the window adjustment frequency of office C was lower than that of offices A and B.

Through the above analysis and discussion, it can be concluded that the window operating behavior has clustering characteristics of time periods and temperature periods. We conducted a coupling analysis on the outdoor temperature and time of day when the window operating behavior occurred.

Fig. 14 shows the coupling analysis of time and outdoor temperature when the window opening action occurred in the three offices. According to the analysis of the transition season in Fig. 14(a), the coupling effect of outdoor temperature and time on window opening actions in office A had no clear trend. It was only concentrated in the time range of 8:00 to 9:00, but the outdoor temperature distribution was very scattered when the opening action occurred. This is because the acceptable degree of the transition season for the office is high; therefore, there is no fixed temperature range for occupants to open windows for ventilation. The window opening action of office B in summer had clear distribution characteristics. As shown in Fig. 14(b), window opening actions occurred very frequently in the range of 7:30–9:30, and there was an outdoor temperature range of concentrated window opening actions of 26–33 °C. The coupling of these two factors made the number

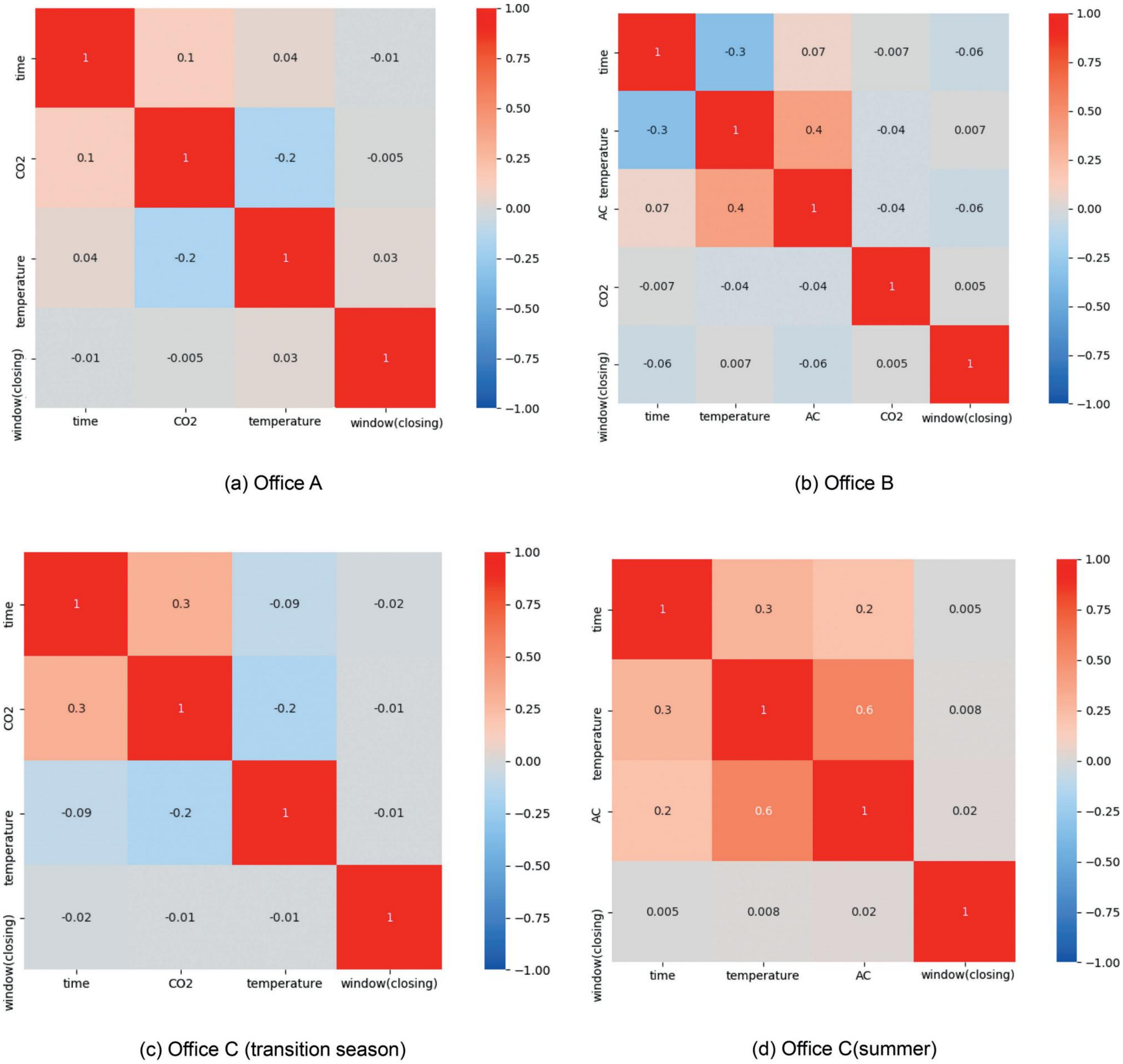

Fig. 18. Window closing action correlation.

of window openings in these time and temperature ranges much higher than those in the other temperature and time intervals. Fig. 14 shows that regardless of season, the window opening behavior of office C had no clear trends in the temperature and time coupling.

Fig. 15 shows the coupling analysis of time and outdoor temperature when the window closing action occurred. Fig. 15(a) shows that for the characteristics of window closing behavior in the transition season, in office A, the coupling effect of outdoor temperature and time on the window closing behavior had no clear trend, which was only concentrated in the range of 8:00–9:00, but the outdoor temperature distribution was very scattered when the action occurred. According to Fig. 15(b), in office B, when the temperature exceeded 30 °C, the window closing action occurred at 9:00 and 12:30. From the above analysis results, it is clear that for office B, the time of day and outdoor temperature had a significant coupling effect on the window regulation behavior in summer. The window closing action of office C also had no clear trends in the coupling of temperature and time regardless of the season.

In addition to environmental factors and schedule factors, it was found from the measured data of office B that equipment factors cannot be neglected. Fig. 16 shows the coupling relationship analysis of the switching action of windows and air conditioners in office B. Each bubble in the figure represents a group of window switching actions. As shown in Fig. 16, at 24:00, the windows and air conditioners were closed and turned off when there were no occupants in the office; therefore, there was an aggregation of closing actions at this time point. In addition, during working hours, the window closing action was mainly concentrated around the two time points of 9:00 and 12:30, and the time when the AC was turned on in summer was also concentrated at these two time points. Therefore, the summer window regulation behavior is clearly affected by equipment factors.

According to Fig. 14–16, the window operating behavior in office B reflects the significant correlation between temperature, time, and equipment, which reveals that the trigger conditions should not be ignored during the simulation of occupants' window operating behaviors.

Spearman Correlation Coefficient was also used to evaluate the correlation between the window switch action and other parameters, as shown in Fig. 17,18. However, limited by the number of measured switch actions, no obvious correlation can be found from statistical analysis.

5. Conclusion

In this study, the window operating behaviors in three different types of open-plan offices in Nanjing, China were presented and compared through subjective and objective analysis. The preliminary results show that influenced by the personnel composition, type of air conditioner and adjustable degree of windows, the window operating behaviors of different office buildings have larger discrepancies than that in the same building. In addition, the window operating behavior in different offices also share some common trends, like clear seasonal differences and coupling influence of schedule, environment and equipment. Besides, some results were inconsistent between the subjective analysis and the objective analysis, like the influence of CO_2. As this phenomenon is common in the investigation and analysis of the three offices, it reveals the need for more in-depth research to reveal the reason behind. The discovered conclusion is currently limited to the studied offices and their specific cultural area, and more cases are needed to reveal the common features. Future studies will be carried out to reflect the influence of offices' characteristics and season changes on window operating behavior. By applying deeper data driven technologies, new window operating behavior model will be developed.

Conflicts of interest

We declare that we have no financial and personal relationships with other people or organizations that can inappropriately influence our work, there is no professional or other personal interest of any nature or kind in any product, service or company that could be construed as influencing the position presented in, or the review of, the manuscript entitled, "Comparative Analysis of Window Operating Behavior in Three Different Open-Plan Offices in Nanjing".

Acknowledgment

This work was supported by the National Natural Science Foundation (51708105).

References

[1] L. Perez-Lombard, J. Ortiz, C. Pout, A review on buildings energy consumption information, Energy Build. 40 (3) (2008) 394–398.
[2] H. Yoshino, T. Hong, N. Nord, IEA EBC Annex 53: total energy use in buildings—analysis and evaluation methods, Energy Build. 152 (2017) 124–136.
[3] D. Yan, T. Hong, B. Dong, et al., IEA EBC Annex 66: definition and Simulation of occupant behavior in buildings, Energy Build. 156 (2017) 258–270.
[4] T. Hong, D. Yan, S. D'Oca, C. Chen, Ten questions concerning occupant behavior in buildings: the big picture, Build. Environ. 114 (2017) 518–530.
[5] S. D'OCa, T. Hong, J. Langevin, The Human Dimensions of Energy Use in Buildings: a Review, Renew. Sustain. Energy Rev. 81 (2018) 731–742.
[6] H.K. Abdullah, H.Z. Alibaba, Window design of naturally ventilated offices in the mediterranean climate in terms of CO_2 and thermal comfort performance, Sustainability 12 (2) (2020) 473.
[7] T. Nagai, Window and HVAC operation to reduce cooling requirement by means of cross-ventilation, Int. J. Vent. 5 (1) (2006) 151–162.
[8] W. Parys, D. Saelens, H. Hens, Coupling of dynamic building simulation with stochastic modelling of occupant behaviour in offices e a review-based integrated methodology, J. Build. Perform. Simul. 4 (2011) 339–358.
[9] H. Gunay, W. O'Brien, I. Beausoleil-Morrison, A critical review of observation studies, modeling, and simulation of adaptive occupant behavior in offices, Build. Environ. 70 (2013) 31–47.
[10] C. Sun, R. Zhang, S. Sharples, et al., A longitudinal study of summertime occupant behaviour and thermal comfort in office buildings in northern China, Build. Environ. 143 (2018) 404–420.
[11] K. Schakib-Ekbatan, F.Z. Cakici, M. Schweiker, A. Wagner, Does the occupant behavior match the energy concept of the building?–Analysis of a German naturally ventilated office building, Build. Environ. 84 (2015) 142–150.
[12] S. D'Oca, T. Hong, A data-mining approach to discover patterns of window opening and closing behavior in offices, Build. Environ. 82 (2014) 726–739.
[13] H.B. Rijal, P. Tuohy, M.A. Humphreys, J.F. Nicol, A. Samuel, J. Clarke, Using results from field surveys to predict the effect of open windows on thermal comfort and energy use in buildings, Energy Build. 39 (2007) 823–836.
[14] S. Herkel, U. Knapp, J. Pfafferott, Towards a model of user behaviour regarding the manual control of window in office buildings, Build. Environ. 43 (4) (2008) 588–600.
[15] S. Shi, H. Li, X. Ding, X. Gao, Effects of household features on residential window opening behaviors: a multilevel logistic regression study, Build. Environ. 170 (2020) 106610.
[16] S. Wei, R. Buswell, D. Loveday, Factors affecting end-of-day' window position in a non-air-conditioned office building, Energy Build. 62 (2013) 87–96.
[17] Y. Zhang, P. Barrett, Factors influencing the occupants' window opening behaviour in a naturally ventilated office building, Build. Environ. 50 (2012) 125–134.
[18] X.Y. Zhong, La Ridley, Verification of behavioural models of window opening: the accuracy of window-use pattern, indoor temperature and indoor PM2.5 concentration prediction, Build. Simul. 13 (2020) 527–542.
[19] X. Zhou, T. Liu, D. Yan, X. Shi, X. Jin, An action-based Markov chain modeling approach for predicting the window operating behavior in office spaces, Build. Simul. (2020), doi:10.1007/s12273-020-0615-4.
[20] J. Park, B. Jeong, Y. Chae, J. Jeong, Machine learning algorithms for predicting occupants' behaviour in the manual control of windows for cross-ventilation in homes, Indoor Built Environ. (2020), doi:10.1177/1420326X20927070.
[21] J. Rouleau, L. Gosselin, Probabilistic window opening model considering occupant behavior diversity: a data-driven case study of Canadian residential buildings, Energy 195 (2020) 116981.
[22] J. Li, K. Panchabikesan, Z. Yu, F. Haghighat, M.E. Mankibi, G. Zhang, Analysis on the driving factors and patterns of window opening and closing behaviour in French households, in: Proceedings of the IOP Conference Series: Materials Science and Engineering, 609, 2019.
[23] W. Chen, Y. Ding, L. Bai, Y. Sun, Research on occupants' window opening behavior in residential buildings based on the survival model, Sustain. Cities Soc. 60 (2020) 102217.
[24] P.F. Pereira, N.M.M. Ramos, M.L. Simoes, Data-driven occupant actions prediction to achieve an intelligent building, Build. Res. Inf. 48 (2020) 485–500.
[25] C. Sun, R. Zhang, S. Sharplesc, Y. Han, H. Zhang, Thermal comfort, occupant control behaviour and performance gap–A study of office buildings in north-east China using data mining, Build. Environ. 149 (2019) 305–321.
[26] Y. Wei, H. Yu, S. Pan, L. Xia, J. Xie, X. Wang, J. Wu, W. Zhang, Q. Li, Comparison of different window behavior modeling approaches during transition season in Beijing, China, Build. Environ. 157 (2019) 1–15.
[27] X. Zhou, T. Liu, X. Shi, X. Jin, Case study of window operating behavior patterns in an open-plan office in summer, Energy Build. 165 (2018) 15–24.
[28] P.F. Pereira, N.M.M. Ramos, Occupant behaviour motivations in the residential context–An investigation of variation patterns and seasonality effect, Build. Environ. 148 (2019) 535–546.

Energy and Built Environment 2 (2021) 188–203

Contents lists available at ScienceDirect

Energy and Built Environment

journal homepage: http://www.keaipublishing.com/en/journals/energy-and-built-environment/

Numerical simulations on atmospheric stability conditions and urban airflow at five climate zones in China

Guoxing Chen, Li Rong*, Guoqiang Zhang

Department of Engineering, Aarhus University, Inge Lehmanns Gade 10, DK-8000 Aarhus C, Denmark

ARTICLE INFO

Keywords:
Urban airflow
Solar-induced thermal boundary conditions
Atmospheric stability
CitySim
CFD

ABSTRACT

Due to the quick development of urbanization, it is important to provide a healthy urban environment for the dweller. Previous studies have obtained valuable conclusions of how to improve the urban airflow distribution under isothermal conditions. How to adopt and interpret those conclusions when considering the solar-induced atmospheric stability conditions have not been clarified yet. In this study, the characteristics of atmospheric stability condition and influence of diurnal varying solar-induced thermal effect on urban airflow inside the idealized building arrays were investigated at five cities located at five climate zones in China. Urban energy model, CitySim, was employed to simulate the annual distribution of solar-induced walls' temperatures inside the idealized building arrays. The diurnal varying wall temperatures at the hottest days were set as thermal boundary conditions in computational fluid dynamic (CFD) simulations. With albedo value of 0.5, the possibility of adopting the results from isothermal condition directly ranged from 7% to 11% for the five cities in China throughout the year. The unstable condition ocuppied from 19% to 24% annually and the stable condition of more than 40% annually was observed. Under the diurnal varying solar-induced thermal effect, the spatially-averaged air speeds and airflow patterns were significantly different from the isothermal conditions. The percent of Richardson number under different atmospheric stability conditions annually based on the Citysim simulation results indicated that the atmospheric stability was most likely determined by the local climate characteristics and albedo value rather than the building layouts at the five selected cities in China, but this should be further investigated when the shadow effects of surrounding buildings were considered in simulations.

1. Introduction

Rapid urbanization has altered the local climate greatly comparing to the rural area. Urban Heat Island effect has brought more attention in recent decades especially with more frequent attacks of heat waves in summers. How to maintain the proper thermal comfort and outdoor air quality is remained as challenges.

Many of the previous studies investigated the urban airflow parametrically under isothermal conditions [1–11] in the spatial scale of neighbourhood (<1 km) and street (<0.1 km). These parameters included urban length, building height variations and layouts, frontal area ratios (ratio of building frontal area to ground surface area, λ_f) and plan area ratios (ratio of building roof to ground surface area, λ_p). However, it was observed that the solar-induced buoyancy force could also influence the flow regime within urban built environment, especially when the wind speed was relatively low. The results of a field experimental study in summer at Nantes [12] showed that the maximum building surfaces' temperature in the afternoon exceeded 50 °C and the uneven temperature distributions on different walls induced strong buoyancy force affecting the airflow distribution in the studied building area. Some wind tunnel studies designed scenarios with the heated leeward-wall, heated windward-wall, heated ground and heated all walls to mimic the atmospheric stable/unstable conditions and to investigate the effects of buoyancy force induced by solar radiation on airflow patterns [13–20]. Some researchers [21–33] adopted CFD modelling to simulate the airflow patterns and quantify the spatially-averaged flow properties by adopting the thermal boundary condition on a single wall or uniform thermal boundary conditions (e.g. constant heat flux). The results from these studies under non-isothermal conditions revealed that the airflow patterns and spatially-averaged flow properties were very different comparing to those obtained from the isothermal conditions where Richardson number was 0.0.

The simplified hypotheses of single wall and all walls heated by solar radiation uniformly might not represent the complex solar-induced wall thermal conditions to study the urban airflow under non-isothermal conditions. Some simulation tools, such as ENVI-met [34] and MITRAS [35], were employed to investigate the airflow distribution under solar-induced diurnal varying weather conditions. However, the numerical models were simplified and spatial resolution was relatively low be-

* Corresponding author.
E-mail address: li.rong@eng.au.dk (L. Rong).

https://doi.org/10.1016/j.enbenv.2020.07.006
Received 3 March 2020; Received in revised form 16 July 2020; Accepted 21 July 2020
Available online 1 August 2020

cause of several phenomena solved simultaneously in these tools. Urban energy model (UEM), such as Temperatures of Urban Facets in 3-D (TUF3D) [36], Indoor-Outdoor Urban Energy Balance Simulator (TUF-IOBES) [37], and CitySim [38], etc. could model the diurnal varying solar radiation to predict the diurnal varying thermal boundary conditions on urban surfaces with one hour interval. By coupling UEM and CFD, studies confirmed that the unstable atmospheric conditions induced by solar radiation altering the airflow patterns and spatially-averaged flow properties significantly with respect to isothermal conditions [39–43]. Our previous study also indicated that the airflow distribution under 'ideal' hypothesis of all uniformly heated walls and the 'realistic' solar-induced wall thermal conditions inside 3-D building array differed significantly especially under low wind speed conditions [44].

The atmospheric stability condition inside the urban built environment (which is a similar concept borrowed from meteorology by analysing the Richardson number) varies with the weather conditions (wind conditions, solar radiation angles etc.) seasonally and diurnally as well. Therefore, CFD simulation of urban airflow under non-isothermal conditions which was closer to the real situations should be conducted by taking the diurnal variation of atmospheric stability condition into consideration while detailed CFD simulations conducted seasonally was not applicable yet due to the limitation of computer capacity. Kwak et al. [45], Liu et al. [39] and Dong et al. [46] investigated the airflow inside an isolated street canyon under predefined diurnally varying unstable atmospheric conditions with the climates of Soul, Harbin and Beijing respectively. The reported resluts obtained from these studies with an isolated canyon provided valuable knowledge on microclimate within the canyon under unstable atmospheric conditions and further confirmed the significance of considering the three-dimensional surface heating boundaries in order to evaluate the urban microclimate. However, in reality such an isolated canyon is mostly unlikely. Yaghoobian et al. [47] studied the airflow, temperature and pressure distribution as well as turbulent transport by using a geometry model of 3 x 5 building array under diurally varying atmospheric conditions in two summer days at Arizona. Following the similar set-ups used by Yaghoobian et al. [47], Nazarian et al. [42,43] analyzed the airflow and thermal distribution as well as pollutant dispersion under diurally varying atmospheric conditions based on horizontal and vertical Richardson numbers. These results provided detailed information of environmental parameters distributio and turbulent transport, but the information of spatially-averaged flow properties were not analyzed, which are also meaningful in evaluation of the urban microclimate during the urban design and planning.

Studies conducted under isothermal/non-isothermal conditions could provide valuable suggestions to improve the airflow distribution in urban area, but a more practical knowledge cannot be achieved without considering the atmospheric (airflow within the urban zone) stability condition, especially with diversified climate zones in China. It is significant to provide the characteristics of atmospheric stability condition as a guideline to adopt and interpret the valuable results obtained under isothermal conditions properly and identify how the diurnally varying atmospheric conditions affect the urban airflow. By employing the weather data of a typical meteorological year and building codes of the selected five cities, locating at five climate zones in China, the main objectives were: (a) to identify the possibility that the isothermal conditions could represent the practical situations based on the annual Richardson numbers at five climate zones in China by using an idealized urban zone; (b) to analyse the differences of spatially-averaged flow property between diurnal varying non-isothermal conditions and isothermal conditions; (c) to compare the airflow patterns between diurnal varying non-isothermal conditions and isothermal conditions.

2. Methodologies

The commonly investigated generic neighbourhood-scale building arrays, square and staggered layouts with medium building density ($\lambda_f = \lambda_P = 0.25$), were adopted in this study, as shown in Fig. 1(a) and Fig. 1(b). The building width (*B*) and distance between buildings (*W*) equal to building height (*H*), ($B = W = H = 30$ m). In order to obtain reasonable solar radiation, the ground surface inside the building array was split into 10 m x 10 m patches, as each green patch shown in Fig. 1(a) and Fig. 1(b). The red planes in the middle of the arrays were selected for the investigation of airflow patterns in the vertical plane. The geometry model was built in the UEM software CitySim and the hourly wall temperatures were obtained from the annual simulation results based on the typical year weather data file. These wall temperatures were extracted for defining the thermal boundary conditions of CFD simulations at the corresponding hours.

2.1. CitySim setup

CitySim [38] is an urban energy model for modelling and optimizing the energy flux in urban area. The energy balance between indoor and outdoor is simulated by integrating radiation model, energy conversion model and stochastic behaviour model. The shortwave and longwave radiation are determined by simplified radiosity algorithm [48] and All-weather model [49]. The solar radiation and radiation exchange between neighbouring building walls, the ground surfaces and the environment can be computed with scales ranging from a small neighbourhood to an entire city. With the input meteorological data of the typical year, horizon characteristics (solar angle and topographical) and building codes, the heat flux through the walls are computed by electrical analogy methodology. Multiple iterations are performed with hourly time-step until the walls' temperatures reach convergence. In current CitySim version, the temperature stratification on each wall caused by surrounding buildings' shielding was not considered and the temperature on each wall was uniform at a specified hour. CitySim has been successfully verified against Building Energy Simulation Test method and field measurement of an EPFL (École polytechnique fédérale de Lausanne) campus building [50]. It uses convective heat transfer coefficients' correlations and it was reported that no large errors were introduced [51]. One-way coupling CitySim and CFD was successfully applied to study the influences of building configurations and walls' albedo values on local wind-thermal environment [52–54].

The meteorological data (the solar irradiance, the wind speed, direction and etc.) and horizon characteristics (solar angle and topographical) of the investigated cities for CitySim simulation were derived from Meteonorm [55]. The investigated cities were Guangzhou, Kunming, Shanghai, Beijing and Harbin, which are located in the climate zones of Hot Summer & Warm Winter, Temperate, Hot Summer & Cold Winter, Cold and Severe Cold respectively. The key building thermal parameters and opening properties of each investigated city were summarized in table 1, which were complied with Chinese Design Standards for energy efficiency of public buildings [56–58]. Besides, the infiltration was set as 1 h^{-1}, with space heating and cooling to maintain the indoor air temperature between 18 °C (16 °C for Guangzhou) and 26 °C. The openable faction of windows was 50% with the shading device of 50%. The recommended value for walls' albedo ranges from 0.25 to 0.85 based on walls' lightness [59]. With the consideration of diversity in wall colour, the albedo (α) of all building walls was set as 0.5 when the thermal boundary conditions were used for CFD simulations while three different albedo values (namely 0.3, 0.4 and 0.5) were used for analysis of atmospheric stability conditions by using annual Richardson number. The ground inside the building array was assumed as asphalt with albedo of 0.5.

2.2. CFD setup

Large Eddy Simulation (LES) and Reynolds-Averaged Navier-Stokes (RANS) [60] were the two main turbulence modelling methods used in urban physics. Santiago et al. validated the simulation results obtained from LES and RANS modelling by using field measurement data.

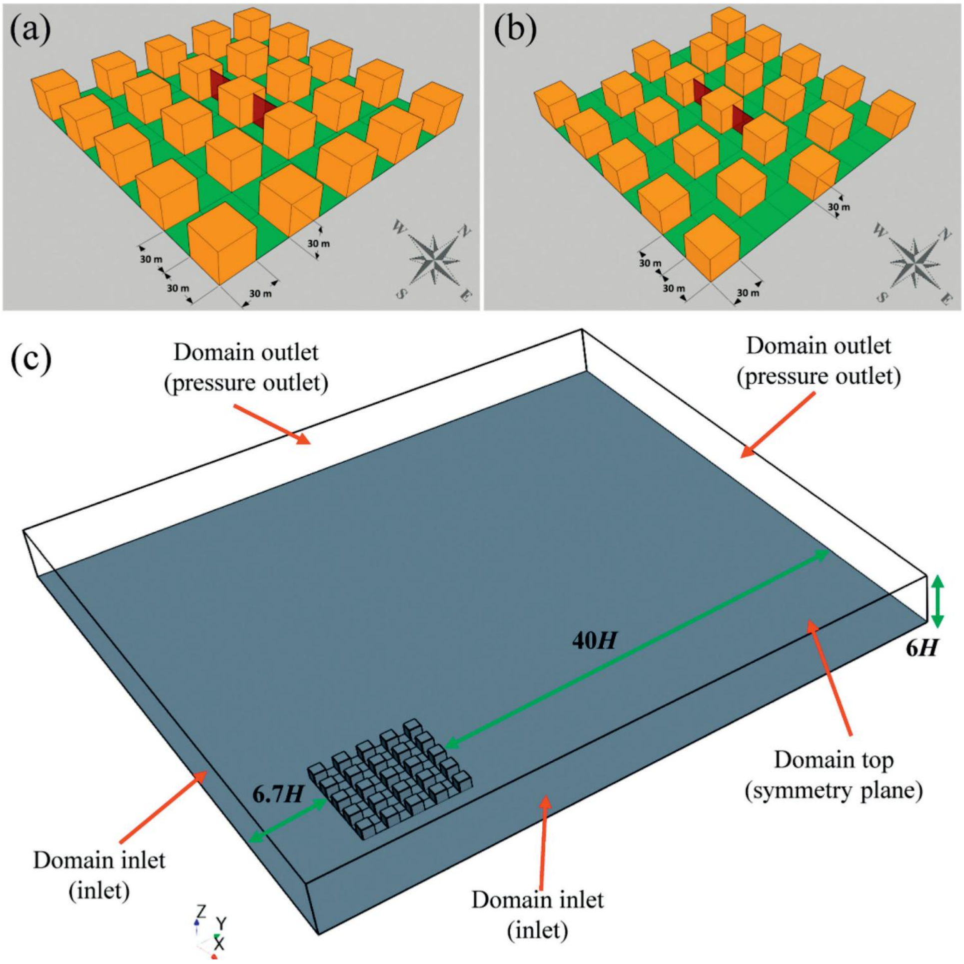

Fig. 1. Sketches of the investigated neighbourhood-scale building arrays in (a) square layout, (b) staggered layout and (c) sketch of the computational domain (in the case of wind coming from south-west).

Table 1
Building thermal parameters and glazing ratio of the investigated cities.

	Surfaces' U-value			Windows		Glazing ratio				
	Wall[W/(m²·K)]	Roof[W/(m²·K)]	Floor[W/(m²·K)]	U-value[W/(m²·K)]	G-value[-]	North[%]	East[%]	South[%]	West[%]	Roof[%]
Guangzhou	0.72	0.44	1.32	2.40	0.20	45%	30%	50%	30%	4%
Kunming	0.72	0.44	1.32	2.40	0.20	40%	35%	45%	35%	4%
Shanghai	0.54	0.39	0.46	2.30	0.32	35%	25%	50%	25%	4%
Beijing	0.46	0.39	0.46	1.77	0.37	30%	35%	50%	35%	4%
Harbin	0.35	0.25	0.25	1.76	0.68	25%	30%	45%	30%	4%

It showed that the difference of the simulation results of the spatially-averaged flow properties were negligible between the two modelling methods while the vertical mean velocity could be better predicted by LES [61]. Standard k-ε model showed the capability to reasonably predict the mean flows appropriately inside the idealized building array under both isothermal and non-isothermal conditions [1,3,24,40,62–65] and was therefore adopted in this study too.

2.2.1. Validation of the case under isothermal condition

The wind tunnel experiment conducted by Brown et al. [66] were widely adopted for CFD validation of airflow inside the idealized building array under neutrally stratified atmospheric boundary layer [1,3,8,67,68]. The building array consisted of 7-row (in stream-wise direction) and 11-column (in span-wise direction) cubic blocks. The cubic blocks' width (B), height (H) and distance between blocks (W) were the same ($B = W = H = 15$ cm, $\lambda_f = \lambda_p = 0.25$). The three velocity components were measured in the vertical central plane of the 3-D idealized building array (V1 to V6), as shown in Fig. A1 of Appendix A.

In CFD validation study, a full-scale building array was used with scale ratio of 200:1 ($B = W = H = 30$ m). As the building array was sufficiently wide in the span-wise direction, the external airflows beyond the lateral boundaries would hardly affect the airflow in the middle main street, it was acceptable to only consider the middle column to reduce computational source [62]. The distance between the building array and the inlet and outlet were 6.7H and 40H respectively in the computational domain, which were the same as previous validation studies [1,3]. The distance from the top surface of the building array to the computational domain top was 5H. The computational domain outlet was set as pressure outlet, and the domain lateral sides and top were set as symmetric boundary conditions. Three types of mesh resolutions were tested for grid sensitivity study: coarse mesh (700,356 cells), medium mesh (1893,956 cells), fine mesh (3032,751 cells). The mesh were generated by trimmed mesher with surface control. The base size was 5.0 m, the global surface growth rate were set as 1.05. The target surface sizes of ground, domain inlet and outlet were 2.0 m. the target surface sizes of domain sides and top were 10.0 m. Prism layer was employed at the ground and building walls with first layer height of 0.5 m and 0.1 m respectively. The target surface sizes of cubic blocks' surface in the coarse mesh, medium mesh and fine mesh were 2.0 m (*H*/15), 1.0 m (*H*/30) and 0.5 m (*H*/60) respectively.

2.2.2. Validation of the case under non-isothermal condition

Standard k-ε model with standard wall function were applied to predict the airflow under the unstable atmospheric conditions by neglecting the detailed heat transfer process near wall surfaces [1,40] and reasonable agreements between simulated and measured results were achieved. This study validated the standard k-ε model, standard wall function with Boussinesq model against another wind tunnel experiment conducted by Cui et al. [16], as shown in Fig. A2 of Appendix A. In the wind tunnel experiment, the thermal buoyancy force was induced by heating the ground between two cubic blocks to generate the temperature difference. The normalized velocity magnitude (U/U_{ref}, $U=\sqrt{\bar{u}^2+\bar{v}^2+\bar{w}^2}$) along the vertical central line in the street canyon under Richardson number (*Ri*) of 0.14 and 0.85 respectively were used for validation. The *Ri,* reflecting the ratio of buoyancy force to inertia force, was defined as:

$$Ri=\frac{g\beta H(T_w-T_{ref})}{U_{ref}^2} \tag{1}$$

where T_{ref} was the reference temperature, K; U_{ref} was the reference wind speed, m s^{-1}; T_w was temperature of walls, K; g was the gravity acceleration and was equal to 9.81, m s^{-2}; H was the building height, m; β was the thermal expansion rate of air and was equal to 0.0033, K^{-1}. For CFD simulated cases, the T_{ref} was taken as the air temperature at the inlet; U_{ref} was the reference wind speed of the inlet at the reference height of 10.0 m (the height of meteorological data measurement in Meteonorm). T_w was calculated by averaging the temperatures of all wall surfaces inside the idealized building arrays. Grid sensitivity studies were conducted. Three mesh resolutions were tested and they were 0.74, 1.03 and 2.09 million respectively for coarse, medium and fine mesh. The base sizes were 0.64, 0.32 and 0.16 m for the coarse, medium and fine mesh respectively. The control on according surfaces were normally determined based on the percent of the base size. For example, the surface sizes of the heated ground and houses were 2% of the base size, namely H/12.5, H/25 and H/50 for the three mesh resolutions respectively. There were also volume control before the low height building and after the higher building with 8% of the base sizes.

2.2.3. CFD simulation model for investigated cases

As the hottest days had rather high ambient air temperature and solar irradiation, the simulation cases were conducted by using steady-state meteorological data at 00:00, 04:00, 08:00, 12:00, 16:00, 20:00 and 24:00 ToD (time of day) on the hottest days of each investigated city without considering the dynamic process of solar radiation and wind conditions. The meteorological data of the investigated ToDs at the five cities were summarized in Appendix B. To study the effect of building layout, the hottest day in Guangzhou was chosen for the investigated scenarios. The building walls were considered as smooth surfaces and the grounds were modelled as rough surfaces. The thermal boundary conditions of the buildings' walls and grounds' surfaces were set as the wall temperatures on the hottest days obtained from CitySim. The thermal boundary condition of the ground outside the building array was set as the same as the incoming air temperature in order to avoid heating up by the approaching air [53]. The incoming air temperature and wind conditions were obtained from the meteorological data too.

The log-law time-average velocity profile [69] was adopted. The inlet vertical profile of velocity U(z), the turbulent kinetic energy k(z) and the turbulence dissipation ε(z) were expressed as Eqs. (2)–(4) respectively.

$$U(z)=\frac{u^*_{ABL}}{k}\ln\left(\frac{z+z_0}{z_0}\right) \tag{2}$$

$$k(z)=\frac{{u^*_{ABL}}^2}{\sqrt{C_\mu}} \tag{3}$$

$$\varepsilon(z)=\frac{{u^*_{ABL}}^3}{k_v(z+z_0)} \tag{4}$$

$$k_s=\frac{9.793z_0}{C_s} \tag{5}$$

where u^*_{ABL} was the atmospheric boundary layer friction velocity, m s^{-1}, C_μ is a constant (0.09), and k_v is von Karman's constant (0.41). The roughness length z_0 was set as 0.1 m which represented the airflow above open rural area with a regular cover of low crop. It was noticed that this value could not represent the urban area well but challenges occurred to generate the reasonable mesh resolution with a higher roughness length value due to the relationship between the roughness length and roughness height shown in Eq. (5). The roughness constant C_s was set as 4.0 following the suggested value by Hang and Li [68]. The reference wind speed (U_{ref}) at the reference height of 10.0 m was achieved from the weather data exported from Meteonorm software.

With parallel wind directions, the surface parallel to the inlet was set as pressure outlet, lateral sides and the top surface of the computational domain were set as symmetry boundary condition. The distances from the boundary of building array to the top surface, lateral sides, inlet and outlet of the computational domain were 5*H*, 5*H*, 6.7*H* and 40*H* respectively, which fulfilled the recommendation in the guideline for CFD Simulation in urban area [70]. With oblique wind directions, there were two outlets and two inlets of the computational domain along with the symmetry boundary condition on the top surface of the domain. The distances from the boundary of building array to the domain top, inlet and outlet of the computational domain were 5*H*, 6.7*H* and 40*H* respectively, seen in Fig. 1(c). The vertical profile of time-averaged velocity components at the two inlets were calculated by Eq. (6)–(8) respectively.

$$\bar{u}=U(z)\cos\theta \tag{6}$$

$$\bar{v}=U(z)\sin\theta \tag{7}$$

$$\bar{w}(z)=0 \tag{8}$$

STAR-CCM+ [71] was employed for CFD simulations in this study. The mesh resolution were similar to the medium mesh in grid sensitivity study of the validation cases and the grid number was around 10.3 million in the simulated cases with square and staggered layout building arrays. The wall *y+* was larger than 70.0 on the surfaces inside the building array and could reach 3000 at some area (it was noticed that the *y+* value larger than 500 could lead to uncertainties but it was difficult to meet all the requirement of mesh quality and the relationship between the roughness height and roughness length). The standard k-ε model was selected to solve the turbulent quantities and the energy conservation equation was activated to solve the temperature distributions. Also, the buoyancy force generated by the temperature difference was accounted by using Boussinesq's approximation. The segregated solver was used and the second-order upwind scheme was selected to discretise the convection terms of the partial differential equations. The under-relaxation factors for velocity, pressure, k-ε turbulence and k-ε turbulence viscosity were 0.7, 0.3, 0.5 and 0.5 respectively. The simulations were monitored by the values of residuals of continuity, turbulent dissipation rate, turbulent kinetic energy and energy as well as velocity magnitude at a few pre-defined points. The criteria of these residuals were 10^{-4} and the values of the monitored parameters at the pre-defined points changed little when the convergence of the simulations were considered to be reached.

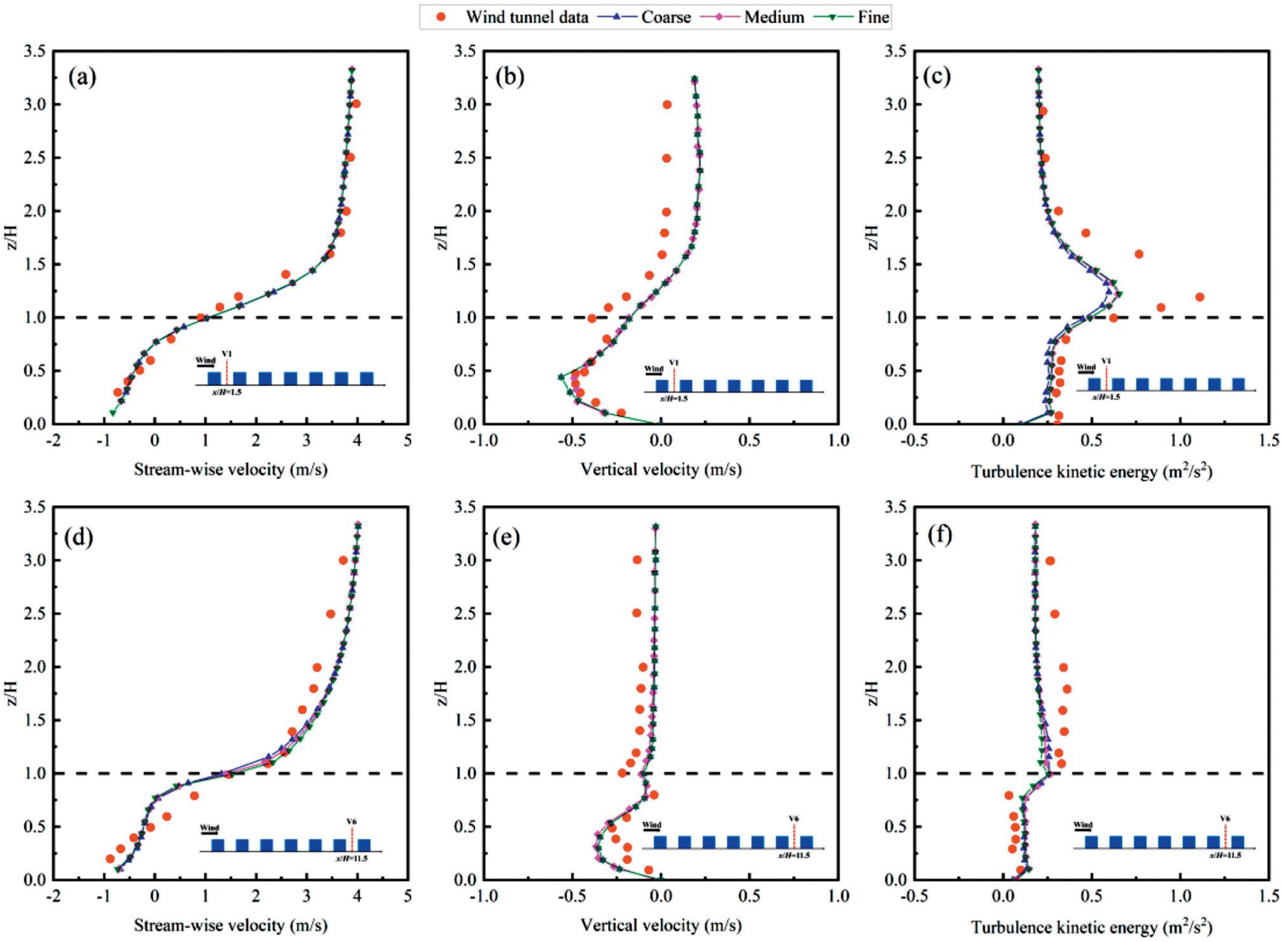

Fig. 2. Comparison of stream-wise velocity, vertical velocity and turbulent kinetic energy between CFD simulations and wind tunnel measurements at line of (a - c) $x/H = 1$ and (d - f) $x/H = 11.5$.

3. Results and discussions

3.1. Validation of CFD simulations

The vertical profiles of stream-wise velocity component, vertical velocity component and the turbulent kinetic energy at lines of $x/H = 1.5$ and $x/H = 11.5$ with three mesh resolutions were compared with experimental data, as shown in Fig. 2. Similar to previous validation studies [1,8,62,67,72] (not shown in Fig. 2 but referred to them), the vertical profiles of stream-wise velocity component obtained from CFD simulations were in reasonable agreements with experimental data. Even though the deviations in velocity vertical component and turbulent kinetic energy were relatively large from the measured values, their shapes were predicted properly, which were also reported in the previous validation studies [62] when standard k-ε model was used. Meanwhile, the simulated results under fine and medium mesh arrangement showed slightly differences.

In the validation against non-isothermal conditions, the vertical profiles of normalized velocity magnitude along the vertical centre-line of the street canyon were compared with experimental data, as presented in Fig. 3. The experimental data were extracted from the published literature by Cui et al. [16] and uncertainties of the extracted experimental data probably existed. The velocity profiles near the ground level under $Ri = 0.14$ and $Ri = 0.85$, and the velocity profile near the roof level with $Ri = 0.14$ obtained from CFD simulation were in reasonable agreements with experimental data. It was also seen that the CFD simulation slightly underestimated the normalized velocity magnitudes in the middle of the street canyon with $Ri = 0.85$.

Table 2
Atmospheric stability conditions catalogued by Richardson number.

Class	Range of Richardson number
Stable	$Ri \leq -0.134$
Slightly stable	$-0.134 < Ri \leq -0.053$
Neutral	$-0.053 < Ri \leq 0.1$
Slightly unstable	$0.1 < Ri \leq 0.37$
Unstable	$0.37 < Ri \leq 0.86$
Very unstable	$Ri > 0.86$

The above CFD validation results showed that the standard k-ε model could reproduce the vertical profiles of velocity magnitudes or stream-wise velocity component reasonably within the building array under both isothermal condition and non-isothermal conditions, was therefore adopted for further CFD simulations in this study.

3.2. Characteristics of atmospheric stability

The annual distributions of atmospheric stability of the five cities were analysed by using Richardson numbers defined in Eq. (1). The atmospheric stability could be catalogued into six classes based on the range of Richardson number [73], summarized in Table 2.

The annual distributions of atmospheric stability with albedo values α of 0.3, 0.4 and 0.5 respectively were shown in Fig. 4. Harbin had the highest percentage of unstable condition (higher percent of the time when the wall temperatures of the buildings were higher than the am-

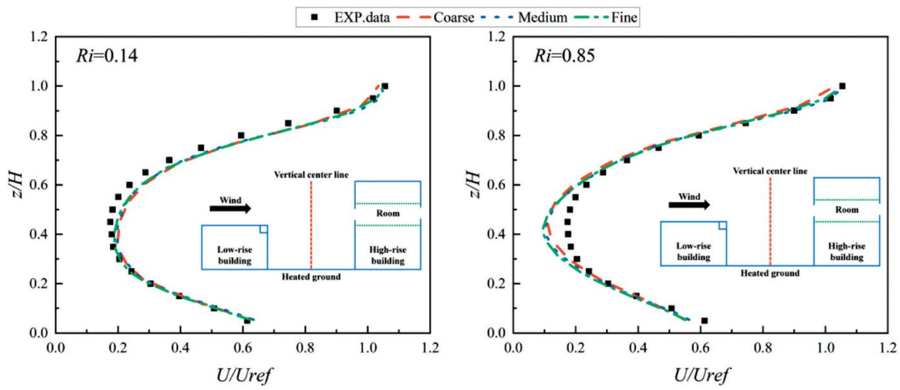

Fig. 3. Normalized velocity magnitude distributions along the vertical central line of the street canyon under non-isothermal conditions with (a) *Ri*=0.14 and (b) *Ri*=0.85.

Fig. 4. Annual distribution of atmospheric stability condition inside (a) square layout and (b) staggered layout of buildings.

bient air temperature). Guangzhou had the highest percentage of stable condition where higher percent of the time was that the wall temperatures of buildings were lower than the ambient air temperature. Kunming had the highest percentage in between the stable and unstable conditions, where highest percent of time was that the *Ri* (in absolute value) was small and the airflow might not be affected greatly by the wall thermal boundary conditions induced by solar radiation. For the five cities in China, stable condition occurred for more than 40% of the time, and neutral condition occupied 7%–11% of the time. Lower value of albedo resulted higher percentage of unstable condition. With albedo values of 0.5, unstable condition occupied 19%–24% annually, while it occupied 24%–28% with albedo values of 0.3. There was no obvious differences in the annual distributions of atmospheric condition between the square and staggered building layouts, but the staggered layouts had slightly higher absolute value of Richardson number than square layout annually. The results indicated that the atmospheric stability condition

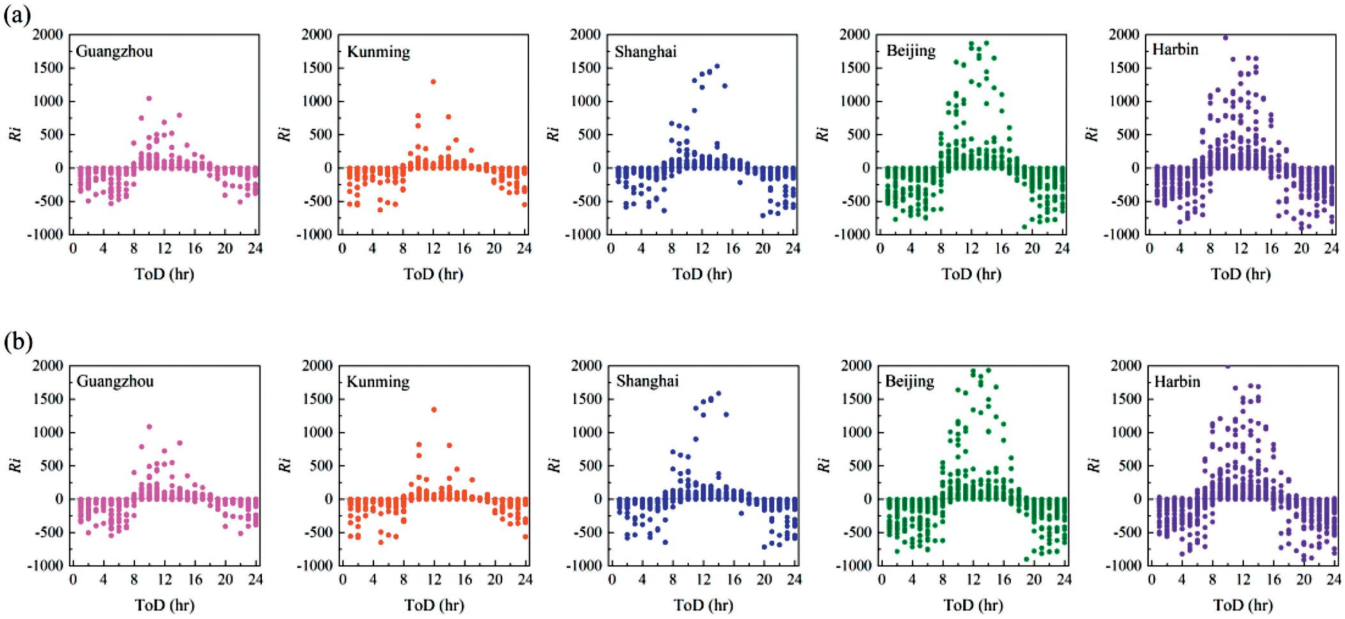

Fig. 5. Distribution of annual *Ri* in hourly series with α of 0.5 inside (a) square layout and (b) staggered layout at the five cities in China.

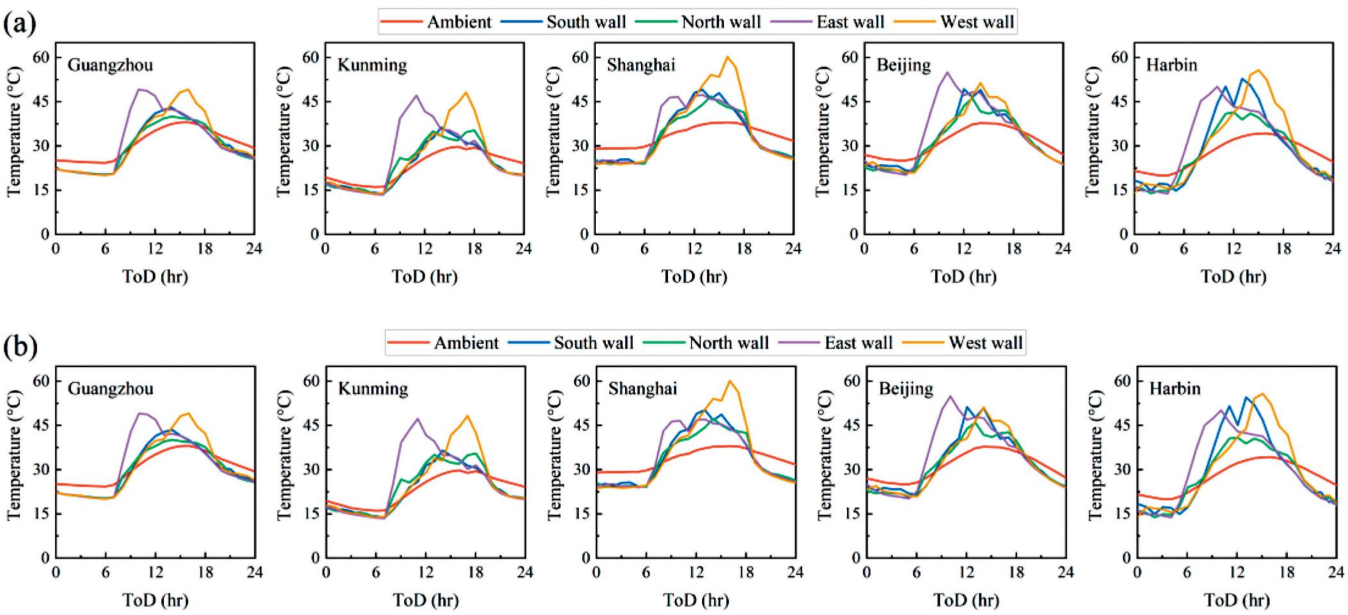

Fig. 6. Diurnal variations of building walls' temperatures with α of 0.5 on the hottest days inside (a) square layout and (b) staggered layout.

was most likely determined by the local climate characteristic (solar irradiation and wind speed), and the albedo value rather than the building layout form when the shadow effect of surrounding buildings was not considered.

Fig. 5 showed the annual Richardson number distributions with hours at the five cities in China under two building layouts. It was observed that the ariflow in the urban area was under stable condition between 20:00 ToD and 05:00 ToD and unstable condition was noticed from 06:00 ToD to 18:00 ToD. It was difficult to conclude what o'clock of the day was under the very unstable condition, but it would occur from 08:00 ToD to 18:00 ToD. This observation was consistent with the previous studies that unstable conditions appeared in the evening after sunset when the heat island intensity was maximum [1] or at the hottest hour of the day when the walls' temperatures were maximum [39].

The according hottest day at the five cities in China were selected to investigate the effects of the solar-induced thermal wall conditions on urban airflow in diurnal circle. The building walls' temperatures inside the layout (surrounded by other buildings) were proximately the same on the walls having the same orientation. Fig. 6 showed the average walls' temperatures of each studied case on its hottest day respectively with α of 0.5. The highest walls' temperatures were noticed on west orientation walls at 16:00 ToD for most cities, and the highest walls' temperature exceeded 60 °C at the hottest hour at Shanghai. The highest walls' temperatures were observed on the East walls at 08:00 ToD at Beijing. Although the similar diurnal variations of walls' temperatures were noticed for both square and staggered layouts, the walls' temperatures were slightly higher (≤0.5 °C) with staggered layout comparing to those with square layout throughout the day, which were also observed in previous study [52]. As the building heights used in both staggered

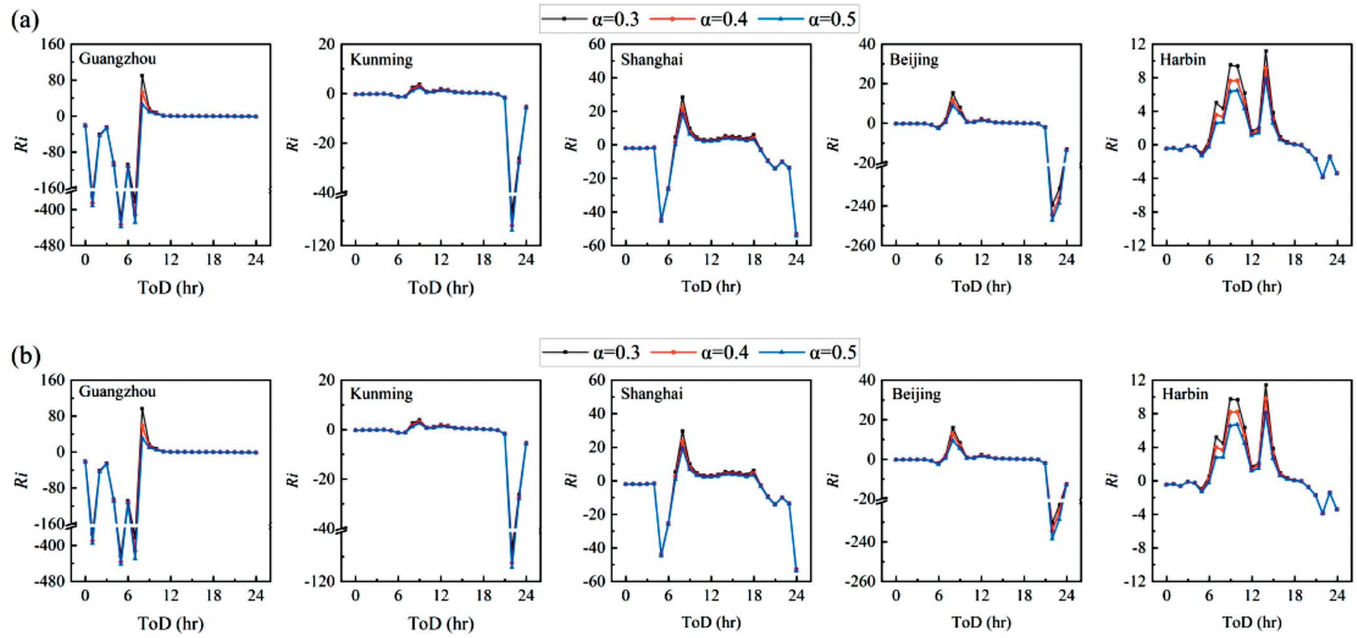

Fig. 7. Diurnal variations of Richardson number on the hottest days inside (a) square layout and (b) staggered layout.

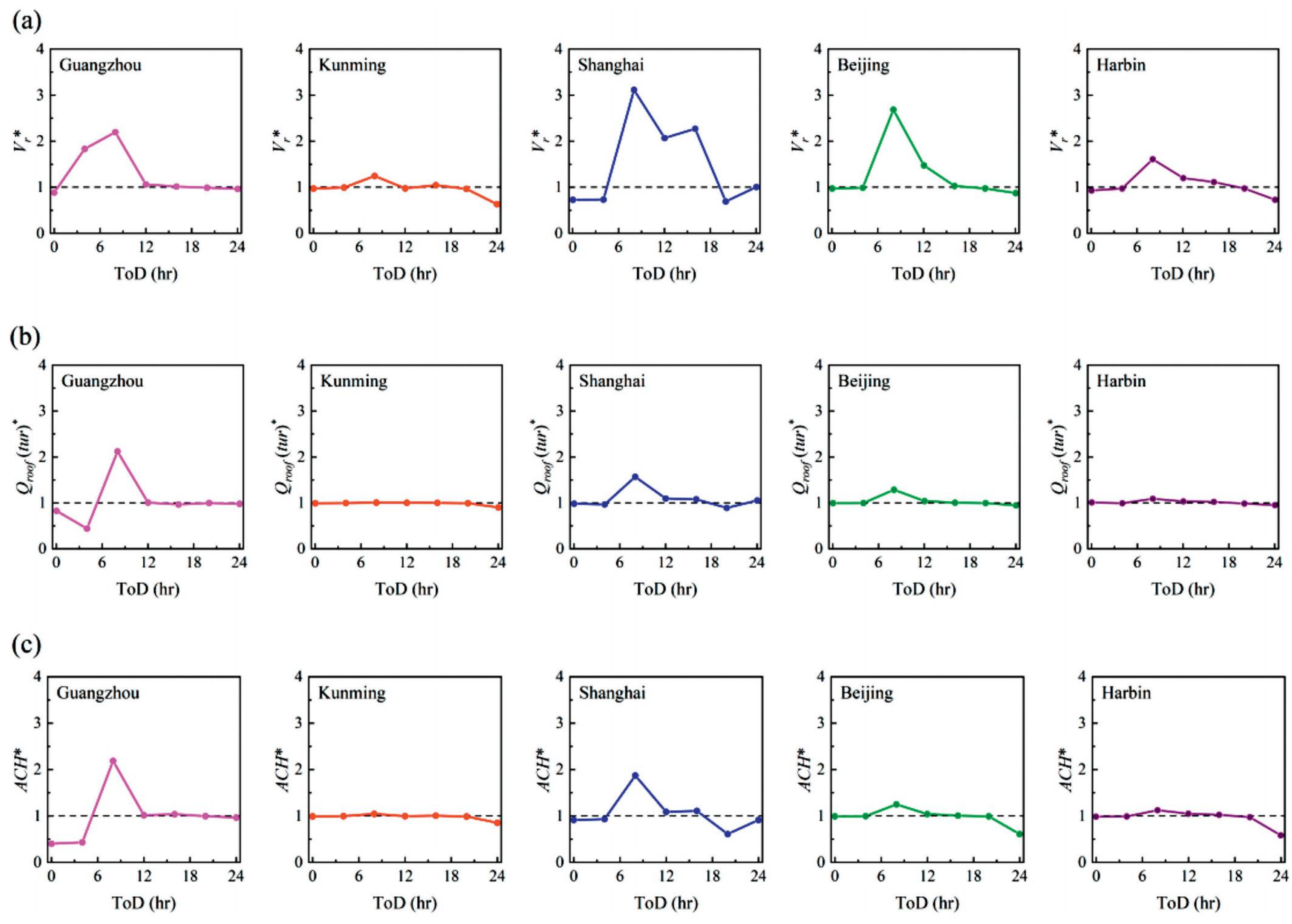

Fig. 8. Diurnal variations of (a) V_r^*, (b) $Q_{roof}(tur)^*$ and (c) ACH^* on the hottest days within square layout.

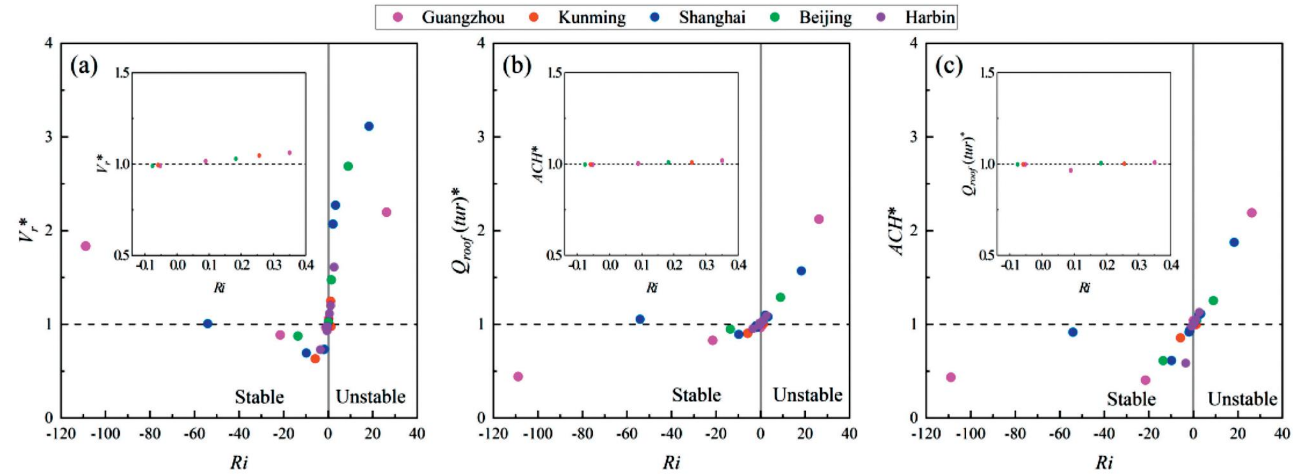

Fig. 9. Variation of (a) V_r^*, (b) $Q_{roof}(tur)^*$ and (c) ACH^* with Richardson number on the hottest day with square layout.

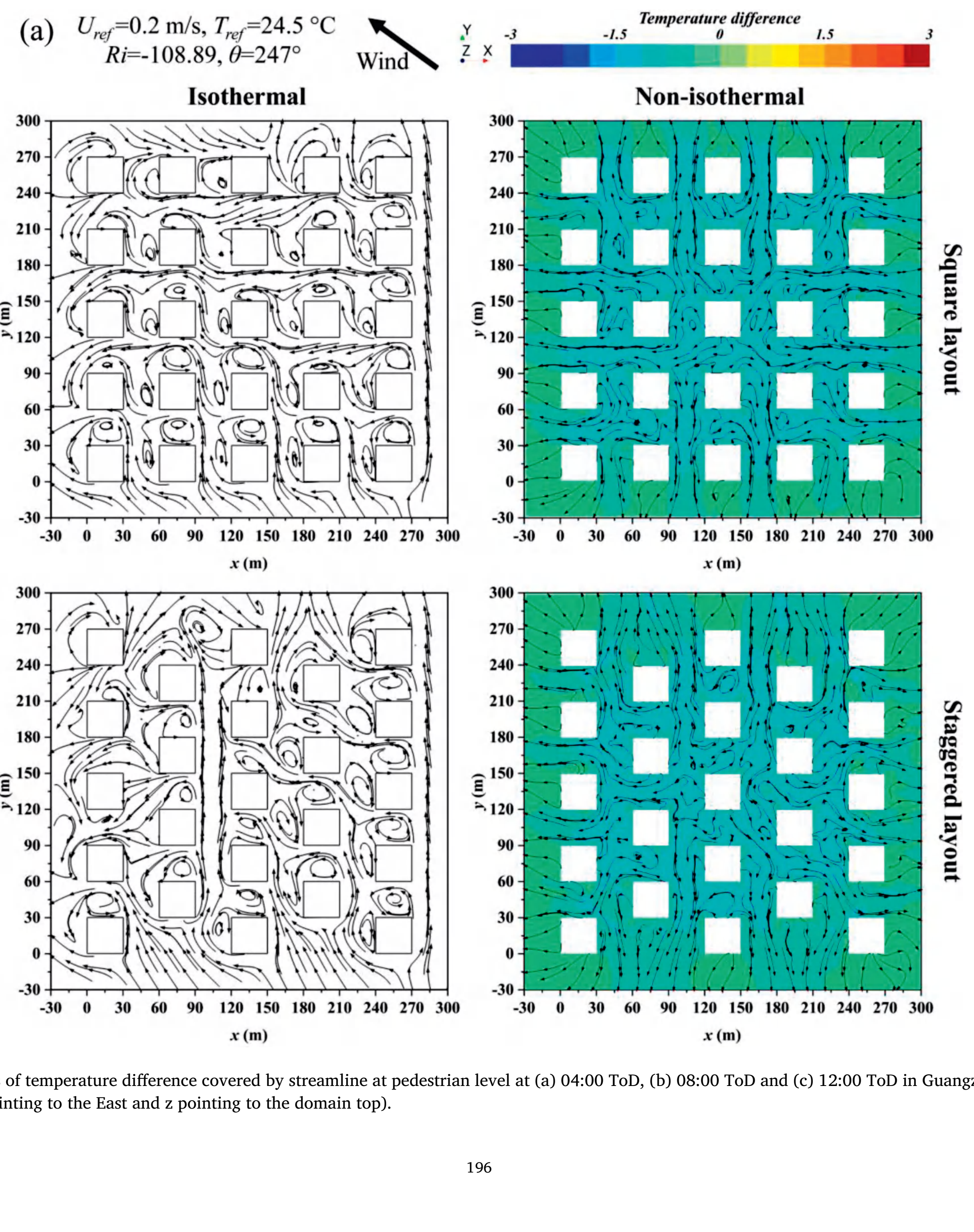

Fig. 10. Contours of temperature difference covered by streamline at pedestrian level at (a) 04:00 ToD, (b) 08:00 ToD and (c) 12:00 ToD in Guangzhou (x pointing to the South, y pointing to the East and z pointing to the domain top).

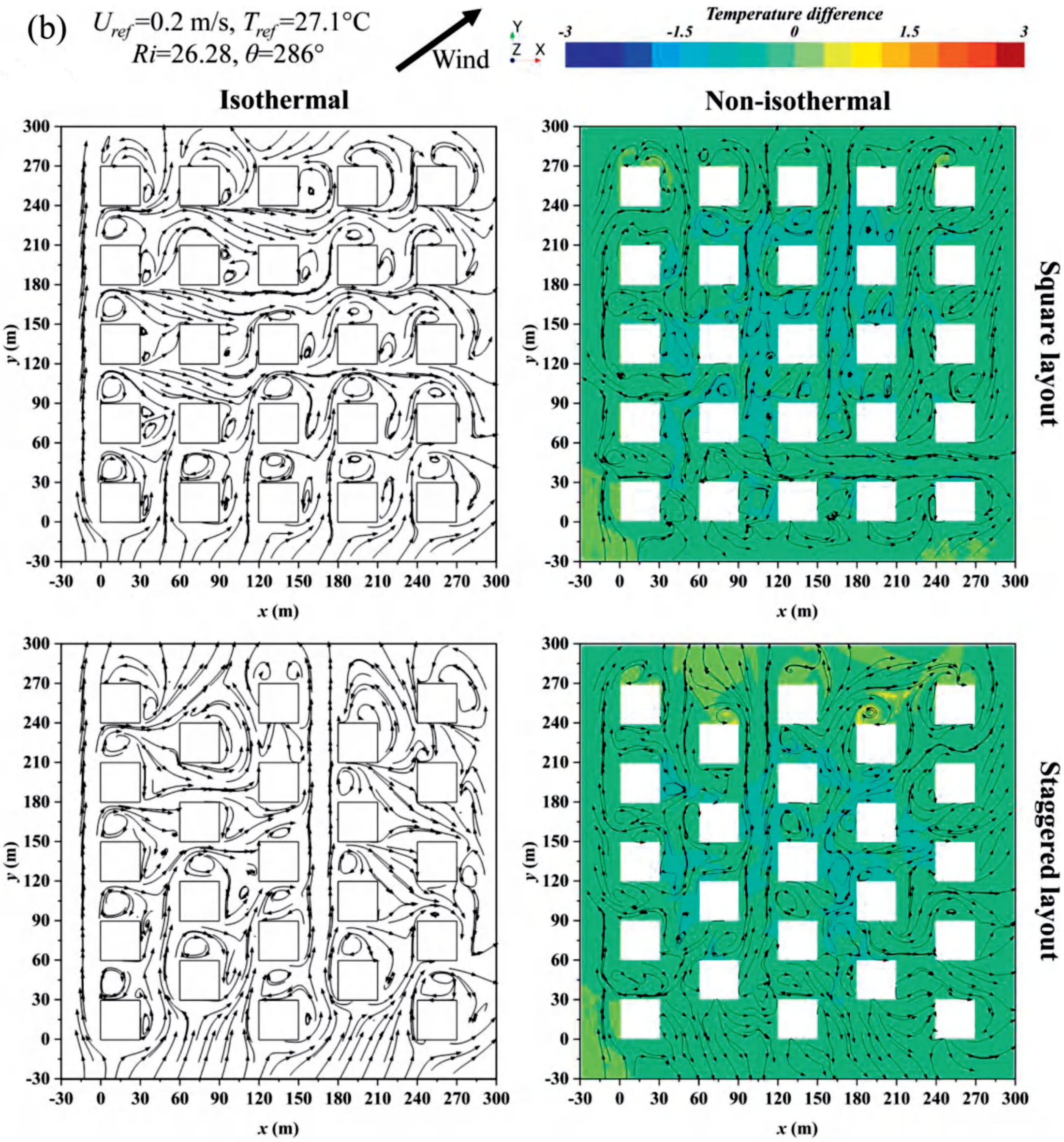

Fig. 10. Continued

and square layouts were identical and the aspect ratio (H/W) was 1.0, the shadow effects on walls' temperatures have already been reduced. As buildings in staggered layout were more close to the edge of the building array and had more areas of ground surfaces, more longwave radiation from the outer ground surfaces would therefore be absorbed by the building walls and this resulted slightly higher walls' temperatures. The urban surfaces' temperatures on the hottest days were used to identify the atmospheric stability in diurnal circle, and also used to define the thermal boundary conditions for CFD simulations.

Regarding the atmospheric stability of the hottest days, the influences of albedo values were obvious. The largest difference of Richardson number was 64 between α of 0.3 and 0.5 in Guangzhou, as presented in Fig. 7. Although the square and staggered building layouts were approximately under the same atmospheric stability condition at the specified hour, the staggered layout had slightly higher absolute value of Richardson number than square layout. With the albedo value of 0.5 in the square layout, the very unstable conditions were observed at around 08:00 ToD at the five cities (be aware of the different ranges of *Ri* for each city shown in Fig. 7. The reason that non-identical range of *Ri* was used for each city was to show the variation of *Ri* with ToD better for the cities with smaller ranges of *Ri*). The atmospheric stability conditions were between stable and unstable at the hottest hours (16:00 ToD) for most of the investigated cities, except that Shanghai was under very unstable condition. The stable conditions were observed between night and dawn at Guangzhou and Shanghai.

3.3. Diurnal variation of thermal wall temperature conditions on spatially-averaged flow properties and airflow patterns

The airflow condition at pedestrian level (1.75 m above the ground) was commonly analysed and evaluated by using velocity ratio (V_r) [74]. The turbulent fluctuations across street roofs significantly contributed to pollutant removal [75]. As the street roofs provide greater total area, the effective flow rates driven by turbulent exchange across street roofs, Q_{roof} (turb), was an important index for the urban canopy layer ventilation. Meanwhile, the overall ventilation efficiency of the entire canopy was examined by using *ACH*. The parameters of V_r, Q_{roof} (turb) and *ACH* were calculated by Eq. (9)–(11) respectively:

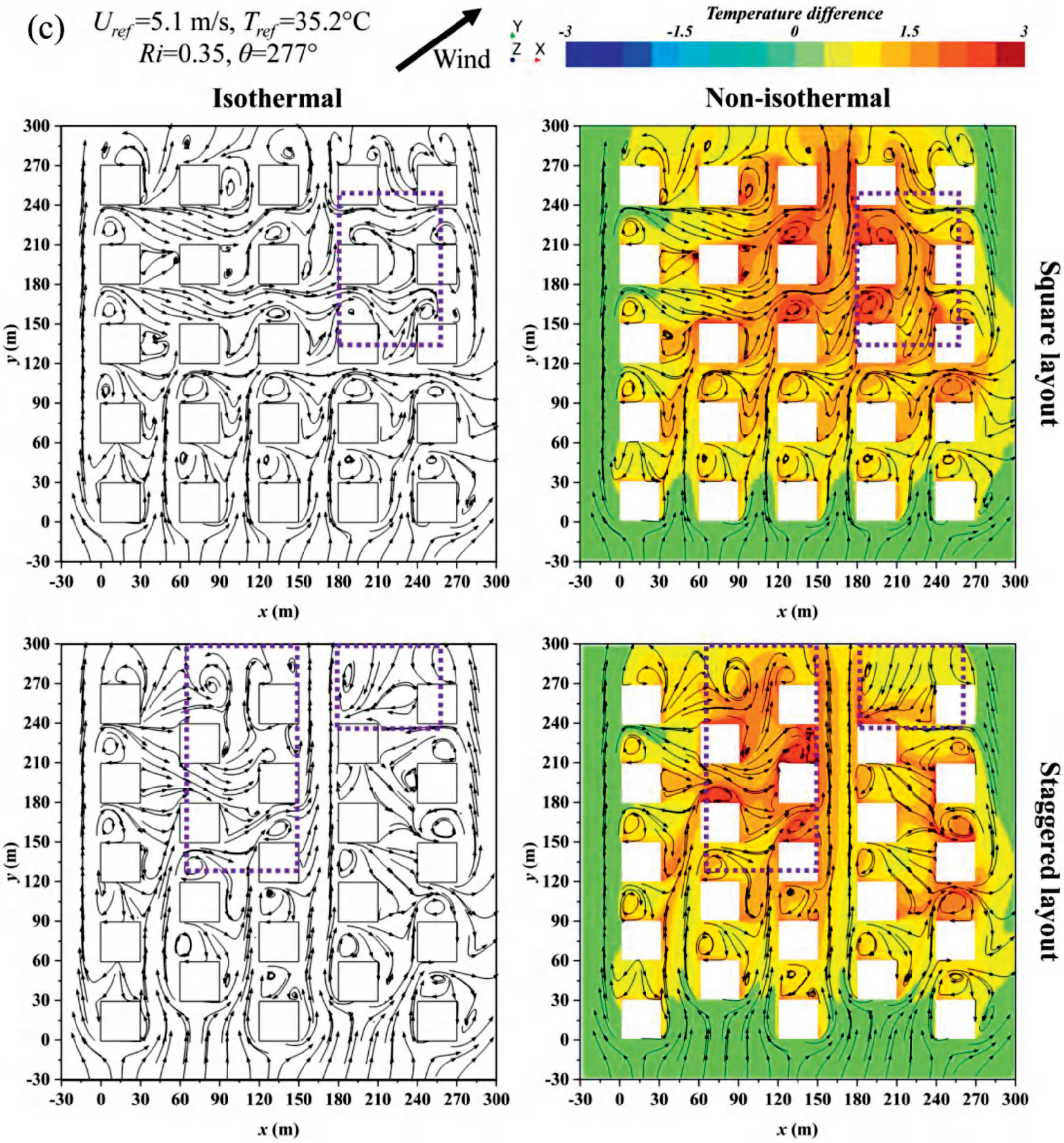

Fig. 10. Continued

$$V_r = \frac{U_P}{U_{ref}} \tag{9}$$

$$Q_{roof}\ (turb) = \sum \pm \int_{A_i} 0.5\sigma_w dA_i \tag{10}$$

$$ACH = 3600 * \frac{Q_T}{vol} \tag{11}$$

where in Eq. (9), U_P was the average wind velocity magnitudes at pedestrian level inside the building array, U_{ref} was the reference wind velocity at inlet with reference height of 10.0 m. In Eq. (10), A_i were the surfaces of street canyons' roof (56 surfaces for 5 × 5 building array). $\sigma_w = \sqrt{\overline{w'w'}} = \sqrt{2k/3}$ was the fluctuation velocity based on the approximation of isotropic turbulence in k-ε turbulent models where u′, v′ and w′ were the stream-wise, span-wise, vertical velocity fluctuations (u′ = v′ = w′) and the turbulent kinetic energy $k = \frac{1}{2}(\overline{u'u'} + \overline{v'v'} + \overline{w'w'})$ [68]. In Eq. (11), Q_T was the total flow rate entering the control volume, m^3/s, vol was the control volume of the entire neighbourhood canopy, m^3.

The influences of solar-induced thermal wall boundary conditions on airflow were weighed by normalized velocity ratio (V_r^*), normalized flow rate ($Q_{roof}\,(turb)^*$) and normalized air change rate (ACH^*), which were the deviation ratio bewteen non-isothermal conditions($Ri \neq 0$) and isothermal conditions ($Ri = 0$), as Eq. (12)–(14).

$$V_r^* = \frac{V_{r,\ non-isothermal}}{V_{r,\ isothermal}} \tag{12}$$

$$Q_{roof}(turb)^* = \frac{Q_{roof}(turb)_{non-isothermal}}{Q_{roof}(turb)_{isothermal}} \tag{13}$$

$$ACH^* = \frac{ACH_{non-isothermal}}{ACH_{isothermal}} \tag{14}$$

The influences of diurnal solar-induced thermal wall boundary conditions on the three parameters were presented in Fig. 8. The deviation of V_r from isothermal conditions were noticeable under diurnal solar-induced thermal wall boundary conditions, especially at Shanghai shown in Fig. 8(a). The outdoor effective flow rates driven by turbulent exchange across the street roofs and ventilation efficiency ($Q_{roof}\,(turb)$) and (ACH) were less sensitive to the diurnal solar-induced thermal wall boundary conditions, as their deviation from isothermal conditions were much smaller, as shown in Fig. 8(b) and Fig. 8(c). At Kunming, the influ-

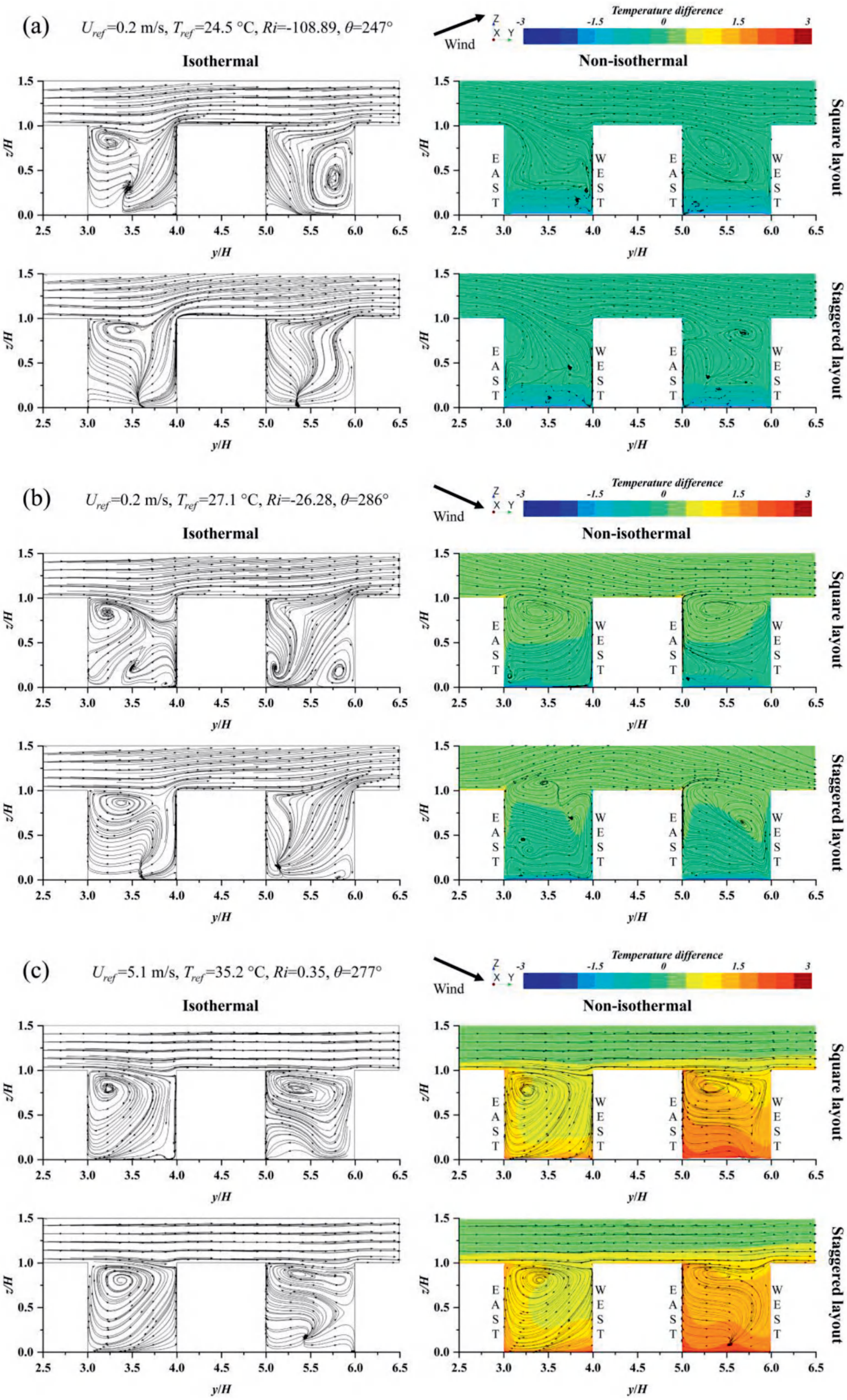

Fig. 11. Contours of temperature difference covered by streamline at vertical section of target street canyons at (a) 04:00 ToD, (b) 08:00 ToD and (c) 12:00 ToD in Guangzhou (x pointing to the South, y pointing to the East and z pointing to the domain top).

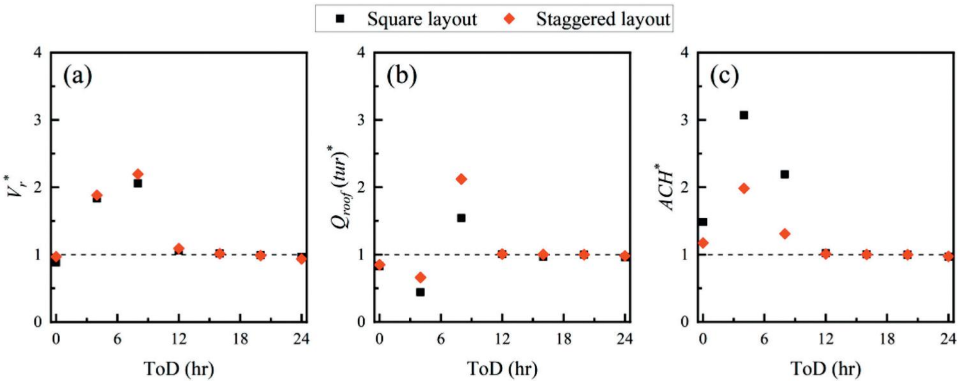

Fig. 12. Diurnal variations of (a) V_r^*, (b) Q_{roof} (tur)* and (c) *ACH** on the hottest day of Guangzhou.

ences of diurnal solar-induced thermal wall boundary conditions on urban airflow were less significant. The results achieved on the hottest day showed that the strongest thermal effect on urban airflow occurred at 08:00 ToD among the simulated cases when the deviation from isothermal conditions were the highest.

The normalized flow properties from the five cities varying with *Ri* were presented in Fig. 9 and the small figures inserted in Fig. 9 were the results between slightly stable and slightly unstable conditions. The wind environment at the pedestrian level were more prone to be affected by thermal effects as the V_r^* responded to the increasing of *Ri* immediately when atmosphere switched from stable conditions to slightly unstable conditions. The influence levels of thermal effect on V_r were more significant under unstable conditions comparing to the stable conditions. Its deviation from isothermal conditions would be three times higher under unstable conditions, while V_r^* was around 1.5 times under the stable conditions compared to the isothermal conditions. The Q_{roof} (tur)* and *ACH** increased almost linearly with larger *Ri*. As all cases were simulated by using the real meteorological data and the wind directions were not identical of the five cities at the same o'clock with the changing wind speeds, the influences of wind direction on the normalized parameters were therefore difficult to be analysed in this study. Our previous study indicated that the wind direction contributed largely to the change of airflow patterns under the same unstable condition comparing to the isothermal condition [44].

The impacts of building layout on airflow under diurnal varying thermal effects were compared on the hottest day of Guangzhou. The contours of temperature difference (the air temperature minus reference air temperature) together with streamlines at pedestrian level and vertical planes of the target street canyons (seen in Fig. 1) were presented in Figs. 10 and 11 under both isothermal and non-isothermal conditions, with x pointing to the South, y pointing to the East and z pointing to the domain top. Under the isothermal conditions, the velocity and airflow pattern were only determined by layout form and wind direction. Under the non-isothermal conditions, the thermal effects would influence the airflow pattern noticeably at both horizontal and vertical planes. When the atmosphere was under very stable condition at 04:00 ToD (*Ri*=−108.89), Fig. 10(a) revealed that the air temperature at pedestrian level was nearly uniform and lower than the reference incoming air temperature and the airflow tended to flow out of the building array compared to the corresponding isothermal conditions where the airflow tended to flow into the building array. However, the airflow tended to flow into the building array at the vertical plane compared to the isothermal conditions where the airflow tended to escape from the vertical canyon, as shown in Fig. 11(a).

When the airflow in the urban area was under very unstable condition at 08:00 ToD (*Ri* = 26.28), the windward walls' (on the West) and the ground surfaces' temperatures were lower than the incoming reference air temperature. With relative lower wind speed, less heat flux were convected from the high temperature walls on the East, the air temperature at pedestrian level was lower than the incoming air temperature, except some area behind walls on the East, as shown in Fig. 10(b). The air temperature increased with the height at the vertical plane and were higher than the incoming air temperature near the roof level. With relatively higher wall temperatures on the East, the flow patterns were more chaotic than the corresponding isothermal conditions, shown in Fig. 10(b). In Fig. 11(b), the flow was observed to fall down following the colder walls on the West and to be heated up along the walls on the East due to the different temperature distributions on these walls. When the Richardson number was more close to neutral condition at 12:00 ToD (*Ri* = 0.35), only minor differences of airflow patterns between isothermal conditions and non-isothermal conditions were observed at the area where had higher local thermal stratification at horizontal direction, as shown in Fig. 10(c) with purple rectangle, while obvious differences existed at the vertical plane of the latter street canyons as shown in Fig. 11(c).

Fig. 12 indicated that the deviation in pedestrian wind velocity ratio was slightly higher inside the staggered layout on the hottest day. One reason was that the staggered layout would induce more turbulence [76] and it would have higher velocity ratio at some cases. On the other hand, the solar-induced thermal wall boundary conditions had slightly larger effects on spatially-averaged flow properties with staggered layout since it introduced slightly higher temperature differences between wall surfaces and ambient temperature as presented in Fig. 7. As the airflow in the urban area was under more stable/unstable conditions with staggered layout, the inflow and outflow through the street roof were larger, namely, higher Q_{roof} (tur)*. Meanwhile, as the staggered layout had larger area for the inflow and outflow, the influences of more stable/unstable conditions was counterbalanced somehow, which led to lower *ACH**.

3.4. Limitations of this study

This study provided the possibility to apply the valuable results from previous studies under isothermal condition into a more 'realistic' urban condition annually. Applying the diversified meteorological data and building codes of five cities in China, this study presented the importance of considering solar-induced thermal wall boundary conditions to analyze the urban airflow. However, the solar-induced thermal wall boundary conditions was affected by factors such as wall albedos, urban morphology, meteorological data, etc.. The current version of CitySim did not consider the effect of shadow caused by surrounding buildings. The distribution of temperatures on each building surface was therefore uniform while in reality there normally has temperature stratification on the walls. The dynamic exchange of heat flux between CFD and CitySim was ignored. More advanced urban energy model and dynamic coupling between UEM and CFD could be conducted for a more detailed solar-induce thermal environment. Meanwhile, in order the minimize the shadow effect, this study just considered building array with identical building heights and medium density, the solar-induced thermal effect on the investigated parameters under varying urban morphologies could be different. The diurnal variations of solar-induced thermal effect were only considered on the respective hottest day of the five cities, more diverse diurnal circle of thermal effect could be simulated in different seasons or on other representative days.

4. Conclusion

The characteristics of atmospheric stability condition and influence of diurnal varying solar-induced thermal effect on urban airflow inside the idealized building arrays were investigated at five cities located at five climate zones in China. The main conclusions are as follows.

(1) The atmospheric stability condition was determined by local climate characteristic and albedo value without considering the effects of shadows caused by surrounding buildings.
(2) The characteristics of atmospheric stability can serve as a guideline to evaluate the possibility of adopting the previous conclusions obtained from studies under isothermal conditions. The stable conditions was more than 40% annually and probably should be investigated more in the future.
(3) The differences of spatially-averaged airflow properties and airflow distribution at horizontal and vertical planes between non-isothermal conditions and isothermal conditions indicated the importance of considering the solar-induced thermal wall boundary conditions under unstable conditions in idealized urban area. Although the differences in airflow pattern at horizontal direction can be ignored when the *Ri* is close to 0.0, namely, close to isothermal condition, the differences of airflow patterns at vertical planes was still noticeable.
(4) Although the form of building layout hardly contributed to the atmospheric stability conditions, the staggered layout had slightly higher absolute value of *Ri* number than square layout in the simulated cases. In the future, the staggered layout with non-identical building heights can be simulated to evaluate the influence of non-isothermal conditions on airflow properties.

Declaration of Competing Interest

The authors declare that they have no known competing financial interests or personal relationships that could have appeared to influence the work reported in this paper.

Acknowledgement

The authors acknowledge the scholarship (JY201704) from Guangzhou Elite Project (GEP) granted for Guoxing Chen's Ph.D. study at Aarhus University.

Appendix A Illustration of the experimental set-ups for the two CFD validation cases

Figs. A1 and A2

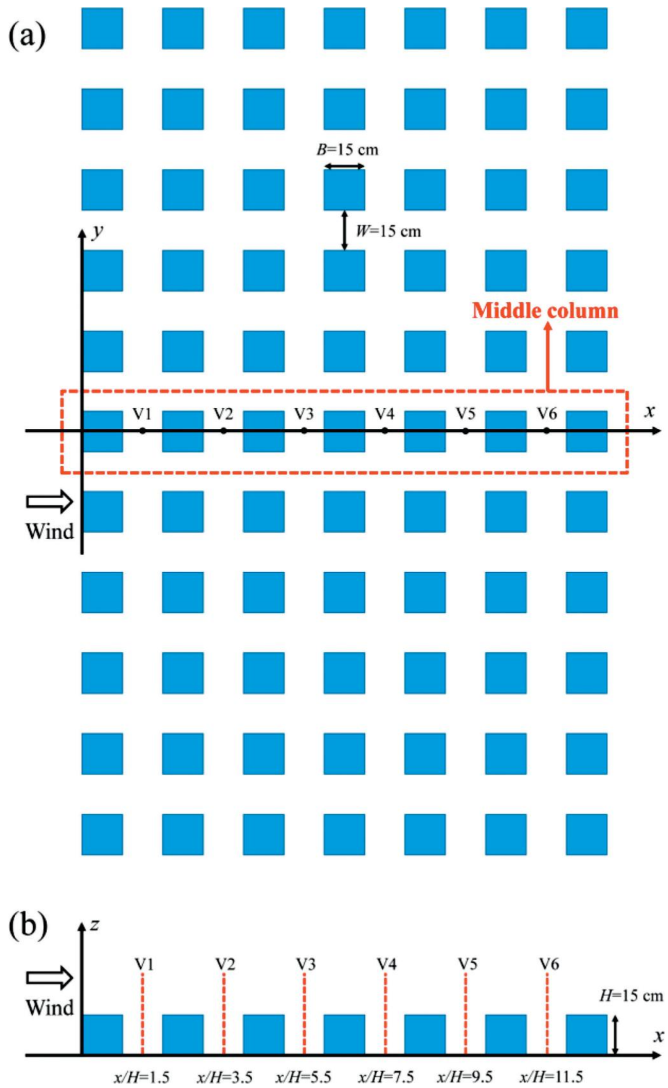

Fig. A1. Sketch of wind tunnel experiment for CFD validation under isothermal condition in (a) horizontal plane and (b) vertical plane.

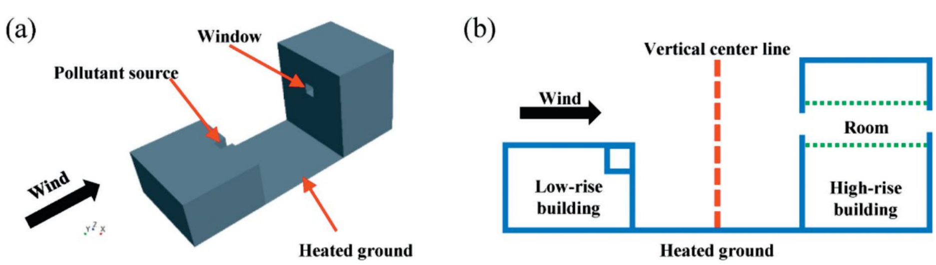

Fig. A2. Sketch of wind tunnel experiment for CFD validation under non-isothermal condition in (a) 3D model and (b) vertical plane.

Appendix B Summary of wind conditions, ambient air temperature and Ri number at eight time of the day on the hottest day of the selected five cities in China

City	Month	Day of the month	Hour (ToD)	Ambient air temperature (°C)	Wind speed (m/s)	Wind direction (°)*	Richardson number
Guangzhou	July	31	00:00	25.2	0.4	210	−21.47
			04:00	24.5	0.2	247	−108.89
			08:00	27.1	0.2	286	26.28
			12:00	35.2	5.1	277	0.35
			16:00	38.1	7.4	291	0.09
			20:00	33.5	6.5	278	−0.05
			24:00	29.3	1.9	222	−1.00
Kunming	July	9	00:00	19.4	3.2	205	−0.25
			04:00	16.6	5	298	−0.06
			08:00	17.9	1.3	194	1.13
			12:00	25.9	3.9	188	1.30
			16:00	29.8	5.7	294	0.26
			20:00	27.2	3.2	291	−0.25
			24:00	24.1	0.8	217	−5.77
Shanghai	July	21	00:00	29	1.3	87	−1.96
			04:00	29.3	1.5	109	−1.65
			08:00	32.6	0.6	130	18.38
			12:00	36.6	2.4	84	2.23
			16:00	38	1.8	82	3.35
			20:00	35.3	0.7	48	−9.77
			24:00	31.7	0.3	84	−54.08
Beijing	July	9	00:00	27	4.2	160	−0.17
			04:00	25.1	5.9	253	−0.08
			08:00	28.9	0.8	194	9.02
			12:00	35.9	3.4	188	1.50
			16:00	37.6	6.4	249	0.18
			20:00	33.6	3	291	−0.15
			24:00	27.1	0.4	217	−13.54
Harbin	June	19	00:00	21.6	3.4	90	−0.45
			04:00	20	4.5	245	−0.28
			08:00	25.8	1.8	204	2.72
			12:00	32.3	3.7	246	1.14
			16:00	34.3	3.4	296	0.61
			20:00	30.5	2.5	318	−0.76
			24:00	24.6	1.3	265	−3.40

* 0 and 360 indicate north.

References

[1] J. Hang, Q. Wang, X. Chen, M. Sandberg, W. Zhu, R. Buccolieri, S. Di Sabatino, City breathability in medium density urban-like geometries evaluated through the pollutant transport rate and the net escape velocity, Build. Environ. 94 (2015) 166–182, doi:10.1016/j.buildenv.2015.08.002.

[2] R. Buccolieri, P. Salizzoni, L. Soulhac, V. Garbero, S. Di Sabatino, The breathability of compact cities, Urban Clim. 13 (2015) 73–93, doi:10.1016/j.uclim.2015.06.002.

[3] M. Lin, J. Hang, Y. Li, Z. Luo, M. Sandberg, Quantitative ventilation assessments of idealized urban canopy layers with various urban layouts and the same building packing density, Build. Environ. 79 (2014) 152–167, doi:10.1016/j.buildenv.2014.05.008.

[4] J. Hang, Y. Li, M. Sandberg, Experimental and numerical studies of flows through and within high-rise building arrays and their link to ventilation strategy, J. Wind Eng. Ind. Aerodyn. 99 (2011) 1036–1055, doi:10.1016/j.jweia.2011.07.004.

[5] J. Hang, Y. Li, M. Sandberg, L. Claesson, Wind conditions and ventilation in high-rise long street models, Build. Environ. 45 (2010) 1353–1365, doi:10.1016/j.buildenv.2009.11.019.

[6] J. Hang, M. Sandberg, Y. Li, Effect of urban morphology on wind condition in idealized city models, Atmos. Environ. 43 (2009) 869–878, doi:10.1016/j.atmosenv.2008.10.040.

[7] C. Yuan, E. Ng, Building porosity for better urban ventilation in high-density cities - A computational parametric study, Build. Environ. 50 (2012) 176–189, doi:10.1016/j.buildenv.2011.10.023.

[8] L. Chen, J. Hang, M. Sandberg, L. Claesson, S. Di Sabatino, H. Wigo, The impacts of building height variations and building packing densities on flow adjustment and city breathability in idealized urban models, Build. Environ. 118 (2017) 344–361, doi:10.1016/j.buildenv.2017.03.042.

[9] S.J. Mei, J.T. Hu, D. Liu, F.Y. Zhao, Y. Li, Y. Wang, H.Q. Wang, Wind driven natural ventilation in the idealized building block arrays with multiple urban morphologies and unique package building density, Energy Build. 155 (2017) 324–338, doi:10.1016/j.enbuild.2017.09.019.

[10] R. Ramponi, B. Blocken, L.B. de Coo, W.D. Janssen, CFD simulation of outdoor ventilation of generic urban configurations with different urban densities and equal and unequal street widths, Build. Environ. 92 (2015) 152–166, doi:10.1016/j.buildenv.2015.04.018.

[11] J. Hang, Y. Li, R. Buccolieri, M. Sandberg, S. Di Sabatino, On the contribution of mean flow and turbulence to city breathability: the case of long streets with tall buildings, Sci. Total Environ. 416 (2012) 362–373, doi:10.1016/j.scitotenv.2011.12.016.

[12] P. Louka, G. Vachon, J.-.F. Sini, P.G. Mestayer, J.-.M. Rosant, Thermal effects on the airflow in a street canyon–Nantes'99 experimental results and model simulations, Water. Air. Soil Pollut. 2 (2002) 351–364.

[13] K. Uehara, S. Murakami, S. Oikawa, S. Wakamatsu, Wind tunnel experiments on how thermal stratification affects flow in and above urban street canyons, Atmos. Environ. 34 (2000) 1553–1562, doi:10.1016/S1352-2310(99)00410-0.

[14] A. Kovar-Panskus, L. Moulinneuf, E. Savory, A. Abdelqari, J.-.F. Sini, J.-.M. Rosant, A. Robins, N. Toy, The influence of solar-induced wall heating on the flow regime within urban street canyons, 3rd Urban Air Qual. Conf., 2001.

[15] R. Dimitrova, J.F. Sini, K. Richards, M. Schatzmann, M. Weeks, E. Perez García, C. Borrego, Influence of thermal effects on the wind field within the urban environment, Boundary-Layer Meteorol. 131 (2009) 223–243, doi:10.1007/s10546-009-9368-4.

[16] P.Y. Cui, Z. Li, W.Q. Tao, Wind-tunnel measurements for thermal effects on the air flow and pollutant dispersion through different scale urban areas, Build. Environ. 97 (2016) 137–151, doi:10.1016/j.buildenv.2015.12.010.

[17] J. Allegrini, A wind tunnel study on three-dimensional buoyant flows in street canyons with different roof shapes and building lengths, Build. Environ. 143 (2018) 71–88, doi:10.1016/j.buildenv.2018.06.056.

[18] Y. Lin, T. Ichinose, Y. Yamao, H. Mouri, Wind velocity and temperature fields under different surface heating conditions in a street canyon in wind tunnel experiments, Build. Environ. (2019) 106500, doi:10.1016/J.BUILDENV.2019.106500.

[19] D. Marucci, M. Carpentieri, Effect of local and upwind stratification on flow and dispersion inside and above a bi-dimensional street canyon, Build. Environ. 156 (2019) 74–88, doi:10.1016/j.buildenv.2019.04.013.

[20] J. Allegrini, V. Dorer, J. Carmeliet, Wind tunnel measurements of buoyant flows in street canyons, Build. Environ. 59 (2013) 315–326, doi:10.1016/j.buildenv.2012.08.029.

[21] J.-J. Kim, J.-J. Baik, Urban street-canyon flows with bottom heating, Atmos. Environ. 35 (2001) 3395–3404, doi:10.1016/S1352-2310(01)00135-2.

[22] J.J. Kim, J.J. Baik, Physical experiments to investigate the effects of street bottom heating and inflow turbulence on urban street-canyon flow, Adv. Atmos. Sci. 22 (2005) 230–237, doi:10.1007/BF02918512.

[23] J. Hang, X. Chen, G. Chen, T. Chen, Y. Lin, Z. Luo, X. Zhang, Q. Wang, The influence of aspect ratios and wall heating conditions on flow and passive pollutant exposure in 2D typical street canyons, Build. Environ. (2019) 106536, doi:10.1016/J.BUILDENV.2019.106536.

[24] G. Jiang, T. Hu, H. Yang, Effects of ground heating on ventilation and pollutant transport in three-dimensional urban street canyons with unit aspect ratio, Atmosphere (Basel) 10 (2019) 286, doi:10.3390/atmos10050286.

[25] P.-.Y. Cui, Z. Li, W.-.Q. Tao, Buoyancy flows and pollutant dispersion through different scale urban areas: CFD simulations and wind-tunnel measurements, Build. Environ. 104 (2016) 76–91, doi:10.1016/J.BUILDENV.2016.04.028.

[26] X. Xie, C.H. Liu, D.Y.C. Leung, M.K.H. Leung, Characteristics of air exchange in a street canyon with ground heating, Atmos. Environ. 40 (2006) 6396–6409, doi:10.1016/j.atmosenv.2006.05.050.

[27] X. Xie, C.H. Liu, D.Y.C. Leung, Impact of building facades and ground heating on wind flow and pollutant transport in street canyons, Atmos. Environ. 41 (2007) 9030–9049, doi:10.1016/j.atmosenv.2007.08.027.

[28] J.-J. Kim, J.-J. Baik, Effects of street-bottom and building-roof heating on flow in three-dimensional street canyons, Adv. Atmos. Sci. 27 (2010) 513–527, doi:10.1007/s00376-009-9095-2.

[29] X.X. Li, R.E. Britter, L.K. Norford, T.Y. Koh, D. Entekhabi, Flow and pollutant transport in urban street canyons of different aspect ratios with ground heating: large-eddy simulation, Boundary-Layer Meteorol 142 (2012) 289–304, doi:10.1007/s10546-011-9670-9.

[30] F. Yang, S.S.Y. Lau, F. Qian, Thermal comfort effects of urban design strategies in high-rise urban environments in a sub-tropical climate, Archit. Sci. Rev. 54 (2011) 285–304, doi:10.1080/00038628.2011.613646.

[31] X. Cai, Effects of differential wall heating in street canyons on dispersion and ventilation characteristics of a passive scalar, Atmos. Environ. 51 (2012) 268–277, doi:10.1016/j.atmosenv.2012.01.010.

[32] S.J. Mei, J.T. Hu, D. Liu, F.Y. Zhao, Y. Li, H.Q. Wang, Thermal buoyancy driven canyon airflows inside the compact urban blocks saturated with very weak synoptic wind: plume merging mechanism, Build. Environ. 131 (2018) 32–43, doi:10.1016/j.buildenv.2017.12.035.

[33] G. Jiang, R. Yoshie, Large-eddy simulation of flow and pollutant dispersion in a 3D urban street model located in an unstable boundary layer, Build. Environ. 142 (2018) 47–57, doi:10.1016/j.buildenv.2018.06.015.

[34] M. Bruse, H. Fleer, Simulating surface-plant-air interactions inside urban environments with a three dimensional numerical model, Environ. Model. Softw. 13 (1998) 373–384, doi:10.1016/S1364-8152(98)00042-5.

[35] K.H. Schlünzen, D. Hinneburg, O. Knoth, M. Lambrecht, B. Leitl, S. López, C. Lüpkes, H. Panskus, E. Renner, M. Schatzmann, T. Schoenemeyer, S. Trepte, R. Wolke, Flow and transport in the obstacle layer: first results of the micro-scale model MITRAS, J. Atmos. Chem. 44 (2003) 113–130, doi:10.1023/A:1022420130032.

[36] S.E. Krayenhoff, J.A. Voogt, A microscale three-dimensional urban energy balance model for studying surface temperatures, Boundary-Layer Meteorol. 123 (2007) 433–461, doi:10.1007/s10546-006-9153-6.

[37] N. Yaghoobian, J. Kleissl, An indoor–outdoor building energy simulator to study urban modification effects on building energy use – Model description and validation, Energy Build. 54 (2012) 407–417, doi:10.1016/J.ENBUILD.2012.07.019.
[38] G. Mutani, S. Coccolo, J. Kaempf, M. Bilardo, CitySim Guide: Urban Energy Modelling, CreateSpace Independent Publishing Platform, 2018.
[39] J. Liu, Z. Luo, J. Zhao, T. Shui, Ventilation in a street canyon under diurnal heating conditions, Int. J. Vent. 11 (2012) 141–154, doi:10.1080/14733315.2012.11683977.
[40] J.L. Santiago, E.S. Krayenhoff, A. Martilli, Flow simulations for simplified urban configurations with microscale distributions of surface thermal forcing, Urban Clim 9 (2014) 115–133, doi:10.1016/j.uclim.2014.07.008.
[41] N. Nazarian, J. Kleissl, Realistic solar heating in urban areas: air exchange and street-canyon ventilation, Build. Environ. 95 (2016) 75–93, doi:10.1016/j.buildenv.2015.08.021.
[42] N. Nazarian, A. Martilli, J. Kleissl, Impacts of realistic urban heating, part i: spatial variability of mean flow, turbulent exchange and pollutant dispersion, Boundary-Layer Meteorol 166 (2018) 367–393, doi:10.1007/s10546-017-0311-9.
[43] N. Nazarian, A. Martilli, L. Norford, J. Kleissl, Impacts of realistic urban heating. Part II: air quality and city breathability, Boundary-Layer Meteorol. 168 (2018) 321–341, doi:10.1007/s10546-018-0346-6.
[44] G. Chen, L. Rong, G. Zhang, Comparison of urban airflow between solar-induced thermal wall and uniform wall temperature boundary conditions by coupling CitySim and CFD, Build. Environ (2020) 172, doi:10.1016/j.buildenv.2020.106732.
[45] K.H. Kwak, J.J. Baik, S.H. Lee, Y.H. Ryu, Computational fluid dynamics modelling of the diurnal variation of flow in a street canyon, Boundary-Layer Meteorol. 141 (2011) 77–92, doi:10.1007/s10546-011-9630-4.
[46] J. Dong, Z. Tan, Y. Xiao, J. Tu, Seasonal changing effect on airflow and pollutant dispersion characteristics in urban street canyons, Atmosphere (Basel) 8 (2017), doi:10.3390/atmos8030043.
[47] N. Yaghoobian, J. Kleissl, U.K.T. Paw, An improved three dimensional simulation of the diurnally varying street canyon flow, Boundary Layer Meteorology 153 (2014) 251–276. In this issue.
[48] D. Robinson, A. Stone, A simplified radiosity algorithm for general urban radiation exchange, Build. Serv. Eng. Res. Technol. 26 (2005) 271–284, doi:10.1097/00006231-200503000-00013.
[49] R. Perez, R. Seals, J. Michalsky, All-weather model for sky luminance distribution—Preliminary configuration and validation, Sol. Energy. 50 (1993) 235–245, doi:10.1016/0038-092X(93)90017-I.
[50] E. Walter, J.H. Kämpf, A verification of CitySim results using the BESTEST and monitored consumption values, in: 2nd Build. Simul. Appl. Conf., 2015, pp. 215–222. https://infoscience.epfl.ch/record/214754/files/p%28139%29v2.pdf%0Ahttps://infoscience.epfl.ch/record/214754.
[51] J. Allegrini, V. Dorer, J. Carmeliet, Analysis of convective heat transfer at building façades in street canyons and its influence on the predictions of space cooling demand in buildings, J, Wind Eng. Ind. Aerodyn. 104–106 (2012) 464–473, doi:10.1016/j.jweia.2012.02.003.
[52] J. Allegrini, V. Dorer, J. Carmeliet, Influence of morphologies on the microclimate in urban neighbourhoods, J. Wind Eng. Ind. Aerodyn. 144 (2015) 108–117, doi:10.1016/j.jweia.2015.03.024.
[53] J. Allegrini, J. Carmeliet, Coupled CFD and building energy simulations for studying the impacts of building height topology and buoyancy on local urban microclimates, Urban Clim. 21 (2017) 278–305, doi:10.1016/j.uclim.2017.07.005.
[54] J. Allegrini, J. Carmeliet, Simulations of local heat islands in Zürich with coupled CFD and building energy models, Urban Clim. 24 (2018) 340–359, doi:10.1016/j.uclim.2017.02.003.
[55] J. Remund, S. Müller, S. Kunz, B. Huguenin-Landl, C. Studer, D. Klauser, C. Schilter, R. Lehnherr, Meteonorm Handbook, 7th Ed., METEOTEST, Bern, Switzerland, 2016 http://meteonorm.com/en/downloads/documents/.
[56] Ministry of Housing and Urban-Rural DevelopmentCode For Thermal Design of Civil Building (GB 50176 - 2016), China Architecture and Building Press, Beijing, 2016.
[57] Ministry of Housing and Urban-Rural DevelopmentDesign Standard For Energy Efficiency of Public Buildings (GB50189 - 2015), China Architecture and Building Press, 2015.
[58] Z. Tong, Y. Chen, A. Malkawi, Z. Liu, R.B. Freeman, Energy saving potential of natural ventilation in China: the impact of ambient air pollution, Appl. Energy. 179 (2016) 660–668, doi:10.1016/j.apenergy.2016.07.019.
[59] State Administration for Market and RegulationSolar Heat Reflecting Insulation Coatings For Buildings (GB/T 25261-2018), Standards Press of China, Beijing, China, 2018.
[60] B. Blocken, Computational fluid dynamics for urban physics: importance, scales, possibilities, limitations and ten tips and tricks towards accurate and reliable simulations, Build. Environ. 91 (2015) 219–245, doi:10.1016/j.buildenv.2015.02.015.
[61] J.L. Santiago, A. Dejoan, A. Martilli, F. Martin, A. Pinelli, Comparison between large-eddy simulation and reynolds-averaged navier-stokes computations for the MUST field experiment. Part I: study of the flow for an incident wind directed perpendicularly to the front array of containers, Boundary-Layer Meteorol. 135 (2010) 109–132, doi:10.1007/s10546-010-9466-3.
[62] F.S. Lien, E. Yee, Numerical modelling of the turbulent flow developing within and over a 3-D building array, Boundary-Layer Meteorol. 112 (2004) 427–466.
[63] P.Y. Cui, Z. Li, W.Q. Tao, Buoyancy flows and pollutant dispersion through different scale urban areas: CFD simulations and wind-tunnel measurements, Build. Environ. 104 (2016) 76–91, doi:10.1016/j.buildenv.2016.04.028.
[64] S. Bottillo, A. De Lieto Vollaro, G. Galli, A. Vallati, CFD modeling of the impact of solar radiation in a tridimensional urban canyon at different wind conditions, Sol. Energy. 102 (2014) 212–222, doi:10.1016/j.solener.2014.01.029.
[65] J. Hang, Z. Luo, M. Sandberg, J. Gong, Natural ventilation assessment in typical open and semi-open urban environments under various wind directions, Build. Environ. 70 (2013) 318–333, doi:10.1016/j.buildenv.2013.09.002.
[66] M.J. Brown, R.E. Lawson, D.S. Decroix, R.L. Lee, Comparison of Centerline Velocity Measurements Obtained Around 2D and 3D Building Arrays in a Wind Tunnel, 2001 New Mexico, United States https://www.osti.gov/biblio/783425-comparison-centerline-velocity-measurements-obtained-around-building-arrays-wind-tunnel .
[67] J.L. Santiago, A. Martilli, F. Martín, CFD simulation of airflow over a regular array of cubes. Part I: three-dimensional simulation of the flow and validation with wind-tunnel measurements, Boundary-Layer Meteorol. 122 (2007) 609–634, doi:10.1007/s10546-006-9123-z.
[68] J. Hang, Y. Li, Wind conditions in idealized building clusters: macroscopic simulations using a porous turbulence model, Boundary-Layer Meteorol. 136 (2010) 129–159, doi:10.1007/s10546-010-9490-3.
[69] P.J. Richards, R... Hoxey, Appropriate boundary conditions for computational wind engineering models using the k-ϵ turbulence model, J. Wind Eng. Ind. Aerodyn. 46–47 (1993) 145–153, doi:10.1016/0167-6105(93)90124-7.
[70] J. Franke, A. Hellsten, H. Schlünzen, B. Carissimo, Best Practice Guideline For the CFD Simulation of Flows in the Urban Environment, COST Action 732, Hamburg, Germany, 2007.
[71] CD-adapcoSTAR-CCM+ Version 12.02A User Guide, 2017 https://mdx.plm.automation.siemens.com/star-ccm-plus.
[72] Y. Lin, G. Chen, T. Chen, Z. Luo, C. Yuan, P. Gao, J. Hang, The influence of advertisement boards, street and source layouts on CO dispersion and building intake fraction in three-dimensional urban-like models, Build. Environ. 150 (2019) 297–321, doi:10.1016/J.BUILDENV.2019.01.012.
[73] J.L. Woodward, Estimating the Flammable Mass of a Vapor Cloud, John Wiley & Sons, Inc., Hoboken, NJ, USA, 1999, doi:10.1002/9780470935361.
[74] E. Ng, Policies and technical guidelines for urban planning of high-density cities - air ventilation assessment (AVA) of Hong Kong, Build. Environ. 44 (2009) 1478–1488, doi:10.1016/j.buildenv.2008.06.013.
[75] J. Hang, Y. Li, M. Sandberg, R. Buccolieri, S. Di Sabatino, The influence of building height variability on pollutant dispersion and pedestrian ventilation in idealized high-rise urban areas, Build. Environ. 56 (2012) 346–360, doi:10.1016/j.buildenv.2012.03.023.
[76] Y. Ishida, T. Okaze, A. Mochida, Influence of urban configuration on the structure of kinetic energy transport and the energy dissipation rate, J. Wind Eng. Ind. Aerodyn. 183 (2018) 198–213, doi:10.1016/J.JWEIA.2018.10.016.

Energy and Built Environment 2 (2021) 204–213

Contents lists available at ScienceDirect

Energy and Built Environment

journal homepage: http://www.keaipublishing.com/en/journals/energy-and-built-environment/

The environmental and financial implications of expanding the use of electric cars - A Case study of Scotland

George Milev[a], Astley Hastings[b], Amin Al-Habaibeh[a,*]

[a] Nottingham Trent University, UK
[b] University of Aberdeen, UK

ARTICLE INFO

Keywords:
Electric
Cars
Vehicles
Environment
Emissions
Carbon
Scotland
Energy

ABSTRACT

This paper investigates the expansion of electric cars and their impact on the environment and the user; assuming a future scenario where all of the light-duty vehicles that use an internal combustion engine will be replaced by electric cars in Scotland. The idea is to investigate the impact on the environment and the financial effect on the user. The methodology is based on analysing the most common electric and conventional vehicles to estimate the amount of additional electricity that would be needed to charge that expansion. The paper has also looked at the running costs. The results show that approximately 4 GWh per annum of additional electricity will be needed to compensate for such growth in electricity demand. With the rise in electricity production, the amount of carbon emissions from the electrical grid is expected to increase slightly by 0.47 megatons CO_2 per annum. Given that the carbon dioxide generated by the light internal combustion vehicles at the moment is 3.6 megatons of CO_2 per year, it is concluded that the total amount of greenhouse gases from the electricity grid will decrease by circa 33.7% if all conventional cars in Scotland are replaced by electric cars. The initial cost of an electric car is found to be higher than conventional diesel or petrol one, but in the long term, the cost to power an electric vehicle is expected to be much cheaper. However, electric cars still have their own drawbacks as they need significant time to be charged, and will consume significant energy for heating the interior and windscreens to prevent condensation in cold weather leading to an estimated reduction in range of approximately 28% in some situations.

1. Introduction

The world population has been increasing dramatically over the past few decades. With the growing population comes an increase in the number of vehicles and therefore the growth of greenhouse gases released from traffic. To mitigate that challenge, scientists and engineers are continuously working to improve conventional vehicles to enhance their performance of using less fuel and hence releasing fewer greenhouse gases to the atmosphere. Another solution on the horizon, and expanding rapidly, is the development of electric cars. Electric vehicles do not release any emissions, they require electricity to run and are considered by many as an eco-friendly solution for the ever-growing demand for more vehicles and more fuel. It is also a way to resolve the growing greenhouse gas and pollution levels in the atmosphere released from traffic. Other alternatives to conventional vehicles are hybrid cars and hydrogen fuel cell vehicles.

It has been estimated that the global social cost for air pollution associated with combustion engines is about 3 trillion dollars per year [1]. The increase in carbon emission not only contributes to poor air quality, but also to an increase in global temperatures; which influences the climate. In 2016, a new record has been set regarding the increase of global temperatures, which led to about 1 °Celsius rise compared to the 20th-century average temperature [2]. The Paris Agreement on Climate change provides the possibility for each country in the world to move forward in decreasing its greenhouse gas levels towards enhancing air quality. Investigating the reduction in greenhouse gas emissions by electrifying transportation is essential, as more than 55 countries emit more than half of the global emissions [1].

The availability of fossil fuel, particularly oil, is not sustainable; hence integrating electric cars and enhancing the use of renewable energy would extend the time of oil's availability, allowing other types of transport such as airplanes and ships to utilise the available resources. Moreover, the batteries of electric vehicles can be exploited as an additional grid storage reserve, where excess renewable energy can be stored and balance the variation in electricity demand. These reserves could also be utilised in emergencies or during unforeseen blackouts [3].

* Corresponding author.
E-mail address: Amin.Al-Habaibeh@ntu.ac.uk (A. Al-Habaibeh).

https://doi.org/10.1016/j.enbenv.2020.07.005
Available online 12 August 2020

A notable advantage that electric cars possess is their high efficiency in energy use. They also produce zero emissions at point of use, which contributes to considerable reduction of greenhouse gas emission from the transportation sector [4].

Despite the advantage of electric cars, widespread implantation of a fleet that consists mainly of EVs would lead to some challenges regarding the grid electricity generation system. Charging a high number of cars during peak hours could cause a considerable increase in electricity demand, leading to a significant overloading on the grid. A possible solution for that would be an adaptation of smart grid technology and demand management into the grid's infrastructure. This can be achieved by scheduling the charging processes accordingly with priority policies by recognising the vehicles with higher urgency of recharging. This would aid in flattening the demand curve and hence avoiding overloading the grid. Then, it is important to determine an appropriate charging rate (i.e. power consumption) for all electric cars that are connected to the grid [4].

The 2009 Climate Change Act for Scotland sets a target to decrease greenhouse gas emissions by 2050 to 80% compared to the emission levels in 1990. Five major steps were identified to achieve such goals [5]. These steps involve the reduction of fossil fuel usage and promoting the implementation of more renewable energy, which would help in reducing greenhouse gas levels. By 2016, Scotland has managed to introduce carbon capture and storage technologies. Also, the reduction of 12% in electricity demand has already been achieved. In addition, the country has closed the last operational coal power station shifting the electricity production to nuclear and renewables [5].

Even in places where the main source of electricity to charge electric cars is from fossil fuel, this would still have a positive impact on the environment. In an experimental case study to charge electric cars in Italy using electricity from fossil fuel, the amount of carbon emissions did not exceed the EU traffic limits of 100 g/km [6].

Some of the disadvantages of electric cars are the long charging times of the batteries, the relative short range of vehicles, and the high initial cost. The running cost of electric cars is considered to be lower compared to internal combustion engine cars, due to lower taxes the price difference between electricity and fossil fuel [7].

This paper suggests a novel approach which investigates a scenario where all conventional light-duty vehicles to be replaced by electric cars in Scotland. Vehicles and energy-related data from the years 2015–2016 is chosen for this paper's analysis. In order to properly investigate the situation, a literature review has been conducted regarding the electricity consumption in Scotland. Greenhouse gas emissions from energy generation and traffic pollution assuming the most popular cars among the gasoline/diesel and the electric technologies are estimated. The assessment of carbon emission when expanding renewable energy generation is also investigated. The paper also highlights a novel mathematical modelling and the implementation of infrared thermography to estimate energy losses in winter for electric cars and the effect on their travel range.

1.1. *Brief description of conventional and electric vehicles*

The amount of emissions released by conventional vehicles depends on the car's condition and how it is used. Those types of vehicles burn fuel to produce the energy which powers the engine. The fuel is drawn from the tank into one of the engine's cylinders. Each of the cylinders draws petrol/diesel in sequences together with the necessary quantity of air. The sparks, or pressure in case of diesel engines, ignite the mixture of fuel and air resulting in sudden expansion in volume within the engine's pistons causing them to move to produce the necessary motion. This motion from the pistons causes the driveshaft to be turned. The driveshaft then moves the axles via the gearbox, and as a consequence of that, the wheels of the car will rotate, producing the car's movement. The burnt fuel creates exhaust gases that are emitted into the atmosphere [8]. In 1870, the first internal combustion engine powered by gasoline (petrol) was invented [9]. On the other hand, electric vehicles do not require chemical fuel. They require electricity to charge their batteries. The energy stored in the battery is utilised to power one or more electric motors via a controller. The electric motor is responsible for driving the vehicle's wheels. Some models have two motors placed on each axle of the car. Since electric vehicles do not use fossil fuels to be powered, they do not produce any emissions [10]. It is well known that at the end of the 19th century, electric cars were very common due to the simplicity of the technology. It has been observed that in 1899, 90 percent of taxi cabs in New York were electric [11]. Electric Vehicles (EVs) are considered to aid in reducing the levels of greenhouse gas emissions, particularly on busy roads. Oil as a resource is limited, and integrating electric cars will reduce the consumption of petroleum, increasing the time for its depletion and allowing other modes of transport, such as air and water to rely on oil. It has been suggested that the batteries on electric vehicles can be exploited as an additional grid storage system to store excess electrical energy to balance supply and demand [12]. Even though electric vehicles are eco-friendly, there are some challenges. One of them is the battery's low capacity, as well as its high cost. The small number of charging stations also poses a challenge at the moment. If more people start to use electric cars, the electricity demand from power stations will rise, hence contributing to greenhouse gas emissions unless more renewable or green energy resources are developed to replace coal, oil, and gas.

Table 1
Sources of electricity in Scotland and their Carbon Factor *reproduced based on data from reference* [16].

Source of electricity	Carbon Factor (gCO_2/kWh)
Nuclear	26
Coal	220
Gas	170
Hydro	7
Renewable	41.25

1.2. *Electricity and carbon emission in Scotland*

According to surveys in the monitoring of greenhouse gas (GHG) levels by the Scottish Government [13], about 20% of the greenhouse emissions are from conventional cars. Approximately 97% of the greenhouse gases are represented by carbon dioxide and a small amount by nitrous oxides, methane, and fluorinated gases [13].

Annually the electricity consumption in Scotland is approximately 38,000 GWh. The country produces on average 50,000 GWh of electricity and the amount that is not consumed locally is exported to England and Northern Ireland [14]. Fig. 1 presents the electricity generated, by source, between 2000 and 2016 and Fig. 2 shows the energy mix in Scotland in 2015–2016.

It has to be mentioned that when electricity is generated and distributed, there are losses through the grid, and Scotland is not an exception; the losses of the grid for the country are estimated to be approximately 17% [15].

Each source of electricity emits a different amount of carbon dioxide per unit of energy produced. The term used to describe this carbon footprint of the source of electricity is called the Carbon Factor. The unit of carbon factor is gCO2/kWh. Table 1 presents the Carbon Factor for each energy source.

Taking into consideration the generation mix for the period 2015–2016, the carbon emissions from the electricity generation are estimated to be approximately 5 $MtCO_2$/year [14]. Depending on the generation mix, the number of emissions would vary. A high number of countries are focusing on building new nuclear power stations and utilising more renewable resources to reduce carbon emission and air pollution.

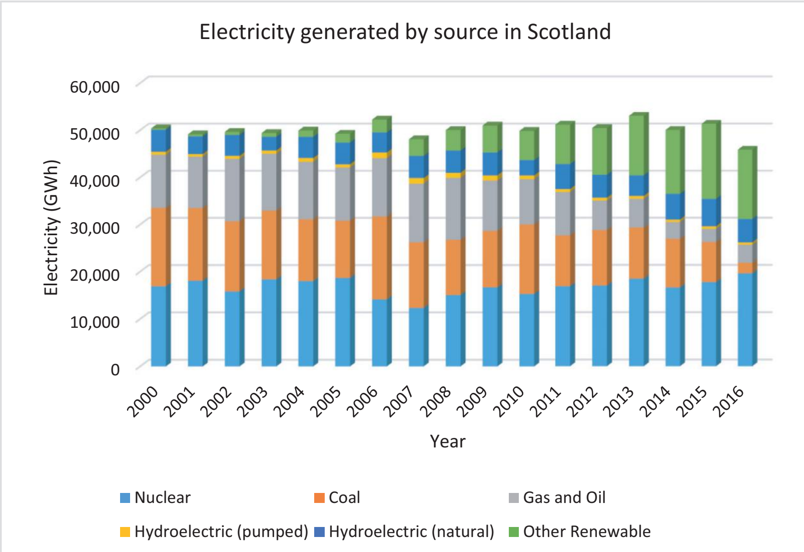

Fig. 1. Electricity produced by source between 2000 and 2016, *figure reproduced based on data from reference* [14].

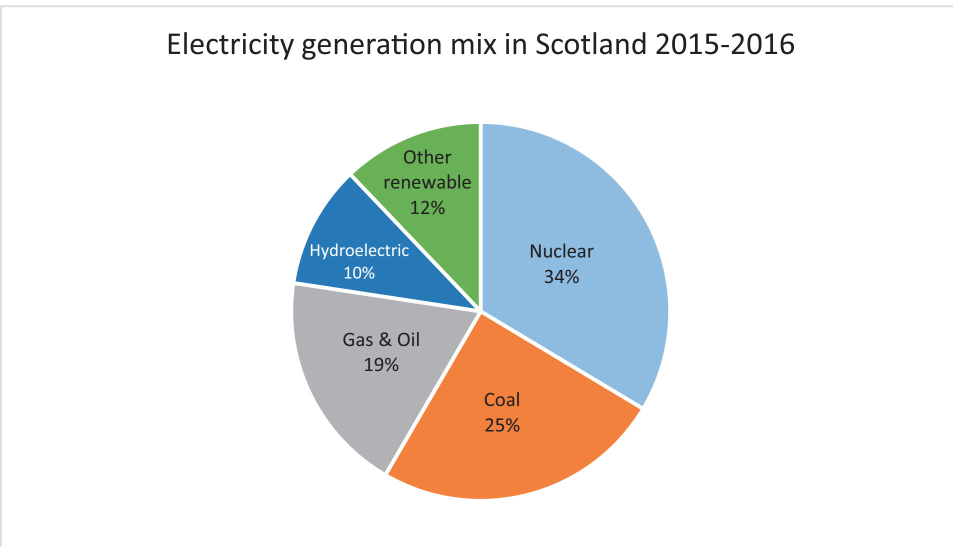

Fig. 2. Electricity generation mix of Scotland (2015), *figure reproduced based on data from reference* [14].

1.3. Traffic levels in Scotland

The average mileage per year of a vehicle in Scotland for the period 2015 – 2016 was roughly 11,362 km [17]. The number of vehicles in the Scottish fleet for the same period was estimated to be approximately 2240,000 [17]. According to data from Scottish traffic monitoring, approximately 80% of the fleet consists of light-duty vehicles [18]. According to this, it was estimated that light-duty cars produce roughly 3.6 Mt Carbon emissions per year [14].

Preferable car brands play an important role in the number of released greenhouse gases. Every conventional vehicle brand releases a different amount of carbon emission, and every electric car consumes a different amount of electricity, therefore, the emission from the electricity generation will vary. Research in the electric vehicles market in 2015 for the UK has revealed that among the most popular cars in this category were Nissan Leaf, BMW i3, Renault Zoe, Volkswagen e-UP, and Tesla Model S. Table 2 presents the top 5 registered electric and their specifications [19].

The same research has also been done for conventional light-duty cars, alongside their specifications, as shown in Table 3.

When comparing between winter and summer, the wasted heat from the internal consumption engine can be utilised to heat the passenger's compartment and prevent condensation on the windscreens. However, electric cars will need to consume energy from the battery to provide thermal comfort for passengers during cold weather. And the faster the car, the more are the heat losses, hence reducing the range of the electric car [21]. The winter in Scotland tends to be consistent with very little variations in temperatures with an average minimum winter temperature of approximately 1 °C [22], see Fig. 3. This is expected to reduce the electric vehicles' range in winter.

1.4. Economics

From an economic perspective, the end-user is affected differently. The amount of money that a car driver is spending annually varies, depending on the type of vehicle, driven distance and driving conditions. Conventional cars require fuel whereas electric ones need electricity. The price of electricity and fuel is significantly different. The price of electricity and fuel varies depending on economic conditions. For the period between 2015 and 2016, that price was estimated to be around 12 pence per kWh of electricity [23]. For the same period, the price of a litre of fuel in the UK was approximately £1.3 [24]. Because Electric vehicles, plug-in EVs in particular, produce less than 50 gCO_2/km are considered emission-less [25]. For that reason, they are eligible to re-

Table 2
Top 5 registered electric vehicles in the UK for 2015, *reproduced based on data from reference* [19].

Brand	Battery capacity (kWh)	Consumption (kWh/100 km)	Number of registered cars in 2015	Price (£)	Distribution (%)
Nissan Leaf	24	14	11,000	29,000	49
BMW i3	22	13	3574	38,000	16
Renault Zoe	22	11	3327	21,000	15
Volkswagen e-UP	18.7	14	2500	19,000	11
Tesla Model S	85	16.9	2000	75,000	9

Table 3
Top 5 registered conventional vehicles in the UK for 2015, their CO_2 factor, price, Distribution, and average fuel consumption, *reproduced based on data from reference* [20].

Vehicle model	CO_2 (g/km)	Price (£)	Distribution (%)	Number of registered cars	Consumption (L/100 km)
Ford Fiesta	147	15,400	30	133,434	4
Vauxhall Corsa	129	10,800	21	92,077	4.7
Ford Focus	159	18,000	19	83,816	3.7
Volkswagen Golf	112	20,600	16	73,409	3.9
Nissan Qashqai	162	19,800	14	60,814	4

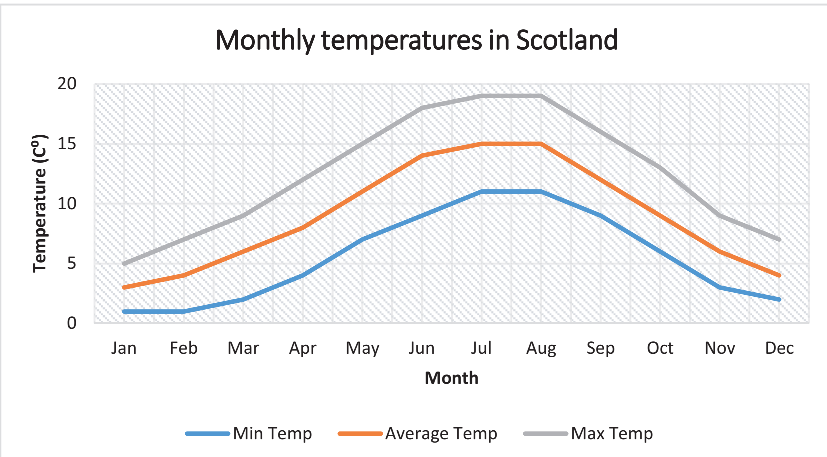

Fig. 3. The average monthly temperatures in Scotland *reproduced based on data from reference* [22].

ceive a 35% grant from the price of the electric car as a subsidy, which in most cases is reduced from the price of the vehicle. The maximum amount of that subsidy is £3500 [25].

1.5. Aim

This paper aims to determine what would be the impact on electricity demand, carbon emission and running and ownership costs, in a proposed scenario where fossil fuel light-duty vehicles are replaced with electric ones in Scotland.

2. Methodology

In order to find out what the effect of switching to electric cars would be, the methodology is divided into three parts: energy demand, carbon emissions, and costs.

2.1. Energy demand

The literature review has provided information on how much electricity is produced in Scotland annually and how much is the demand in a year. The number of light-duty cars is presented for the period 2015 – 2016. The first step of the methodology is to determine the increase in demand for electricity when moving from fossil fuel to electricity. In order to acquire an appropriate number, it has been found important to discover what are the most popular electric cars for Scotland, Eq. (1) is utilised to determine the average value of electricity consumption among the most popular electric cars based on the market share for each brand and its specifications. The equation is as follows:

$$EC_{total} = \sum_{i=1}^{n} \left(EC_i \times PP_i \right) \qquad \text{(Eq. (1))}$$

Where *EC* represents the Electricity consumption (kWh/100 km) and *PP* is the Percentage Proportion of the vehicles according to the brand's popularity, represented as (value)% per 100; *n* is the number of cars included in the investigation.

Knowing how much is the annual mileage done by a car and how much is the average energy consumption of electric cars, the energy demand of a single car can be determined as:

$$RE = (ADT \div 100) \times AEC \qquad \text{(Eq. 2)}$$

Where, ***RE*** represents the Required Electricity for a single electric car (kWh), *ADT* is the Annual Distance Travelled (km), and *AEC* is the Average Electricity Consumption of an electric car (kWh/100 km). After determining *RE*, it is multiplied by the number of light-duty vehicles (2240,000). Through the literature review, the losses through the electricity grid have been established to be 17% which will be lost from the total electricity generated, hence 17% additional energy will need to be generated to compensate for that.

Determining the required variables, Eq. (2) will determine how much electricity a single car on average would need. By multiplying that value by the number of light-duty cars in Scotland, the annual electricity required to power all the electric vehicles for a year can be determined.

Fig. 4. The infrared image of the tested car during winter with calibrated temperatures based on the measured values from the temperature data logger.

It has been found also important to include the grid losses, which will give a more accurate value of the required future energy. Both current and future scenarios of electricity generation will be compared in this paper.

2.2. Heating of car's passenger compartment

Electric Vehicles will need to consume some of the power from the battery for heating the passengers' compartment. Hence, heating will affect electricity consumption and the available range. When considering the average interior space volume of light-duty vehicles, it has been estimated to be 2.93 m^3 [26]. Assuming the internal temperature is kept at 21 °C as the desired temperature, the minimum average ambient temperature in Scotland during the winter season is estimated to be 1 °C [22]. The following equation hence can be used to determine the heat required to warm up the car's interior:

$$E = m \times c \times \left(T_d - T_c\right) \quad \text{(Eq. (3))}$$

Where: $\boldsymbol{E}$ is the energy required to reach the desired temperature $\boldsymbol{T_c}$; $\boldsymbol{m}$ is the mass of air inside the car; $\boldsymbol{c}$ is the specific heat capacity of the air inside the car in J/kg. °C; and $\boldsymbol{T_d}$ is the desired temperature in °C.

Before applying Eq. (3), the mass of air ($\boldsymbol{m}$) is determined using the following calculation:

$$m = \rho \times V \quad \text{(Eq. (4))}$$

Where ρ is the density of the air in kg/m^3; and V is the volume of the car's interior space volume in m^3.

The heat losses through the windows and external envelop are calculated using Eq. (5) [27]:

$$P = 5.67 \times \varepsilon_{hot} \times \left[\left(\frac{T_i}{100}\right)^4 - \left(\frac{T_{out}}{100}\right)^4\right] + 3.8054 \times \vartheta \times \left(T_i - T_{out}\right) \quad \text{(Eq. (5))}$$

Where: P is the thermal power loss through convection and radiation in W/m^2; ε_{hot} is the emissivity which for glass is 0.93 [28] and for iron/aluminium is 0.29 [28]; Ti is the surface temperature in K; T_{out} is the ambient temperature in K; *3.8054* is the convection heat transfer coefficient in W/m^2.K; ϑ is the wind speed in m/s. For ϑ the speed of a car is chosen to be on 60 miles/h or 97 km/h, which is in SI units will be 27 m/s.

In order to determine T_i for the windows' surface and the car's body surface properly, a thermal image of a vehicle is taken and a temperature data logger was attached to the external body of the car to evaluate the temperature performance. The car was driven at 60 miles per hour and the external surface temperature of the car was measured. Fig. 4 presents the infrared image of the car, with calibrated temperature readings. The results have indicated that T_i for the windows was 9.9 °C and the vehicle's body surface was 5.5 °C. The authors have used a diesel engine car to estimate the windows and body temperature when the internal compartment is at 21 °C. The assumption is that an electric car will need to maintain the same internal temperature from the batteries for a similar journey and weather conditions.

Eq. (5) is used for the total windows and windscreens area which is estimated to be at a temperature of 9.9 °C and an area of 2.96 m^2; and also for the car body (doors and panels) which is estimated to have an area of 5.57 m^2 [29] and at a temperature of 5.5 °C. Eq. (4) is used to calculate the energy needed to keep the passengers' compartment at a temperature of 21 °C with the assumption that the driver is the only person on-board without other passengers. This analysis will provide the amount of energy that will be needed from the battery to keep the driver at a comfortable temperature and prevent condensation on the windscreen (ignoring any electric heaters used directly to heat the windscreen). This is expected to influence the actual range of the car in cold weather and the analysis will provide an insight into this. The average range of an electric car is calculated using Eq. (1) to determine the average battery capacity and Eq. (2) to find out the average range of an EV. Eq. (2) is used to calculate the range when the heating is needed and to compare the range in warm weather when heating is not needed but ignoring air conditioning systems for cooling). The analysis assumed the driver's body will produce 100 W of heat while in the car.

2.3. Carbon emission

The literature review has provided useful information on how much carbon emission light-duty vehicles produce and the carbon factor of each source of electricity in Scotland for the period of 2015–2016, and the information needed on how much electricity Scotland produces per annum and the carbon factor of each source. The carbon emission level can be calculated for each energy source using Eq. (6):

$$CE = AE \times CF \quad \text{(Eq. (6))}$$

Where *CE* is the Carbon Dioxide Emission from the electricity production in kg; *AE* is the amount of electricity in kWh; and *CF* is the carbon factor of the source of energy in kgCO_2/kWh. To simplify the presentation of figures, the Carbon Emission values are presented in kilotons (kTons).

Following the calculation of the carbon emission from each source, the total carbon emission for each scenario is calculated taking into consideration the electricity generation mix by percentages and an estimated 17% of grid losses. Using the same methodology as above,

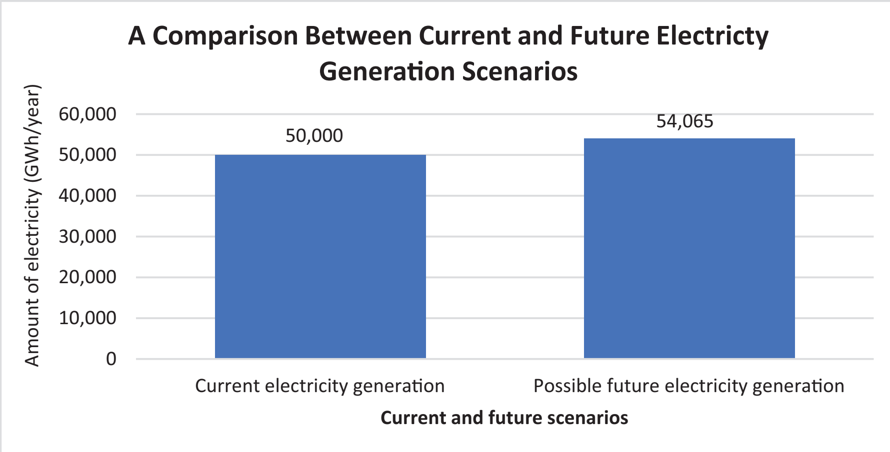

Fig. 5. A comparison between the current and future scenarios of electricity generation.

the amount of carbon emission from the additional energy generation needed for electric cars is calculated. Hence, the carbon emission level between the current time period (2015–2016) and the possible future scenario of electricity generation is considered. From the literature review, it has been found that the CO_2 emission from the current traffic is about 3.6 Megatons (MTons) per year.

2.4. Initial and running costs

It has been found essential to estimate the ownership and the running cost of electric cars in comparison to conventional technology. Eqs. (1) and (2) are utilised to determine the average fuel consumption among conventional cars in Scotland and how much fuel the total amount of light-duty vehicles in Scotland would need. Such values are needed in order to calculate the cost of fuel for a year per vehicle. Knowing consumption values and the price of fuel (£/L) and electricity (£/kWh), the cost of running an electric car versus a conventional car can be compared.

3. Results

3.1. Energy demand

Using Eq. (1), the average electricity consumption among popular electric cars in Scotland is calculated to be 13.65 kWh/100 km. This value is used in Eq. (2), which allowed us to determine the annual energy required for a single electric car, which is estimated to be 1551 kWh. By multiplying the required energy per vehicle to the number of light-duty vehicles on the road (2240,000 vehicles), the total energy required for all the electric cars in Scotland would be 3474,045,120 kWh, or simply 3474 GWh. The grid loss of 17% has been considered as well to get a more accurate value for the required energy that will need to be produced. Hence the total energy to be generated is 1.17 × 3474 GWh, making the minimum future energy generation to be 4065 GWh. Fig. 5 presents the electricity production needed in both scenarios.

3.2. Car heating

The power needed to heat the car's interior during the winter, including heat losses through windows and car's body surface; assuming a car speed of 60 miles per hour and the ambient temperature of 1 °C, is calculated to be 5.36 kW. Which when expressed in terms of range, this will be equivalent to a reduction in the range of about 28%, given the above-assumed conditions and that only the driver is on-board. Fig. 6 presents an example of the expected difference in the range of an electric vehicle during cold and warm seasons due to the power needed to heat the car's interior and windscreens in cold weather.

3.3. Carbon emissions

By applying Eq. (6), the carbon dioxide emission from the electricity generation produced from each source for the period of 2015–2016 and in the case of the future scenarios are presented in Table 4 and Fig. 8, which compare between five scenarios of carbon emissions of Scotland, as follows:

(a) The current scenario with the current energy mix (the current number of conventional cars).
(b) A future scenario of carbon dioxide emission, assuming the same current energy mix, for the additional electricity to charge the new electric cars.
(c) A future scenario of carbon dioxide emission with fixed current coal production levels but no further energy coal production for the additional energy.
(d) The assumed current scenario of carbon dioxide emission if the energy from coal is replaced by other sources as relative benchmark.
(e) A future scenario of carbon dioxide emission when no electricity is produced from coal and the rest of the energy mix maintains the same energy ratio.

Adding the additional amount of CO_2 emissions to the current scenario, (scenario a), reveals that the future carbon dioxide levels would be approximately 5503.3 kTons for the same energy mix (scenario b). It is expected that coal will be phased out either only for the additional energy produced for electric cars (scenario c); or completely eliminated (scenario e), where more renewable and nuclear energy will be utilised to generate electricity.

Scenario (d) is an assumed scenario for the current carbon emission from the electricity grid when coal is eliminated from the energy mix while maintaining the same ration of other energy sources. This suggests that carbon emissions from the grid will be reduced as renewable energy produce about 47.25 gCO_2/kWh, whereas coal is emitting approximately 220 gCO_2/kWh.

The resultant carbon emission and percentage of energy mix are presented in Fig. 7, where scenario (e) could be achieved by removing all coal from the mix, this should achieve a reduction in carbon dioxide emission of about $\frac{5089.50-3372.94}{5089.50} = 33.7\%$.

From Fig. 8, it can be concluded that the total amount of emissions from traffic and electricity production combined will decrease when electric cars are implemented in the Scottish fleet. This is an estimated decrease of approximately $\frac{27.2-24.1}{27.2} = 11.4\%$, this is the overall reduction from all sectors combined including residential, grid, transportation, industrial and agriculture.

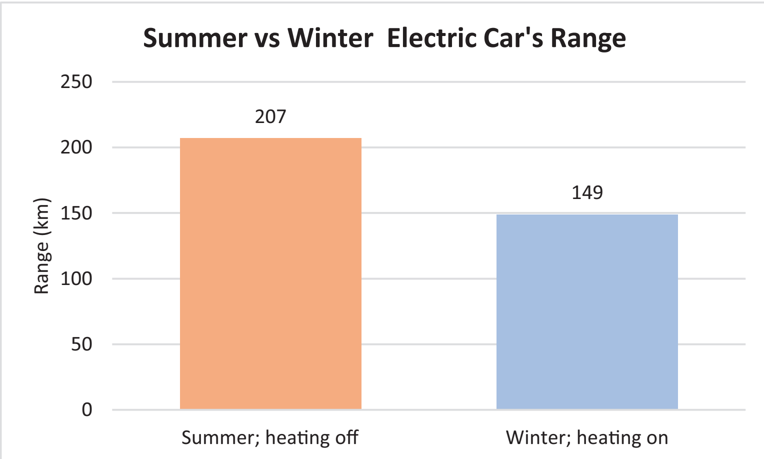

Fig. 6. A comparison between an EV during the summer and an EV during the winter with heating on.

Table 4
The amount of CO_2 emitted from the electricity generation produced from each source for current and future scenarios.

	Scenario (a) Current Emissions	Scenario (b) Future Emissions (*assuming current% of energy mix*)	Scenario (c) Future Emissions (*with fixed coal production levels*)	Scenario (d) Current Emission (*assumed replacement of all coal energy sources*)	Scenario (e) Future Emissions (*no coal sources*)
Source	**Emissions per source (kTons CO_2/year)**	**Emissions per source (kTons CO_2/year)**	**Emissions per source (kTons CO2/year)**	**Emissions per source (kTons CO_2/year)**	**Emissions per source (kTons CO_2/year)**
Nuclear	442	447.94	489.91	589.33	637.25
Coal	2750	2973.59	2750	0	0
Gas	1615	1746.3	1790.07	2153.33	2328.4
Hydro	35	37.85	38.79	46.67	50.46
Renewables	247.5	267.62	274.33	330	356.83
TOTAL	**5089.5**	**5503.3**	**5343.1**	**3119.33**	**3372.94**

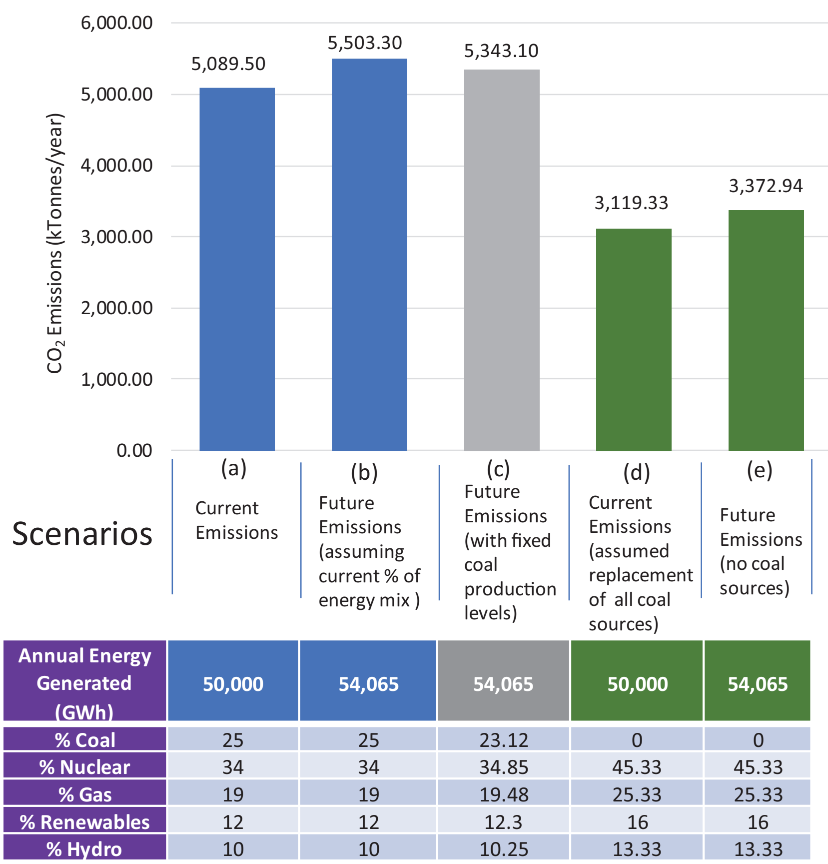

Fig. 7. A comparison between five scenarios of carbon dioxide emissions from electricity generation.

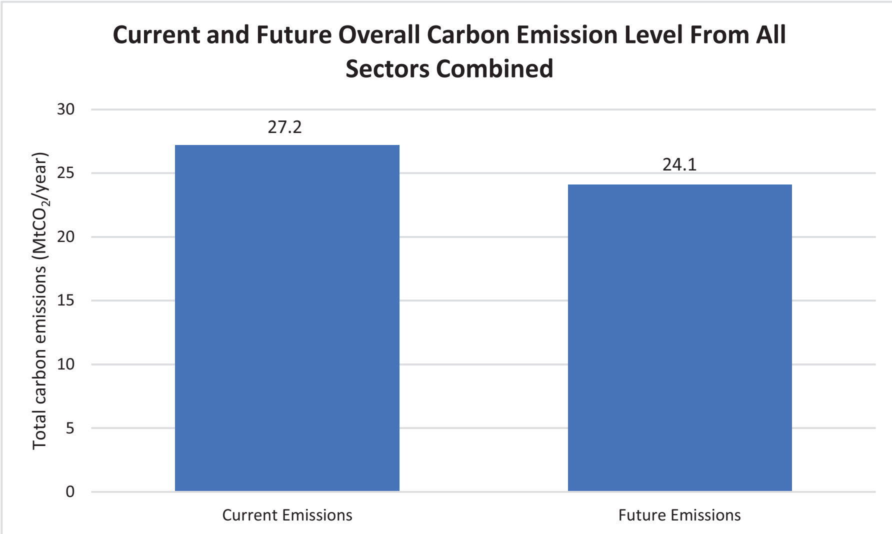

Fig. 8. A comparison between the current and future total carbon emission in Scotland from all sectors.

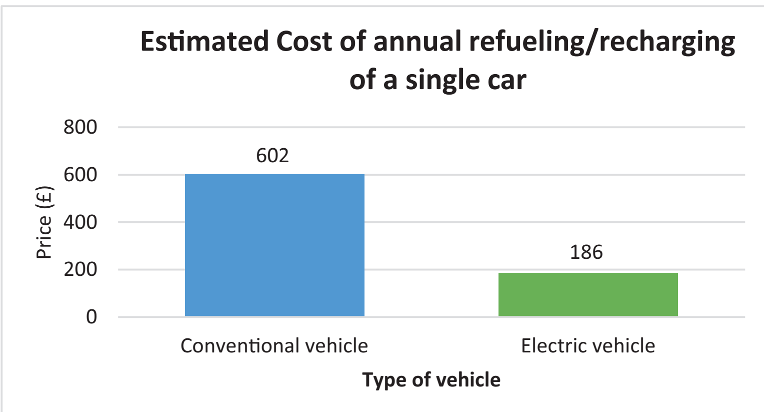

Fig. 9. A Comparison of refuelling/recharging cost for 1 year.

3.4. Estimated costs of ownership and use

The application of Eq. (1). Eq. (2) has revealed that a petrol/diesel car would need approximately 483 Litres of fuel in order to cover the expected annual mileage of 11,362 km per vehicle. For the same distance, an electric vehicle would need about 1551 kWh to cover the required distance per annum. Taking the price of fuel and electricity into consideration, the results are presented in Fig. 9 where the estimated running costs of a petrol/diesel fuel and electric vehicle are estimated to be £602 and £186 respectively. Hence, it is clear that electric cars are about 69.1% cheaper to be powered. In this analysis, maintenance costs are ignored for both types of vehicles.

Fig. 10 presents the initial ownership cost of both types of vehicles. Currently, it is estimated that electric cars are currently 97% more expensive than conventional ones without any subsidy.

Since the maximum subsidy of an electric vehicle that can be granted in the UK is £3500, **Fig. 11** presents the overall cost indicating electric cars to be only 75.7% more expensive.

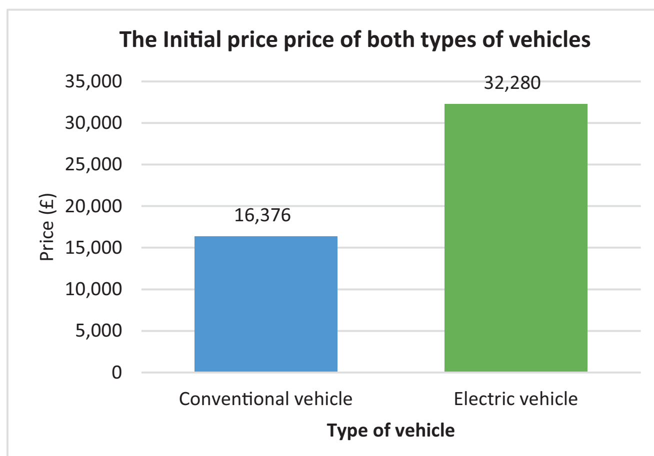

Fig. 10. The initial cost comparison between electric and conventional cars.

4. Discussion

This paper has looked at a case study scenario where every light-duty vehicle in Scotland is assumed to be replaced by an electric car. The investigation and the calculations are based on the popular brands and models of both types of vehicles for the period of 2015–2016. For popular cars, the number of registered ones in 2015 is considered. In the future, changes can be expected, because new and more efficient vehicles may appear in the market. Due to such expected changes, the prices of vehicles and fuel/electricity may vary through the years. Car models that have been considered new for that period will drop in price with time. The situation with the price of electricity and fuel is similar, their price varies slightly through the years. When the demand for electricity increases it is expected that its cost might rise as well. Since 2016 the prices of electricity from solar panels and wind turbines have

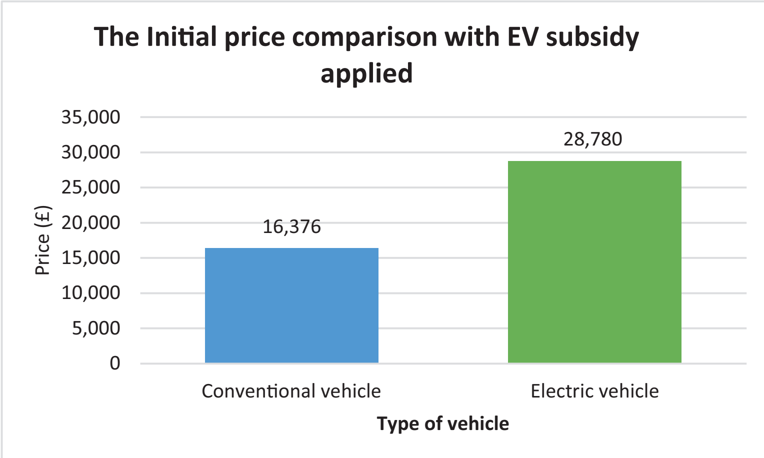

Fig. 11. Initial cost comparison between electric and conventional cars with EV subsidy applied.

significantly decreased. In fact, nowadays wind energy is considered to be the cheapest source for electricity production. According to Wind Europe [30], the cost of offshore wind is expected to decrease to €60 (£55)/MWh by 2025. Bloomberg New Energy Finance (BloombergNEF) also predicted that by 2022 the ownership cost of electric cars will decrease below the conventional diesel and petrol ones. In addition, the cost of lithium-ion batteries has dropped by 65% between 2010 and 2016 and it is expected that by 2030 the price of EV batteries will drop below $120/kWh (circa £98/kWh) [31].

Regarding the economic point of view, this paper has not taken into consideration the maintenance cost of conventional and electric vehicles, more specifically the engine and battery life. Another important point excluded from this paper is the fact that Battery EV (Plug-in EV) owners are exempt from road tax [32]. From the economic perspective, another point which is not taken into consideration is the cost of the charging stations that owners may pay for. Those costs normally include a monthly fixed fee and a demand charge [33].

In March 2016, Longannet, the 2400 MW coal-fired power station was closed, leaving Scotland with very little energy generated from that source [34]. Since then the country distributed that demand across gas and wind energy. This has led to a more sustainable future which is discussed in this paper causing a positive prediction regarding carbon emissions from the energy generation sector. CO_2 levels are expected to be reduced over the coming years in Scotland. Hence, further research in the area will be required when more renewable energy is added to the grid [35]. As for the emissions in Scotland, only values from the traffic and the electricity generation are considered in this paper. The emission from the manufacturing of both types of cars is not considered in this paper. Research show that there are no significant difference in the carbon emission; however, electric cars require slightly more carbon to be manufactured due to the battery [36]. However, life-cycle assessment of both types of vehicles should be investigated further in order to acquire more accurate numbers on the long term, given the expected improvement of the technology of the battery.

The production of electric car batteries contributes to the generation of carbon emissions, which has not been taken into consideration in this paper. Conventional vehicles do not only contribute directly to CO_2 emissions by burning the fuel, but also indirectly by the extraction of oil, its process operations, and the transportation of gasoline/diesel to the gas stations, which all produce carbon emissions. That is not included in this investigation either. Moreover, the additional energy that will be needed for heating during cold seasons is not included in the analysis of energy demand for electric cars, and it will be the subject of futures studies due the variation in weather conditions. Further research is still required to explore further the effect of the electric cars on the environment, and their cost impact on the owners.

5. Conclusion

The scenario of replacing all diesel and petrol light-duty vehicles in Scotland with electric cars would have diverse pros and cons. As a result of the massive expansion of electric vehicles, the electricity demand will be expected to rise and hence the production of more energy leading to a slight increase in carbon emission levels. Although the CO_2 levels are expected to rise in such a situation, the traffic emissions will decrease significantly because there would not be any light-duty vehicles to pollute during operation. Therefore, this will lead to a reduction in the total amount of carbon emissions from the electricity grid by approximately 33.7%.

In addition, during cold weather, owners would need to use the electric heating of the car, which uses energy from the battery, this is expected to reduce the range by 28%.

With extended utilisation of electric vehicles, owners would spend more money as an initial cost compared to conventional cars (about 75.7%%) even with the EV subsidy in the UK. In the long term, electric vehicles would save money to their owners, because of the considerably low price of electricity compared to that of petrol and diesel fuel, with estimated savings of about 69.1% per annum.

All in all, the extended usage of electric vehicles in such scenario is expected to have a positive impact on the environment. Although, it depends on what the electricity generation mix is. The more eco-friendly sources are used to generate electricity, such as renewables and nuclear power plants, the more the positive impact would be. One of the main advantages is reducing pollution on busy roads and in cities, which should contribute to better public health conditions.

Declaration of Competing Interest

The authors declare that there is no conflicts of interest.

CRediT authorship contribution statement

George Milev: Software, Validation, Writing - original draft, Visualization, Formal analysis, Conceptualization, Investigation. **Astley Hastings:** Supervision, Conceptualization, Methodology, Validation, Writing - review & editing. **Amin Al-Habaibeh:** Supervision, Conceptualization, Methodology, Investigation, Validation, Writing - review & editing, Visualization, Formal analysis.

Acknowledgment

The authors would like to thank DTA3 COFUND H2020/Marie Skłodowska-Curie PhD Fellowship programme for partially funding this research work (Grant Agreement Number: 801604).

References

[1] L. Erickson, Reducing greenhouse gas emissions and improving air quality: two global challenges, Environ. Prog. Sustai.n Energy 36 (4) (2017) 982–988.
[2] NOAAState of the climate: Global Analysis For Annual 2016, NOAA National Centers for Environmental Information, Washington, DC, 2017 www.ncdc.noaa.gov/.
[3] Amoroso, F.A. (2014) Eco-Friendly Innovation in Electricity Transmission and Distribution Networks.
[4] Z.-.H. Zhu, Z.-.Y. Gao, J.-.F. Zheng, H.-.M. Du, Charging station location problem of plug-in electric vehicles, J. Transp. Geogr. 52 (2016) 11–22, doi:10.1016/j.jtrangeo.2016.02.002.
[5] Deben, L. et al. "Reducing Emissions In Scotland". Committee on Climate Change 2015 Progress Report (2015): 9-30; 42–49.
[6] T. Donateo, et al., Evaluation of emissions Of CO_2 and air pollutants from electric vehicles In Italian cities, Appl. Energy 157 (2015) 675–687.
[7] M. Aziz, T. Oda, M. Ito, Battery-assisted charging system for simultaneous charging of electric vehicles, Energy 100 (2016) 82–90, doi:10.1016/j.energy.2016.01.069.
[8] Stefansson, J.. "What Makes the Wheels Move on a Car?" sciencing.com, https://sciencing.com/wheels-move-car-6302814.html. 29 October 2019.
[9] E. Eckermann, in: World History of the Automobile, SAE Press, 2001, p. 14.
[10] Moss, D. (2019). How do Electric Cars Work?. [online] What Car?. Available at: https://www.whatcar.com/advice/buying/how-do-electric-cars-work/n18091 [Accessed 29 Oct. 2019].
[11] D. Hiskey, In 1899 Ninety Percent of New York City's Taxi Cabs Were Electric Vehicles, 2011 [online] Today I Found Out. Available at: https://www.todayifoundout.com/index.php/2011/04/in-1899-ninety-percent-of-new-york-citys-taxi-cabs-were-electric-vehicles/ [Accessed 20 May 2019].
[12] Amoroso, F.A. (2014) Eco-Friendly innovation in electricity transmission and distribution networks. Available at: http://ac.els-cdn.com/B9781782420101000173/3-s2.0-B9781782420101000173-main.pdf?_tid=8ec36222-150e-11e6-b1da-00000aacb360&acdnat=1462706475_6f2dc0e2e96f63589282373fc7937dd3 [Accessed 29 Oct. 2019].
[13] Scottish Greenhouse Gas Emissions (2013). Gov.scot. N.p., 2016. Web. [Accessed 29 Oct. 2019].
[14] "Energy - Electricity Generation". Gov.scot. N.p., (2016). Web. Accessed [29.10.2019].
[15] "Energy In Scotland 2015″. Gov.scot. N.p., (2016). Web. [Accessed 29 Oct. 2019].
[16] House of Parliament, in: Carbon Footprint of Electricity Generation, Parliamentary Office of Science & Technology. [online] London: House of Parliament, 2011, pp. 1–4. Available at: https://www.parliament.uk/documents/post/postpn_383-carbon-footprint-electricity-generation.pdf, [Accessed 29 Oct. 2019].
[17] Transport Scotland (2014) Table 1: basic travel statistics – national travel survey: http://www.transport.gov.scot/statistics/j314725-05.htm [Accessed 29 Oct. 2019].
[18] Transport Scotland (2016) Chapter 5: road traffic. Available at: http://www.transport.gov.scot/statistics/j357783-08.htm [Accessed: 29 Oct. 2019].
[19] Lane, B. (2016) Quick links. Available at: http://www.nextgreencar.com/electric-cars/statistics/ [Accessed 29 Oct. 2019].
[20] Top 6 conventional cars, their price, and carbon factor: https://www.autoexpress.co.uk/best-cars/90327/best-selling-cars-2015-record-year-for-uk-car-sales [Accessed 29 Oct. 2019].
[21] Zart, N. (2019). Yes, Electric Vehicles Work In Winter — Better Than Gas Cars! | CleanTechnica. [online] CleanTechnica. Available at: https://cleantechnica.com/2019/02/17/yes-electric-vehicles-work-in-winter-better-than-gas-cars/ [Accessed 18 Nov. 2019].
[22] Scotland Info Guide. (2019). Scotland Weather and Climate. [online] Available at: https://www.scotlandinfo.eu/scotland-weather-and-climate/ [Accessed 18 Nov. 2019].
[23] Electricity price in the UK - https://www.ukpower.co.uk/home_energy/tariffs-per-unit-kwh [Accessed 29 Oct. 2019].
[24] Price of fuel in the UK between 2015 and 2019 https://www.statista.com/statistics/299552/average-price-of-diesel-in-the-united-kingdom/ [Accessed 30 Oct. 2019].
[25] GOV.UK. (2019). Low-emission vehicles eligible for a plug-in grant. [online] Available at: https://www.gov.uk/plug-in-car-van-grants [Accessed 8 Nov. 2019].
[26] Fueleconomy.gov. (2019). Frequently Asked Questions. [online] Available at: https://www.fueleconomy.gov/feg/info.shtml#sizeclasses [Accessed 22 Nov. 2019].
[27] A. AL-HABAIBEH, G. ANDERSON, K. DAMJI, G. JONES, K. LAM, Using infrared thermography for monitoring thermal efficiency of buildings - case studies from Nottingham Trent University, in: Proceedings of the Seventh Jordanian International Mechanical Engineering Conference (JIMEC'7), Amman, Jordan, 27-29 September 2010, 2010.
[28] Engineeringtoolbox.com. n.d. *Emissivity Coefficients Materials*. [online] Available at: <https://www.engineeringtoolbox.com/emissivity-coefficients-d_447.html> [Accessed 30 June 2020].
[29] Jackson, L. (2008). Why There Won't Be a Solar Powered Car - Washington Times. [online] Washingtontimes.com. Available at: https://www.washingtontimes.com/blog/spinning-wheels-community-car-lovers/2008/jul/26/why-there-wont-be-a-solar-powered-car/ [Accessed 22 Nov. 2019].
[30] Wind Europe. 2020. Economics | Windeurope. [online] Available at: https://windeurope.org/policy/topics/economics/#:~:text=Unsubsidized%20onshore%20wind%20energy%20is,)%2FMWh%20in%20H1%202018 [Accessed 1 July 2020].
[31] Carrington, D., 2016. *Electric Cars 'Will Be Cheaper Than Conventional Vehicles By 2022'*[online] the Guardian. Available at: https://www.theguardian.com/environment/2016/feb/25/electric-cars-will-be-cheaper-than-conventional-vehicles-by-2022 [Accessed 30 June 2020].
[32] Pod-point.com. (2019). Road Tax on Electric Cars | Pod Point. [online] Available at: https://pod-point.com/guides/driver/road-tax-on-electric-cars [Accessed 11 Nov. 2019].
[33] Knupfer, S., Noffsinger, J. and Sahdev, S. (2019). How Battery Storage can Help Charge the Electric-Vehicle Market. [online] McKinsey & Company. Available at: https://www.mckinsey.com/business-functions/sustainability/our-insights/how-battery-storage-can-help-charge-the-electric-vehicle-market [Accessed 11 Nov. 2019].
[34] Macalister, T. (2016). Longannet Power Station Closes Ending Coal Power Use in Scotland. [online] the Guardian. Available at: https://www.theguardian.com/environment/2016/mar/24/longannet-power-station-closes-coal-power-scotland [Accessed 8 Nov. 2019].
[35] L. Erickson, G. Brase, Reducing Greenhouse Gas Emissions And Improving Air Quality. Two Interrelated Global Challenges, 1st ed., CRC Press, 2019.
[36] K. Holmberg, A. Erdemir, The impact of tribology on energy use and CO2 emission globally and in combustion engine and electric cars, Tribol. Int. 135 (2019) (2019) 389–396 Pages.

Energy and Built Environment 2 (2021) 214–222

Contents lists available at ScienceDirect

Energy and Built Environment

journal homepage: http://www.keaipublishing.com/en/journals/energy-and-built-environment/

Full Length Article

Energy saving analysis of a transparent radiative cooling film for buildings with roof glazing

Zhitong Yi[a], Yingyan lv[a], Dikai Xu[b], Jingtao Xu[a,*], Hua Qian[b,c], Dongliang Zhao[b,c,*], Ronggui Yang[d,e]

[a] Ningbo Ruiling Advanced Energy Materials Institute Co., Ltd, Ningbo 315500, China
[b] School of Energy and Environment, Southeast University, Nanjing 210096, China
[c] Engineering Research Center of Building Equipment, Energy, and Environment, Ministry of Education, China
[d] School of Energy and Power Engineering, Huazhong University of Science and Technology, Wuhan 430074, China
[e] State Key Laboratory of Coal Combustion, Huazhong University of Science and Technology, Wuhan 430074, China

ARTICLE INFO

Keywords:
Transparent radiative cooling film
Spectrum selective
Window film
Building energy saving

ABSTRACT

A transparent radiative cooling (T-RC) film with low transmittance in solar spectra and selectively high emissivity in the atmospheric window (8–13 μm) is applied on roof glazing for building energy saving. To evaluate the performance of the T-RC film, two identical model boxes (1.0 $m \times 0.6\ m \times 1.2$ m, $L \times W \times H$) were constructed and the inside air temperatures were measured in August in Ningbo, China. Results show that the maximum temperature difference between the two model boxes with and without the T-RC film was 21.6 °C during the experiment. A whole building model was built in EnergyPlus for the model box. With a good agreement achieved between the calculation results and the measured temperature data, the experimentally validated EnergyPlus model was then extended to an 815.1 m^2 exhibition building with roof glazing to analyze the annual air conditioning (AC) energy consumption. The results show that by incorporating both the T-RC film's cooling benefit in summer and heating penalty in winter, the annual AC energy consumption of the exhibition building can be reduced by 40.9–63.4%, varying with different climate conditions.

1. Introduction

Energy saving and environment protection are critical issues in the world today. Buildings account for 20–40% of total energy consumption in different countries [1–3]. In hot climates, up to 50% of the building cooling load could come from the large amount of solar energy passing through glazing systems [4–6]. Therefore, it is desirable to realize building energy saving through adjusting thermophysical properties of the glazing systems, especially for those buildings with large areas of roof glazing systems.

The overall heat transfer coefficient (h), which characterizes air to air heat transfer through the glazing system, can be reduced by an order of magnitude through coatings, increasing thickness of glass pane, using multiple glass panes, increasing the gap between the glass panes, as well as using extremely low thermal conductivity materials in the gap [7–9]. Researchers have also focused on adjusting optical properties of the glazing systems to reduce solar heat gain, which can reach 1000 W/m^2 in hot climates [10]. A low solar heat gain coefficient (SHGC) can significantly reduce the initial investment and operational cost of air conditioning (AC) system [11–14]. In the meantime, visible transmittance (T_v), a factor that determines visibility of glazing material, should be maintained at a relatively high level to avoid additional energy consumption for artificial lighting [13]. Therefore, the ideal optical properties of selective transmission spectra in solar irradiation range are: zero transmittance in the ultraviolet (0.3–0.4 μm) and the near-infrared (0.7–2.5 μm) range, and enough transmittance (usually > 0.6) in the visible range (0.4–0.7 μm). A few technologies, for example, tinted glazing, coated glazing, and window films, fall in this category [7,9].

Emissivity is another important thermophysical property for glass pane thermal radiation in the mid-infrared range (2.5–20 μm). The well-known low emissivity (low-e) coating exhibits relatively low SHGC and high reflectance (low emissivity) in the mid-infrared range. By reflecting thermal radiation from outdoor (in summer) and indoor environment (in winter), the low-e coatings achieve energy saving by maintaining relatively stable indoor temperatures [15–17]. However, it may hinder heat dissipation in summer when temperature of the glass pane is high. Therefore, the low-e coating technique is not always favorable for building energy saving in all climates.

Glass pane that has high selective emissivity in the atmospheric window (8–13 μm) is more beneficial for reducing building cooling load in

* Corresponding authors.
E-mail addresses: ichi0014@hotmail.com (J. Xu), dongliang_zhao@seu.edu.cn (D. Zhao).

https://doi.org/10.1016/j.enbenv.2020.07.003
Available online 26 July 2020

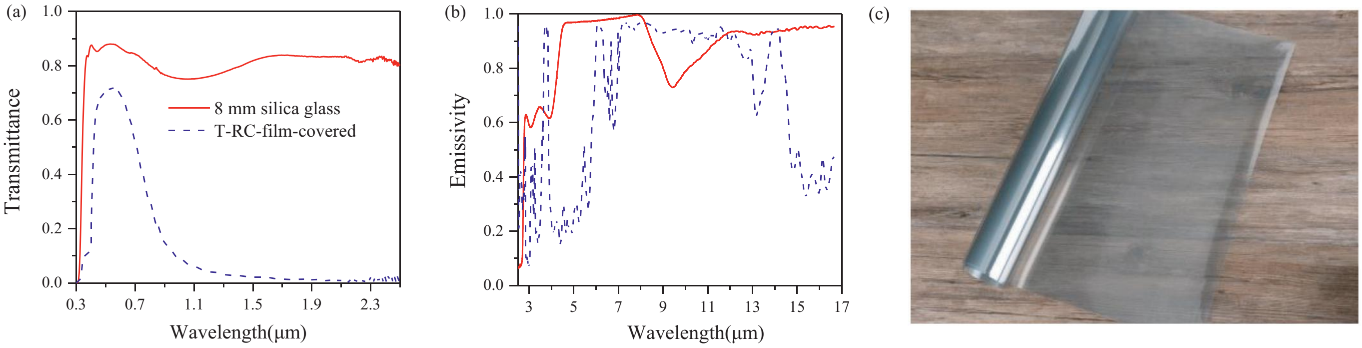

Fig. 1. The spectral curves for the silica glass with and without the T-RC film: (a) solar transmittance; (b) infrared emissivity; (c) a photo of the T-RC film.

hot climates. Radiative sky cooling phenomena allows such glass pane to emit mid-infrared electromagnetic waves directly to the outer space through the atmospheric window [18-29]. Regular silica glasses usually have a high emissivity with a dip in 8–13 μm wavelengths region (see Fig. 1b), which absorb considerable thermal radiation from the atmosphere and the ambient environment. A glazing system with selectively high emissivity (~0.9) in 8–13 μm and low emissivity in 2.5–8 μm and 13–20 μm wavelengths region can significantly reduce absorption of thermal radiation outside the atmospheric window while enhancing the radiative sky cooling effect. Installing such a roof glazing system in public buildings, such as exhibition halls, shopping malls, libraries, and sports stadiums, can be an effective way for building energy saving.

Earlier radiative cooling films achieve cooling effect through simultaneously solar reflection and infrared emission [30–33]. Therefore, these films are opaque in the visible wavelengths, which make them not appropriate for glazing applications. In this study, a transparent radiative cooling (T-RC) film, which is different from opaque radiative cooling films [23], is applied on roof glazing for building energy saving. The T-RC film has almost ideal optical properties: transparent for visible light with a small SHGC in the solar spectra, and high emissivity (~0.9) in the atmospheric window and low emissivity in 2.5–7 μm and 13–20 μm wavelengths. The unique optical properties of the T-RC film make it appropriate for glazing systems. More importantly, the film can be fabricated by the mature roll-to-roll method at low cost, which makes it suitable for large scale deployment. To evaluate the performance of the T-RC film, two identical model boxes were constructed and the temperatures of air inside were measured in August in Ningbo, China. Results show that the maximum temperature difference between the two model boxes with and without the T-RC film was 21.6 °C during the experiment. A whole building simulation model was built in EnergyPlus to reproduce the measured temperatures for the model boxes. After validation of the simulation model, it was then extended to an 815.1 m^2 exhibition building with roof glazing to analyze the annual building air conditioning (AC) energy saving with the T-RC film. By incorporating both the T-RC film's cooling benefit in summer and heating penalty in winter, the annual AC energy consumption of the exhibition building can be reduced by 40.9–63.4%, varying with different climate conditions, which suggest that the T-RC film can be applied on roof glazing systems for building energy saving.

2. System description and modeling

2.1. The transparent radiative cooling (T-RC) film

The 0.2-mm-thick T-RC film is a hybrid metamaterial made of polyethylene terephthalate (PET) and silica microspheres [23]. The silica microspheres are randomly distributed in the PET matrix. The detailed manufacturing process can be found in our previous work [23]. Figs. 1a and 1b show the solar spectral transmittance and the mid-infrared spectral emissivity of an 8-mm-thick silica glass with and without the T-RC film. Fig. 1c shows a photo of the T-RC film. After applying the T-RC film, the 8-mm-thick silica glass shows almost ideal optical properties: low SHGC (~0.4), appropriate visible transmittance Tv (~0.63), and selectively high emissivity (>0.90 in 8–13 μm wavelength range). Up to now, 10 months of outdoor aging test show less than 0.2% change in T-RC film optical properties, and 750 h of accelerated aging test (85 °C temperature, 70±10% relative humidity, and 180 W/m^2 UV intensity) show less than 0.5% change in optical properties. According to [34], 250 h of artificial accelerated aging test is equivalent to about 1 year of nature outdoor aging. Therefore, it is concluded that the T-RC film should have less than 0.5% change of optical properties in 3 years in outdoor conditions.

2.2. Experimental setup

Two identical model boxes were built, as shown in Fig. 2. The dimension of the two boxes was 1.0 $m \times 0.6$ $m \times 1.2$ m ($L \times W \times H$). 50-mm-thick XPS thermal insulation was used on the interior walls and floors. The top glazing of the model box A was 8-mm-thick silica glass, and the top glazing of the model box B is the same glass covered by the T-RC film, as shown in Figs. 2a) and 2b). The detailed parameters of the model boxes are listed in Table 1. The model boxes were placed on a flat and unsheltered roof in Ningbo, China.

Three K-type thermocouples were used in each model box to measure temperature of the air inside with their positions shown in Fig. 2c. A weather station (Model NHQXZ601) was used to measure the local weather conditions, *i.e.*, ambient temperature, solar irradiation, humidity, and wind speed. The recording time interval of the abovementioned parameters is one minute.

Fig. 3 gives the schematic diagrams of the heat transfer processes between the two model boxes and the ambient. With the T-RC film applied, more incoming solar irradiation is reflected, and at the meantime, radiative sky cooling effect is enhanced, which results in a lower air temperature inside. In the morning, the solar heat gain through the glass increases with the increase of the solar irradiation, yet, heat conduction, convection, and radiation energy coming out of the glazing is not enough to dissipate the absorbed solar energy. Therefore, the inside air temperature rises until when the solar irradiation peaks. After then, the heat conduction and convection start to play a major role with the decreasing of the solar irradiation. And the inside air temperature decreases accordingly. This trend will last until sunset. Then, the radiative sky cooling plays a primary role and the inside air temperature continues to drop till the next sunrise. The difference in solar heat gain, heat conduction, radiative sky cooling, and convective cooling of the top glazing results in different air temperatures inside the two boxes.

2.3. Experimental results

To evaluate the cooling performance of the T-RC film, measurement of the inside air temperatures in the two model boxes were conducted

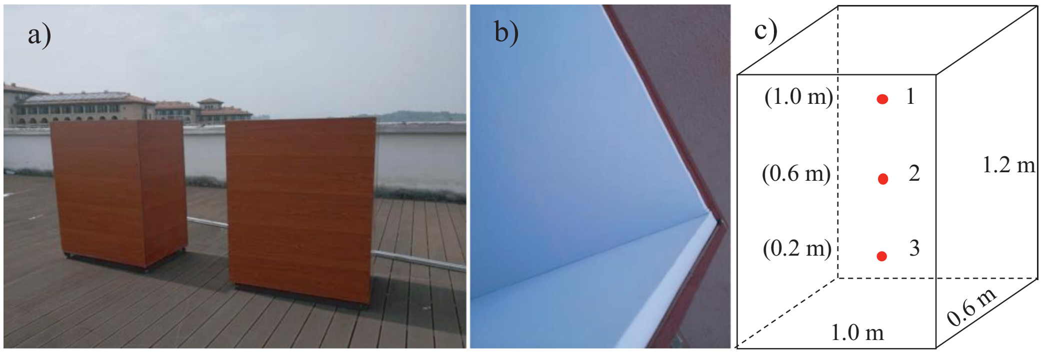

Fig. 2. The experimental platform of the two model boxes: (a) exterior view; (b) interior view; (c) the positions of the thermocouples.

Table 1
Detailed envelope information of the model boxes.

Components	Envelope (from exterior to interior)	Thermal conductivity W/(m K)	Density (kg/m^3)	Specific heat [J/(kg•K)]
Wall	Glued wood (20 mm)	0.17	600	1200
	XPS (50 mm)	0.042	30	1386
	White wallpaper (-)	–	–	–
Floor	Glued wood (20 mm)	0.17	600	1200
	XPS (100 mm)	0.042	30	1386
Roof	Box B: T-RC film (0.2 mm) covered on the silica glass (8 mm)	0.5 (film), 1.04(glass)	1.4 (film), 2100 (glass)	2.2 (film), 740 (glass)
	Box A: Silica glass (8 mm)	1.04	2100	740

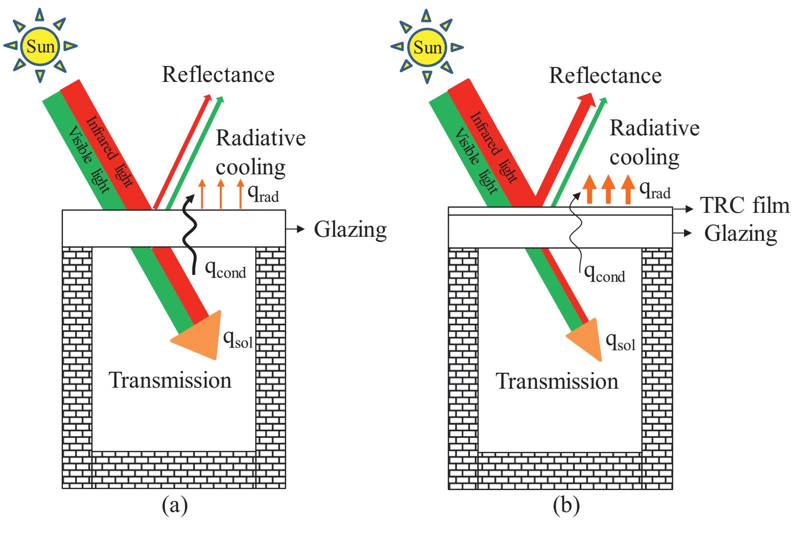

Fig. 3. Schematic of solar irradiation and heat transfer through the two boxes: (a) a typical silica glazing; (b) the T-RC-film-covered glazing.

on August 15th to 16th, 2019, as shown in Fig. 4. The meteorological data during the experiments were also recorded, as shown in Fig. 5. Figs. 4a–4c) show the inside air temperatures at points 1–3 of the boxes respectively, and Fig .4d) shows the average inside air temperature. The average temperature was used as the inside air temperature to analyze the difference between the box A and box B, as well as the model validation.

The inside air temperatures of the box A and box B decrease from sunset to sunrise. The inside air temperature of box B was slightly lower than that of box A at night due to higher emissivity of the T-RC film in the atmospheric window. When the sun rises, as solar irradiation increases, the inside air temperature differences of these two model boxes sharply increase due to the different optical properties of the glazing with and without the T-RC film in solar transmittance and infrared emissivity. The variation trend of the inside air temperature was almost consistent with that of the total solar irradiation. As shown in Fig. 5, the total solar irradiation fluctuates violently from 10:00 to 14:00, Aug 15th. Accordingly, inside air temperatures in both Box A and B fluctuate violently. Due to the high solar transmittance, the increase and decrease rates of the inside air temperatures of box A was higher than that of box B. The peak inside air temperature of box A was 79.6 °C, while that of box B was 61 °C. The maximum temperature difference between these two model boxes was 21.6 °C. And the inside air temperature of box B was always lower than that of box A due to the adjusted solar transmittance and selective absorptance in infrared wavelengths.

Furthermore, according to the experimental results, the temperature stratifications were 8.5 °C and 3.7 °C for the box A and box B, respectively, as shown in Fig. 4a)–4c). The improvement in temperature uniformity of box B should also owe to the adjusted solar transmittance and selective absorptance at the infrared wavelengths. Predictably, with the application of the T-RC film, not only building's AC energy consumption can be reduced, but also occupant thermal comfort can be improved.

2.4. Validation of the EnergyPlus model

The whole building simulation software EnergyPlus (version 8.7) is used to predict the temperature of air inside the two model boxes. EnergyPlus is a reliable whole building simulation tool that researchers

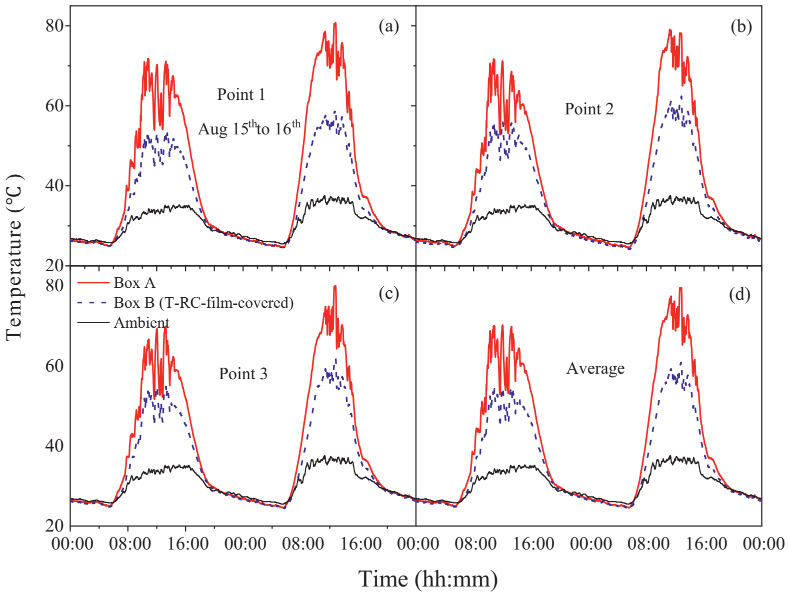

Fig. 4. Field-measured inside air temperatures of measuring point 1 to 3 and their average value.

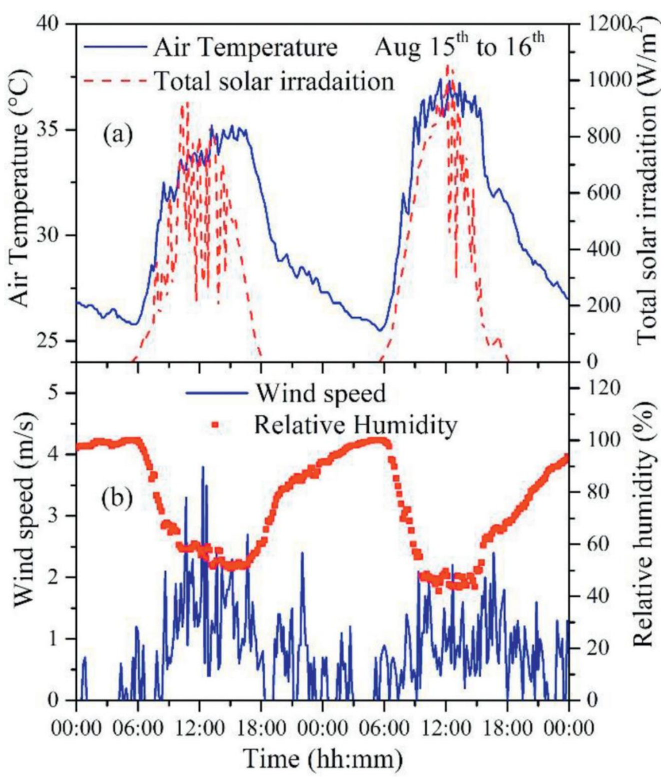

Fig. 5. Measured meteorological data during the experiments.

worldwide use to model energy consumption in buildings. For the model boxes, the input parameters for the EnergyPlus model such as dimensions (see Fig. 2), envelope parameters (see Table 1), optical characteristics (see Fig. 1), and weather data (*e.g.*, ambient temperature, wind speed, and solar irradiation) are set to be the same as in the experiments. The inside air temperatures obtained by using the developed simulation model were validated by comparing with the experimentally measured air temperatures.

Fig. 6 gives the comparison of inside air temperatures obtained by the simulation model and the experiments (the average temperature, see Fig. 4d)). The maximum absolute deviation between simulated and experimental data for the model boxes were 2.5 °C (box A) and 2.7 °C (box B), respectively. Larger deviations usually occur at night and at the time when solar irradiation experiencing strong fluctuation (*e.g.*, sunrise and sunset). Two representatively statistical indicators were used to assess the accuracy of the developed model [35]. The normalized mean bias error (NMBE) can better reflect the actual error of the predicted value, and the coefficient of variation of the root-mean-square error, C_V(RMSE), is used to measure the deviation between the simulation data and the experimental data. Limits of the NMBE and C_V(RMSE) are ± 10% and 30%, respectively [36]. The NMBE and C_V(RMSE) are given by Eqs. (1),(2).

$$NMBE = \frac{\sum_{i=1}^{n} \left(T_{sim,i} - T_{exp,i}\right)}{n} \times \frac{100\%}{\bar{T}} \tag{1}$$

$$C_V(RMSE) = \sqrt{\frac{\sum_{i=1}^{n} \left(T_{sim,i} - T_{exp,i}\right)^2}{n}} \times \frac{100\%}{\bar{T}} \tag{2}$$

where $T_{sim,i}$ and $T_{exp,i}$ are the simulated and experimental value for the i period (hourly), respectively; n is the number of the measured value; $\bar{T}$ is the mean of the measured values.

The NMBE between simulated and experimental data for the two model boxes are 2.15% (box A) and 2.10% (box B), respectively, and the C_V (RMSE) are 3.81% and 3.72%. Therefore, the simulation model developed by EnergyPlus agrees well with the experiments.

3. Model of an exhibition building with roof glazing

3.1. Building description

The simulation results of the box model developed by EnergyPlus was validated by the measured data. And it was then extended to a building with roof glazing, which is a part of a real building (built in 1986) located in Ningbo, China, as shown in Figs. 7a and 7b, to calculate the indoor air temperature and the annual AC energy consumption by using the T-RC film (0.2-mm-thick, see Table 1) on the roof glazing system. The real building has three floors at the east and west adjacent to the glazing-topped exhibition, but has only one floor for the glazing-topped exhibition. This study focuses on the energy saving of the glazing-topped exhibition by using the T-RC film. The exterior dimensions of the building model are 21.36 m × 38.16 m × 16 m (L × W × H), and six windows (2.1 m × 2.5 m, L × H) are installed on the north and south walls, respectively, as shown in Fig. 7c. As a base case, the original glazing system of the building model, with a glazing area of 878.1 m² (roof

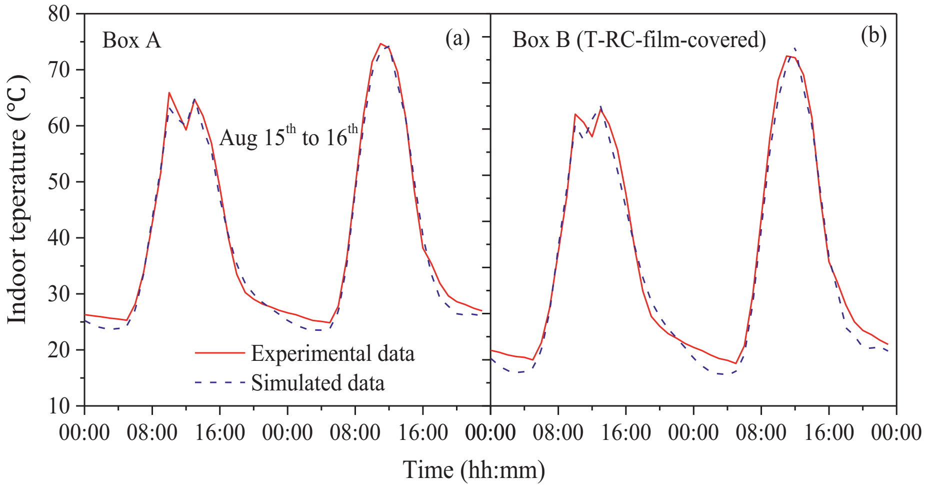

Fig. 6. Comparison of the measured and simulation average inside air temperatures of the two model boxes.

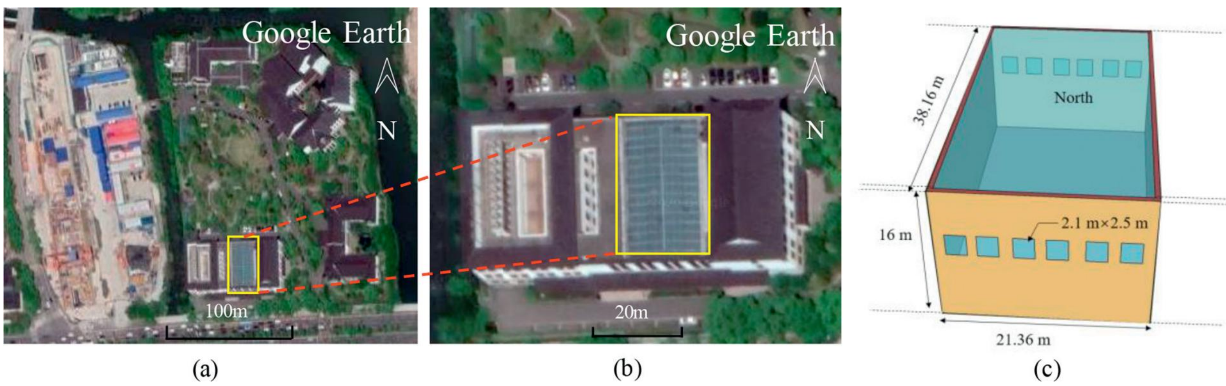

Fig. 7. a) The building is located in Ningbo, China, (b) A closer view of the exhibition building's roof glazing, (c) Schematic diagram of the exhibition building model in EnergyPlus.

Table 2
Summary of the given boundary conditions of the simulation exhibition building model.

Items	Values
Lighting [37]	5 W/m^2, daily from 17:00 to 22:00
Maximum occupant density [38]	0.16 person/m^2, 180 W/person, daily from 08:00 to 22:00
Cooling set point temperature [39]	25 °C, daily from 08:00 to 22:00
Heating set point temperature [40]	18 °C, daily from 08:00 to 22:00
Infiltration rate,%	30
COP of AC system	3.0

and windows), consists of a double-pane clear silica glass (6-mm-thick) with an air gap (12-mm-thick), has an overall heat transfer coefficient of $h = 2.43$ W/(m^2•K)). The east and west walls are the internal walls of the building, which are set to be adiabatic in the building model. To investigate the energy saving potential with the T-RC-film-covered glazing in different climate conditions, four cities in hot summer and cold winter region (*i.e.*, Hangzhou, Chongqing, Shanghai, and Nanjing), and four cities in hot summer and warm winter region (*i.e.*, Fuzhou, Shenzhen, Nanning, and Haikou) are selected in China. The thermal conductivity of all envelope materials meets the requirement of buildings standards. The detailed information of the building envelope is listed in Supplementary Table 1 and Table 2, where δ, λ, and h are thickness, thermal conductivity, and overall heat transfer coefficient, respectively. The lighting load, occupant density, and air-conditioning setup parameters are listed in Table 2.

3.2. The effect of the T-RC film in hot summer and cold winter region

Fig. 8 shows the simulation results of the hourly indoor air temperatures of base case and the T-RC-film-covered building in cities in hot summer and cold winter region when the AC systems are assumed to be not in operation. The peak indoor air temperatures of base case are 49.3 °C, 47.9 °C, 50.5 °C, and 47.2 °C in Hangzhou, Chongqing, Shanghai, and Nanjing, respectively. With the application of the T-RC film, the peak indoor temperatures are 36.2 °C, 36.5 °C, 37.3 °C, and 35.8 °C, respectively. The maximum temperature differences for the given building are over 12.3 °C in these four cities. The indoor air temperature decreases throughout the year due to the significantly low SHGC and higher emissivity in the atmospheric window. In summer, due to the high solar radiation intensity, the average cooling effect fluctuates at around 10 °C in the daytime, while the average cooling effect fluctuates

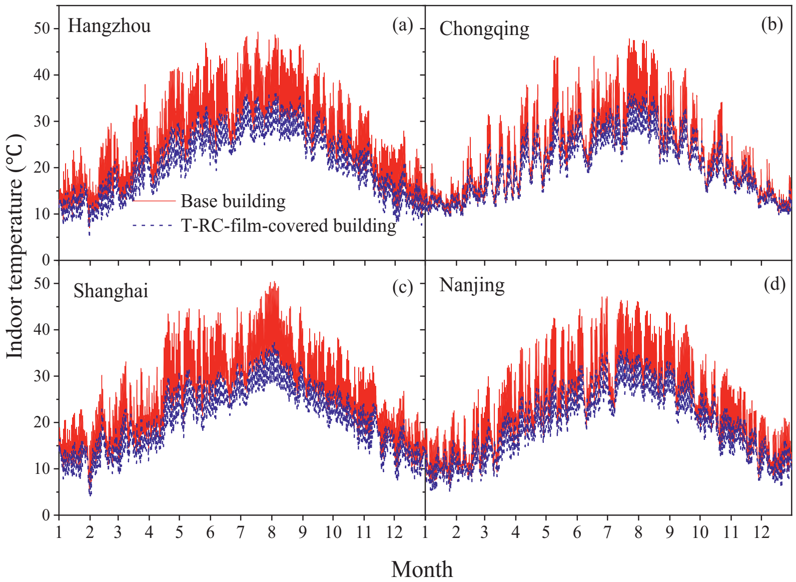

Fig. 8. Comparison of indoor air temperatures of the simulation building in: (a) Hangzhou; (b) Chongqing; (c) Shanghai; (d) Nanjing. .

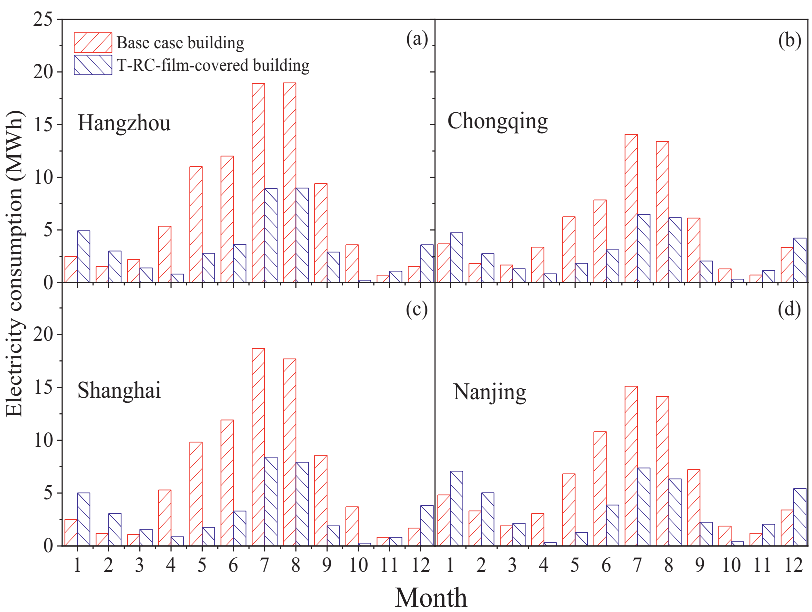

Fig. 9. Comparison of monthly cumulative AC energy consumption in four cities in hot summer and cold winter region with an assumed AC system COP of 3.0.

at around 4∼6 °C at night. It should be noted that the T-RC film still has cooling effect in winter. Fortunately, the average cooling effect fluctuates at around 4∼5 °C in the daytime and 1∼2 °C at night, respectively. The reason is the lower solar irradiation and lower ambient temperature in winter. Predictably, the cooling load decreases and the heating load increases with the application of the T-RC film. However, considering a whole year operation, there's still considerable energy saving due to large indoor temperature reduction in summer.

Fig. 9 shows the monthly cumulative AC energy consumption for the given building in these four cities in hot summer and cold winter region. Apparently, Fig. 9 shows that the energy consumption by using T-RC film in winter increase by 95%, 41%, 96%, and 57% in Hangzhou, Chongqing, Shanghai, and Nanjing, respectively. However, the energy consumption of base case in winter only accounts for 7.1%, 15.0%, 7.5% and 17.3% of the annual AC energy consumption, respectively. According to Fig. 9, the cooling energy consumption in summer is significantly reduced with the application of the T-RC film. Fig. 9 also shows that the cumulative cooling energy consumption from April to October decreased by 64.3%, 60.3%, 67.7%, and 63.2% in Hangzhou, Chongqing, Shanghai, and Nanjing, respectively. The reduction of cooling energy consumption in July and August contributed 44%, 51.8%, 45.3%, and 51.5% to the reduction of annual AC energy consumption, respectively. After coupling the cooling benefit in summer and the heating penalty in winter, the annual cumulative AC energy consumption in the hot summer and cold winter cities decreased by 51.8%, 45.0%, 53.3%, and 40.9%, respectively. The results show that the T-RC film exhibits an excellent performance for energy saving in hot summer and cold winter region.

Moreover, the peak cooling load significantly reduces (between 43.9% and 51.3%) while the peak heating load increases with the application of the T-RC film, as shown in Fig. 10, which indicates that the T-RC film can reduce not only the operational cost but also the initial investment of the AC system for the given building.

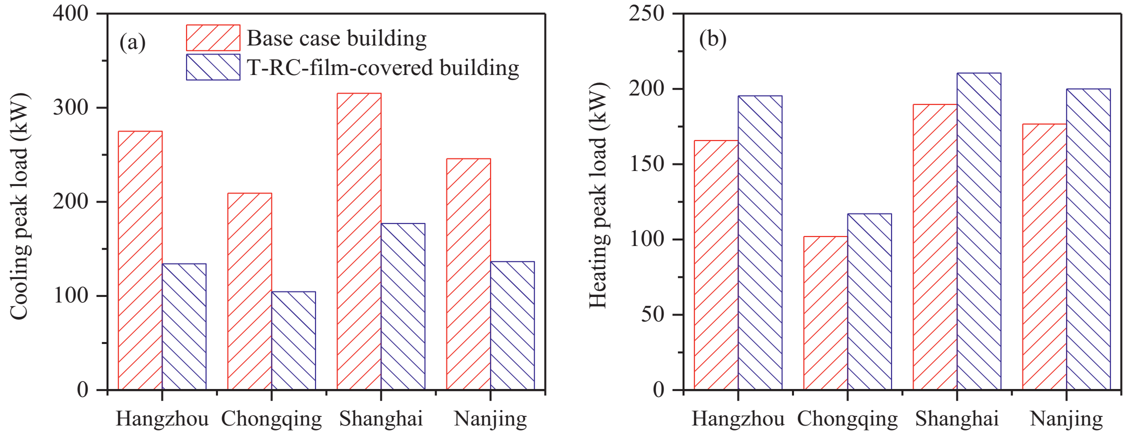

Fig. 10. Comparison of peak cooling and heating loads in four cities in hot summer and cold winter region.

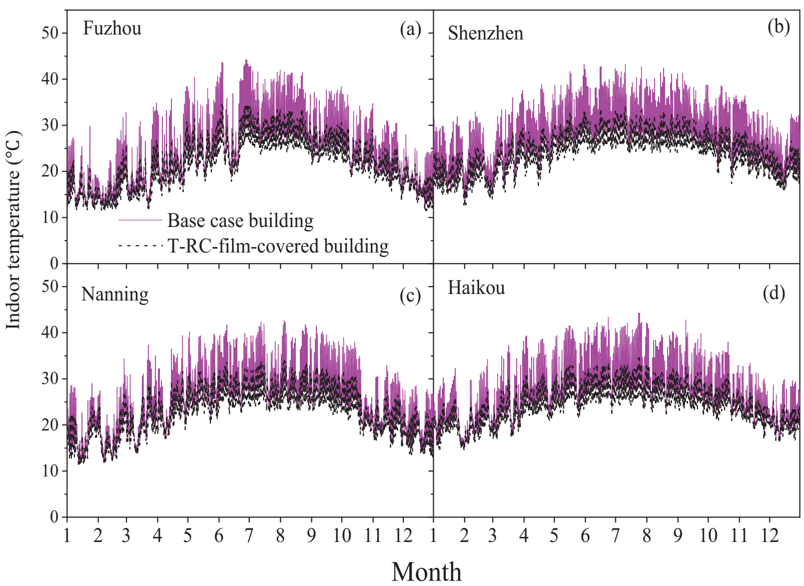

Fig. 11. Comparison of indoor air temperatures of the simulation building in: (a) Fuzhou; (b) Shenzhen; (c) Nanning; (d) Haikou.

3.3. The effect of the T-RC film in hot summer and warm winter region

Fig. 11 shows simulation results of the hourly indoor air temperatures of the base case and the T-RC-film-covered building in cities in hot summer and warm winter region when the AC systems are assumed to be not in operation. The peak indoor air temperatures of the base cases are 42.7~44.4 °C in Fuzhou, Shenzhen, Nanning, and Haikou. While the maximum temperature differences between the base case and the T-RC-film-covered building are 9.3~10.1 °C in these four cities. The peak indoor air temperature and maximum temperature difference in cities in hot summer and warm winter region are lower than those of hot summer and cold winter region cities due to the lower insulation level of the building envelope. Compared to the hot summer and cold winter region cities, heating is rarely needed for those cities in hot summer and warm winter region due to higher ambient temperatures in winter, as shown in Figs. 8 and 11, which is beneficial for energy saving.

Fig. 12 shows the monthly cumulative AC energy consumption for the given building of the four cities in hot summer and warm winter region. The cooling energy consumption is significantly reduced with the application of the T-RC film from March to November in Fuzhou, Shenzhen, Nanning, and Haikou. Since the latitude of Fuzhou (latitude N 25°52′–26°48′) is relatively high, the heating energy consumption will increase in winter, and the effect of the T-RC film in Fuzhou is similar to that in cities in the hot summer and cold winter region, as shown in Fig. 12a). The energy saving can be achieved during the whole year in Shenzhen (latitude N 22°24′–22°52′) and Haikou (latitude N 19°32′–20°05′), as shown in Figs. 12b) and 12d). Since the benefit from cooling energy reduction is offset by the adverse effect of the heating energy enhancement, the total AC energy consumption in winter of Nanning is almost equal to the situation of the base case, as shown in Fig. 12c). After incorporating both the cooling benefit in summer and the penalty in winter, the annual cumulative AC energy consumption in hot summer and warm winter cities are reduced by 63.4%, 61.5%, 55.3%, and 58.2%, respectively, which is much better than those cities in hot summer and cold winter region. Similarly, the peak cooling load significantly reduces (between 49.8% and 52.7%) while the peak heating load increases with the application of the T-RC film in hot summer and warm winter region, as shown in Fig. 13.

4. Conclusions

The selectively high reflectance in solar spectra and selectively high emissivity in atmospheric window of the T-RC film lead to significantly energy saving potential when applied on building roof glazing. Here, two identical model boxes were constructed for comparison study. A simulation model was built in EnergyPlus and validated by using field-measured data. After validating the model, an exhibition building model with roof glazing was established to analyze the annual temperature

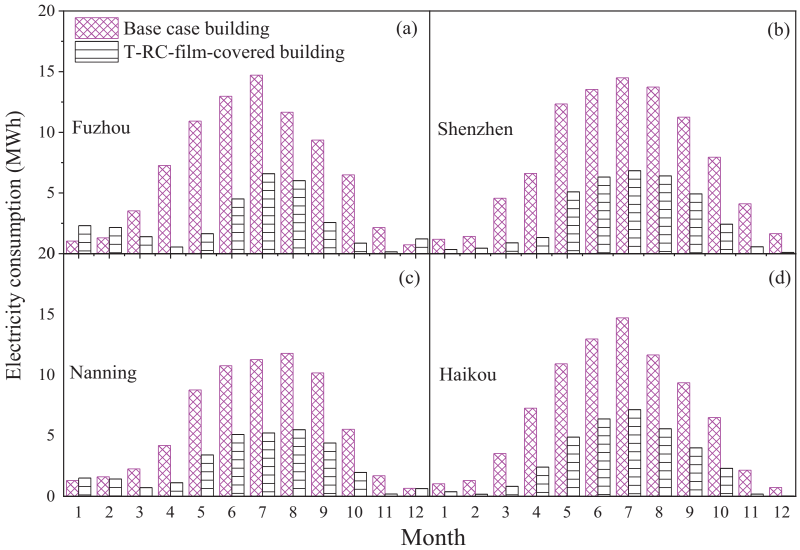

Fig. 12. Comparison of monthly cumulative AC energy consumption in four cities in hot summer and warm winter region with an assumed AC system COP of 3.0.

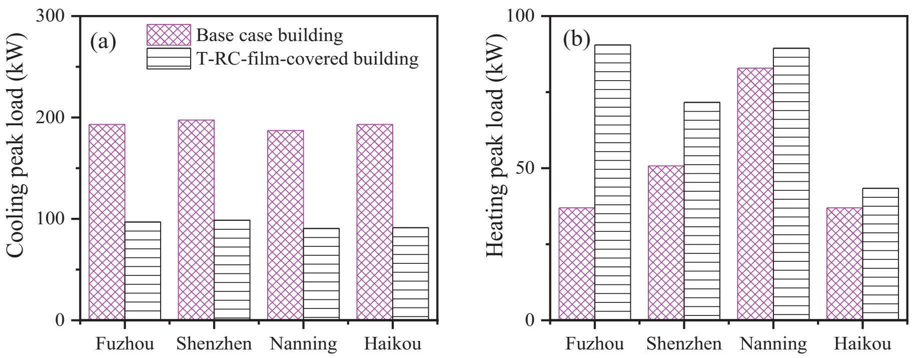

Fig. 13. Comparison of the peak cooling and heating loads in four cities in hot summer and warm winter region.

changes and annual building's AC energy saving with the application of the T-RC film in different regions. The following conclusions can be drawn.

- When the T-RC film is applied on a 1.0 m × 0.6 m × 1.2 m (L × W × H) model box with roof glazing, the inside air temperature of the model box was reduced by a maximum value of 21.6 °C.
- In hot summer and cold winter region, the cooling energy consumption reduces in summer and the heating energy consumption increases in winter by applying the T-RC film. However, incorporating both effects in summer and winter, the annual AC energy saving of the given building is between 40.9% and 51.8%.
- In hot summer and warm winter region, the heating penalty of the T-RC film in winter is almost negligible, especially for Shenzhen (latitude N 22°24′–22°52′) and Haikou (latitude N 19°32′–20°05′). The annual AC energy saving of the given building is between 55.3% and 63.4%.
- With the application of the T-RC film, there is not only a significant AC energy saving, but also a clear economic prospection by reducing AC system's initial and operational cost.

Credit author statement

R.Y., D.Z., and J.X. conceived the concept of this work, Z.Y. and J.X. developed the experimental methodology, Y.L. did EnergyPlus simulation, Z.Y. wrote the original draft, J.X., D.Z., and R.Y. finalized the paper, while all co-authors participated in the discussion.

Conflicts of interest

The authors declare that there is no conflicts of interest.

Acknowledgment

D.Z. acknowledges the support from "the Fundamental Research Funds for the Central Universities" under award number 2242020R10017.

Supplementary materials

Supplementary material associated with this article can be found, in the online version, at doi:10.1016/j.enbenv.2020.07.003.

References

[1] W.J. Hee, M.A. Alghoul, B. Bakhtyar, O. Elayeb, M.A. Shameri, M.S. Alrubaih, K Sopian, The role of window glazing on daylighting and energy saving in buildings, Renew. Sust. Energ. Rev. 42 (2015) 323–343.
[2] E.G. Dascalaki, C.A. Balaras, S. Kontoyiannidis, K.G Droutsa, Modeling energy refurbishment scenarios for the Hellenic residential building stock towards the 2020 & 2030 targets, Energ. Build. 132 (2016) 74–90.
[3] L. Pérez-Lombard, J. Ortiz, C Pout, A review on buildings energy consumption information, Energ. Build. 40 (2008) 394–398.
[4] R. Yin, P. Xu, P Shen, Case study: energy savings from solar window film in two commercial buildings in Shanghai, Energ. Build. 45 (2012) 132–140.
[5] Z. Fang, N. Li, B. Li, G. Luo, Y Huang, The effect of building envelope insulation on cooling energy consumption in summer, Energ. Build. 77 (2014) 197–205.
[6] R. Kou, Y. Zhong, J. Kim, Q. Wang, M. Wang, R. Chen, Y Qiao, Elevating low-emissivity film for lower thermal transmittance, Energ. Build. 193 (2019) 69–77.
[7] S.D. Rezaei, S. Shannigrahi, S Ramakrishna, A review of conventional, advanced, and smart glazing technologies and materials for improving indoor environment, Sol. Energ. Mater. Sol. C 159 (2017) 26–51.

[8] M. Casini, Active dynamic windows for buildings: a review, Renew. Energ. 119 (2018) 923–934.
[9] J.L. Aguilar-Santana, H. Jarimi, M. Velasco-Carrasco, S Riffat, Review on window-glazing technologies and future prospects, Int. J. Low-Carbon Tech. 15 (1) (2020) 112–120.
[10] R. Alik, A Jusoh, Modified perturb and observe (P&O) with checking algorithm under various solar irradiation, Sol. Energy 148 (2017) 128–139.
[11] J. Xamán, Y. Olazo-Gómez, I. Zavala-Guillén, I. Hernández-Pérez, J.O. Aguilar, J.F Hinojosa, Thermal evaluation of a room coupled with a double glazing window with/without a solar control film for Mexico, Appl. Therm. Eng. 110 (2017) 805–820.
[12] J. Xamán, C. Pérez-Nucamendi, J. Arce, J. Hinojosa, G. Álvarez, I Zavala-Guillén, Thermal analysis for a double pane window with a solar control film for using in cold and warm climates, Energ Build. 76 (2014) 429–439.
[13] E. Moretti, E. Belloni, Evaluation of energy, thermal, and daylighting performance of solar control films for a case study in moderate climate, Build. Environ. 94 (2015) 183–195.
[14] A. Bahadori-Jahromi, A. Rotimi, A. Mylona, P. Godfrey, D Cook, Impact of window films on the overall energy consumption of existing UK hotel buildings, Sustain.-Basel 9 (2017) 731.
[15] S.S. Solntsev, V.S Denisova, Reaction-cured composite coatings and glasses, Glass Ceram. 76 (3–4) (2019) 126–130.
[16] B.P. Jelle, S.E. Kalnæs, T Gao, Low-emissivity materials for building applications: a state-of-the-art review and future research perspectives, Energ Build. 96 (2015) 329–356.
[17] R. Kou, Y. Zhong, J. Kim, Q. Wang, M. Wang, R. Chen, Y Qiao, Elevating low-emissivity film for lower thermal transmittance, Energ Build. 193 (2019) 69–77.
[18] T.L. Bergman, Active daytime radiative cooling using spectrally selective surfaces for air conditioning and refrigeration systems, Sol. Energy 174 (2018) 16–23.
[19] D. Zhao, A. Aili, Y. Zhai, S. Xu, G. Tan, X. Yin, R Yang, Radiative sky cooling: fundamental principles, materials, and applications, Appl. Phys. Rev. 6 (2019) 21306.
[20] K. Zhang, D. Zhao, Y. Zhai, X. Yin, R. Yang, G Tan, Modelling study of the low-pump-power demand constructal T-shaped pipe network for a large scale radiative cooled-cold storage system, Appl. Therm. Eng. 127 (2017) 1564–1573.
[21] H. Fang, D. Zhao, J. Yuan, A. Aili, X. Yin, R. Yang, G Tan, Performance evaluation of a metamaterial-based new cool roof using improved Roof Thermal Transfer Value model, Appl. Energ. 248 (2019) 589–599.
[22] D. Zhao, A. Aili, Y. Zhai, J. Lu, D. Kidd, G. Tan, X. Yin, R Yang, Subambient cooling of water: toward real-world applications of daytime radiative cooling, Joule 3 (2019) 111–123.
[23] Y. Zhai, Y. Ma, S.N. David, D. Zhao, R. Lou, G. Tan, R. Yang, X Yin, Scalable-manufactured randomized glass-polymer hybrid metamaterial for daytime radiative cooling, Science 355 (2017) 1062–1066.
[24] D. Zhao, C.E. Martini, S. Jiang, Y. Ma, Y. Zhai, G. Tan, X. Yin, R Yang, Development of a single-phase thermosiphon for cold collection and storage of radiative cooling, Appl. Energ. 205 (2017) 1260–1269.
[25] J. Liu, Z. Zhou, J. Zhang, W. Feng, J Zuo, Advances and challenges in commercializing radiative cooling, Mater. Today Phys. 11 (2019) 100161.
[26] B. Zhao, M. Hu, X. Ao, N. Chen, G. Pei, Radiative cooling: a review of fundamentals, materials, applications, and prospects, Appl. Energ. 236 (2019) 489–513.
[27] M. Hu, B. Zhao, X. Ao, J. Feng, J. Cao, Y. Su, G Pei, Experimental study on a hybrid photo-thermal and radiative cooling collector using black acrylic paint as the panel coating, Renew. Energ. 139 (2019) 1217–1226.
[28] X. Yu, C. Chen, A simulation study for comparing the cooling performance of different daytime radiative cooling materials, Sol. Energ. Mater. Sol. C 209 (2020) 110459.
[29] J. Liu, Z. Zhou, D. Zhang, S. Jiao, J. Zhang, F. Gao, J Zuo, Research on the performance of radiative cooling and solar heating coupling module to direct control indoor temperature, Energ. Convers. Manag. 205 (2020) 112395.
[30] A.P. Raman, M.A. Anoma, L. Zhu, E. Rephaeli, S. Fan, Passive radiative cooling below ambient air temperature under direct sunlight, Nature 515 (7528) (2014) 540–544.
[31] J. Mandal, Y. Fu, A.C. Overvig, M. Jia, K. Sun, N.N. Shi, Y. Yang, Hierarchically porous polymer coatings for highly efficient passive daytime radiative cooling, Science 362 (6412) (2018) 315–319.
[32] T. Li, Y. Zhai, S. He, W. Gan, Z. Wei, M. Heidarinejad, J. Dai, A radiative cooling structural material, Science 364 (6442) (2019) 760–763.
[33] A. Leroy, B. Bhatia, C.C. Kelsall, A. Castillejo-Cuberos, L. Zhao, L. Zhang, E.N. Wang, High-performance subambient radiative cooling enabled by optically selective and thermally insulating polyethylene aerogel, Sci. Adv. 5 (10) (2019) eaat9480.
[34] H. Takebayashi, K. Miki, K. Sakai, Y. Murata, T. Matsumoto, S. Wada, T. Aoyama, Experimental examination of solar reflectance of high-reflectance paint in Japan with natural and accelerated aging, Energ. Build. 114 (2016) 173–179.
[35] J. Pereira, M.G. Gomes, A.M. Rodrigues, M Almeida, Thermal, luminous and energy performance of solar control films in single-glazed windows: use of energy performance criteria to support decision making, Energ. Build. 198 (2019) 431–443.
[36] H. Teixeira, M.G. Gomes, A.M. Rodrigues, J Pereira, Thermal and visual comfort, energy use and environmental performance of glazing systems with solar control films, Build. Environ. 168 (2020) 106474.
[37] Standard for energy consumption of buildings GB 51161-2016. Ministry of housing and urban-rural development, P.R. China, Beijing. 2016.
[38] B. Raji, M.J. Tenpierik, A van den Dobbelsteen, An assessment of energy-saving solutions for the envelope design of high-rise buildings in temperate climates: a case study in the Netherlands, Energ. Build. 124 (2016) 210–221.
[39] S. Mirrahimi, M.F. Mohamed, L.C. Haw, N.L.N. Ibrahim, W.F.M. Yusoff, A Aflaki, The effect of building envelope on the thermal comfort and energy saving for high-rise buildings in hot–humid climate, Renew. Sust. Energ. Rev. 53 (2016) 1508–1519.
[40] M. Mehrpooya, H. Hemmatabady, M.H Ahmadi, Optimization of performance of combined solar collector-geothermal heat pump systems to supply thermal load needed for heating greenhouses, Energ. Convers. Manag. 97 (2015) 382–392.

Energy and Built Environment 2 (2021) 223–232

Contents lists available at ScienceDirect

Energy and Built Environment

journal homepage: http://www.keaipublishing.com/en/journals/energy-and-built-environment/

Impact of metabolism and the clothing thermal resistance on inpatient thermal comfort

Hualing Zhang[a,b,*], Xunshu Xie[a], Shiyao Hong[a], Haitao Lv[a]

[a] School of Civil Engineering, Chongqing University, Chongqing 400045, China
[b] Key Laboratory of Three Gorges Reservoir Region's Eco-Environment, Ministry of Education, Chongqing University, Chongqing 400045, China

ARTICLE INFO

Keywords:
Indoor thermal environment
Thermal comfort
Hospital wards
Clothing thermal resistance

ABSTRACT

For the purpose that relieves the suffering of the patients and shortens their hospital stay, it is crucial to design and manage the environment control systems reasonably to maintain an appropriate indoor thermal environment. However, all of the current thermal comfort theories are based on a healthy population. There are significant differences in metabolism and clothing thermal resistance between inpatients and healthy people, which are regarded as vital influenced factors on people's thermal comfort. Therefore, these existing thermal comfort models may not be applicable for inpatients. In this paper, the patients' comfort equation was derived by modifying the metabolism and the clothing thermal resistance based on the thermal comfort model of Professor Fanger, and the rationality of the model was tested by using field experiment data obtained in general wards. Validated by t-tests, the value of AMV and PMV calculated by the modified equation is not markedly different on a 5% significant level for all patients lying on bed in winter. Moreover, the typical comfort diagrams of inpatients were established by solving the thermal comfort equation. The results of this study are intended to assist in the formulation of useful guidelines to facilitate the assessment and management of hospital ward thermal environments.

1. Introduction

The issues involved with indoor thermal environment and comfort are always the focus of HVAC engineers. As we know that appropriate indoor thermal environments can relieve the suffering of the patients, shorten the patient's hospital stay. Current researches are primarily concerned with the thermal comfort of healthy people but less for the patients. As we know that appropriate indoor thermal environments can relieve the suffering of the patients, shorten the patient's hospital stay. There are differences in thermal comfort demands between patients and healthy people, and it is necessary to consider the coexistence of patients, caretakers and medical staff when HVAC engineers design and manage hospital thermal environments.

Nowadays, there is numerous literature on thermal comfort studies in hospitals and medical buildings. Some researchers were focused on studying parameters of hospital environments; some other studies have been conducted on the thermal response of patients and medical personnel. And there has been some literature focused on assessing the effects of temperature and air humidity changes on hospital air quality and disease infection [1–3]. Current field studies (shown in Table 1) focused on the thermal comfort evaluation of patients applied Fanger's thermal comfort model admitted by ASHARE 55 standard [42] frequently. The detailed results of these researches are as followed: Skoog et al. [4] found that the difference in metabolic rate between patients and staff made their thermal requirements different. Pourshaghaghy and Omidvari [5] conducted field experiments in a hospital in the morning, noon and evening, found out that the females' thermal sensitivity was weaker than males', the range of thermal comfort was more extensive, and the interviewees preferred cool environment. Hwang et al. [6] studied the hospital thermal comfort in Taiwan using ASHRAE Standard 55, but the research did not consider the lying patients. Lee et al. [7] studied on the rank of thermal comfort in various sites of a hospital, and pointed out the thermal environment of wards was the best (PMV=0.44), and the lobby was the worst. In effect, the inpatient's health conditions are quite different from healthy people that conduces to the discrepancy between the metabolism of the former and that of the latter. Due to the same reason, the suffering always maintains postures of lying that result in thermal insulation differences. While Fanger's comfort model posited metabolic rate and clothing insulation as critical factors in determining the human body's steady-state heat balance, therefore, the conclusions of the literature mentioned above may need to be refined.

* Corresponding author at: School of Civil Engineering, Chongqing University, Chongqing 400045, China.
E-mail address: hlzhang@cqu.edu.cn (H. Zhang).

https://doi.org/10.1016/j.enbenv.2020.07.002
Available online 28 July 2020

Table 1
Field studies on thermal comfort in hospitals.

Authors	Region	Experiment sites	Subjects
Skoog et al. [4] (2005)	Sweden	Orthopaedics wards	Patients, staff
Hwang et al. [6] (2007)	Taiwan	Medical and surgical wards	Patients
Verheyen et al. [9] (2011)	Belgium	Wards (Maternity, oncology, neurology, gastro-enterology, abdominal surgery and thoraco-vascular surgery)	Patients
Pourshaghaghy et al. [5] (2012)	Iran	Wards, urgency, radiology, surgery, laboratory	Patients, staff, visitors
Lee et al. [7] (2015)	Korea	Wards, lobby, offices, restaurant	Patients, staff, visitors
Del Ferraro et al. [8] (2015)	Italy	Wards	Patients, staff
Lan et al. [10] (2017)	Singapore	Patient wards	Patients, staff
Alotaibi et al. [11] (2020)	Saudi Arabia	Patient wards	Patients

Del Ferraro et al. [8] studied on thermal responses of inpatients and medical staff in the hospital and pointed out that the gender and age should be considered assessing thermal comfort in the hospital. The authors also applied test results of Ling and Deng to evaluate the total thermal insulation of lying inpatients by adding merely the clothing thermal resistance and thermal resistance of the bedding system together. Verheyen et al. [9] assessed lying patients' thermal comfort using the Lin-Deng's comfort model in sleeping environments. However, the model used metabolism of 40 W/m^2 (approximately 0.7met) that were the metabolic rate of healthy people in a sleeping situation, and total clothing resistance included the addition of bedding system and clothing in brief. These researches considered the influence brought by metabolism and thermal heat resistance, respectively; nevertheless, they both didn't take the combination of the two factors into account meanwhile. ISO TS 14415 [46] and ASHARE 55 mentioned changes in thermophysiology, thermosensation, thermoregulatory responses and thermal comfort perception when the subjects are the disabled. In addition, ISO TS 14415 [46] also adds to the determination and interpretation of thermal comfort in the case of people with special requirements.

These thermal comfort models conventionally utilized were all developed basing on healthy people, but they may not be directly applicable to patients occupying in hospital environments. Therefore, It is necessary to study theoretically on a patients' thermal comfort and establish a reasonable evaluation model.

In this paper, a comfort equation applicable to inpatients (divided into seated and lying patient) was derived by conducting reasonable modifications to Fanger's comfort equation. PMV and PPD indexes for assessing the thermal comfort of patients can also be obtained. Further, in order to provide the usability and convenience for hospital managers and HVAC engineers, some comfort diagrams were developed through solving the comfort equation, which can be available to determine neutral thermal environments under typical conditions in summer and winter.

2. Improving model

Reviewed from the documents reported by Fanger [12], Gagge and Hardy [13], and Gagge and Nishi [14], it can be found that the calculation for all items of thermal equilibrium equation was based on the ASHRAE Handbook of Fundamentals [15]. Considering inpatients and healthy people's variations in metabolic rate and thermal resistance, this study based on the classical thermal comfort model introduced some modifications to meet the inpatient's actual conditions. The field survey was conducted in general wards in Chongqing, and the patients' comfort equation was validated by applying field subjective and objective test data.

2.1. Improving comfort equation for seated patients

The thermal exchange of the human body with the ambient environment is a combination of varieties of heat transfer. Based on this theory, the body's energy balance equation can be obtained. The mathematical description of energy balance for a human body and the various terms of the thermal equilibrium equation is described explicitly in the ASHRAE Handbook of Fundamentals [15]. The thermal equilibrium equation for the human body, per unit nude body surface area, may be written as follows:

$$M - W = C + R + E_{sk} + E_r + S \tag{1}$$

Where M is the metabolic heat production, W/m^2, W is the mechanical work accomplished, W/m^2; C is the convective heat exchange from the outside surface of the clothed body to air, W/m^2, R is the radiative heat exchange from the outside surface of the clothed body to surrounding, W/m^2, E_{sk} is the evaporative heat loss from body skin, W/m^2, E_r is the respiratory heat loss, latent and dry, W/m^2, and S is the heat storage, W/m^2.

Total evaporative heat loss from the skin E_{sk} divides into two parts, the heat loss of evaporation due to sweating regulation (E_{sw}) and the free diffusion of water via skin (E_{dif}). Here the clothing latent thermal resistance simplified as a set value in the general indoor environment, ignoring the impact of the normal perspiration on E_{dif}:

$$E_{dif} = 3.05\left(0.254t_{sk} - 3.335 - P_a\right) \tag{2}$$

Where P_a and t_{sk} are the water vapor pressure in ambient air and the skin temperature.

From the thermal equilibrium equation can find that respiration heat loss (E_r), values of t_{sk} and E_{rsw} that provide thermal comfort are all associated with the body's metabolism. Respiratory heat loss, E_r, is usually explicated by dry heat loss of respiration, C_{res}, and latent heat loss of respiration, E_{res}. The values of E_{res} and C_{res} are smaller than the other terms in the thermal equilibrium equation and can be estimated by the following equations:

$$E_{res} = 0.0173M\left(5.867 - P_a\right) \tag{3}$$

$$C_{res} = 0.0014M\left(34 - t_a\right) \tag{4}$$

Where t_a is the temperature of ambient air.

The values of t_{sk} and E_{sw} providing thermal comfort for inpatients are indicated as following [14]:

$$t_{sk} = 35.7 - 0.0275(M - W) \tag{5}$$

$$E_{sw} = 0.42(M - W - 58.2) \tag{6}$$

Therefore, the thermal comfort equation under the steady state [13]:

$$\begin{aligned}(M - W) = {} & C + R + 3.05\left[5.733 - 0.007(M - W) - P_a\right] \\ & + 0.42(M - W - 58.2) + 1.73 \times 10^{-2} M\left(5.867 - P_a\right) \\ & + 0.0014M\left(34 - t_a\right)\end{aligned} \tag{7}$$

There had been a lot of theoretical researches on patients' thermal comfort, and it is worth noting that these studies subjects were patients, but their metabolic rates without exception used metabolism data of healthy people recommended in ISO7730 [16]. The metabolic value of ISO7730 might bring about some false conclusions. Relevant researches showed that the patient's metabolic mechanism was significantly different from that of healthy people [17, 18]. The metabolic rates of patients were generally higher than that of healthy people. Surgery, trauma and infection such as stress often made the body metabolism rate increase [45]. It is evident that the body metabolic rate is one of the main factors influencing the heat balance of a human body, then there is a necessity to modify metabolic rate (*M*) so as to the heat balance equation to become applicable for patients.

Total energy expenditure (TEE) includes three parts, which are energy expenditure for physical activity (EEPA), basal energy expenditure (BEE) and specific dynamic action. BEE is the energy expenditure required for the maintenance of respiration, body temperature and other body's basic metabolic activities. It is closely related to resting energy expenditure. Due to the difficulty in measuring the value of BEE and it is almost equal to resting energy expenditure (REE), it can generally use REE instead of BEE. REE is the energy expenditure which required for a body to keep resting condition during 24 h. Main measurement methods of TEE [19, 20] are currently the calorimetric method (including direct and indirect measuring hot methods), the doubly labeled water method (DLW), the heart rate monitoring method (HRM). Other methods, such as motion sensors [21], the method of predictive equations [22–28] and self-report method [29-30], can also accurately measure TEE, but the method of motion sensors is not suitable to test inpatients' TEE. This study adopts the method of predictive equations because there are many difficulties for other methods to meet their test conditions.

There are many predictive equations for energy estimation of patients, including Harris-Benedict equation [22], Ireton-Jones equation [23], Penn State equation (2003) [24], Mifflin equation [25], Schofield equation [26], Owen equation [27], Swinamer Equation [28] etc. Yu and Zhang [31] found that Penn State equation (2003), Ireton-Jones 1992 equation can predict patients' resting energy expenditure more accurately after comprehensively analyzing these predictive equations in terms of accuracy and deviation. Penn State equation (2003) includes two variables, which are the highest temperature during 24 h and minute ventilation volume, and the two parameters are difficult to get. The main reason is that measuring the two parameters not only demands special instruments and the support of medical staff but also gets the permission of patients and their families. Therefore, Ireton-Jones 1992 equation was chosen to predict the patient's resting energy expenditure:

$$\text{Spontaneous breath}: \ \text{REE} = 629 - (11 \times \text{AGE}) + (25 \times G) - (609 \times \text{OB}) \tag{8}$$

Where REE is the resting energy expenditure, kcal/day, G is the body weight, kg, AGE is the age of the patient, and OB can be calculated as follow:

Table 2
Suggested PAL of inpatients.

Physical activity level	PAL Male	Female
Seated	1.45	1.40
Lying	1.30	1.25

$$\text{OB} = \begin{cases} 1, & BMI > 30 \\ 0, & else \end{cases} \tag{9}$$

$$\text{BMI}\left(\text{Body Mass Index}\right) = G/l^2 \tag{10}$$

Where l is the body height, m.

REE is the daily energy expenditure for a human body, but the metabolic rate in the thermal comfort equation is heat energy production per unit body surface area. Therefore, the metabolic rate of a human can be obtained, which is the value of REE divided by his body surface area. The most common measured formula of body surface area proposed by Du Bois [15] in 1916, it was described as follows:

$$A_D = 0.202 \times l^{0.725} \times G^{0.425} \tag{11}$$

Where A_D is the body surface area, m^2.

The basal metabolism accounts for about 60 –80% of the daily calorie energy expenditure for one person [20, 32]. It is influenced by the levels of physical activity and specific dynamic action. TEE is that REE multiplies by the corresponding physical activity level coefficient (PAL) (i.e., TEE = REE × PAL) [33]. Table 2 gives the suggested PAL of inpatients based on existing documents [33–35]. The general inpatient's metabolic rate (*M*) is that TEE divides by the body surface area (i.e., $M = \text{TEE}/A_D$).

Furthermore, the clothing thermal resistance of patients seated in chairs can be calculated by applying the following equation [36], and if chairs are cushioned, the additional insulation value of chair (0.15clo) can be taken into account [37]:

$$R_c = 0.161 + 0.835 \times \Sigma R_{clu} \tag{12}$$

Where R_c is the clothing thermal resistance, $(m^2 \cdot K)$ /W, R_{clu} is the thermal resistance of clothing, which constitutes garments ensemble, $(m^2 \cdot K)$ /W, and is valued according to the clothing checklist of the meter [36].

2.2. Improving comfort equation for lying patients

Thermal comfort model of professor Fanger is generally appropriate for idle state or near sedentary active states (such as reading or writing). Patients spend approximately all their time on bed rest in wards, and on this account, it is necessary to modify this thermal comfort model to become applicable to patients in bed. The Fanger's comfort model has four physical parameters that create the thermal environment (air temperature, mean radiant temperature, air velocity and air humidity) and two personal factors (activity level, the total resistance of garments). The main differences between patients' thermal comfort model and the health's are metabolism and thermal resistance of clothing. In consideration of lying patients, it is not enough to only take the thermal resistance of clothing into account. Lin and Deng deduced a comfort equation in the sleeping environment by introducing the total resistance R_t which is affected by quilt, sleepwear, mattress, air velocity, lying posture and the coverage rate of the human body surface with quilt and bed, etc. [38]. The thermal comfort equation of lying patients can be got by modifying the metabolism based on the Lin-Deng's comfort model in sleeping environments [38], which is as follows:

$$M - W = \frac{1}{R_T}\left[\left(t_{sk,req} - t_o\right) + 3.762\left(p_{sk,s} - p_a\right)\right] + 0.0014M\left(34 - t_a\right) + 0.0173M\left(5.87 - p_a\right) \tag{13}$$

Where W is the accomplished mechanical work, about zero at rest state. R_T is the total thermal resistance of a clothed body at different bedding systems. $t_{sk, req}$ and t_o are the mean skin temperature required for comfort and the operative temperature, and can be calculated as follow:

$$t_{sk,req} = 35.7 - 0.0275(M - W) \tag{14}$$

$$t_o = \frac{h_r \overline{t_r} + h_c t_a}{h_r + h_c} \tag{15}$$

Where $\overline{t_r}$ is the temperature of mean radiant, h_c and h_r are the convective heat transfer coefficient at surface and radiative heat transfer coefficient.$p_{sk, s}$ is the water vapor pressure in saturated air at t_{sk}.

It is noted that the lying patient's metabolism should be calculated based on the mentioned above, but the total thermal resistance of lying patients cannot only add the clothing thermal resistance and thermal resistance of the bedding system together. Patients can lie on beds in the supine position, lateral position or reclining position; the total thermal resistance will be different under different lying postures even if the clothing and bedding system is the same. The total thermal resistance can be theoretically calculated by simplifying the complex heat transfer, and the following assumptions were made [40].

The heat flow Q from the lying human body to its environment divided into seven parts, which were: Q_1 through the part of the nude skin surface which contacts directly with quilts; Q_2 to the air layer which was consisted of the nude skin surface, quilt and mattress; Q_3 through the bed with mattress; Q_4 directly from the nude skin surface (such as the head) to ambient air; Q_5 directly from the clothed body to ambient air; Q_6 to the air space consisted by part of the clothed body, quilt and mattress; Q_7 through the part of the clothed body, which contacts closely with quilts. In this study, Pan's thermal resistance equation was improved according to real cases of patients. Firstly, human body was divided into two parts (the upper body and lower body), and the angle of reclining φ (angle between upper body and bed) was introduced to calculate the thermal resistance of all postures, including reclining posture. Then the percentage of the surface area of each body parts under supine posture was obtained by McCullough et al.'s research [41]. Thus the percentage of the surface area of each body segment under different lying postures was deduced.

Assuming no heat transferred from human body to mattress under steady-state states [42], therefore the thermal resistance of mattress (R_3) would approach to infinity, the thermal resistance equation for lying patients is obtained according to the Pan's study [39]:

$$R_T = R_{T,1} + R_{T,2} \tag{16}$$

$$\frac{1}{R_{T,j}} = \frac{\alpha_1}{R_1} + \frac{\alpha_2}{R_2} + \frac{\alpha_4}{R_4} + \frac{\alpha_5}{R_c + R_4} + \frac{\alpha_6}{R_c + R_2} + \frac{\alpha_7}{R_c + R_1} \tag{17}$$

$$R_b = 0.03984 \times H_{fab} \tag{18}$$

$$R_1 = R_b + \frac{1}{h} + \frac{1}{h_c} \tag{19}$$

$$R_2 = R_b \cdot \sin\theta \tag{20}$$

$$R_4 = \frac{1}{h} \tag{21}$$

$$h = h_c + h_r \tag{22}$$

Table 3
Body surface area of body segment relating to each α_i for patients shown as Fig. 3.

	$\alpha_1 + \alpha_2$	α_4	α_5	$\alpha_6 + \alpha_7$
Half-sleeved gowns	⑥, ⑧, ⑩, ⑪	①, ②	③	④, ⑤, ⑦, ⑨
Long-sleeved gowns	⑧, ⑪	①, ②	③	④, ⑤, ⑥, ⑦, ⑨, ⑩

Where $R_{T, 1}$ and $R_{T, 2}$ are the total thermal resistance of the upper and lower body on beds. α_i is the fraction of surface area of the body segment to the whole body surface area corresponding to Q_i.R_b is the total thermal resistance of the quilt, H_{fab} is the quilt thickness.h is the composite heat transfer coefficient. θ is the angle between the quilt and the bed.

Pan et al. [39, 40] simplified the bedding system related Q_2 or Q_6 as a triangular air layer which consists of the human body surface, the mattress and the quilt, then the relation between A_q and A_b is as follow:

$$\frac{A_b}{A_q} = \sin\theta \tag{23}$$

Where A_q and A_b are the surface area of the quilt related and human body related.

Based on the Pan et al.'s study, θ was approximately taken as 30° for a patient with a supine position and 60° for a patient with lateral position. If a patient were lying with a reclining position, θ would change with the change of φ, as shown in Fig. 1. When the angle of reclining exceeds a specific value ($\varphi > 60°$), the upper body is usually not covered by a quilt, and there are only Q_4 and Q_5 existed, and the value of θ does not make sense.

In the deductive process of the thermal resistance equation, Pan et al. [40] assumed that the body's cross-section was approximately to be a rectangle and the ratio between width and thickness of the human body (a: b) was about 3:1. Fig. 2 showed the percentage of surface area for each body parts in reclining or supine decubitus position obtained according to McCullough et al.'s research, the corresponding data in lateral decubitus position is also worked out by modifying the data of supine posture. The percentage of skin surface covered only by quilt ($\alpha_1 + \alpha_2$), percentage of nude body surface (α_4), percentage of clothed body surface (α_5) and percentage of clothed body surface covered by quilt ($\alpha_6 + \alpha_7$), all can be obtained by adding percentages of surface area with corresponding body segments together based on the actually covered situations. For example, a supine patient who is as shown in Fig. 3, the body surface area of body segment relating to each α_i can be obtained based on Table 3.

According to pan's study [39], the relation between α_1 and α_2, α_6 and α_7 were as follow:

$$\frac{\alpha_7}{\alpha_6} = \frac{\alpha_1}{\alpha_2} = \begin{cases} \frac{a}{2b} = \frac{3}{2}, & \textit{reclining or supine position} \\ \frac{b}{2a} = \frac{1}{6}, & \textit{lateral position} \end{cases} \tag{24}$$

Therefore, no matter what a lying patient is decubital, Eq. (16_–(22) can calculate theoretically total thermal resistance of the clothed body at different bedding systems combined with the field test.

2.3. PMV and PPD index

Fanger proposed PMV and PPD index, which can predict the mean thermal response of people on the basis of the thermal sensation scale in ASHRAE. Furthermore, the related the values of PMV to the disequilibrium of the practical heat flow of the human body with a given environment. The heat sensitive coefficient (β) in PMV formula is only related to the patients' metabolism. In this study, due to considering the metabolic difference between healthy people and patients, so the heat flow satisfying requirement of optimum comfort at a particular activity

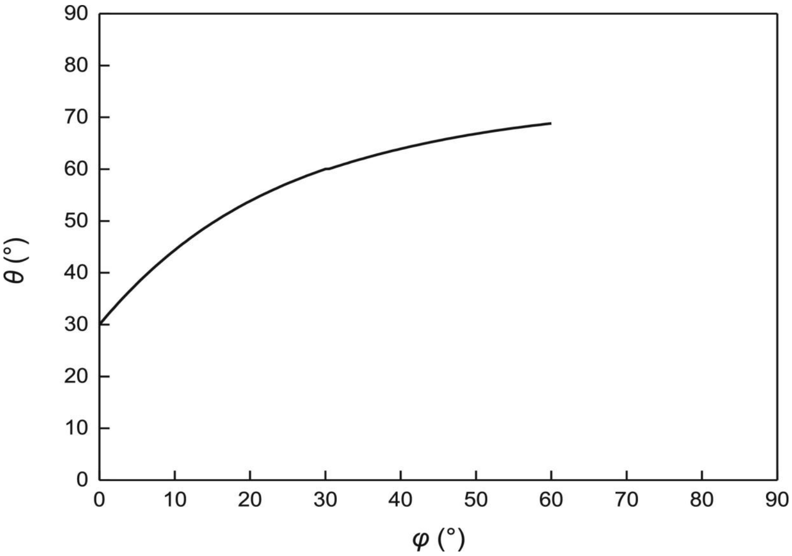

Fig. 1. Relation between the angle of reclining (φ) and θ.

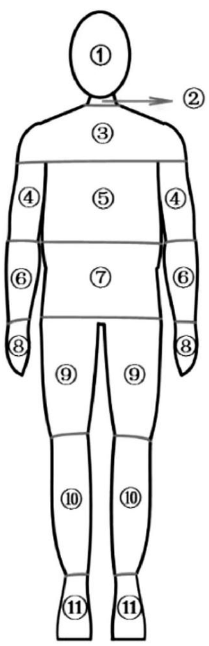

		Supine	Lateral
	α_3	23.3%	12.3%
①	α_{head}	5.3%	5.3%
②	α_{neck}	0.6%	0.6%
③	$\alpha_{shoulder}$	8.2%	9.8%
④	$\alpha_{upper\text{-}arms}$	4.3%	3.6%
⑤	α_{chest}	10.8%	18%
⑥	$\alpha_{lower\text{-}arms}$	4%	3.3%
⑦	$\alpha_{abdomen}$	7.7%	12.8%
⑧	α_{hands}	4.6%	4.6%
⑨	α_{thighs}	14.3%	14%
⑩	α_{shanks}	10.9%	10.8%
⑪	α_{feet}	6%	4.9%

Fig. 2. Percentage of surface area for each body parts (excluding part contacted the mattress α_3).

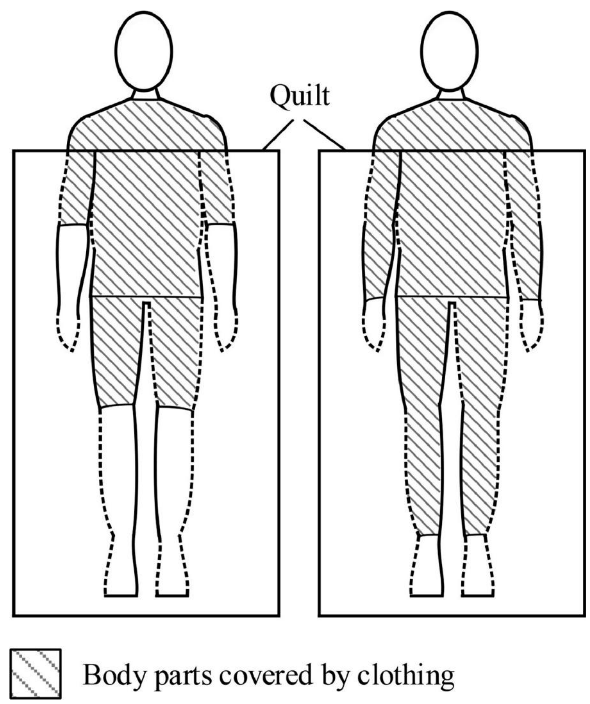

Fig. 3. The quilt coverage of a patient with half-sleeve or long-sleeved gowns in the supine position.

can be adopted as following [12]:

$$\text{PMV} = \left[0.303\exp(-0.036M) + 0.028\right]L = \beta L \quad (25)$$

Where β is the sensitivity coefficient. L is the thermal load of the human body, which is the difference between the left-side and the right-side of the comfort equation.

$$\text{PPD} = 100 - 95\exp\left[-\left(0.03353\text{PMV}^4 + 0.2179\text{PMV}^2\right)\right] \quad (26)$$

In Eq. (25)The patients' thermal load (L) can be calculated using Eq. (7) for patients in chairs or Eq. (13) for patients in beds.

3. Model verification

In order to verify the modified models, a series of field studies, which included the subjective survey and the physical environment parameters measurement, had been organized and carried out. Data analysis was conducted to survey whether the actual thermal senses and acceptability of inpatients to their thermal environment were significantly different from the PMV and the PPD calculated by the model in this paper.

3.1. Data collection

The field studies were conducted in wards of 4 general hospitals in Chongqing from December 2015 to January 2016 (winter) and June 2016 to July 2016 (summer). The central air-conditioning systems were on during the field experiment periods. The questionnaire was designed based on the Thermal Environment Survey in ASHRAE Standard 55 [42], including gender, age, height, weight, patient's thermal sensation and so on. A total of 370 sets of valid data (120 in winter and 250 in

Table 4
The number of different weight samples corresponding to different metabolic ranges.

Weight	<=40kg	40–50 kg	50–60 kg	60–70 kg	>70 kg
Summer					
<35 W/m^2	13	21	3	0	0
35<,<50 W/m^2	1	59	139	119	29
>50 W/m^2	0	0	6	10	12
Winter					
<35 W/m^2	7	24	4	0	0
35<,<50 W/m^2	0	49	102	100	30
>50 W/m^2	0	0	2	5	9

Table 5
The number of different age samples corresponding to different metabolic ranges.

Age	<=45	45–55	55–65	65–75	>75
Summer					
<35 W/m^2	0	4	9	24	0
35<,<50 W/m^2	124	112	75	36	0
>50 W/m^2	27	1	0	0	0
Winter					
<35 W/m^2	0	1	13	21	0
35<,<50 W/m^2	110	64	78	29	0
>50 W/m^2	16	1	0	0	0

summer) were obtained. Tables 4 and 5 list physiologic data of patients collected in this filed study.

Environmental key parameters were measured, including black bulb temperature, air temperature, air humidity, air velocity and so on. Table 6 shows measurement instruments of field test. The measuring equipment was placed in the zone of 1 m around the patients. Table 6 lists instruments used for measurement of environmental parameters. For seated patients, the measuring heights were 0.6 m; for lying patients, 0.2 m higher than bed-level. All the equipment used in the study meet GBT 50785–2012 in China [43].

3.2. Data analysis

Statistical analysis was conducted utilizing the parameter test (i.e., two samples *t*-test, binomial test). Two sample t-tests were performed on the thermal senses to reveal whether the thermal senses predicted vote (PMV) calculated by modified models and actual thermal senses (AMV) have a significant difference on a 5% level. The binomial test is performed to determine whether the PPD calculated from Eq. (16) and PPD_T obtained from subjective dissatisfied votes have a significant difference on a 5% level. The data analysis methods are consistent with those described in ISO 10551 [44].

Values in Table 7, including mean PMV, STD PMV and PPD were based on data of inpatients' PMV values which were calculated using the method mentioned in this paper based on the objective measurement data. The value of mean AMV, STD AMV calculated from personal thermal sensation votes and Mean PPD_T calculated from personal subjective dissatisfied votes.

Table 7 showed that mean PMV calculated by modified models and mean AMV for inpatients were almost no significantly different. This indicated that predicting the patient's thermal sensation can be made using the improved inpatient's thermal comfort model presented in this paper. Further analysis reveals that the seated patients' mean subjective thermal senses were little higher than the predicted mean votes, but the lying patients' were little lower than the predicted mean votes. it was resulted from their difference of health status.

Two-sample t-tests showed that individual AMV and individual PMV were not significantly different on a 5% level for all inpatients in general wards except for seated patients in winter. A second analysis of t-tests was conducted using the same methods but after rejecting outliers, which judged by Grubbs' test on a 5% significance level. The results remained the same. This indicated that the accuracy of the improved model was high when applying to evaluate the patients' thermal comfort.

Binomial tests revealed PPD calculated according to Eq. (26). Moreover, PPDT obtained from subjective thermal dissatisfied votes had no significant difference, which meant that the calculation method for PPD by Eq. (25) could be used to predict thermal dissatisfied degrees for inpatients in general wards concluded in this study.

4. Results and discussion

4.1. Comfort diagrams of different metabolic rate, wet bulb temperature, operative temperature

There are numerous combinations of parameters (such as operative temperature, relative humidity, patients' metabolism, the total thermal resistance and so on) that may satisfy the optimal comfort conditions for patients in wards. An EXCEL calculation program was developed to solve the patients' comfort equation at different combinations of parameters, and comfort charts were drawn by the software of Origin 9.0. Comfort charts (Figs. 4–7) were established under two typical thermal resistances of winter and summer, which could be used for determining thermal neutrality environments under one given patient's metabolic rate. The program can also apply to establish more comfort charts for patients with other thermal resistance values and metabolic rates in further study.

Figs. 4–7 illustrate the comfort diagrams were established by the optimal combination of wet bulb temperature, operative temperature and patient's metabolic rate; under that case thermal neutral environment can be achieved. Fig. 4 is a comfort chart for the seated patient in winter (the patient's clothing thermal resistance is 1.1 clo on average), and Fig. 5 is for the seated patient in summer (the patient's clothing thermal resistance is 0.6 clo on average). Fig. 6 is a comfort chart for lying patients in winter (the patient's total thermal resistance is 2.8 clo on average) and Fig. 7 is for lying patient in summer (the patient's total thermal resistance is 1.9 clo on average). The total thermal resistance of lying patients is higher than the clothing thermal resistance of seated patients.

It can be seen from Figs. 4 and 5 that the change of relative humidity influences operative temperature for a seated patient more greatly. A change from dry environment to thoroughly moist environment (RH = 0–100%) can be offset by only 2.4–3.4 °C in winter and 2.2–2.8 °C in summer (at the range of 40–90 W/m^2 metabolic rate) reduction of operative temperature. The higher the patient's metabolic rate, the more the reduction of operative temperature. For example, when changing relative humidity from 0% to 100% in winter, if the patient's metabolic rate is 40 W/m^2, 3.4 °C decrease of operative temperature will adequately offset its influence, but 2.7 °C decrease of operative temperature if the metabolic rate is 90 W/m^2.

From Figs. 6 and 7, it is easy to see that the change of relative humidity weakly influences the optimal temperature for a lying patient, which is different from the seated patient. A change from dry environment to thoroughly moist environment (RH = 0–100%) can be offset by only 1.1–1.7 °C in winter and 1.5–1.9 °C in summer (at the range of 30–60 W/m^2 metabolic rate) decrease of operative temperature. This analysis means that thermo-neutral temperatures are rarely affected by relative humidity when the thermal resistances are large enough.

From Figs. 6 and 7, it is observed that the influence of thermal resistance on the thermo-neutral environment for inpatients. For example, thermo-neutral temperatures are 28.9 °C and 27.1 °C at the clothing thermal resistance of 0.6 clo and 1.1 clo respectively for a seated patient with 40 W/m^2 metabolic rate at 60% relative humidity, and 24.8 °C and 20.4 °C at the total thermal resistance of 1.9 clo and 2.8 clo respectively for a lying patient at the same condition. This result indi-

Table 6
Measurement instruments of field test.

Instrument	Measurement	Range	Precision	Accuracy
KANOMAX thermal environment tester (A531)	temperature	0~60 °C	±0.5 °C	0.1 °C
	humidity	2~98%	2~80%:±2% 80~98%:±3%	0.1%
	air velocity	0.1~30 m/s	±0.15 m/s	0.01 m/s
Black bulb thermometer	radiant temperature	−100~+400 °C	±0.3 °C	0.1 °C

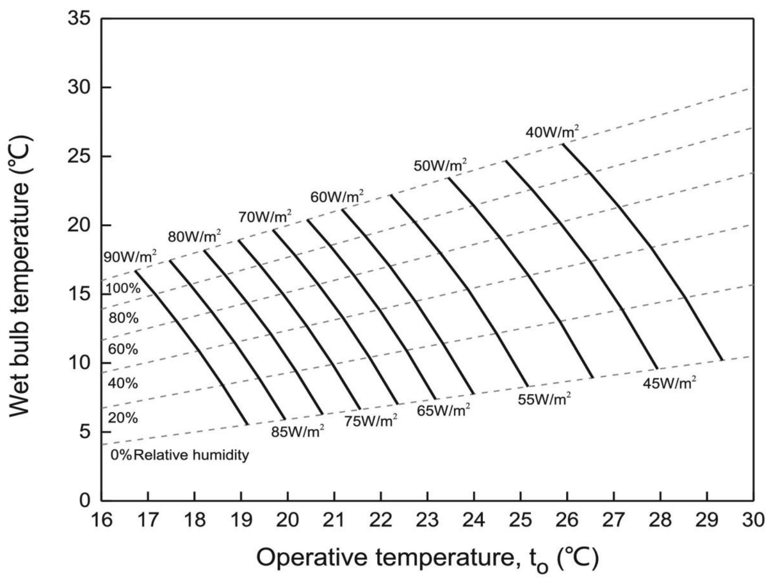

Fig. 4. Comfort diagrams for seated patients in winter (1.1clo, air speed ≤ 0.15 m/s).

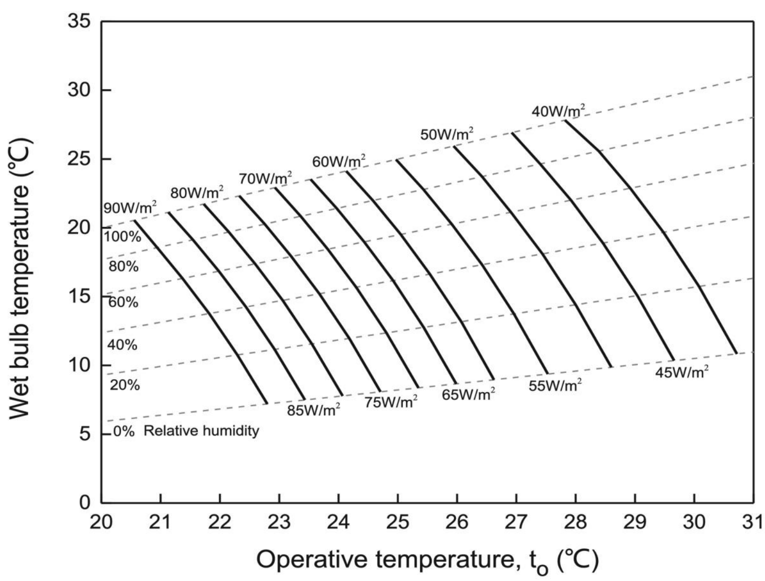

Fig. 5. Comfort diagrams for seated patients in summer (0.6clo, airspeed ≤ 0.15 m/s).

cates a strong negative correlation between thermo-neutral temperature and total thermal resistance.

4.2. Comfort diagram of different metabolic rates, clo-value and operative temperature

Fig. 8 is a comfort chart for inpatients when airspeed is not greater than 0.15 m/s, and relative humidity is 60%. The comfort diagrams corresponding to different patient's metabolic rates are curves through different combinations of clo-value and operative temperature, under which thermal neutrality can be achieved. The thermo-neutral temperature of inpatients can be obtained from this diagram under a given condition of total thermal resistance and metabolism. For example, a lying patient is clothed in 1.9 clo and 40 W/m^2 metabolic rate. From Fig. 8, the operative temperature, which provides thermal comfort, is 24.8 °C. Compared to healthy people in the sleeping environment [38], when the thermo-neutral temperature 25.3 °C for a person with metabolic rate is 40 W/m^2 and 1.9 clo total thermal resistance at 60% relative humidity, there is 0.5 °C reduction of operative temperature caused by relatively high patient's metabolic rate.

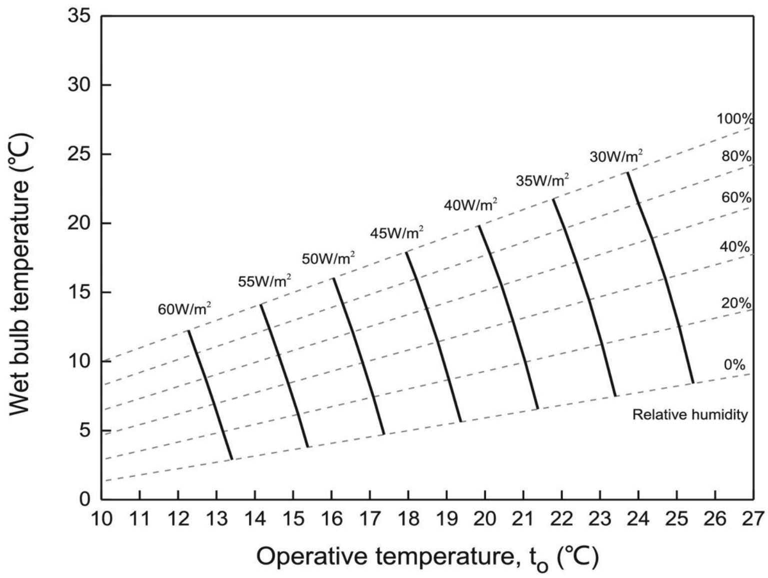

Fig. 6. Comfort diagrams for lying patients in winter (2.8clo, air speed ≤ 0.15 m/s).

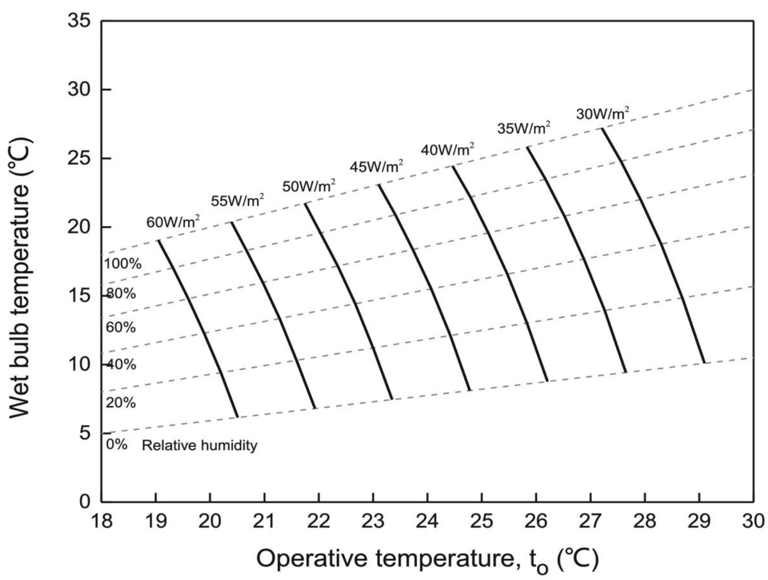

Fig. 7. Comfort diagrams for lying patients in summer (1.9clo, airspeed ≤ 0.15 m/s).

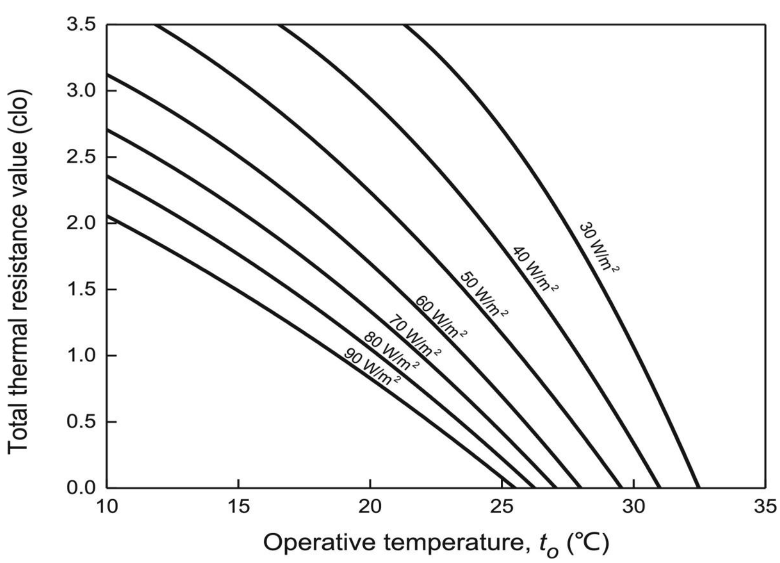

Fig. 8. Relationship between t_o and the total thermal resistance value (60% relative humidity and airspeed ≤ 0.15 m/s).

Table 7
Comparation between actual subjective thermal responses and objective results calculated by predicted equation.

a 5% significance level		Number of samples	Mean PMV	Mean AMV	STD PMV	STD AMV	Difference between PMV and AMV (Two-sample t-test)	Mean PPD	Mean PPD_T	Difference between PPD and PPD_T (Binomial test)
Winter	Seated patient	20	−0.07	0.2	0.12	0.17	Significant ($p = 0.026$)	9.22	10.10	Not significant ($p = 0.538$)
	Lying patient	100	0.35	0.24	0.26	0.21	Not significant ($p = 0.071$)	10.47	11.20	Not significant ($p = 0.670$)
Summer	Seated patient	50	−0.11	0.06	0.18	0.10	Not significant ($p = 0.052$)	6.13	8.84	Not significant ($p = 0.521$)
	Lying patient	200	0.25	0.18	0.32	0.34	Not significant ($p = 0.055$)	9.65	10.42	Not significant ($p = 0.555$)

Note: STD = standard deviation.

5. Conclusions

A comfortable thermal environment of wards should meet patients' thermal comfort, it needs to clear on the patients' thermal comfort requirements to create the environment. Nowadays, thermal comfort studies for patients were limited, and there was not yet a document to elaborate on the patients' thermal comfort theory. The thermal comfort equation of ASHRAE standard is based on healthy people, and this theory possibly does not apply for inpatients.

Inpatients are mainly in a state of rest in the ward spending most of the time lying on the bed in the supine position, lateral position or reclining position; at the other time, they are sitting in the chair. The theoretical calculation methods of total thermal resistance were studied for inpatients in different postures. Usually, the patient's metabolism is slightly higher than the health's. In this paper, improving patients' thermal comfort model had been obtained by introducing a reasonable predictive equation of the patient's metabolism and calculation model of thermal resistance for patients. Compared to the metabolic rate measurement such as heart rate monitoring and oxygen consumption presented in ISO 8996 [19], the accuracy of equation evaluation in this paper might not be enough, some further study is in demand.

Two-sample t-tests show that the value of AMV and PMV is not significantly different on a 5% significant level for all individual patients except for seated patients in winter. Binomial tests reveal PPD calculated from predicted tools in this study, and PPD obtained from subjective thermal dissatisfied votes have no significant difference. These mean that the calculation method for PMV and PPD based on this paper can be applied to predict mean thermal senses and the degree of dissatisfaction for inpatients of general wards.

Based on the comfort equation for patients, comfort charts have been established under two typical thermal resistances of winter and summer. The comfort charts can be available to determine thermal neutral environmental conditions of patients under the given metabolism and total thermal resistance. Furthermore, if requiring of assessing patients' thermal comfort, PMV-PPD indexes can be obtained as well by the calculation method of this study.

The results of the study can be applied as the theoretical basis for establishing criteria on patients' thermal comfort in hospital wards and can offer reference to the environmental control system design and management for general wards.

Declaration of Competing Interest

We declare that we have no competing interests with other people or organizations.

CRediT authorship contribution statement

Hualing Zhang: Conceptualization, Methodology, Supervision, Writing - original draft, Funding acquisition. **Xunshu Xie:** Resources, Data curation, Writing - original draft, Writing - review & editing. **Shiyao Hong:** Software, Formal analysis, Investigation, Writing - original draft. **Haitao Lv:** Resources, Data curation, Writing - original draft.

Acknowledgment

The authors offer sincere appreciation to all occupants of the hospital surveyed. This work is supported by Fundamental Research Funds for Central Universities of "The combination of medicine and engineering" (2019CDYGYB026) and the National Science Foundation of China (No. 51278506).

References

[1] J. Khodakarami, N. Nasrollahi, Thermal comfort in hospitals – a literature review, Renew. Sustain. Energy Rev. 16 (6) (2012) 4071–4077.

[2] C. Carvalhais, J. Santos, Vieira dSM, Analytical and subjective interpretation of thermal comfort in hospitals: a case study in two sterilization services, J. Toxicol. Environ. Health Part A 79 (7) (2016) 299–306.
[3] F. Azizpour, S. Moghimi, E. Salleh, S. Mat, C.H. Lim, K Sopian, Thermal comfort assessment of large-scale hospitals in tropical climates: a case study of University Kebangsaan Malaysia Medical Centre (UKMMC), Energy Build. 64 (5) (2013) 317–322.
[4] J. Skoog, N. Fransson, L Jagemar, Thermal environment in Swedish hospitals: summer and winter measurements, Energy Build. 37 (8) (2005) 872–877.
[5] A. Pourshaghaghy, M. Omidvari, Examination of thermal comfort in a hospital using PMV-PPD model, Appl. Ergon 43 (6) (2012) 1089–1095.
[6] R.L. Hwang, T.P. Lin, M.J. Cheng, J.H Chien, Patient thermal comfort requirement for hospital environments in Taiwan, Build. Environ. 42 (8) (2007) 2980–2987.
[7] B. Lee, J. Kim, K.S. Kim, H. Kim, K Lee, Assessment of thermal comfort in a general hospital in winter using predicted mean Vote (PMV), J. Environ. Health Sci. 41 (6) (2015) 389–396.
[8] S. Del Ferraro, S. Iavicoli, S. Russo, V Molinaro, A field study on thermal comfort in an Italian hospital considering differences in gender and age, Appl. Ergon 50 (2015) 177–184.
[9] J. Verheyen, N. Theys, L. Allonsius, F Descamps, Thermal comfort of patients: objective and subjective measurements in patient rooms of a Belgian healthcare facility, Build. Environ. 46 (5) (2011) 1195–1204.
[10] Lan Lan, Wayes Tushar, Kevin Otto, Chau Yuen, Thermal comfort improvement of naturally ventilated patient wards in Singapore, Energy Build 154 (2017) 499–512.
[11] Badr S. Alotaibi, Stephen Lo, Edward Southwood, Evaluating the suitability of standard thermal comfort approaches for hospital patients in air-conditioned environments in hot climates, Build. Environ. 169 (2020).
[12] P.O Fanger, Thermal Comfort, Danish Technical Press, Copenhagen, 1970.
[13] A.P. Gagge, J.D. Hardy, Thermal radiation exchange of the human by partitional calorimetry, J. Appl. Physiol. 23 (2) (1967) 248–258.
[14] A.P. Gagge, Y Nishi, Heat exchange between human skin surface and thermal environment, Handbook of Physiology, Reaction to Environment Agents, American Physiological Society, 1977 Chapter5.
[15] Handbook of Fundamentals. American Society of Heating, Refrigerating and Air Conditioning Engineers, Inc, Atlanta, 2017.
[16] ISO. ISO Standard 7730. Moderate thermal environments e determination of PMV and PPD indices and specification of the conditions for thermal comfort. Geneva, Switzerland: International Organization for Standardization; 2005.
[17] M. Merli, O. Riggio, R. Servi, A. Zullo, S.A. De, A.F. Attili, L Capocaccia, Increased energy expenditure in cirrhotic patients with hepatocellular carcinoma, Nutrition 8 (5) (1992) 321–325.
[18] L.S. Brandi, M. Oleggini, S. Lachi, M. Frediani, S. Bevilacqua, F. Mosca, E Ferrannini, Energy metabolism of surgical patients in the early postoperative period: a reappraisal, Crit. Care Med. 16 (1) (1988) 18–22.
[19] ISO. ISO8996, Determination of Metabolic Rate. 2004.
[20] M. Mccloskey, A.O. Redmond, S. Pyper, C. Mccabe, K.R. Westerterp, J.S Elborn, Total energy expenditure in stable patients with cystic fibrosis, Clin. Nutr. 20 (3) (2001) 235.
[21] G. Plasqui, K.R. Westerterp, Physical activity assessment with accelerometers: an evaluation against doubly labeled water, Obesity 15 (10) (2007) 2371–2379.
[22] J.A. Harris, F.G. Benedict, A Biometric Study of Basal Metabolism in Man, Carnegie Institute, Washington, DC, 1919 Publication No. 279.
[23] C.S. Ireton jones, W.W. Turner Jr, G.U. Liepa, C.R Baxter, Equations for the estimation of energy expenditures in patients with burns with special reference to ventilatory status, J. Burn Care Rehabil. 13 (3) (1992) 330–333.
[24] D.C. Frankenfeild, W.A. Rowe, J.S. Smith, R.N Cooney, Validation of several established equations for resting metabolic rate in obese and non-obese people, J. Am. Diet Assoc. 103 (9) (2003) 1152–1159.
[25] M.D. Mifflin, S.T. St Jeor, L.A. Hill, B.J. Scott, S.A. Daugherty, Y.O Koh, A new predictive equation for resting energy expenditure in healthy individuals, Am. J. Clin. Nutr. 93 (4) (1990) 241–247.
[26] W.N Schofield, Predicting basal metabolic rate, new standards and review of previous work, Hum. Nutr. Clin. Nutr. 39 (Suppl 1) (1985) 5–41.
[27] O.E. Owen, J.L. Holup, D.A. Dalessio, E.S. Craig, M. Polansky, K.J. Smalley, E.C. Kavle, M.C. Bushman, L.R. Owen, M.A. Mozzoli, Z.V. Kendrick, G.H Boden, A reappraisal of the caloric requirements of men, Am. J. Clin. Nutr. 46 (6) (1987) 875–885.
[28] D.L. Swinamer, M.G. Grace, S.M. Hamilton, R.L. Jones, P. Roberts, E.G King, Predictive equation for assessing energy expenditure in mechanically ventilated critically ill patients, Crit. Care Med. 18 (6) (1990) 657–661.
[29] L.E. Bratteby, B. Sandhagen, H. Fan, G Samuelson, A 7-day activity diary for assessment of daily energy expenditure validated by the doubly labelled water method in adolescents, Eur. J. Clin. Nutr. 51 (9) (1997) 585–591.
[30] R.R. Pate, Physical activity assessment in children and adolescents, Crit. Rev. Food Sci. Nutr. 33 (4–5) (1993) 321–326.
[31] J. Yu, H.L. Zhang, Thermal comfort of the patients and its influence bout evaluating of thermal environment, Refrig. Air Cond. 5 (2015) 505–508.
[32] T.M Manini, Energy expenditure and aging, Ageing Res. Rev. 9 (1) (2010) 1.
[33] Chinese Nutrition Society, Chinese dietary reference intakes, DRIs, Chin. J. School Health 23 (3) (2002) 193–196.
[34] A.E. Black, W.A. Coward, T.J. Cole, A.M Prentice, Human energy expenditure in affluent societies: an analysis of 574 doubly-labelled water measurements, Eur. J. Clin. Nutr. 50 (2) (1996) 72–92.
[35] C.J. Crespo, S.J. Keteyian, G.W. Heath, C.T Sempos, Leisure-time physical activity among US adults. Results from the Third National Health and Nutrition Examination Survey, Arch. Intern. Med. 156 (1) (1996) 93–98.
[36] ISO. ISO 9920, Ergonomics of the Thermal Environment – Estimation of Thermal Insulation and Water Vapour Resistance of a Clothing Ensemble. 2007.
[37] Brager G., Fountain M., Benton C., Arens E.A., Bauman F. A Comparison of Methods for Assessing Thermal Sensation and Acceptability in the Field. 1993.
[38] Z.P. Lin, S.M. Deng, A study on the thermal comfort in sleeping environments in the subtropics - Developing a thermal comfort model for sleeping environments, Build. Environ. 43 (1) (2008) 70–81.
[39] D.M. Pan, Study On Human Thermal Comfort in Sleep Environment, Tongji University, China, 2009, pp. 21–30.
[40] D.M. Pan, Z.P. Lin, S.M Deng, A mathematical model for predicting the total insulation value of a bedding system, Build. Environ. 45 (8) (2010) 1866–1872.
[41] E.A. McCullough, P.J. Zbikowski, B.W Jones, Measurement and prediction of the insulation provided by bedding systems, ASHRAE Trans. 93 (Part 1) (1987) 1055–1068.
[42] ASHRAE. ANSI/ASHRAE Standard 55-2017, Thermal environmental Conditions for Human Occupancy, 2017.
[43] GBT 50785-2012, Evaluation Standard for Indoor Thermal Environment in Civil Buildings. China; 2012.
[44] ISO. ISO 10551, Ergonomics of the Thermal Environment – Assessment of the Influence of the Thermal Environment Using Subjective Judgement Scales. 2001.
[45] G. Kreymann, M. Adolph, M.J Mueller, Working group for developing the guidelines for parenteral nutrition of The German Association for Nutritional Medicine. Energy expenditure and energy intake – guidelines on parenteral nutrition, German Med. Sci. 7 (25) (2009) 1–23.
[46] ISO. ISO TS 14415, Ergonomics of the Thermal Environment – Application of the International Standards to People with Special Requirements, 2005.